

AD636981

AFFDL-TR-65-36

**INVESTIGATION OF HYPERSONIC INLET  
SHOCK-WAVE BOUNDARY LAYER INTERACTION**

**PART II**

CONTINUOUS FLOW TEST AND ANALYSES

Paul H. Kutschenreuter, Jr.

David L. Brown, Werner Hoelmer, et al

Distribution of this document is unlimited

CLEARING HOUSE FOR FEDERAL SCIENTIFIC AND TECHNICAL INFORMATION			
Hardcopy	Microfiche		
\$6.00	\$1.25	263	pp 25
1 ARCHIVE COPY			

**INVESTIGATION OF HYPERSONIC INLET  
SHOCK-WAVE BOUNDARY LAYER INTERACTION**

**PART II**

**CONTINUOUS FLOW TEST AND ANALYSES**

Paul H. Kutschenreuter, Jr.

David L. Brown, Werner Hoelmer, et al

Distribution of this document is unlimited

## FOREWORD

This report was prepared by the Advanced Technology and Demonstrator Programs Department of the General Electric Company, Evendale, Ohio for the Air Force Flight Dynamics Laboratory, Research and Technology Division, Air Force Systems Command, United States Air Force, on Contract AF33(657)-11747. The contract was initiated under Project 651-E. The inclusive dates of over-all program activity were July 1963 to April 1966.

The investigations reported herein cover the final part of a two-phase program. The results of the Phase I program were documented earlier in AFFDL-TR-65-36, "Investigation of Hypersonic Inlet Shock-Wave Boundary Layer Interaction", dated March 1965. Phase II studies were conducted with supplementary funding from the NASA Ames Research Center. Mr. L. E. Surber of the Air Force Flight Dynamics Laboratory's Internal Aerodynamic Section was the project monitor for both the Phase I and Phase II activities.

The principal investigators participating in this Phase II research for the General Electric Company were Messrs. Paul H. Kutschenreuter, Jr., David L. Brown, and Werner Hoelmer. Special acknowledgement is made of the assistance provided by Messrs. James S. Keith, Paul H. Nettleton, and James A. Weil.

The manuscript was released by the authors for publication as an RTD Technical Report.

This technical manuscript release statement report has been reviewed and is approved.

*for*   
Philip P. Antonatos  
Chief, Flight Mechanics Division  
Air Force Flight Dynamics Laboratory

## ABSTRACT

The final phase of a two part investigation of hypersonic shock-wave boundary layer interaction effects from a secondary shock system on supersonic/hypersonic combustion inlet performance has been completed. In support of this effort, the following has been accomplished:

1. The computational procedure developed in Phase I for estimating laminar boundary layer properties through impinging shock induced laminar boundary layer interactions has been modified to account for entropy change of the inviscid streamlines in that isentropic assumptions were used in the initial formulation. Perturbation studies on the effects of wall shear on interaction length have identified the importance of the profile shape factor in such calculations. Initial correlations have been developed, on the basis of solutions obtained with the formulated program, for making rapid estimates of wall pressure distributions through the interaction region for cases where the laminar boundary layer remains attached. A Users' Manual for the laminar computational program is contained herein.
2. Three incident shock models were designed for use in the experimental program conducted in the Ames 3.5 Foot Hypersonic Tunnel. Tests with the resulting models provided laminar and turbulent boundary layer shock induced separation data including direct measurements of up and downstream boundary layer profiles as well as wall static pressure distributions through the interaction region. Results of subsequent data analysis were compared with applicable theories for predicting boundary layer separation characteristics.
3. Aided by analysis of the experimental data, a simplified flow model was formulated for the case of a two-dimensional turbulent boundary layer incident shock interaction. Techniques for estimating the change in boundary layer thickness across the shock impingement region were developed which give results in general agreement with those obtained in the experimental program. Using the formulated flow model concept, a method for predicting imminent separation was developed which was also found to be consistent with experimental results, as well as qualitatively indicating the increased stability of the turbulent boundary layer at decreased wall temperature and/or increased upstream power law profile parameter values.



## TABLE OF CONTENTS

SECTION I	PAGE
INTRODUCTION	1
SECTION II	
ANALYTICAL PROGRAM	
A.    LAMINAR SHOCK/BOUNDARY LAYER ANALYSIS	
a.    ENTROPY RISE EFFECT	2
b.    STRONG SHOCK CONVERGENCE	4
c.    PERTURBATION STUDIES	5
d.    INTERACTION CORRELATION	7
B.    TURBULENT SHOCK/BOUNDARY LAYER SEPARATION FORMULATION	9
SECTION III	
EXPERIMENTAL PROGRAM	
A.    MODELS AND INSTRUMENTATION	
a.    MODEL C	13
b.    MODEL D	17
c.    MODEL E-3	17
B.    FACILITY DESCRIPTION	20
C.    RUN LOG	
a.    MODEL C/D	23
b.    MODEL E-3	26
D.    TEST RESULTS AND ANALYSIS	
a.    MODEL C	30
b.    MODEL D	42
c.    MODEL E-3	45
E.    CONCLUSIONS	50
SECTION IV	
APPENDIX I (User's Manual)	52
APPENDIX II (Computation Procedure for Estimating Turbulent Boundary Layer Thickness Change Across an Impinging Shock Wave)	64

TABLE OF CONTENTS Cont'd

	PAGE
APPENDIX III (Data Reduction Techniques)	66
SECTION V	
REFERENCES	74
SECTION VI	
ILLUSTRATIONS, TABLES	

## LIST OF ILLUSTRATIONS

### SECTION II

#### ANALYTICAL PROGRAM

##### A. LAMINAR SHOCK/BOUNDARY LAYER ANALYSIS

Mach 2.21 Theory/Data Interaction Pressure Distribution	1
Schematic of Laminar Flow Model	2
Mach 10.4 Entropy Effect on Interaction Pressure Distribution	3
Example of Iteration Required for Interaction Solution	4
Illustration of Momentum Thickness Iteration	5
Shear Perturbation Effect on Pressure Distribution	6
Perturbation Effect on Pressure Distribution	7
Perturbation Effect on Integral Properties	8
Perturbation Effect on Integral Properties	9
Interaction Pressure Distributions Selected for Correlation	10
Correlation of Interaction Pressure Distributions	11

##### B. TURBULENT SHOCK/BOUNDARY LAYER SEPARATION FORMULATION

Schematic of Turbulent Flow Model	12
Theory/Data Comparison of Inviscid Interaction Length	13
Boundary Layer Edge and Wall Pressure Distributions	14
Mach 7.3 Interaction Schlieren at $\theta_c = 4^\circ$	15
Mach 7.3 Interaction Schlieren at $\theta_c = 8^\circ$	16
Mach 7.3 Interaction Schlieren at $\theta_c = 10^\circ$	17
Theory/Data Comparison of Boundary Layer Thickness Ratio	18
Theoretical Separation Limited Mach Number Ratio	19
Predicted Separation Pressure Ratio ( $N_1 = 7$ )	20
Predicted Separation Pressure Ratio ( $N_1 = 9$ )	21
Predicted Separation Pressure Ratio ( $N_1 = 11$ )	22

### SECTION III

#### EXPERIMENTAL PROGRAM

##### A. MODELS AND INSTRUMENTATION

Model C Ramp	23
Model C Ramp Undercarriage	24
Model C Cowl Plate	25
Model C Cowl Superstructure	26
Model C Ramp Instrumentation	27
Model C Ramp Instrumentation Installation	28
Model C Cowl Instrumentation	29
Probe Actuator	30
NASA/Ames Boundary Layer Probe	31
NASA/Ames Boundary Layer Probe Installation	32
Model C Boundary Layer Trip Configurations	33

## LIST OF ILLUSTRATIONS (Cont'd)

### SECTION III (Cont'd)

Model C Ramp Installation	34
Model C Ramp and Cowl Installation	35
Model C Assembly Drawing	36
Model D Vane Installation	37
Model D Vane Instrumentation and Geometry	38
Model D Vane Instrumentation Installation	39
Model E-3 Ramp and Cowl Geometry	40
Model E-3 Ramp	41
Model E-3 Cowl Assembly Drawing	42
Model E-3 Ramp Instrumentation	43
Model E-3 Cowl Instrumentation	44
Model E-3 Boundary Layer Trip Configuration	45
Model E-3 Ramp Installation	46
Model E-3 Ramp and Cowl Installation	47
Model E-3 Ramp Leading Edge Modification	48
Model E-3 Cowl Support Struts	49
 B. FACILITIES DESCRIPTION	
NASA/Ames 3.5 Foot Hypersonic Wind Tunnel	50
View of 3.5 Foot Wind Tunnel Test Section	51
 D. TEST RESULTS AND ANALYSIS	
Model C	
Theory/Data Shock Shape Comparison	52
Typical Mach 10.5 Power Law Profile Data Representation	53
Typical Mach 7.4 Power Law Profile Data Representation	54
Natural Transition Reynolds Number Data Summary	55
Power Law Profile vs Reynolds Number Data Comparison	56
Momentum Thickness Variation Theory/Data Comparison	57
Incompressible Laminar Boundary Layer Theory/Data Comparison	58
Incompressible and Compressible Laminar Profile Comparison	59
Incompressible and Compressible Turbulent Profile Comparison	60
Typical Laminar Pitot Pressure Profile	61
Typical Laminar Total Temperature Profile	62
Typical Laminar Mach Number Profile	63
Typical Laminar Static Temperature Profile	64
Typical Laminar Velocity Profile	65
Typical Laminar Density Profile	66
Typical Laminar Unit Mass Flow Profile	67
Typical Turbulent Pitot Pressure Profile	68

## LIST OF ILLUSTRATIONS (Cont'd)

### SECTION III (Cont'd)

Typical Turbulent Total Temperature Profile	69
Typical Turbulent Mach Number Profile	70
Typical Turbulent Static Temperature Profile	71
Typical Turbulent Velocity Profile	72
Typical Turbulent Density Profile	73
Typical Turbulent Unit Mass Flow Profile	74
Laminar Schlieren-Pressure Distribution ( $\theta_c = 4^\circ$ )	75
Laminar Schlieren-Pressure Distribution ( $\theta_c = 8^\circ$ )	76
Laminar Schlieren-Pressure Distribution ( $\theta_c = 10^\circ$ )	77
Turbulent Schlieren-Pressure Distribution ( $\theta_c = 4^\circ$ )	78
Turbulent Schlieren-Pressure Distribution ( $\theta_c = 8^\circ$ )	79
Turbulent Schlieren-Pressure Distribution ( $\theta_c = 10^\circ$ )	80
Inviscid Shock and Boundary Layer Edge Flow Angle Comparison	81
Mach 7.3 Theory/Data Shock Pressure Ratio Comparisons	82
Mach 10.5 Theory/Data Shock Pressure Ratio Comparisons	83
Mach 10.4 Laminar Pressure Distribution ( $\theta_c = 3^\circ$ )	84
Mach 10.4 Laminar Pressure Distribution ( $\theta_c = 4^\circ$ )	85
Mach 10.4 Laminar Pressure Distribution ( $\theta_c = 5^\circ$ )	86
Mach 10.4 Laminar Pressure Distribution ( $\theta_c = 8^\circ$ )	87
Mach 10.4 Laminar Pressure Distribution ( $\theta_c = 10^\circ$ )	88
Mach 7.3 Laminar Pressure Distribution ( $\theta_c = 2^\circ$ )	89
Mach 7.3 Laminar Pressure Distribution ( $\theta_c = 4^\circ$ )	90
Mach 7.3 Laminar Pressure Distribution ( $\theta_c = 6^\circ$ )	91
Mach 7.3 Laminar Pressure Distribution ( $\theta_c = 8^\circ$ )	92
Mach 7.3 Laminar Pressure Distribution ( $\theta_c = 10^\circ$ )	93
Correlation of Laminar Boundary Layer Separation Length	94
Laminar Theory/Data Pressure Distributions ( $M_o = 7.3$ )	95
Laminar Theory/Data Pressure Distributions ( $M_o = 10.4$ )	96
Theoretical Laminar Mass Flow Variation ( $M_o = 7.3$ )	97
Theoretical Laminar Mass Flow Variation ( $M_o = 10.4$ )	98
Theoretical Laminar Shear Parameter ( $M_o = 7.3$ )	99
Theoretical Laminar Shear Parameter ( $M_o = 10.4$ )	100
Turbulent Separation Theory/Data Comparison	101
Separation Sensitivity to $T_w/T_T$ and N	102
Turbulent Thickness Ratio Theory/Data Comparison	103
Turbulent Incident Shock Mass Flux Ratio	104
Measured Profile Shape Change Across Interaction ( $M_o = 10.5$ )	105
Measured Profile Shape Change Across Interaction ( $M_o = 7.3$ )	106
Turbulent-Turbulent Interaction Data Composite ( $M_o = 7.3$ )	107
Laminar-Laminar Interaction Data Composite ( $M_o = 7.3$ )	108

LIST OF ILLUSTRATIONS (Cont'd)

SECTION III (Cont'd)

Laminar-Turbulent Interaction Data Composite ( $M_0 = 7.3$ )	109
Turbulent-Turbulent Interaction Data Composite ( $M_0 = 10.5$ )	110
Turbulent-Turbulent Interaction Data Composite ( $M_0 = 10.5$ )	111
Laminar-Transitional Interaction Data Composite ( $M_0 = 10.4$ )	112
Laminar-Turbulent Interaction Data Composite ( $M_0 = 10.4$ )	113
<u>Model D</u>	
Shock-Expansion Technique-Calculation Procedure	114
Shock-Expansion Technique-Flow Model	115
Model D Vane Pressure Distribution	116
Turbulent Flow Ramp Pressure Rise, $M_0 = 10.55, \theta_v = 6^\circ$	117
Turbulent Flow Ramp Pressure Rise, $M_0 = 10.55, \theta_v = 8^\circ$	118
Laminar Flow Ramp Pressure Rise, $M_0 = 10.40, \theta_v = 6^\circ$	119
Turbulent Flow Ramp Profile Data, $M_0 = 10.55, \theta_v = 6^\circ$	120
Turbulent Flow Ramp Profile Data, $M_0 = 10.55, \theta_v = 8^\circ$	121
Laminar Flow Ramp Profile Data, $M_0 = 10.40, \theta_v = 6^\circ$	122
Laminar Flow Ramp Profile Data, $M_0 = 10.40, \theta_v = 6^\circ$ (1 vane)	123
Ramp Boundary Layer Thickness and Unit Mass Flow Variation	124
<u>Model E-3</u>	
Static Pressure Variation at 1st Probing Station	125
Static Pressure Variation at Mid Probing Station	126
Comparison of MOC Static Pressure Variation at Aft Probing Station	127
Model E-3 Pressure Distribution Comparison	128
Momentum Thickness Versus Reynolds Number	129
Displacement Thickness Versus Reynolds Number	130
Shape Factor Versus Reynolds Number	131
Boundary Layer Mass Flow vs. X Variation (Mach 10.5)	132
Boundary Layer Mass Flow vs. X Variation (Mach 7.3)	133
Model E-3 Mach Number Distribution	134
Comparison of Model C & E-3 Turbulent Profiles	135
Laminar Boundary Layer Schlieren Profile Comparison	136
Turbulent Boundary Layer Schlieren Profile Comparison	137
Final Pressure Rise Ratio (Mach 7.3)	138
Final Pressure Rise Ratio (Mach 10.5)	139
Low Reynolds Number Pressure Distribution (Mach 7.3)	140
High Reynolds Number Pressure Distribution (Mach 7.3)	141
Low Reynolds Number Pressure Distribution (Mach 10.4)	142
High Reynolds Number Pressure Distribution (Mach 10.5)	143
Typical Laminar Shock Interaction (Mach 10.4)	144
Typical Turbulent Shock Interaction (Mach 10.5)	145
Typical Laminar Shock Interaction (Mach 7.3)	146
Typical Turbulent Shock Interaction (Mach 7.3)	147
Comparison of Pressure Distributions at Similar Test Conditions	148

## LIST OF ILLUSTRATIONS (Cont'd)

### SECTION III (Cont'd)

Schlieren Comparison at Similar Test Conditions	149
Plateau Pressure Comparison at Mach 7.3	150
Plateau Pressure Comparison at Mach 10.4	151
Model E-3 Schlieren with Separated Flow	152
Model E-3 Turbulent Separation Pressure Distribution	153

### SECTION IV

#### A. APPENDIX I

Mach Number Change Versus Total Pressure Recovery at $\gamma = 1.667$	154
Mach Number Change Versus Total Pressure Recovery at $\gamma = 1.4$	155
Boundary Layer Pressure Gradient Parameter	156
Typical Laminar Boundary Solution Print-Out	157

#### B. APPENDIX II

Power Law Profile Distortion Function	158
---------------------------------------	-----

#### C. APPENDIX III

Comparison of Theoretical & Experimental Velocity Profiles	159
Sample Computer Print-Out	160
Typical Model C Static Pressure Distribution	161
Static Pressure Distribution at Probe Station 1	162
Static Pressure Distribution at Probe Station 2	163
Static Pressure Distribution at Probe Station 3	164
Typical Low Pressure Static Pressure Distribution	165
Comparison of Temperature Profiles at High Reynolds Number	166
Comparison of Temperature Profiles at Low Reynolds Number	167
Typical Experimental Total Temperature Profile	168

## LIST OF TABLES

- I. Model C Cowl-Off Profile Analysis Summary
- II. Model C Cowl-On Profile Analysis Summary
- III. Model E-3 Profile Analysis Summary

## LIST OF SYMBOLS

$a$	speed of sound
$A_p$	arbitrary constants
$B_x, B_p$	arbitrary constants
$C_D$	drag coefficient
$C_f$	local skin friction coefficient
$C_p$	pressure coefficient
$C$	constant in skin friction equation
$E$	convection thickness
$f_1, f_2$	universal functions (Erdos & Palone)
$g$	gravitational constant
$G$	kinetic energy/momentum thickness ratio
$H$	shape factor
$H$	total enthalpy
$f(H_1)$	distortion function
$J$	Joules' constant
$K$	constant in skin friction equation
$\ell$	shear parameter
$\ell'$	unadjusted 'similar solution' value of $\ell$
$L$	inviscid interaction length
$\dot{m}$	mass flow
$M$	Mach number
$n$	pressure gradient parameter
$n$	compressible power law profile parameter
$\hat{n}$	second derivative parameter (Cohen & Reshotko)



LIST OF SYMBOLS (Cont'd)

N	incompressible power law profile parameter
P	pressure
Pr	Prandtl number
q	dynamic pressure
R	recovery factor
R	universal gas constant
Re	Reynolds number
T	temperature
u	velocity (compressible)
U	velocity (incompressible)
$W_{BL}$	mass flow parameter
x	axial distance
$\Delta x$	characteristic length of the interaction region
y	normal distance
z	constant in skin friction equation
$\alpha$	sweep induced downstream flow deflection angle
$\beta$	Mach number parameter, $\sqrt{M^2 - 1}$
$\gamma$	ratio of specific heats
$\delta$	boundary layer thickness
$\delta^*$	displacement thickness
$\delta^{**}$	energy thickness
$\eta$	transformed normal distance
$\theta$	momentum thickness
$\Theta$	flow deflection angle

LIST OF SYMBOLS (Cont'd)

$\Delta\theta$	impinging shock strength
$\lambda$	viscosity parameter (Sutherland's law)
$\mu$	absolute viscosity
$\nu$	Prandtl-Meyer angle
$\rho$	density
$\tau$	shear stress
$\phi$	kinetic energy dissipation function
$\phi'$	unadjusted "similar solution" value of $\phi$
$\omega$	exponent in $T - \mu$ relation
$\Omega$	sweep angle

Subscripts

0	free-stream
1	downstream of leading edge shock
3	downstream of shock impingement
c	cowl
e	boundary layer edge
i	incompressible
n	normalized
ref	reference
R	reference (Erdos & Pallone)
tr	transformed
T	total
v	vane
w	wall

LIST OF SYMBOLS (Cont'd)

$x$	axial distance
$\theta$	momentum thickness
$\Omega$	sweep induced

## SECTION I

### INTRODUCTION

At hypersonic flight speeds, the design of inlet compression surfaces necessarily involves the use of secondary shock system compression to achieve the increased combustor entrance pressure and temperature levels compatible with high levels of engine internal performance at low values of external drag. At these higher flight speeds, viscous effects play an increasingly important role in the design and performance of inlet component compression surfaces. While various methods are available for treating the resulting combined viscous/inviscid flow fields for cases of continuous adverse pressure gradient resulting from single family wave compression, methods for handling viscous effects associated with oblique shock impingement are much more limited in scope. Treatment of such problems necessarily involves consideration of boundary layer separation phenomena. At supersonic speeds, a considerable amount of adiabatic wall test data are available in the literature which can be used in assessing the probability of secondary shock induced boundary layer separation for lower speed inlet applications. The applicability of such lower speed techniques to higher Mach number applications, however, requires evaluation and possibly modification. In some instances it is to be expected that new methods of analysis will have to be formulated. The investigations described in this report have been addressed to these problems, with the overall objective of significantly contributing to their resolution as well as providing necessary insight to further required study. In accomplishing this purpose, a combined analytical and experimental program was conducted such that theory/data comparisons could be made for both laminar and turbulent boundary layer-incident shock interactions at hypersonic speeds. The computational techniques which were formulated for the treatment of laminar and turbulent interactions were found to give results consistent with those obtained from tests conducted with the component surface models at Mach 7 and 10 as well as with data reported by other investigators, and thus are considered appropriate for current engineering use in the design and performance analysis of hypersonic inlets.

## SECTION II

### ANALYTICAL PROGRAM

#### A. LAMINAR SHOCK/BOUNDARY LAYER ANALYSIS

Reference 1 documented the formulation of a method for the analysis of a laminar boundary layer/incident shock wave interaction following the initial approach of Lees and Reeves in Reference 2. A User's Manual incorporating the most recent modifications to the resulting program is presented in Appendix I of this report. The calculation procedure simultaneously accounts for the combined interaction of the inviscid and viscous flow field and establishes the extent of the forward propagation of the upstream pressure disturbances given the upstream inviscid conditions and the shock impingement point. Solutions can be obtained throughout the complete laminar interaction. The results of such calculations have generally been found to agree favorably with supersonic test data as indicated in Figure 1 of this report for the data of Reference 3. Similar agreement at supersonic test conditions was noted earlier in Reference 1 with the data of Reference 4. Similar comparisons with data obtained at hypersonic speeds have been less successful; due in part to the onset of boundary layer transition downstream of the interaction. During the second phase of this study attention was directed at modifications to the original program for the purpose of obtaining better theory/data agreement at hypersonic speeds and to increase the class of laminar problems for which complete iterated solutions could be obtained. The modified computer program was subsequently used for hypersonic theory/data comparisons presented in Section III-D of this report.

##### a. Entropy Rise Effect

Boundary layer growth calculations are commonly carried out on the basis of isentropic external flow at the boundary layer edge. Indeed, the transformation between the compressible boundary layer equations and the low speed form of these equations upon which the calculations are based is dependent upon the external isentropic flow assumption. Although this restriction is undesirable, it has not particularly limited the engineering usefulness of the results. In fact, such an approximation was employed in the initial formulation of the Laminar Shock Boundary Layer interaction calculation procedure reported in Reference 1. Even at hypersonic speeds where the external flow may be highly rotational (due to a curved leading edge shock wave) such quantities as shear stress and boundary layer momentum decrement are found to be insensitive to the external total pressure. Instead, the free stream stagnation enthalpy level and the local static pressure are found to be the principal controlling parameters.

The effect of total pressure change in a shock boundary layer interaction, however, is less obvious especially at hypersonic speeds and increased shock strengths. At low Mach numbers the laminar boundary layer

is separated by a rather weak incident shock and thus the downstream total pressure is usually not very different from the upstream total pressure; there is little need for including entropy variation effects in such analyses. At higher Mach numbers, however, the normal shock Mach number (of the oblique incident shock wave) can be much larger and therefore the total pressure variation is of concern; particularly at increased values of turning across the incident shock wave system. As a consequence of this, a modification has been made to the Laminar-Shock/Boundary Layer Interaction computer program of Reference 1 which now accounts for the variation in total pressure across the incident shock.

In accomplishing this modification, the boundary layer edge conditions are still based upon the Prandtl-Meyer equations:

$$\nu + \theta = \nu_0$$

$\nu$  = Prandtl-Meyer angle at  
boundary layer edge

$$\nu - \theta = \nu_\infty$$

$\theta$  = flow angle at boundary  
layer edge

which are valid upstream and downstream of the incident shock wave respectively. The value of  $\nu_0$  is determined from the input value of Mach number; the value of  $\nu_\infty$  is calculated from the specified shock strength. Specifically, the boundary layer growth and edge Mach number are calculated up to 2 in Figure 2, and the downstream conditions at 3 are determined by a constant pressure boundary shock reflection calculation. A knowledge of the change in  $\nu$  and  $\theta$  across the shock expansion system leads to the following equation for  $\nu_\infty$ :

$$\nu_\infty = \nu_0 - \Delta\theta_s - (\nu_2 - \nu_{2A})$$

where  $\Delta\theta_s$  is the given flow deflection angle through the shock wave.

The calculation procedure has been formulated so that values of displacement thickness and momentum decrement (momentum decrement equals  $\rho_e u_e^2 \theta - P\delta^*$ , where  $\theta$  is a boundary layer momentum thickness) are held invariant together with static pressure from 2 to 3 in Figure 2. Other quantities must now necessarily be discontinuous. Whereas the isentropic calculation procedure of Reference 1 permitted continuity across the interface, the entire profile within the boundary layer must now be discontinuous as well as the boundary layer edge values of total pressure, static temperature, density, Mach number and velocity.

Computed results using both the original isentropic method of Reference 1 and this subsequent non-isentropic modification are shown in Figure 3. At these conditions, the effect on the static pressure distribution of accounting for the entropy rise appears to be small. The comparison shown is for a given flow deflection of  $5^\circ$  across the impinging shock wave. By including

the total pressure loss ( $P_{T3}/P_{T2} = .923$ ) in the calculation, the overall static pressure rise has been reduced somewhat as would be expected. Although the entropy effect would be more noticeable for higher impinging shock strengths, an input value of  $\Delta \bar{e}_s = 7.96$  at these free stream conditions was found to be too strong to permit a complete solution to be obtained with the present laminar boundary layer model.

#### b. Strong Shock Convergence

Modifications to the Laminar-Shock/Boundary Layer Interaction program have been made to increase reliability of the original convergence procedure. During a typical calculation, an integration of the boundary layer/Prandtl-Meyer equations is performed from a downstream point (station 4) to the oblique shock incidence point (station 3). This integration involves assuming trial values of momentum thickness  $\theta_4$  at station 4 and then iterating to obtain

$$\begin{bmatrix} \rho_e & u_e^2 & \theta \end{bmatrix}_3 = \begin{bmatrix} \rho_e & u_e^2 & \theta \end{bmatrix}_2 \quad (1)$$

where subscripts 2 and 3 denote interface values immediately upstream and downstream of the shock wave incidence point. Occasionally, during the solution of some problems, values of  $\theta_4$  may be selected by the iteration procedure which cause the integration to fail before reaching station 3. The difficulty is associated with the momentum thickness decreasing to zero as shown by the typical example of Figure 4.

When this situation is detected in the program, corrective action is now taken as follows: in order to continue the iteration for the appropriate  $\theta_4$  a negative (fictitious) value of momentum thickness is calculated by the simple relation

$$\theta_3 = -\sqrt{.44 \frac{X_{\theta=0} - X_{SK}}{Re_1}} \quad (2)$$

$Re_1/x$  = input Reynolds number per unit length

(See Figure 4 for definitions of  $X_{\theta=0}$  and  $X_{SK}$ )

A plot of an actual iteration process using this procedure is presented in Figure 5 exhibiting the present capability to obtain solutions to a class of problems not previously possible. It should be pointed out, however, that even with this increased capability, complete laminar solutions are not always possible at the higher shock strengths. This analytical result is in accord with the experimental results which conclusively indicated that increased shock strength induced transition in that the separating laminar boundary layer subsequently reattached and transitioned to turbulent flow downstream of the interaction.

### c. Perturbations Studies

To better understand the behavior of the laminar boundary layer undergoing a sudden pressure rise, it is, perhaps, desirable to investigate the computed effects resulting from the perturbation of basic parameters. It was felt that a perturbation study would demonstrate the significance of certain parameters and, in particular might also allow determination of a possible parametric variation which would result in a smaller interaction zone with hypersonic flow. The results of this study are discussed in the following paragraphs.

Primarily, the variation of the shear parameter  $\ell$  has been studied. Modifications were thus made to the Laminar-Shock/Boundary Layer Interaction program so that the dimensionless shear parameter

$$\ell = \frac{\tau_w}{\mu_e u_e} \quad (3)$$

could be arbitrarily adjusted by the relation

$$\ell = A_X \ell' + A_P \quad (4)$$

where  $\ell'$  is the unadjusted "similar solution" value of  $\ell$ , and  $A_X$  and  $A_P$  are arbitrary constants which apply over the region downstream (upstream or both upstream and downstream) of the shock wave impingement. Provision was also made for perturbation of the kinetic energy dissipation function

$$\phi = B_X \phi' + B_P \quad (5)$$

With such an approach, however, it should be noted that a condition imposed on all of the shock boundary layer calculations, including the current perturbation study, is that at the beginning and at the end of the interaction region the boundary layer must reach an "equilibrium" state. That is, the dimensionless velocity profile does not change for a small distance upstream or downstream of the terminal station. This implies that the KE/momentum equation (Equation 32 of Reference 1) must, therefore take on the value of zero at the upstream and downstream boundaries since  $dG/dX$  must be zero:

$$\frac{\rho_e u_e^3}{\mu_e} \frac{dG}{dX} = 2\theta - G\ell - n \left[ G(H_{tr} - 1) - \frac{2E}{\theta} \right] = 0 \quad (6)$$

Since it is also usually assumed that the pressure gradient is zero, ( $n = 0$ ) at the terminal stations, the above equation reduces to

$$2\phi - G\ell = 0 \quad (7)$$



Unfortunately this equation will not remain satisfied if one of the parameters  $\phi$ ,  $G$  or  $l$  is varied independently. Furthermore, at the upstream and downstream boundaries of the interaction region, the value of the low speed form factor,  $H_{tr}$ , is chosen so that Equation (7) is satisfied. This requires a shift in  $H_{tr}$  from the nominal (flat plate) value if, for example,  $l$  is perturbed. In the first three sets of calculations to be discussed, the value of  $l$  was independently perturbed upward. This resulted in  $H_{tr}$  (and  $\delta^*$ ) taking on a larger value. In the fourth set of calculations both  $l$  and  $\phi$  were selected so that other profile parameters would remain constant. For the four sets of perturbation computations carried out, the results are shown in Figures 6 through 9 and are discussed below.

- 1)  $l = 1.25l'$  downstream of shock impingement only:  
 $\delta^*$  (i.e.  $H_{tr}$ ) increased at the downstream boundary to accommodate the "equilibrium" condition. Consequently, the (initially unexpected) result was that the shear parameter was reduced from the intended perturbed value to a level which duplicated the unperturbed value. Just downstream of the shock impingement, the magnitude of the negative shear was found to increase and the pressure gradient was slightly steeper.
- 2)  $l = l' + .04$  downstream of the shock impingement only:  
This resulted in a somewhat larger perturbation at the downstream boundary from the previous case. Due to the "equilibrium" condition, the resulting value of shear actually decreased.  $\delta^*$  was larger over the entire region, and to match the  $\delta^*$  at the shock impingement point, the leading edge of the interaction moved forward.
- 3)  $l = l' + .04$  both upstream and downstream of the shock impingement:  
Similar but more pronounced effects were found than in (2). The length of the interaction was increased considerably.
- 4)  $l = l' + .04$ ,  $\phi = \phi' + .0315$  downstream of the shock impingement:  
Using Equation (7) perturbation values of  $l$  and  $\phi$  were selected so that the other profile parameters ( $G$ ,  $H_{tr}$ ,  $\hat{n}$ , etc.) would remain unchanged (at the downstream boundary). In this case a truly increased value of shear was obtained over the entire range of the perturbation. However, the pressure distribution and the length of the interaction were only slightly affected.

It is concluded from this study that the parameters  $l$  and  $\phi$  (and probably  $G$  and  $E/\theta$  also) play second order effects compared to the form factor,  $H_{tr}$ . Interaction effects with the free stream are determined by the rate of boundary layer growth. As the value of momentum thickness does not change drastically over the interaction region, changes in the value of  $\delta^*$  follow closely changes in the parameter  $H_{tr}$ . For the turbulent boundary layer, the form factor is smaller than for the laminar layer. The corresponding small interaction region of the turbulent boundary layer as observed in a subsequent section is consistent with these laminar perturbation solution results in that the length of the interaction seems to be primarily

dependent upon the change in layer thickness or more specifically, on  $H_{tr}$ .

#### d. Interaction Correlation

By making certain approximations, in Reference 7 Erdos and Pallone developed a correlation of the axial pressure distribution for a "free interaction" boundary layer separation region. Such a "free interaction" will exist upstream of an impinging shock wave if its strength is sufficient to separate the boundary layer and form the familiar pressure plateau. Unfortunately, the extent of forward feed of the pressure rise (or "free interaction") has not been correlated successfully. This forward feed, or conversely, the degree to which the pressure plateau is evident is a function of the shock wave strength. By introducing a shock strength correlation parameter, the concepts of Erdos and Pallone are here extended to include both the separation and reattachment zones in the shock-boundary layer interaction. Thus the axial pressure distribution, including the extent of upstream and downstream separation, is correlated for various values of the shock strength parameter. Based on laminar boundary layer calculations, the correlation appears to be valid for a limited range of conditions.

The approximations used in the correlation development are presented below:

- 1) The normal gradient of shear stress at the wall, throughout the interaction region, is related to the wall shear and boundary layer thickness at some reference point, and a universal function  $f_2$ .

$$\left. \frac{\partial \tau}{\partial y} \right|_w = \frac{\tau_{wR}}{\delta^*_R} f_2 \left( \frac{X - X_R}{\Delta X} \right) \quad (8)$$

The subscript 'R' denotes the reference point, which Erdos and Pallone take as the beginning of the pressure rise. Most significant, the function  $f_2$  is assumed to apply at all Reynolds number-Mach number conditions;  $\Delta X$  is a characteristic length of the interaction region.

- 2) Similarly, the boundary layer edge slope is related to a reference value of  $\delta^*$  and a distance from the reference point by a second universal function,  $f_1$

$$\frac{d\delta^*}{dx} = \frac{\delta^*_R}{X - X_R} f_1 \left( \frac{X - X_R}{\Delta X} \right) \quad (9)$$

- 3) The Prandtl-Meyer relation

$$v_2 - v_1 = \int_{P_1}^{P_2} \frac{8}{\gamma PM^2} dP \quad (10)$$

is approximated by

$$v_2 - v_1 = \frac{\beta_R}{\gamma_R^P M_R^2} (P_2 - P_1) \quad (11)$$

Approximations (9) and (10) imply that the length of the interaction is small (or constant) relative to distance from the effective origin of the boundary layer. That is, the change in boundary layer edge slope and  $\tau_w/P$  due to the natural boundary layer growth (without a shock wave impingement) must be small compared to the changes imposed by the sudden pressure rise. The turbulent boundary layer meets these requirements more closely than the laminar boundary layer since  $d\delta^*/dX$  and  $\tau_w/P$  nominally vary with the .2 power of  $X$  rather than the .5 power. Approximation (11) limits the correlation to weak interactions.

In spite of possible limitations of the correlation formula, especially for a laminar interaction, it is worthwhile to explore the calculated results using the Laminar-Shock/Boundary Layer Interaction theory. In order to generalize Erdos and Pallone's work to the entire interaction region, a shock strength parameter

$$\frac{\Delta\theta_S}{\sqrt{\frac{1}{2} \beta_R C_{fR}}} \quad (12) \quad \left[ \Delta\theta_S = \text{flow angle deflection through the impinging shock wave, in radians} \right]$$

is introduced. The pressure and distance parameters are:

$$\frac{P - P_R}{q_R \sqrt{2 C_{fR} / \beta_R}} \quad \left( q = \frac{1}{2} \rho_e u_e^2 \right) \quad (13)$$

$$\frac{X - X_R}{\delta_R^* \sqrt{2 / (\beta_R C_{fR})}} \quad (14)$$

Erdos and Pallone chose the reference point, denoted by 'R', as the beginning of the interaction region. However, because of the difficulty of locating the beginning of the smooth pressure rise, it was elected to calculate the reference values,  $\beta_R$  and  $C_{fR}$ , at the shock impingement point assuming undisturbed flow, instead.  $R$

The resulting correlation is found to be only moderately satisfactory for laminar layers. Calculated results for a shock strength parameter of unity and a range of Mach number and Reynolds number conditions are shown in Figures 10 and 11. Figure 10 shows the actual calculated wall pressure distributions for an oblique shock wave impinging on a flat plate. Note

that the impinging shock is quite weak so that in these examples no pressure plateau is formed. In Figure 11 the same data are plotted in terms of the correlation parameters. The  $M_0 = 10$ ,  $Re_{X_{SK}} = 1.6 \times 10^6$  condition is included for comparison although Approximation (11) is badly violated, in this particular case.

It appears that the correlations obtained have applicability in regions of low Mach number and high Reynolds number for a laminar boundary layer and thus in some instances could be used in place of more formal computer solutions.

#### B. TURBULENT-SHOCK/BOUNDARY LAYER SEPARATION FORMULATION

Comparison of schlieren and wall static pressure data (Section III D a, Figures 75 through 80) document contrasting differences between the laminar and turbulent-incident shock wave/boundary layer interactions. Of particular importance in the formulation of simplified flow models is the observation that the shock impingement and reflection from a non-separating laminar boundary layer occurs more or less as a constant pressure boundary phenomena, whereas with the turbulent interaction the impinging shock penetrates deep into the viscous flow and reflects in a manner similar to that associated with a non-uniform flow field interaction. Such differences, coupled with the fact that data obtained under this program, as reported in Section III-D, have consistently documented the stability of the non-adiabatic wall hypersonic turbulent boundary layer over a range of shock impingement strengths such as might be associated with hypersonic inlet operation, led to the formulation of the simplified flow model depicted in the schematic of Figure 12.

With respect to analysis in connection with the simplified two-dimensional flow model of Figure 12, the following key assumptions are made:

1. The inviscid and viscous conditions up to A are known.
2. There is no significant mass addition in the region A to B.
3. Wall friction is negligible in the region A to B in regard to its influence on profile shape.
4. Boundary layer edge conditions and flow direction can be determined from the known incident shock strength.
5. The reflected shock strength is that required to turn the boundary layer edge flow back parallel to  $M_1$  at B.
6. The wall temperature to stream total temperature is constant.
7. Constant pressure mass addition occurs in the region B to C.

8. The distorted boundary layer profile at B mixes out to a typical turbulent profile at C.

In spite of the fact that such a formulation is an over-simplification of this complex problem, it is believed that results obtained from subsequent related analysis will be of engineering usefulness in current hypersonic inlet design applications until more detailed analyses are conducted.

Many of the preceding flow model assumptions are an outgrowth of data analysis subsequently presented in Section III-D of this report. For instance, in Figure 13 it is seen that such a flow model leads to reasonable approximations for the inviscid boundary interaction length while providing indirect substantiation for assumptions 4 and 5. The degree to which assumptions 7 and 8 are experimentally justified, beyond expediency of analysis, can be assessed from the wall and boundary layer edge pressure distribution comparisons of Figure 14 and probe station 3 boundary layer profile measurements reported and discussed in Section III-D. The schlieren photographs of Figures 15 through 17 document visual similarities with the simplified flow model of Figure 12 and suggest that such a formulation might be acceptable for incorporation with combined Method of Characteristics-Boundary Layer analysis of the inlet flow field, providing boundary layer integral properties (particularly displacement thickness) can be reasonably estimated immediately downstream of the interaction.

Consequently, during the course of this study, two methods of analysis constrained by the preceding assumptions were developed for estimating boundary layer integral property change across the immediate region of an impinging shock interaction. Numerical results obtained from both methods are similar and agree favorably with data obtained under this program. Limited checks with data reported by other investigators indicated similarly favorable agreement.

In the first method, it is assumed that compressible flow profiles can be adequately represented by the modified Crocco enthalpy distribution and the power law velocity expression:

$$\frac{u}{u_e} = \left(\frac{y}{\delta}\right)^{\frac{1}{n}}$$

Momentum and continuity are balanced across the boundary layer control volume from A to B in Figure 12. This is an iterative calculation to determine the downstream shape factor at B in Figure 12 through simultaneous solution of:

$$\text{CONTINUITY: } \frac{\delta_1}{\delta_3} = \frac{P_3}{P_1} \frac{M_3}{M_1} \frac{\sqrt{1 + \frac{\gamma-1}{2} M_3^2}}{\sqrt{1 + \frac{\gamma-1}{2} M_1^2}} \frac{(1 - \delta^*/\delta)_3}{(1 - \delta^*/\delta)_1} \quad (15)$$

$$\text{MOMENTUM: } \frac{1}{\delta_3} = \frac{\left\{ 1 - \frac{P_3}{P_1} - 2\gamma M_3^2 \frac{P_3}{P_1} \left[ 1 - \frac{\delta^*}{\delta} - \frac{\theta}{\delta} \right] \right\}_3}{\left\{ \frac{P_3}{P_1} - 1 - 2\gamma M_1^2 \left[ 1 - \frac{\delta^*}{\delta} - \frac{\theta}{\delta} \right] \right\}_1} \quad (16)$$

The second method, described in detail in Reference 5 is an integral method approach. The incompressible form of momentum equation is solved to obtain an expression for the change in incompressible shape factor. Simple power law profiles in the incompressible plane are transformed using the Stewartson transformation to obtain a compressible solution. The Crocco temperature distribution is utilized to obtain non-adiabatic wall solutions. The latter indicate a significant increase in stability (in terms of shock strength) due to wall cooling. The computational procedure as prepared for desk calculation is presented in Appendix II along with the necessary integral computational curves.

Numerical results are compared with incident shock Model C data in Figure 18. The shock pressure ratio and Mach number ratios used in the analytical estimates are based on oblique shock solutions for the shock generating cowl angle of attack. The upstream boundary layer profile characteristics used in the analysis are based on results obtained from single probe profile traverses. The experimentally determined boundary layer thickness ratios were established through interpretation of schlieren photographs supported by the upstream profile measurements. Considering the simplifying assumptions inherent in the analytical model upon which the formulated calculation procedure is based, the degree of agreement indicated between the numerical results and the data over such a wide range of shock strengths is considered most gratifying.

The trend of the data and the numerical results exhibited in Figure 18 suggest an interesting trade-off occurs between boundary layer thinning due to compression of the boundary layer "stream tube" and thickening due to profile distortion. At the weaker shock strengths, there is little profile distortion and the downstream boundary layer thins as a result of the continuity balance associated with the compression process. As the shock strength is increased, the downstream profile becomes significantly enough distorted to promote a thickening trend. Ultimately, as separated flow conditions are approached the profile distortion dominates, with the net result that the boundary layer thickness ratio begins to increase as the shock strength is increased.

If it is tacitly assumed that boundary layer separation is imminent upon distortion of the incompressible profile at B (Figure 12) to a value of  $N = 1$ , then a limiting Mach number ratio for attached boundary layer across the shock interaction can be computed using the procedures outlined in Appendix II with results as presented in Figure 19. (The choice of a limiting value of  $N = 1$  results from the observation that reverse profile

curvature, similar to that encountered as separated flow conditions are approached, occurs for  $N \leq 1$ ). In examining the curves of Figure 19, it is noted that the predicted influence of wall temperature ratio is in accord with experimental observations. At supersonic speeds, where near adiabatic wall temperatures are generally the case, less compression (in terms of Mach number reduction) is predicted before boundary layer separation is imminent. On the other hand, at hypersonic speeds, where wall cooling is a physical necessity, and particularly at the low wall temperature ratios associated with shock tunnel testing, significantly more compression potential is predicted before the on-set of boundary layer separation.

Accepting the results of Figure 19, it is then desirable to re-cast such separation criteria into a form perhaps more suitable for general application. Boundary layer separation pressure plateau levels are frequently expressed as a function of parameters such as Mach number, skin friction coefficient, and Reynolds number just upstream of the shock impingement point. (See for instance, Reference 6 and 7.) On the basis of the experimental results reported in Section III-D however, it is apparent that a wide range of non-separated boundary layer shock induced pressure rise ratios, such as might be employed in hypersonic inlet compression processes, are attainable before a turbulent separation pressure plateau occurs. Consequently, it seems appropriate, and is perhaps of greater engineering usefulness to express such separation criteria in terms of the inviscid shock strength for which separation is imminent at a prescribed level of upstream wall shear. In accomplishing this end, Figures 20 through 22 were prepared by combining the separation prediction of Figure 19 with the turbulent flat plate skin friction law developed by Spence in Reference 8 which can be expressed for compressible flow as:

$$C_f = 2C \left( \frac{T_e}{T_r} \right)^{1 - \frac{2u}{N+1}} \left( Re_\theta \right)^{-\frac{2}{N+1}} \quad (17)$$

(See page 32 of Section III-D-a for additional information.) This particular skin friction law was selected because of its generality with respect to  $N$  and because of the variation of  $N$  encountered in the test results of this program. The predicted sensitivity of turbulent boundary layer separation to  $N$  (Figure 19) amplifies, for the present application, the relative scatter in correlation plots of this power law parameter as a function of Reynolds number (curves presented in References 9 and 10 for example). It was thus decided best, at present, not to reflect a correspondence between the power law profile index and Reynolds number in separation curves such as those of Figures 20 to 22.

In using the latter curves to assess the probability of incident shock induced turbulent boundary layer separation, it should be noted that for any given impinging shock strength ( $\Delta\theta$ ) and upstream flow conditions, the corresponding values of  $C_f(Re_\theta)^{\frac{2}{N+1}}$  given in Figures 20 to 22 represent, on

the basis of the formulated analysis, the minimum values required to avoid separation. Thus for conditions with greater

$$C_f(Re_\theta) \frac{2}{N+1} \quad \text{no separation}$$

is predicted, and correspondingly, at lower values of  $C_f(Re_\theta) \frac{2}{N+1}$ , separation is presumed imminent. This criteria is used in Section III-D-a in conjunction with shock impingement data obtained under this program, and is also compared against data obtained by other investigators (Figure 101) wherein required upstream boundary layer profile data as well as shock strengths required for separation were reported. The relative agreement between the experimental results and the predictions are considered to substantiate the engineering usefulness of this relatively simple formulation.

### SECTION III

#### EXPERIMENTAL PROGRAM

##### A. MODELS AND INSTRUMENTATION

###### a. Model C

###### (1) Design and Fabrication

Model C is basically a twice scale version of Model A which was shock tunnel tested earlier in the program at Cornell Aeronautical Laboratory (CAL) and at General Electric Missiles and Space Division (MSD) as reported in Reference 1. For the Model A shock tunnel tests emphasis was placed on static pressure, heat transfer, and skin friction distributions for shock induced boundary layer interaction phenomena. The emphasis during Model C testing in the NASA-Ames 3.5 foot Hypersonic Wind Tunnel was on boundary layer profile and ramp pressure measurements.

Model C was designed and fabricated as two independent major assemblies: the fixed 3 degree ramp assembly, Figures 23 and 24, and the remotely positionable flat plate cowl assembly, Figures 25 and 26.

The fixed 3 degree ramp assembly consists of an 18" wide X 48" long 7075 Aluminum ramp plate (forward portion watercooled) with a detachable tool steel, water cooled, sharp leading edge component, and a detachable cast aluminum undercarriage housing with a steel U section adapter. Top and bottom view photographs of the ramp assembly (before instrumentation) are shown in Figures 23 and 24. The aluminum undercarriage housing rigidly supported the ramp plate and housed the probe actuators and other attendant instrumentation. Final finishing of the ramp aerodynamic surface was accomplished with the undercarriage housing installed. The transition from the steel leading edge component surface to the aluminum ramp surface was perfectly smooth and remained so during the 79 test runs. The U shaped steel adapter, attached to the undercarriage housing and the bottom of the ramp plate, mounted on the steel NASA-Ames Pressure Transducer Pod Housing which in turn was supported by the tunnel strut system.



The cowl assembly consists of an 18" wide X 41" long 7075 Aluminum cowl plate (forward portion watercooled) with a detachable tool steel, watercooled, sharp leading edge component, a 7" long aluminum cowl extension plate, cowl side plates, a 4130 Steel support and pivot assembly, and a cowl drive assembly. Top and bottom view photographs of the cowl plate with cowl extension plate and support fittings installed are shown in Figures 25 and 26.

## (2) Instrumentation

The Model C ramp was instrumented with 69 static pressure taps and 11 surface-embedded thermocouples. The location and identification of the taps and thermocouples are shown in Figure 27. The .063 OD X .042 ID leadout tubing installation and one probe actuator installation are shown in the photograph of Figure 28. All the .063 OD pressure tubes were press-fitted into pre-drilled holes in the ramp plate and honed flush with the top surface. Each tube was painted with Glyptol where it emerged from the underside of the ramp plate to insure an airtight seal.

The Model C cowl plate was instrumented with 10 static pressure taps and 4 surface-embedded thermocouples. The location and identification of the taps and thermocouples are shown in Figure 29.

The small probe actuator used to drive the NASA-Ames pitot pressure-static pressure-total temperature combination probe is shown in the photograph of Figure 30 (shown approximately full size). The actuator consists of a 17,100 RPM DC motor and appropriate gear reduction to provide .80 inch travel in approximately 10 seconds. This rapid travel time is of the same order as the probe instrumentation response time. Thus the boundary layer pitot pressure survey data points were obtained shortly after the probe instrumentation equilibrated. The actuator included a 10 turn potentiometer for measuring probe position. The potentiometer was connected as two arms of a bridge circuit which enabled zeroing at any position. As the probe height changed, the unbalanced bridge voltage was displayed on a digital voltmeter to provide continuous probe position readings. Pre-test calibration of the probe height positioning circuits indicated that the probe could be repositioned at any height with an accuracy of  $\pm .002"$ . Also provided on the probe actuator were two limit switches. These switches limited the probe travel so that the probe would not emerge from the surface of the ramp beyond the design limit of .7" and would not become jammed against the ramp surface during probe withdrawal.

A pitot pressure-static pressure total temperature combination probe developed by NASA-Ames was used for the ramp boundary layer profile surveys. The three-prong probe is shown in Figure 31. Views of the probe and a typical installation on the ramp surface are depicted in the photographs of Figure 32. Alternate static probe "Y" was used for all data presented in this report. The combination probe was remotely positioned at various points across the boundary layer and its height position and the three measured quantities were simultaneously recorded on the Beckman recording

system. The output tape from the Beckman system was then processed using the NASA data acquisition program. The probe's height position, pitot pressure, static pressure and total temperature were printed out for use in subsequent data reduction.

### (3) Boundary Layer Trips

For the Model C - NASA Ames tests several factors known to influence transition were fixed by the 3.5 foot tunnel test facility set-up. These were Mach number, wall to free stream temperature ratio, and free stream turbulence level. The magnitude of the Reynolds number, based on distance from the model leading edge, was limited by total conditions available and model size.

To promote boundary layer transition, a series of boundary layer trip configurations were utilized. Limited testing was accomplished on several trip configurations as indicated in the schematic sketch of Figure 33. However, trip configuration #5 (which incorporates trip configuration #3) proved most effective and was used for the balance of the Mach 10 testing program.

Trip configuration #3 consisted of 1/8" diameter steel balls on 3/8" centers being embedded into and then high temperature brazed onto a .020" thick steel strip. The overall height of the trip was .130". This configuration was secured to the ramp surface with epoxy and also at 12 intermediate positions across the width of the ramp with small screws.

Trip configuration #5 was comprised of Trip configuration #3 (at ramp station  $X = 9.8''$ ) plus two rows (at ramp stations  $X = 4''$  and  $X = 7''$ ) of #2-64 Fillister Head screws on 3/8" centers across the width of the ramp.

### (4) Installation

The Model C ramp assembly, without the cowl assembly, was installed in the tunnel for the first 34 test runs. The installation is shown in the photograph of Figure 34. The ramp was axially oriented in the test section so as to utilize three of the five available schlieren windows. The three windows, designated windows #2, #3, and #4, are centered at test section stations 46", 63", and 80" respectively. The leading edge of the ramp was located at test section station 41.25" or approximately 1" downstream of the upstream edge of the #2 window glass. A special steel panel was fitted into the #5 window frame (centered at station 102") for instrumentation, accessory, and watercooling lines.

Prior to the ramp installation, the NASA-Ames Pressure Transducer Pod Housing (with provisions for 72 Statham pressure transducers with electrical disconnect assemblies) was mounted on the ramp undercarriage adapter and then all model to transducer instrumentation hookups were completed and checked out.

The Model C cowl assembly was installed in the tunnel for test runs 35 through 66. The Model C ramp and cowl installation is shown in the photograph of Figure 35. Complete Model C assembly and installation details are documented in the reduced size assembly drawing of Figure 36.

A special 4130 Steel hatch plate, 10" wide X 40" long X 2 1/4" thick, was fabricated as part of the cowl assembly. This plate fitted into the existing hatch opening on top of the tunnel test section and served as the mounting plate for the cowl support yoke and the cowl drive assembly. Vertical adjustment (3/4") of the cowl was provided by spacers inserted between the hatch plate and the cowl support yoke. Axial adjustment (1" upstream) of the cowl was also provided.

The cowl was driven through 13 degrees angle of attack by means of a commercially available worm gear jack assembly (2 ton capacity, 6" travel) which, in turn, was driven by a direct-current, variable speed motor. Both the jack assembly and the motor assembly were mounted on the hatch plate outside the tunnel. The screw of the jack assembly was attached to a 1.50" diameter 4140 Steel shaft extending through the bearing surface and "O" ring pressure seal in the hatch plate. The shaft in turn was bolted and pinned to a steel yoke which carried a cam follower. The follower rode in the cam-slot of an inverted T-section (slide follower) bolted to the forward and outboard side of the cowl plate. The cowl angle position was determined by a linear motion potentiometer mounted outside the tunnel on the jack assembly support housing. The shaft of the potentiometer was, in turn, connected to the cowl drive shaft. The resolution of the potentiometer provided cowl angle position to within 0.1 degree.

A sheet metal streamlined heat shield (1/8" thick 4130 Steel) was attached to the underside surface of the hatch plate to protect the outboard portion of the drive assembly strut from heat distortion. A similar shield was attached to the cam-follower yoke to protect the inboard portion of the strut and the cam-follower yoke assembly. The two shields overlapped with sufficient clearance for the required 4 1/2" movement of the strut. The flexible hose water lines leading from the cowl were routed to fittings threaded into the underside of the hatch plate.

No major problems were encountered in the installation and operation of the cowl assembly. However, one minor modification was required after the first cowl-on test run. A slight deflection of the cowl assembly drive shaft caused the cam follower to move in the cam slot, allowing an angular shafting of the cowl. This problem was solved by restraining the shaft with a brass bushing supported within the outboard heat shield.

The Model C ramp and cowl assembly remained steady during the 79 test runs; no vibration or shifting of the model was evident. Both the 3.5 foot tunnel and the model started without difficulty in spite of a frontal area blockage ratio of 17%.

## b. Model D

Model D was a modified version of Model C and consisted of two 60 degree swept vane compression surfaces mounted on the fixed 3 degree ramp surface of the Model C ramp assembly as shown in Figure 37. The purpose of testing Model D was to investigate the interaction between vane generated shocks and the ramp boundary layer such as exists in three-dimensional SCRAMJET inlet configurations.

The vanes are designated Right Vane and Left Vane as viewed from the aft end of the model looking upstream. The vanes were manually pivoted from 6 degrees to 8 degrees on the ramp surface (and locked in position) to provide variable strength vane shock pressure rises. Boundary layer trip configuration #5 (Figure 33) is shown installed on the ramp surface (top photograph) for one of the test runs. A total of 11 test runs (runs 24 through 34) were made with the Model D configuration prior to the installation of the Model C cowl assembly.

Vane geometry and instrumentation location and identification are documented in the schematic sketch of Figure 38. The internal wedge angle of each vane was 6 degrees when in the design position as shown in the installation configuration of the schematic sketch. The sharp-pointed leading edge of each vane was located 16.65 inches from the ramp leading edge with the vane set in the design position. The right vane was instrumented with 17 static pressure taps on the compression surface and 2 static pressure taps on the top surface. The left vane was instrumented with 5 static pressure taps located in the same positions as 5 of the taps in the right vane and was used to check symmetry of vane internal flow field. Five surface-embedded thermocouples were also installed in the left vane in the same positions as 5 of the static pressure taps on the right vane. These thermocouples were installed to monitor the vane temperatures so as to prevent overheating of the several thin sections of the 7075 Aluminum vanes.

The outboard sides of the vanes were milled out as shown in Figure 39 to facilitate drilling the holes for the pressure and temperature instrumentation. The pressure tubing was press fitted into the pre-drilled holes in the compression surface and honed flush. The right vane is shown fully instrumented with the pressure tubing held secure with nichrome strips tack welded to steel strips which were in turn bolted to the aluminum vane.

## c. Model E-3

### (1) Design and Fabrication

Model E-3 is a two dimensional isentropic compression ramp with a shock generating cowl. The model size and surface coordinates of the ramp and cowl were obtained by scaling up by a factor of 2, Model E-1 which was tested earlier in the program in the CAL and MSD shock tunnel facilities. Model E-3 ramp, cowl contour geometry and overall dimensions are shown in the schematic drawing of Figure 40.

The Model E-3 ramp compression surface plate was fabricated from 6061-T6 Aluminum in the same manner as was the Model C ramp surface plate. The same approach to the design of the watercooling system and detachable tool steel, watercooled, sharp leading edge component was used as shown in the photograph of Figure 41. However, the Model E-3 ramp (and cowl) width was reduced from 18" (Model C) to 14" to minimize tunnel blockage. The NASA combination probe positioner plates, the .062" diameter predrilled static pressure holes, and the boundary layer trip tapped holes are also shown in the figure. The Model E-3 48" long ramp surface plate utilized the Model C ramp cast aluminum undercarriage with its steel adapter section and three probe actuators.

The Model E-3 cowl assembly consisted of a 14" wide X 15" long 6061-T6 Aluminum contoured cowl plate (forward portion watercooled) with a detachable tool steel, watercooled, sharp leading edge component, and a 4130 steel cowl support and positioning device as documented in the reduced size drawing of Figure 42. The cowl positioning device was manually pre-set prior to each test run and provided for both horizontal and vertical cowl displacement in accomplishing cowl angle of attack changes. Flexible-hose water lines leading from the cowl watercooling system tubes provided the flexibility required for cowl positioning.

Although the Model C cowl was remotely positioned through angles of attack in a continuous manner, a similar arrangement for the Model E-3 cowl was not practical. The Model C cowl was actuated through the overhead hatch plate at test section station 43" which was a considerable distance upstream (approximately 30") of the shorter Model E-3 cowl leading edge. Consequently, cowl drive shaft interference and stagger significantly complicated the efficient design of a similar system for Model E-3.

## (2) Instrumentation

The Model E-3 ramp was instrumented with 80 static pressure taps and 11 surface-embedded thermocouples. The location and identification of the taps and thermocouples are documented in the schematic sketch of Figure 43. All static taps were drilled normal to the curved surface of the ramp. The method of installing the .063" OD X .042 ID pressure tubing and the three probe actuators was the same as described for the Model C ramp. The underside of the Model E-3 ramp plate, however, was milled to accept the probe actuators (at the three probe stations) for normal to ramp curved surface immersion of the NASA-Ames combination probe.

The Model E-3 cowl was instrumented with 11 static pressure taps (normal to the contoured surface) and 2 surface-embedded thermocouples. The location and identification of the taps and thermocouples are documented in the schematic of Figure 44.

The three probe actuators and the NASA-Ames boundary layer combination probe previously described for the Model C testing program were also used for Model E-3 testing. The NASA-Ames combination probe reading stations for

Model E-3 testing are indicated in Figure 40 as are the reading stations for the total pressure probe rakes A and B. Rake A was a fixed rake while Rake B was a movable rake, the shaft of which attached to the vertical member of the cowl support.

The individual probe centerline heights in inches above the ramp surface for each rake were as follows:

Probe No.	Rake A	Rake B
	(14 Probes)	(12 Probes)
	Probe C Height	Probe Q Height
1	.028	.20
2	.070	.70
3	.106	1.20
4	.145	1.70
5	.189	2.20
6	.262	2.70
7	.344	3.20
8	.417	3.70
9	.512	4.20
10	.616	4.70
11	.717	5.20
12	.821	5.70
13	.920	--
14	1.008	--

Data obtained with rakes A and B were generally in the field of the cowl trailing edge expansion and thus were of limited value in regard to evaluating downstream profile distortion effects.

### (3) Boundary Layer Trips

During the Model E-3 Mach 10 testing program a total of 16 test runs were made with boundary layer trips installed. The boundary layer trip configuration selected for the Model E-3 ramp is documented in the schematic sketch of Figure 45. Three rows of #2-64 tapped holes on 3/8" centers were installed across the width of the ramp at stations 4", 5 1/2", and 7" from the ramp leading edge respectively. Gaps in the spacing of the tapped holes in rows 2 and 3 were necessary to forestall breaking into the water cooling chambers feeding the cross-over water lines in the aluminum ramp.

For test runs 3, 4, 10 and 11, #2-64 stainless steel set screw trips were installed in rows 1 and 2 with trip heights set at .040" and .060" respectively. For the remaining 12 test runs utilizing trips, the set screw trips were installed in rows 1 and 3 with trip heights set at .060" and .085" respectively. A typical installation of the boundary layer trips (row 1 with trip heights .060" and row 3 with trip heights .085") is shown in the photograph of Figure 48.

#### (4) Installation

A total of 35 test runs at Mach 10.5 and Mach 7.3 were made with the Model E-3 ramp assembly installed as shown in the photograph of Figure 46. The fixed axial orientation of the Model E 3 ramp assembly in the test section was the same as the axial orientation of the Model C ramp assembly.

The complete Model E-3 installation is shown in the photograph of Figure 47. The cowl is shown with aluminum side plates installed. The method of attaching the cowl support and positioning device to the ramp and cowl is documented in the reduced size drawing of Figure 42. Cowl angle of attack positions ranging from  $-3^{\circ}$  to  $+18^{\circ}$  were manually set within  $.01^{\circ}$  accuracy using a gunner's quadrant graduated in mils.

Test runs 15 through 41 at Mach 10.5 and test runs 61 through 92 and 96 through 107 at Mach 7.3 were made with the complete Model E-3 installation. During test run 20 a severe crack developed in the ramp detachable leading edge component. The crack was located near the centerline of the model and extended from the sharp leading edge approximately 1" aft, then laterally across the component along a  $3/16$ " diameter watercooling passage. The cause of the failure was attributed to inadequate heat treatment or stress relieving of the leading edge component during fabrication. In order to continue testing with minimum delay, the damaged leading edge component was removed from the ramp and the Model C watercooled leading edge component was installed. Although otherwise interchangeable, the Model C leading edge component was 18" wide and provisions had to be made as shown in the photograph of Figure 48 to adapt to the 14" wide Model E-3 ramp. The transition from the Model C steel leading edge component surface to the Model E-3 aluminum ramp surface was smooth and continuous, and the modified installation was used successfully for the remaining 89 test runs of the program.

Cowl side support struts, which were installed early in the cowl-on phase of test runs to prevent movement of the cowl during tunnel operation, are shown in the photograph of Figure 49. Not shown are  $5/8$ " wide streamlined spacer blocks installed between the cowl and ramp and the cowl support struts. These spacers were necessary to prevent local shock impingement from the support struts upon the ramp, a condition which could cause non-start or choking of the inlet.

#### B. FACILITY DESCRIPTION

Models C, D and E-1 were tested in the NASA-Ames 3.5 foot Hypersonic Wind Tunnel facility which is shown in the sketch of Figure 50. This tunnel is an intermittent blowdown tunnel with running times ranging from 1 to 4 minutes and contoured nozzle Mach number capabilities of 5, 7, and 10. The tunnel was operated at Reynolds number per foot varying from  $2 \times 10^5$  to  $3.5 \times 10^6$  at Mach number 7 and  $5 \times 10^5$  to  $2.2 \times 10^6$  at Mach number 10. The stagnation pressure varied from 50 to 600 psia at Mach number 7 and from 400 to 1800 psia at Mach number 10.

The tunnel operates with a combination of initially high pressure air and pre-test vacuum pumpdown. High pressure air from storage cylinders is routed through the 20000R pebble-bed air heater into the nozzle section. The heated air is expanded through the nozzle (cooled by a helium injection system) and enters the test section of the tunnel. The air passes over the model into the diffuser section and eventually dumps into four interconnected large vacuum spheres which are initially pumped down to 1/4 psia for tunnel starting. The combination of the high pressure air and the vacuum pumpdown results in a pressure ratio necessary for tunnel starting. Model starting loads are held to a minimum during the tunnel starting phase by gradually raising the tunnel total pressure. As a safety precaution the tunnel starting procedure includes the sequential operation of a series of interlocks.

A view of the tunnel test section with the Mach 7 nozzle section installed is shown in the photograph of Figure 51. In the foreground of the photograph is a partial view of the schlieren system. The three windows located between the test section door actuator arms are those used for Models C, D and E-3 schlieren photography. The downstream window frame contains the special access panel for watercooling lines and instrumentation lines. The raised door in the background is the one normally used for access to the test section and model installation.

The tunnel test section is 156" long from the nozzle exit flange face to the diffuser entrance flange face. The test section inlet diameter is 42.00" (Station 0") and the exit diameter is 45.307" (Station 156"), resulting in a straight test section wall taper angle of  $0^{\circ} 36.5'$  for the full 156" length. Door openings on each side of the test section are 110" long (Station 8" to Station 118") and taper in height from 21.42" at Station 8" to 22.53" at Station 118". The inside walls of the remotely operated doors are curved and tapered to conform to the interior walls of the test section. The doors also incorporate the schlieren windows which are centered at Stations 24", 46", 63", 80", and 102". The windows are normally 6" high and 12" long, but the actual exposed glass of the windows measured 5 1/4" X 11 1/4" for this testing program. Windows centered at Stations 46", 63" and 80" (designated as windows #2, #3 and #4 respectively) were utilized for schlieren photography. A hatch opening 6" wide X 36" long (Station 18" to Station 54") on top of the test section was utilized for the special hatch plate for the Model C cowl drive assembly. A facility hatch cover, with its interior surface conforming to the interior wall curvature of the test section, is installed for normal testing.

The gimballed vertical section of the model support assembly is vertically adjustable and enters the bottom of the test section with its centerline at Station 108". The 8" OD horizontal section of the model support assembly extends upstream to Station 97.7" and accepts a keyed 5" OD model strut. The NASA-Ames Pressure Transducer Pod Housing, upon which Models C and E-3 were mounted, incorporated a 4.997" OD X 2.4" ID integral shaft with a 7" long keyed bearing surface which entered the horizontal model support bore.



A single pass Z type schlieren system with a mercury vapor light source was used in the Model C and Model E-3 testing programs. The schlieren system had provisions for simultaneously viewing the model and taking schlieren photographs. Polaroid photographs also could be taken of the viewing plate for immediate perusal or comparison with the test data.

Data acquisition was accomplished by sampling of the electrical signals from the Model PA208TC Statham absolute pressure transducers (lowest range 0 - 5 psia) on the data tape of the 100 channel high speed Beckman analog to digital recorder. Model surface pressure and temperature measurements were handled in a standard manner by computing (using the Ames computer program) on the IBM 7094 the surface to free stream static pressure ratio, etc., from the Beckman system data tape.

#### C. RUN LOG

A run log for tests conducted with Models C, D and E-3 is included here for reference purposes. Test data obtained during the Mach 7.3 and 10.5 testing at NASA-Ames was compiled for use in data analysis in References 11 and 12.

RUN LOG - MODEL C/D

RUN	P <sub>T</sub> (psi)	T <sub>T</sub> (°R)	M <sub>O</sub>	Re <sub>O</sub> <sup>-1</sup> (FT)	TRIP CONF.	DOUBLE PITOT PROBE	PROBE STATION	α (DEG)	α <sub>V</sub> (DEG)	SURFACE PITOTS	REMARKS
1	1300	1500	10.40	7.92/5 *	--	--	--	--	--	--	
2	1330	1450	10.54	1.88/6	--	--	--	--	--	--	
3	1341	2017	10.57	1.98/6	--	--	--	--	--	--	
4					--	--	--	--	--	X	
5	1320	1401	10.55	1.93/6	#2	--	--	--	--	X	Trip #2 failed
6	1332	1417	10.56	2.07/6	#1	--	--	--	--	X	Surface pitots removed after this run
7	1332	1402	10.56	1.98/6	#1	--	--	--	--	--	
8	1337	1434	10.56	2.04/6	#1	--	2	--	--	--	Probe #1 (long static)
9	1337	1471	10.56	1.96/6	#1	--	2	--	--	--	Probe #2 (short static)
10	1314	1935	10.55	2.01/6	--	--	2	--	--	--	used
11	1315	1856	10.40	7.73/5	--	--	2	--	--	--	Probe #1 used for the remainder of the test
12	1011	1403	10.45	1.19/6	--	--	2	--	--	--	
13	1216	1601	10.40	7.34/5	--	--	3	--	--	--	
14	1514	1900	10.55	2.07/6	--	--	3	--	--	--	
15	1314	1822	10.55	2.27/6	--	--	3	--	--	--	
16	1331	1422	10.56	2.29/6	#3 & 4	--	--	--	--	X	Rerun of Run 14
17					#3	--	2	--	--	X	
18	1334	1440	10.56	2.00/6	#5	--	3	--	--	X	
19	1332	1420	10.56	2.05/6	#5	--	2	--	--	X	
20	1330	1435	10.56	2.02/6	#5	--	1	--	--	X	No cooling of model
21	1320	1449	10.55	1.90/6	#5	--	2	--	--	X	No cooling of model
22	1324	1434	10.55	2.03/6	--	--	1	--	--	--	
23	1325	1400	10.40	7.77/5	--	--	1	--	--	--	
24	1323	1449	10.40	8.37/5	--	--	--	--	--	--	
25	1334	1404	10.56	2.11/6	#5	--	--	--	--	--	Vanes installed - Model D

\* 7.92/5 = 7.92 x 10<sup>5</sup>

RUN LOG - MODEL C/D (Cont'd)

RUN	P <sub>T</sub> (psia)	T <sub>T</sub> (°R)	M <sub>0</sub>	Re <sub>0</sub> -1 (FT)	TRIP CONF.	DOUBLE PITOT PROBE	PROBE STATION	θ <sub>C</sub> (DEG)	θ <sub>V</sub> (DEG)	SURFACE PITOTS	REMARKS
26	1821	1956	10.55	1.98/6	#5	--	2	--	6	--	
27	620	1880	10.40	7.55/5	--	--	2	--	6	--	
28	618	1869	10.40	7.63/5	--	X	3	--	6	--	
29	1822	1968	10.55	1.95/6	#5	X	3	--	6	--	
30	1826	1972	10.55	1.95/6	#5	X	3	--	8	--	
31	1825	1953	10.55	1.99/6	#5	X	2	--	8	--	
32	617	1891	10.40	7.43/5	--	X	2	--	6	--	
33	620	1640	10.40	9.87/5	--	--	2	--	6	--	Left vane removed
34	618	1785	10.40	8.38/5	--	--	3	--	6	--	Left vane off
35	618	1788	10.40	8.34/5	--	--	--	0,1.5,3, 5,1.5,0	--	--	Cowl installed. Extension plate on cowl
36	629	1759	10.40	9.20/5	--	--	--	1.5, 3, 5, 0,5,8,10	--	--	Extension plate removed
37	1824	1975	10.55	2.01/6	#5	--	--	5	--	--	
38	1813	1855	10.55	2.19/6	#5	--	1	10	--	--	
39	1826	1846	10.55	2.23/6	#5	--	1	5	--	--	Repeat of Run 38
40	1835	1901	10.56	2.11/6	#5	--	1	5	--	--	Extension plate on cowl
41	627	1831	10.40	8.06/5	--	--	1	1.5	--	--	
42	626	1875	10.40	8.09/5	--	--	1	1.5	--	--	Cowl moved 1.25" forward or 10.95" forward of ramp
43	605	1802	10.40	8.04/5	--	--	2	1.5	--	--	L.E.
44	607	1824	10.40	7.87/5	--	--	2	5	--	--	Pitot pressure trans - ducer overloaded
45	1830	1889	10.56	2.13/6	#5	--	2	5	--	--	
46	1832	1886	10.56	2.14/6	#5	--	2	10	--	--	Repeat of Run 45
47	1830	1858	10.56	2.20/6	#5	--	2	5	--	--	No cowl extension plate
48	1830	1929	10.56	2.04/6	#5	--	3	5	--	--	No cowl extension plate
49	1833	1840	10.56	2.25/6	#5	--	3	10	--	--	No cowl extension plate
50	630	1835	10.40	7.5/5	--	--	3	1.5	--	--	Extension plate installed on cowl
51	629	1871	10.40	7.74/5	--	--	3	5	--	--	
52	628	1901	10.40	7.49/5	--	--	--	2,3,4,5, 8, & 10	--	--	No cowl extension plate
53	1836	1922	10.56	2.06/6	#5	--	2	13	--	--	

RUN LOG - MODEL C/D (Cont'd)

RUN	P <sub>T</sub> (psia)	T <sub>T</sub> (°R)	M <sub>0</sub>	Re <sub>0</sub> <sup>-1</sup> (FT) <sup>-1</sup>	TRIP CONF.	DOUBLE PITOT PROBE	PROBE STATION	θ (DEG)	θ <sub>v</sub> (DEG)	SURFACE PITOTS	REMARKS
54	627	1402	7.34	3.14/6	#6	--	--	0,3,5,8, & 10	--	--	Cowl moved 1.25" back to original position
55	222	1333	7.31	1.23/6	--	--	--	0,1.5,3, 5,8, & 10	--	--	
56	223	1311	7.31	1.27/6	--	--	2	1.5	--	--	
57	218	1353	7.31	1.18/6	--	--	2	5	--	--	
58	627	1328	7.34	3.46/6	#6	--	2		--	--	
59	621	1296	7.34	3.58/6	#7	--	--	0,2,4,6, 8,10	--	X	1 row of boundary layer trips only. @ X = 4"
60	112	1381	7.30	5.85/5	--	--	--	0,2,4,6, 8,10	--	--	
61	111	1406	7.30	5.90/5	--	--	2	2	--	--	
62	107	1357	7.30	5.97/5	--	--	2	2.5, 8	--	--	
63	113	1456	7.30	5.09/5	--	--	1	2	--	--	
64	114	1359	7.30	5.63/5	--	--	1	3	--	--	
65	626	1433	7.34	2.86/6	--	--	--	0,2,4,6, 8,10	--	--	
66	111	1463	7.34	2.90/6	#7	--	2	5	--	--	1 row of boundary layer trips .060" high @ X = 4"
67	114	1434	7.30	5.58/5	--	--	2	--	--	--	Cowl removed. Ramp C only
68	610	1440	7.34	2.92/5	#7	--	2	--	--	--	Ramp C only
69	622	1340	7.34	3.38/6	#7	--	1	--	--	--	Ramp C only
70	107	1408	7.30	5.39/5	--	--	1	--	--	--	Ramp C only
71	601	1416	7.34	2.93/6	--	--	1	--	--	--	Ramp C only
72	113	1257	7.30	6.99/5	--	--	3	--	--	--	Ramp C only
73	602	1338	7.34	3.28/6	#7	X	3	--	--	--	1 row of boundary layer trips @ X = 4" Ramp C only
74	618	1570	7.34	2.52/6	--	X	3	--	--	--	Ramp C only
75	619	1397	7.34	3.12/6	#7	X	3	--	--	--	Ramp C only
76	622	1414	7.34	3.07/6	--	--	2	--	--	--	Ramp C only
77	618	1363	7.34	3.26/6	#6	--	2	--	--	--	Ramp C only
78	114	1234	7.30	7.26/5	--	--	--	--	--	--	Ramp C only
79	109	1197	7.30	7.35/5	--	--	--	--	--	--	Ramp C only

RUN LOG - MODEL E-3

RUN	P <sub>T</sub> (psia)	T <sub>T</sub> (°R)	M <sub>0</sub>	Re <sub>0</sub> -1 (FT)	PROBE STATION	B/L TRIPS			θ <sub>C</sub> (DEG)	THROAT HEIGHT (IN)	L.E. HEIGHT (IN)	L.E. STATION (IN)	REMARKS
						4" Row 1	5-1/2" Row 2	7" Row 3					
1	626	1929	10.40	7.25/5*	--	--	--	--	--	--	--	--	
2	1831	1950	10.56	2.00/6	--	--	--	--	--	--	--	--	
3	1796	1891	10.55	2.09/6	--	.040	.060	--	--	--	--	--	
4	1799	1932	10.55	2.00/6	1	.040	.060	--	--	--	--	--	
5	594	1863	10.40	7.38/5	1	--	--	--	--	--	--	--	
6	627	1880	10.40	7.64/5	1	--	--	--	--	--	--	--	
7	1832	1892	10.56	2.13/6	1	--	--	--	--	--	--	--	
8	629	1926	10.40	7.30/5	2	--	--	--	--	--	--	--	
9	1841	1938	10.55	2.03/6	2	--	--	--	--	--	--	--	
10	1841	1943	10.56	2.02/6	2	.040	.060	--	--	--	--	--	
11	1832	1907	10.56	2.09/6	3	.040	.060	--	--	--	--	--	
12	1832	1935	10.56	2.03/6	3	--	--	--	--	--	--	--	
13	626	1782	10.40	8.51/5	3	--	--	--	--	--	--	--	
14	423	1666	10.37	6.60/5	3	--	--	--	--	--	--	--	
15	624	1645	10.40	9.93/5	--	--	--	--	2.0	.547	2.50	28.00	
16	626	1884	10.40	7.60/5	--	--	--	--	3.5	.163	2.50	28.00	
17	623	1889	10.40	7.52/5	--	--	--	--	-1.0	1.307	2.50	28.00	Cowl moved during run
18	1854	1926	10.56	2.07/6	--	.060	--	.085	-1.0	1.307	2.50	28.00	
19	1846	1957	10.56	2.00/6	--	.060	--	.085	2.5	.392	2.50	28.00	
20	1800	2100	10.55	--	--	.060	--	.085	3.5	.220	2.60	28.00	Side supports for cowl installed
21	1800	2140	10.55	--	--	.060	--	.085	3.0	.360	2.60	28.00	Replaced E-3 LE with Model C LE
22	425	2100	10.37	--	--	--	--	--	3.0	.360	2.60	28.00	Did not start
23	425	2140	10.37	--	--	--	--	--	2.5	.442	2.56	28.00	Did not start
24	425	2060	10.37	--	--	--	--	--	2.5	.434	2.55	28.00	Did not start
25	1833	1869	10.56	2.18/6	--	.060	--	.085	2.5	.434	2.55	28.00	Started
26	621	1917	10.40	7.28/5	--	--	--	--	2.5	.436	2.60	28.00	
27	625	2160	10.40	--	3	--	--	--	2.5	.434	2.50	28.00	Did not start
28	625	2100	10.40	--	3	--	--	--	2.5	.432	2.50	28.00	Did not start
29	625	1927	10.40	7.25/5	3	--	--	--	-1.0	1.093	2.32	27.81	
30	1835	1966	10.55	1.97/6	3	.060	--	.085	-1.0	1.093	2.32	27.81	
31	428	1863	10.38	5.35/5	--	--	--	--	6.0	1.870	4.94	27.69	

\*7.25/5 = 7.25 X 10<sup>5</sup>

RUN LOG - MODEL E-3 (Cont'd)

RUN	P <sub>T</sub> (psia)	T <sub>T</sub> (°R)	M <sub>0</sub>	Re <sub>0</sub> (FT)-1	PROBE STATION	4" Row 1	B/L TRIPS 5-1/2" 7" Row 2 Row 3	θ <sub>C</sub> (DEG)	THROAT HEIGHT (IN)	L.E. HEIGHT (IN)	L.E. STATION (IN)	REMARKS
32	400	2100	10.50	--	--	--	--	8.0	1.721	5.00	24.03	Did not start
33	428	1723	10.37	6.25/5	--	--	--	7.1	1.971	5.02	24.06	
34	430	1744	10.38	6.13/5	--	--	--	12.0	2.491	6.80	24.31	
35	425	1675	10.37	6.57/5	--	--	--	15.1	3.100	8.24	24.50	
36	1854	1931	10.56	2.06/6	--	--	--	15.1	3.100	8.24	24.50	
37	432	1826	10.38	5.61/5	3	--	--	15.1	3.100	8.24	24.50	
38	1841	1909	10.56	2.0/6	3	.060	.085	15.1	3.100	8.24	24.50	
39	400	2100	10.50	--	--	--	--	15.1	3.100	8.24	24.50	
40	426	1911	10.37	5.06/5	--	--	--	15.1	3.100	8.24	24.50	Tunnel malfunction
41	1858	1963	10.56	2.00/6	--	.060	.085	15.1	3.100	8.24	24.50	
42	1864	1981	10.56	1.97/6	--	.060	.085	15.1	3.100	8.24	24.50	
43	426	1908	10.37	5.07/5	--	--	--	--	--	--	--	
44	425	1867	10.37	5.28/5	3	--	--	--	--	--	--	
45	1842	1995	10.56	1.92/6	3	.060	.085	--	--	--	--	
46	1839	1939	10.56	2.03/6	2	.060	.084	--	--	--	--	
47	422	1877	10.37	5.19/5	2	--	--	--	--	--	--	
48	400	2100	10.50	--	2	--	--	14.9	--	--	--	Tunnel unstart
49	426	1762	10.37	5.95/5	2	--	--	14.9	--	--	--	
50	1838	1916	10.56	2.08/6	2	.060	.085	14.9	--	--	--	
51	114	1663	7.30	4.27/5	--	--	--	--	--	--	--	
52	627	1851	7.34	1.89/6	--	--	--	--	--	--	--	
53	100	2050	7.40	--	2	--	--	--	--	--	--	No programmed data
54	626	1817	7.34	1.96/6	2	--	--	--	--	--	--	
55	121	1531	7.30	5.24/5	2	--	--	--	--	--	--	
56	632	1905	7.34	1.81/6	1	--	--	--	--	--	--	
57	114	1773	7.30	3.94/5	1	--	--	--	--	--	--	
58	626	1683	7.34	2.25/6	3	--	--	--	--	--	--	
59	116	1581	7.30	4.73/5	3	--	--	--	--	--	--	Probe loose
60	120	1686	7.30	4.36/5	3	--	--	--	--	--	--	Rerun of 59
61	114	1654	7.30	4.31/5	--	--	--	--	--	--	--	
62	627	--	7.34	--	--	--	--	3.0	1.035	3.34	28.00	
63	120	1682	7.30	4.39/5	--	--	--	3.0	1.035	3.34	28.00	
64	120	1612	7.30	4.75/5	--	--	--	11.9	2.485	--	24.25	
65	68	1476	7.30	3.17/5	--	--	--	15.0	3.105	8.25	24.50	Tunnel started at 75 psi
					--	--	--	15.0	3.105	8.25	24.50	Tunnel started at 30 psi

RUN LOG - MODEL E-3 (Cont'd)

RUN	P <sub>T</sub> (psia)	T <sub>T</sub> (°R)	M <sub>O</sub>	Re <sub>O</sub> -1 (T)	PROBE STATION	B/L TRIPS			THROAT HEIGHT (IN)	L.E. HEIGHT (IN)	L.E. STATION (IN)	REMARKS
						4"	5-1/2"	7"				
						Row 1	Row 2	Row 3				
66	625	1758	7.34	2.08/6	--	--	--	--	3.105	8.25	24.50	
67	87	1693	7.30	3.14/5	--	--	--	--	3.105	8.25	24.50	
68	87	1623	7.30	3.39/5	--	--	--	--	3.730	9.42	24.75	
69	632	1868	7.34	1.88/6	--	--	--	--	3.730	9.42	24.75	
70	87	1684	7.30	3.19/5	--	--	--	--	2.526	6.85	24.25	
71	87	1658	7.30	3.27/5	--	--	--	--	1.737	5.08	24.13	
72	80	2080	7.40	--	--	--	--	--	0.850	5.60	24.20	Model inlet did not start
73	87	1630	7.30	3.38/5	--	--	--	--	1.259	5.38		Feun of 72
74	65	1512	7.30	2.88/5	--	--	--	--	1.259	5.38		Cowl in extreme aft position
75	63	1641	7.30	2.41/5	3	--	--	--	3.104	8.20	24.50	
76	626	1759	7.30	2.41/5	3	--	--	--	3.104	8.20	24.50	Tunnel trouble
77	95	1638	7.30	3.63/5	3	--	--	--	3.104	8.20	24.50	Tunnel choked
78	93	1551	7.30	3.96/5	3	--	--	--	3.104	8.20	24.50	Started
79	59	1489	7.30	2.79/5	3	--	--	--	3.0	1.028	28.00	
80	58	1573	7.29	2.38/5	2	--	--	--	3.102	8.20	24.50	
81	--	--	--	--	--	--	--	--	--	--	--	Run aborted
82	625	1833	7.34	1.92/6	2	--	--	--	3.102	8.20	24.50	
83	62	1698	7.30	2.23/5	--	--	--	--	1.737	5.080	24.13	
84	69	1600	7.30	2.77/5	--	--	--	--	1.250	3.28	25.40	
85	69	1647	7.30	2.61/5	--	--	--	--	3.240	4.96	31.31	1/2" high bar across width of ramp at x = 43"
86	61	1514	7.30	2.71/5	--	--	--	--	3.240	4.96	31.31	
87	85	1726	7.30	2.98/5	--	--	--	--	5.43	9.82	31.00	
88	58	1562	7.29	2.43/5	--	--	--	--	3.032	8.162	24.50	
89	632	1802	7.34	2.00/5	--	--	--	--	3.032	8.162	24.50	
90	216	1568	7.31	8.96/5	3	--	--	--	3.175	4.825	31.19	
91	50	1395	7.29	2.55/5	3	--	--	--	3.175	4.825	31.19	
92	599	1762	7.34	1.98/5	3	--	--	--	2.475	5.000	31.06	
93	60	1497	7.30	2.72/5	2	--	--	--	--	--	--	
94	63	1682	7.30	2.29/5	1	--	--	--	--	--	--	
95	61	1589	7.30	2.47/5	--	--	--	--	--	--	--	
96	62	1678	7.30	2.27/5	--	--	--	--	1.800	3.12	28.19	
97	61	1521	7.30	2.70/5	--	--	--	--	1.800	3.05	27.94	

RUN LOG - MODEL E-3 (Cont'd)

RUN	P <sub>T</sub> (psia)	T <sub>T</sub> (°R)	M <sub>0</sub>	Re <sub>0</sub> -1 (FT)	PROBE STATION	B/L TRIPS			μ <sub>c</sub> (DEG)	THROAT HEIGHT (IN)	L.E. HEIGHT (IN)	L.E. STATION (IN)	REMARKS
						4"	5-1/2"	7"					
						Row 1	Row 2	Row 3					
98	75	1560	7.30	3.15/5	--	--	--	--	-1.0	1.800	3.05	28.00	
"	102	1612	7.30	4.04/5	--	--	--	--	-1.0	1.800	3.05	28.00	
99	50	1393	7.29	2.57/5	2	--	--	--	8.0	1.700	4.97	23.75	
100	69	1595	7.30	2.76/5	2	--	--	--	8.0	1.700	4.97	23.75	
101	69	1508	7.30	3.10/5	3	--	--	--	8.2	1.700	4.97	23.75	
102	59	1515	7.29	2.60/6	3	--	--	--	-1.0	1.740	2.95	28.00	
103	60	1482	7.30	2.76/5	--	--	--	--	-2.9	3.675	4.21	25.00	
104	630	1752	7.34	2.10/6	--	--	--	--	-2.9	3.675	4.21	25.00	
105	45	1502	7.29	2.07/5	--	--	--	--	8.0	1.830	5.15	24.25	
106	69	1463	7.30	3.23/5	--	--	--	--	-1.0	1.800	3.075	28.22	
107	624	1723	7.34	2.15/6	--	--	--	--	3.0	--	--	--	
108	64	1513	7.30	2.84/5	--	--	--	--	--	--	--	--	1/8" high bar across width of ramp
109	632	1786	7.34	2.04/6	--	--	--	--	--	--	--	--	



## D. TEST RESULTS AND ANALYSES

### a. Model C

#### (1) Flat Plate Results

Initial data for the model of Figure 35 was obtained without the shock generating cowl installed, for the purpose of determining the nature of the boundary layer as required for interpretation of subsequent shock impingement test results. The 3 station boundary layer profile measurements provided a basis for evaluating regions of laminar and turbulent flow, detailed boundary layer integral properties, and local skin friction as discussed in the following sub-sections. Reduced boundary layer profile data are tabulated in Table I.

Wall Pressure Data and Leading Edge Shock Shape - At the lower values of wall static pressure measured on the 30° wedge surface of Model C, it was necessary to make a small correction for an apparent reference pressure error as described in Section IV-C. The net result of such a correction was to bring both the inviscid field ramp Mach number in line with measured pitot data and to obtain better agreement between measured wall static pressure levels and values computed from substantiated theoretical techniques. Such corrections had no significant effect on higher values of measured pressure such as in the region of a shock impingement.

Using the corrected pressure levels, the leading edge shock shape was computed using the GE/Bertram technique of Reference 1 which accounts for the combined effects of bluntness and viscous induced interactions. This solution is superimposed on the schlieren of Figure 52 and the agreement is seen to be excellent. Similar agreement was noted earlier in the program for shock tunnel tests with Model A as also reported in Reference 1.

Transition - As a nominal assessment of the state of the boundary layer and of boundary layer trip effectiveness, direct use was made of the compressible profile power law parameter  $n$  in the expression:

$$\frac{u}{u_e} = \left( \frac{y}{\delta} \right)^{\frac{1}{n}} \quad (18)$$

The flow was considered laminar for values of  $n$  from 1 to 2, transitional for  $n$  from 2 to 5, and turbulent for values of  $n$  greater than 5. The procedure for determining  $n$  was to establish the velocity profile from the probe data using the procedure described in Section IV-C. The value of  $n$  was then measured directly from the resulting velocity distribution when plotted on log-log paper as typified in Figures 53 and 54 indicating that such an approach permits reasonable analytical representation of the measured profile data.

Summarizing the results indicated in Table I, at Mach 10.5, the low Reynolds number data was laminar at all three probe stations indicating that natural transition would be expected to occur at a value of  $Re_\theta$  greater than 950. The low Reynolds number data taken at Mach 7.4, also indicates the onset of boundary layer transition at values of  $Re_\theta$  greater than 950. At maximum unit Reynolds number, natural transition was initiated at the first and second probe stations respectively for Mach 7.3 and 10.5, corresponding to values of  $Re_\theta$  of approximately 1690 and 1360 respectively.

The addition of boundary layer trips for high Reynolds number testing resulted in the onset of transition ahead of the first probe station at Mach 7.3, but a subsequent decrease in the profile parameter  $n$  at the second and third probe station suggest that the resulting boundary layer profile was not completely in equilibrium. On the other hand, the boundary layer trips used for high Reynolds number testing at Mach 10.5 not only promoted earlier boundary layer transition, but also permitted the attainment of increased equilibrium values of profile parameter  $n$ .

As a matter of interest, the natural transition characteristics exhibited in this test data obtained with the Model C are compared in Figure 55 with those determined from shock tunnel tests and heat transfer measurements made earlier in this program with flat plate Model A and curved surface Model E-1 at Cornell. (Reference 1.) The value of  $n$  for Run 14, Model C data, where the boundary layer profile is measured at the third probe station at maximum Reynolds number, indicated the flow to be turbulent. At the same test conditions, the boundary layer at the second probe station appeared to be transitional. Consequently, in Figure 55 the data point for Run 14 is plotted in such a manner to indicate that boundary layer transition had been completed at a value of  $Re_\theta$  of approximately 2000. At this same probe position, at the lower unit Reynolds number, the boundary layer was still laminar, and thus, it is seen that for both tests, transition occurred for an  $Re_\theta$  greater than 1000 and less than 2000 on the flat plate models as compared to an  $Re_\theta$  of slightly less than 1000 on the curved surface pressure gradient model.

Variation of  $n$  with  $Re_\theta$  - To determine the extent to which the values of  $n$  for the hypersonic non-adiabatic wall turbulent boundary layer of these tests correlate with near-adiabatic wall results at lower Mach numbers, Figure 56 was prepared comparing the results from Table I with data presented by Persh in Reference 9 and by Pinckney in Reference 10. Data from this program taken both with and without boundary layer trips are included. The natural transition data not only indicate higher values of  $n$  at lower  $Re_\theta$  than the correlation of Reference 9, but also steeper rate of change of  $n$  with increase in  $Re_\theta$ . At Mach 10.5, the addition of boundary layer trips resulted in a significant increase in  $n$  with only a small change in  $Re_\theta$  from the nominal value of 2000. On the other hand, at Mach 7.4 with boundary layer trips installed, the contrasting decrease in  $n$  with increasing  $Re_\theta$  again suggests that the boundary layer profiles for these particular test conditions were not in complete equilibrium. Consequently, it is implied that the high rate of mixing and turbulence induced by the boundary layer

trips at Mach 7.3 could not be sustained by natural turbulence levels existing at these conditions. Somewhat better correlation is obtained when  $n$  is plotted as a function of effective length Reynolds number, as also indicated in Figure 56, but the trend is similar.

Momentum Thickness Comparison - The laminar values of momentum thickness as presented in Table 1 have been compared against the values predicted for flat plate flow at the measured boundary layer edge conditions using the methods of Van Driest (Reference 13) and Cohen-Reshotko (Reference 14). This comparison is shown in Figure 57 in a manner also conducive to the establishment of a laminar skin friction law based on the test data. For zero pressure gradient flow, assuming a constant value of  $n$  (as substantiated by the profile measurements) a skin friction law can readily be established from the classical hypothesis that  $S/x \propto (Re_x)^{-Z}$  as follows:

$$\frac{\theta}{x} = K (Re_x)^{-Z} \quad (19)$$

$$\frac{d\theta}{dx} = \frac{C_f}{2} = \frac{(1-Z) K}{(Re_x)^Z} \quad (20)$$

From the slope of a line through the data in Figure 57,  $Z$  is determined to be .50.  $K$  can be evaluated from any point on the curve to be .310. Thus

$$\frac{C_f}{2} = \frac{.305}{(Re_x)^{.5}} \quad (21)$$

is the experimentally determined laminar skin friction law which is seen to be reasonably well predicted by the laminar theories of References 13 and 14.

A similar development of a skin friction law for the turbulent boundary layer data is not justified in that the effective origin necessarily varied with test conditions and boundary layer trip configuration. As an alternative, use is made of the incompressible skin friction law:

$$C_{f_1} = 2C(Re_\theta)^{-\frac{2}{N+1}} \quad (22)$$

developed by Spence in Reference 8 and adapted to compressible flow through the Eckert Reference Temperature relation:

$$\frac{T_{ref}}{T_e} = \frac{1}{2} \left[ \frac{T_w}{T_{T_e}} \left( 1 + \frac{\gamma-1}{2} M_e^2 \right) + 1 \right] + 0.22 R \frac{\gamma-1}{2} M_e^2 \quad (23)$$

with the result:

$$C_f = 2C (Re_\rho)^{\frac{-2}{N+1}} \left( \frac{T_e}{T_{ref}} \right)^{1 - \frac{2\omega}{N+1}} \quad (24)$$

where:

$$C = \left[ \frac{(N+1)(N+2)}{N} K^N \right]^{-\frac{2}{N+1}} \quad (25)$$

$$K = NAe^{\frac{B}{NA} - 1} \quad (26)$$

$$A = 2.5 \quad B = 5.5$$

$$N = \text{incompressible profile exponent in } \frac{U}{U_e} = \left( \frac{Y}{\Lambda} \right)^{\frac{1}{N}}$$

With the aid of such an expression and the measured profile data, the effective origin associated with each profile measurement was computed from:

$$x = \frac{2\theta}{C_f} \cdot \frac{N+1}{N+3} \quad (27)$$

with the results as reflected in Figures 56 and 57. Equations 21 and 24 provide a basis for estimating values of laminar and turbulent boundary layer properties at positions immediately upstream of shock impingement interactions.

Boundary Layer Profile Property Comparisons - For nearly all of the profile data, the compressible power law profile parameter,  $n$ , was calculated. In addition, for selected cases, the incompressible value of the power law profile parameter,  $N$ , was also calculated. The incompressible cases were calculated primarily for comparison against theoretical profiles. In Figure 58 several of the laminar profiles measured on Model C and E-3 are compared against the Blasius and Cohen-Reshotko flat plate solutions. As can be seen, the experimental data falls below the Blasius solution indicating a fuller profile. There is also a point of inflection in the Model E-3 profile indicating the effect of the slight adverse pressure gradient. It should be noted, however, that the experimental data can be brought into closer agreement by using a different criteria for establishing the boundary layer edge conditions. The edge conditions are shown based on a velocity ratio of .995 of the inviscid wedge flow velocity. Consequently, with this definition, any entropy layer due to the leading edge shock-boundary layer interaction is included in the boundary layer. As an alternative approach, matching could have been forced near the wall, and boundary layer edge conditions (exclusive of any entropy layer) defined as a by-product of the lower region profile matching.

Several comparisons were also made of corresponding compressible and incompressible profiles as indicated in Figures 59 and 60. As would be expected, for a typical turbulent profile the compressible value of the profile parameter ( $n$ ) is smaller than the incompressible value ( $N$ ). The value of  $n$  was determined as indicated previously. The incompressible power law profile parameter  $N$  for the expression  $U/U_e = \left(\frac{y}{\Delta}\right)^{1/N}$  was determined through numerical integration of the test data using the Stewartson relation as follows:

$$\tau_w = \int_0^y \frac{\rho}{\rho_e} dy \quad (28)$$

and the log-log plotting procedure previously described for the determination of  $n$ .

In Figures 61 to 74, for purposes of documentation, typical boundary profile data are plotted in terms of selected profile properties as calculated in the course of the data reduction.

From the skin friction laws reflected in Figure 57, for those cases where the profile parameter  $n$  is essentially invariant with Reynolds number, the growth rate was established for subsequent use in connection with incident shock data as follows:

$$\delta = \left[ KH \left( \frac{\delta}{\delta^*} \right) \right] \frac{x}{(Re_x)^Z} \quad (29)$$

where  $K$  and  $Z$  have the previously established values. Thus from Figure 57 it is seen that the hypersonic laminar boundary layer growth along the Model C ramp was in proportion to the square root of the Reynolds number as would classically be predicted from low speed theory. For any particular set of similar turbulent data the growth rate can, of course, be expressed in a comparable manner, but is a function of the particular value of  $N$  associated with that data.

Summary - From analysis of the Model C ramp data it can be concluded that for incident shock tests conducted at low test facility unit Reynolds numbers the boundary layer separation characteristics should be those of a laminar layer with consistent growth rate and local skin friction variations derived from the profile measurements in general agreement with predicted trends. For tests conducted at Mach 7.3 and the maximum facility unit Reynolds number, the incident shock-boundary layer interactions should be those associated with a naturally turbulent hypersonic boundary layer. At other test conditions, boundary layer trips are required to establish turbulent boundary layer profiles. In that the boundary layer trips had a pronounced effect on the profile shape, this should be taken into consideration in the interpretation of incident shock wave-boundary layer interaction data. For the hypersonic boundary layer measurements made both with and without trips, it was found that reasonable representation

of profile shape is possible through the use of simple power law profiles.

## (2) Incident Shock Results

With the cowl installed, (Figure 35) interaction between the Model C ramp boundary layer and the impinging cowl shock was studied. Test conditions and boundary layer trip geometry were predicated on earlier tests conducted without the cowl installed. At Mach 10.5, the unit Reynolds number was regulated between approximately .7 and  $2 \times 10^6$  per foot, while the cowl shock strength was varied through the range from 0 to  $13^\circ$  of turning. For Mach 7.3, the unit Reynolds number was regulated from .5 to  $3.3 \times 10^6$  and the shock strength varied from 0 to  $10^\circ$  of turning. Nominal thermocouple determined wall to total temperature ratios were .40 at Mach 7.3 and .30 at Mach 10.5.

Flow Model Comparisons - The series of composite schlieren-pressure distributions of Figures 75 to 80 indicate the distinct differences between the hypersonic laminar and turbulent boundary layer interactions for comparable incident shock strengths. (Mach 7.3 schlierens were selected for these comparisons because of their clarity compared to those obtained with the lower density Mach 10.5 flow.) The interaction region for the separated laminar boundary layer is seen to closely resemble the theoretical model of Section II-A. The shock reflection consists of a constant pressure boundary interaction followed by an isentropic compression back to a flow direction parallel to the wall. The isentropic compression coalesces to form the recompression shock.

As evident from the figures, the turbulent boundary layer did not separate for the range of shock strengths used in this program. The turbulent interaction region, in contrast to that of the laminar, is characterized by deep penetration of the boundary layer by the cowl shock. The downstream boundary layer is thinned by the compression to a height compatible with continuity and momentum constraints. The reflected shock emanates from a region near the wall and penetrates through the upper regions of the boundary layer into the inviscid flow field. Compared to the laminar case there is little forward propagation of the resulting pressure disturbance evident in the wall static pressure data.

From schlieren photographs such as those of Figures 78 to 80, measurements of the observable inviscid interaction length and boundary layer edge flow deflection were made for comparison with the formulated flow model discussed in Section II-B. The results as presented in Figures 13 and 81 indicate that the boundary edge flow deflection through the impinging shock wave,  $\Delta\theta$ , can be approximated by the inviscid shock deflection angle  $\theta_c$  and the inviscid interaction length then estimated from:

$$\frac{L}{\delta_1} = \left(1 - \frac{\delta_3}{\delta_1}\right) \cot \theta_c \quad (30)$$

based on the flow geometry.

Attainment of Two-Dimensional Static Pressure Ratio - The overall shock induced pressure rise ratios are summarized in Figures 82 and 83 for the Mach 7.3 and 10.5 data respectively. At Mach 10.5, the Model C data is also compared against the Model A shock tunnel data taken earlier in the program and reported in Reference 1. For comparison, corresponding theoretical pressure rise ratios were computed both inviscidly and viscously. The viscous calculations were made using the G.E./Bertram solution to obtain the effective shock strength due to the viscous and bluntness induced leading edge interaction. The effective shock strength was then used to calculate the final pressure rise. The data agrees very well with the estimates; generally falling between the limits set by the inviscid and viscous solutions, both for the separated and attached flow cases.

Laminar Theory/Data Separation Plateau Comparisons - The hypersonic laminar separation data was compared to the Erdos and Pallone formulations, which give good agreement at lower Mach numbers, for the prediction of plateau levels and interaction lengths (Reference 7). For this purpose, the series of pressure distributions shown in Figures 84 to 93 were prepared. At both Mach 7.3 and 10.5, separation plateaus are seen to form at cowl angles of 3 to 4° (Figures 84, 85 and 90). As the shock strength is increased, the length of the pressure plateau increases. Superimposed on these pressure distributions is the pressure plateau levels predicted by the theory of Erdos and Pallone using the laminar skin friction law established from cowl-off testing of this model as reported in the previous section. The excellent agreement is taken to indicate that the Erdos and Pallone semi-empirical formulation:

$$C_{pP} = 1.47 \sqrt{\frac{2C_f}{\beta}} \quad (31)$$

based on low Mach number data, accurately predicts laminar separation plateau pressure levels at hypersonic speeds.

Laminar Separation Length Theory/Data Comparisons - In Reference 7 Erdos and Pallone formulated an expression for the separation length which correlates well with low Mach number data in terms of boundary layer thickness and final pressure rise minus plateau pressure rise. In comparing this formulation with the present data, a strong Mach number dependence was found as indicated in Figure 94. To further evaluate the validity of this apparent Mach number dependence, two recent sets of data from independent sources were examined. As also indicated in Figure 94, the Reference 15 data, at a nominal Mach number of 10 and at a length Reynolds number of  $.5 \times 10^6$  (compared to  $1.5 \times 10^6$  for the present Mach 10.5 test) agree with the trend of the data obtained in this program. Reference 3 data, on the other hand, generally is in agreement with the Erdos and Pallone formulation. It was, however, taken at Mach 2.21, closely corresponding to the conditions of the original Erdos and Pallone correlation.

Failure to observe the apparent Mach number dependence evident in Figure 94 when predicting laminar separation lengths is seen to result in substantial over-estimation at hypersonic speeds. Admittedly, any shock induced boundary layer transition effects present in the data could be a factor in the reduced separation lengths, but this appears somewhat unlikely considering the consistent pattern of the present data and the agreement with the experiment of Reference 15.

Laminar Theory/Data Pressure Distribution Comparison - Results obtained with the present Laminar-Shock/Boundary Layer Interaction program discussed in Section II-A were compared with the Model C laminar interaction data at both Mach 10.5 and 7.3. Since profile measurements indicated none of the separated data remained laminar downstream of the reattachment point, only two runs with relatively weak interaction give evidence of wholly laminar flow and could be compared directly with the theory. Run 61 at Mach 7.3 was the only run with a laminar boundary layer measured downstream of the interaction (probe station 3 was approximately 17 inches downstream of the shock impingement point) and Run 50 at Mach 10.5 had a laminar-transitional interaction. Data from both of these runs are compared with the computer program calculations in Figures 95 and 96. The predicted forward propagation of the pressure and the initial slope of the pressure rise appear to be in very good agreement with the experimental data. The overall pressure rise is matched near the end of the plate, however, there is a definite overshoot of the experimental pressure data in the interaction region which is not theoretically predicted. (The maximum pressure level in this region could have been more nearly approximated theoretically by using an increased shock strength such as might be associated with a wave generated by a viscous cowl. A correction of less than .4 degrees to the shock induced turning angle would increase the final theoretical pressure rise until it matched the experimental data peak.)

Laminar Theory/Data Mass Flow Comparisons - Figures 97 and 98 reflect the theoretical mass flow variation through the interaction region for the laminar-laminar case (Run 61) and the laminar-transitional case (Run 50) as determined by the Laminar-Shock/Boundary Layer Interaction program (laminar-laminar calculation). The parameter plotted in Figures 97 and 98 is a mass flow parameter related to the actual mass flow by the following expression:

$$\dot{m} = W_{BL} \rho_1 u_1 \quad (32)$$

Where:  $\dot{m}$  = mass flow in boundary layer slug/sec

$W_{BL}$  = mass flow parameter - from Laminar-Shock/  
Boundary Layer Interaction program

$$= \frac{\rho_e u_e}{\rho_1 u_1} (\delta - \delta^*)$$



$\rho_1$  = density at boundary layer edge before interaction

$u_1$  = velocity at point (1)

$\rho_e$  = local density at boundary layer edge

$u_e$  = local velocity at boundary layer edge

$\delta$  = local boundary layer thickness

$\delta^*$  = local displacement thickness

Figures 97 and 98 indicate a slight, temporary decrease in boundary layer mass during the interaction. This could be caused by the similar solution approximation used in the formulation of the Laminar-Shock/Boundary Layer Interaction program. The decrease in mass occurs in the free interaction region and is most apparent for the incipient separation cases. This discrepancy does not appear to have a significant effect on the overall mass flow predictions, however.

The theoretical ratio of the mass flow downstream to the mass flow upstream,  $(\dot{m}_1/\dot{m}_2)$  was compared with the boundary layer mass flow ratio measured across the interaction region during the experimental program. For the laminar-laminar interaction the mass flow ratio across the interaction agrees very well with the ratio predicted theoretically. From the experimental data obtained during Run 61 the mass flow ratio across the interaction, measured at probe stations number 1 and 2 was determined to be 1.28 whereas a theoretical value of 1.294 at the same stations is predicted using the Laminar-Shock/Boundary Layer Interaction program. For the laminar-transitional interaction (Run 50), the experimentally determined mass flow ratio across the interaction was much higher, confirming that this interaction was transitional (2.95 experimentally as compared to 1.71 theoretically).

Laminar Theory/Data Displacement Thickness Comparison - A theory/data comparison of the displacement thickness at the aft probing station indicated very favorable agreement between the shock boundary layer prediction and the reduced experimental data. For the laminar-laminar case, the displacement thicknesses for the theoretical and experimental cases are .134 and .138 inches respectively. For the laminar-transitional case, the displacement thicknesses are .190 and .220 inches respectively.

Theoretical Interaction Region Laminar Skin Friction - In Figures 99 and 100 the shear parameter ( $\ell$ ) is plotted versus axial location for the Mach 10.5 and 7.3 test conditions used in the previous comparisons. The shear parameter is defined as follows:

$$\ell = \frac{\theta}{u_e} \frac{T_w}{T_e} \left( \frac{\partial u}{\partial y} \right)_w = \frac{Re_\theta C_f}{2\lambda} \quad (33)$$

Where:  $\ell$  = shear parameter

$\theta$  = momentum thickness

$u_e$  = velocity at boundary layer edge

$T_w$  = wall temperature

$T_e$  = temperature at boundary layer edge

$\left( \frac{\partial u}{\partial y} \right)_w$  = velocity gradient at wall

$Re_\theta$  = Reynolds number based on  $\theta$

$C_f$  = skin friction coefficient based on boundary layer edge conditions

$\lambda$  = viscosity parameter =  $\frac{T_e + 198.6}{T_w + 198.6} \sqrt{\frac{T_w}{T_e}}$

Separation is indicated by negative values of  $\ell$ .

As can be seen from these plots, incident shock/boundary layer separation was not predicted in either case, as indicated by the positive value of the skin friction parameter throughout the interaction region. For all of the separated flow cases, test data analysis indicates that the boundary layer had transitioned downstream and was fully developed turbulent flow by the aft probing station. Consequently, theory/data comparisons for those conditions are not applicable.

Turbulent Theory/Data Separation Comparison - With upstream turbulent boundary layer, no observable separation was noted either in the pressure distributions or in the schlieren pictures. Based upon pre-test estimates, turbulent, free interaction pressure plateau levels of the order of:

$$C_{P_P} = 6.00 \sqrt{\frac{2C_f}{\beta}} \quad (34)$$

were anticipated, based on estimates made using the method of Reference 7. Theoretical plateau pressure ratios (based upon the turbulent flow conditions:

$P_T = 1800$  psia,  $T_T = 1950^\circ\text{R}$ ,  $M = 10.5$ ) of approximately 4.3 were calculated. This compares to the maximum final pressure rise ratio of 40 measured during Run 53 when the cowl was set at a maximum angle of  $13^\circ$  and no separation plateau was observed. More detailed analysis subsequently delineated the importance of upstream shape factor on such separation predictions as reflected in the theoretical curves of Figure 19 in Section II-B. The turbulent shock/boundary layer flow model developed in Section II-B was used for post-test estimates of the onset of boundary layer separation. This procedure indicated that the boundary layer should not be expected to separate at the Model C test conditions. Limited additional theory/data comparisons were made using test data from the literature, wherein both upstream profile data and wall static pressure data (from which the nature of the flow; separated versus attached could be assessed) were reported. The results are summarized in Figure 101, suggesting the method of Section II-B is an acceptable engineering approximation for assessing imminent boundary layer separation. In that the computed results are sensitive to upstream profile shape and wall to total temperature ratio, it is important that reasonably accurate measurements of the parameters be made as indicated in the parametric results of Figure 102.

Boundary Layer Thickness Ratio Theory/Data Comparison - Results obtained for estimates of the boundary layer thickness change across the shock impingement, using the turbulent boundary layer formulation presented in Section II-B, are compared against data taken during the Model C Mach 7.3 tests. Measurements of boundary layer thickness on either side of the interaction were made from schlieren pictures such as those in Figures 78 to 80. As can be seen from Figure 103, there is good agreement between the theory and the data. The importance of properly accounting for the shock induced downstream profile distortion is also apparent from the comparison of Figure 103. The assumption of a constant profile parameter  $n$  across the immediate interaction region is seen to result in a significant over-estimation of downstream profile thinning at the higher shock strengths. The relative agreement obtained when profile distortion is accounted for (Reference 5) is considered indirect substantiation for the supposition that mass flux rates measured downstream of the immediate interaction did not occur across the interaction, but are rather the result of subsequent downstream mixing.

Turbulent Interaction Mass Flux - The boundary layer profile measurements and integral properties established from cowl-on Model C testing are summarized in Table II. Since the total test conditions varied slightly between wind tunnel runs, the mass flow was subsequently normalized to a standard set of test conditions. The normal total conditions for Mach 10.5 are a total pressure of 600 psia and a total temperature of  $1800^\circ\text{R}$  for the low Reynolds number runs, and 1800 psia and  $2000^\circ\text{R}$  respectively for the high Reynolds number runs. At Mach 7.3, the normal total conditions are 100 psia and  $1400^\circ\text{R}$  for the low Reynolds number and 600 psia and  $1500^\circ\text{R}$  for the high Reynolds number runs. The following expressions were used to determine the normalized mass flow:

$$\dot{m}_n = \dot{m} P_{Tn}/P_t \quad \text{Laminar Flow} \quad (35)$$

and

$$\dot{m}_n = \dot{m} (T_T/T_{Tn})^{.6} (P_{Tn}/P_T)^{.8} \quad \text{Turbulent Flow} \quad (36)$$

Where:  $\dot{m}_n$  = normalized mass flow  
 $\dot{m}$  = measured mass flow  
 $T_{Tn}$  = normalized total temperature  
 $T_T$  = total temperature  
 $P_{Tn}$  = normalized total pressure  
 $P_T$  = total pressure

The above two expressions are based upon the assumption that the boundary layer grows as the  $x^{.5}$  and  $x^{.8}$  for the laminar and turbulent case respectively; where  $x$  is the axial distance along the plate. The cowl-off data analysis of the preceding section bears out the laminar growth rate, whereas consideration of effective origin and variation on  $n$  reduce the accuracy of such an assumption for the turbulent data.

Profile measurements made downstream of the shock impingement point, at probe station 3, with upstream turbulent flow also indicate significant mass flux occurred compared to the normal boundary layer growth rate upstream of the shock impingement point. This is summarized in Figure 104 indicating a general increase in mass flux as shock strength is increased. Comparative calculations were made using the downstream boundary layer edge conditions to establish a new unit mass flow and a new effective origin for the downstream flow based on the boundary layer thickness immediately downstream of the shock interaction (using the technique of Section II-B) and assuming a downstream growth rate at the new effective Reynolds number similar to that for the upstream profile. Such calculations were found to consistently underestimate the mass flux as indicated by the station 3 probe measurements and are taken as an indication that the downstream profile distortion should be considered in more detailed analysis of downstream mass flux. It should be noted, however, that the Mach 7.3 data point (Run 58) does not outwardly appear to agree with the Mach 10.5 curve. This apparent discrepancy may be caused by the fact that for the Mach 10.5 case the probing station was 9" downstream of the interaction region compared to approximately 2" for Mach 7.3, suggesting that the greatest mass flux occurred downstream of the immediate interaction region. This is in direct contrast to the observation that the Mach 7.3 and Mach 10.5 laminar data do agree reasonably well even though there is the same substantial difference between the location of the probing station with respect to the interaction region, suggesting that the transition induced mass flux occurred in the immediate region of, or shortly downstream of the interaction region.

Profile Change Across the Shock Interaction - A comparison of the shock interaction profile data with the flat plate data as typified in Figure 105 indicates the nature of the profile change across the shock interaction. For the turbulent interaction at Mach 10.5, the downstream value of  $n$ , at the probe station 3, is approximately the same as that of the upstream profile. The corresponding shape factor decrease is thus primarily due to a decrease in Mach number across the interaction. This is illustrated from the data of Runs 19 and 48. The experimental ratio of the shape factors ( $F_{19}/H_{48}$ ) is 1.89. Assuming a constant profile parameter,  $n$ , using the measured variation in boundary layer Mach number, the theoretical ratio is 1.96. It should again be noted that the probing station at Mach 10.5 is approximately 9" downstream from the interaction region which explains why a disturbed profile was not measured. For the Mach 7.3 case, however, the probing station was closer to the interaction region (approximately 2" downstream). A plot of the flat plate and incident shock profiles for this condition is shown in Figure 106 and is evidence that the profile has already adjusted into a higher power law type profile instead of a more distorted profile requiring more than a single parameter, such as  $n$ , for reasonable analytical representation. Consequently, such data provides additional substantiation for the turbulent flow formulation of Section II-B and of Reference 5.

To graphically illustrate and document the results of Table II, a series of summary figures were prepared (Figures 107 to 113) which show the velocity profile both upstream and downstream of the shock interaction with respect to the pressure distribution. The mass flow, boundary layer edge Mach number, and velocity profile parameter are also indicated in these figures. (The velocity profiles presented have been plotted from computer program data reduction results based on actual profile measurements.)

Summary - From the analysis of the incident shock Model C data it can be concluded that the hypersonic laminar boundary layer separation pressure plateau levels can be accurately predicted by the method of Erdos and Pallone, whereas the measured interaction lengths exhibit a significant Mach number dependency which must be accounted for. Laminar separation was found to occur at a shock induced pressure ratio of 5 at Mach 10.5. The apparent stability of the hypersonic turbulent boundary layer, as documented by the attached flow characteristics in spite of shock pressure rise ratios of 40 at Mach 10.5 and 13 at Mach 7.3 is in accord with the formulation of Section II-B but was not anticipated on the basis of lower Mach number correlations. Limited comparisons with turbulent boundary layer separation data obtained by other investigators attest to the engineering usefulness of the formulation of Section II-B for predicting imminent separation. It can thus be concluded that analyses of the incident shock/turbulent flow data have provided the sought basis for a formulation of an appropriate flow model.

#### b. Model D

Flow Model Formulation - The purpose of this test was to examine the effect of swept vane generated shocks on the Model C ramp laminar and

turbulent boundary layers. Measurements consisted of ramp centerline and vane surface pressures, and ramp pitot profile data taken at Model C probe stations 2 and 3 behind the swept shock "X" wave intersection. Data were obtained for vane shock angles of 6 and 8°. A simplified flow model was formulated for analysis of the inviscid compression system.

For swept wedges of infinite span, that is without tip effects, a simple but accurate estimation of the chordwise pressure distribution including viscous and bluntness effects can be made based on the G.E./Bertram technique discussed in Reference 1. From simple inviscid sweep theory, it can be shown that the deviation in direction with respect to the free stream, of the resultant ramp velocity vector is expressed by:

$$\alpha = \arcsin \left( \frac{\sin \delta}{\sin \delta_e} \right) - \arctan \left( \frac{M_{2N}}{\sqrt{T_0/T_2} M_0 \sin \Omega} \right) \quad (37)$$

Calculations indicate that for most hypersonic inlet applications, this angle is small (of the order of several degrees) and thus suggest that strip theory should be adequate in the absence of significant cross flow effects. Consequently, for the case of sharp leading edges, the G.E./Bertram analysis can be utilized directly. For the more practical case of blunted leading edges, the pressure increment induced by bluntness can again be estimated using the G.E./Bertram method, but with the leading edge drag coefficient corrected for sweep effects:

$$C_{D_\Omega} = C_{D_{\Omega=0}} \cos^2 \Omega \quad (38)$$

as is also suggested by simple sweep theory. The same iterative calculation procedure developed for the unswept leading edge with combined bluntness and viscous interaction can then be applied.

For the case of a finite span swept ramp such as that represented by vertical installation on a compression ramp such as Model D, an additional boundary condition must be considered to treat the flow influenced by the finite span. For this case, inviscid analysis based on simple sweep theory can be modified to assure that the flow vector downstream of the swept vertical ramp compression surface, in the vicinity of the corner, is not only in the plane of the vane, but is also in the plane of the horizontal compression surface as well. The flow model shown in Figures 114 and 115 was hypothesized for establishing inviscid flow field properties such as required in establishing boundary layer edge conditions. This formulation represents an extension of inviscid swept wedge theory in that it also handles associated corner flow, as is found in Model D. The flow direction boundary conditions for the Model D swept wedge-corner combination can be satisfied by hypothesizing the existence of a downstream two-dimensional centered expansion fan originating along the junction line between the vane generated shock sheet and the ramp surface. With such an expansion fan the final flow vector can be positioned both in the plane of the vane and the ramp. Figure 114 depicts this "shock-expansion" flow model and lists the

equations needed to calculate this flow angle.

Vane and Main Ramp Pressure Data/Theory Correlation - The measured vane pressure distributions shown in Figure 116 support the flow model of Figures 114 and 115. Pressure levels upstream of the expansion fan are predicted by strip theory and downstream pressure levels tend toward the values associated with the shock-expansion approach. In the intermediate region, pressures reach a common level by communication via the subsonic flow in the boundary layer. Of interest is the "lag" of the upper row pressures in all instances. Since both upper and lower sets of orifice locations have been normalized with respect to their distances from the vane leading edge (see symbol key insert on Figure 116) the "lag" represents evidence of the physical existence of a downstream expansion.

Measured ramp centerline pressure distributions are shown in Figures 117, 118 and 119. Superimposed on the data are the inviscid theoretical "X" wave pressure levels. Again good agreement with the modified shock expansion theory is obtained. Strip theory (about the same pressure level as swept wedge theory) over-estimates the measured pressure level to such an extent that it becomes inadequate for handling the swept wedge-corner flow problem. Of interest is the three-dimensionality of the vane shock generated flow field which is indicated to some extent by the relative levels of the off-centerline ramp pressures. In using the shock-expansion technique a correction in the downstream displacement thickness slope of  $1^\circ$  for both  $6^\circ$  vane settings and  $1.5^\circ$  for the  $8^\circ$  vane setting was made. These values represent nominal estimates based on ramp boundary layer profile measurements made both with and without vanes.

As can be seen from the preceding figures, no vane shock induced boundary layer separation was observed in the case of the  $6^\circ$  and  $8^\circ$  vane-turbulent flow tests. For the  $6^\circ$  vane setting, the laminar boundary layer did separate as evidenced in Figure 119. As in the case of the Model C data, the Erdos and Pallone theory predicts the correct laminar plateau level. The separation region in this case is longer than that observed on Model C for a similar downstream pressure rise. The complex cross flow induced three-dimensionality of this problem necessitates the acquisition of data at other conditions before a comprehensive correlation with two-dimensional flow separation lengths, such as determined in Model C testing, can be obtained.

Main Ramp Profile Data Analysis - Profile data shown in Figures 120, 121, 122 and 123 again demonstrate the complexity of the vane shock "X" wave flow field. Since the static probe measurements were of limited value, only first order corrections for normal pressure gradients (such as when the probe passed through a vane shock) could be made in reducing the pitot probe data to Mach number profiles. The validity of the static pressure corrections is supported by the agreement between measured boundary layer edge Mach numbers and predictions based on the shock-expansion theory. Increases in boundary layer thickness and mass flow through the vane shock system are shown in Figure 124.

The profile data taken in the vane shock field indicate that the rate of mass flux into the boundary layer increases as the vane angle increases. This growth rate, in excess of the normal flat plate rate, is attributed to the reduction in downstream ramp wetted area as well as the reduced effective Reynolds number across the vane shock system. Downstream of the vane generated shock system local lower Mach number-higher pressure areas tend to counteract the boundary layer thickening associated with this increased axial mass flux. The overall boundary layer thickening observed through this swept vane compression system is contrary to the thinning generally observed in tests conducted with the two-dimensional incident shock Model C. Future formulation of techniques for analyzing the boundary layer characteristics should provide for mass addition across the shock system resulting from mixing rates associated with profile distortion as well as that due to effective origin shift and change in boundary layer edge unit Reynolds number.

Summary - In evaluating the effect of the Model D swept vane shock induced pressure rise on the Model C compression ramp boundary layer, it was found necessary to extend swept wedge flow theory to also handle the Model D type corner flow. This modification in the theory, here called the shock-expansion approach, yields results well substantiated experimentally by vane and ramp surface pressure levels.

For the  $6^\circ$  and  $8^\circ$  vane settings tested no turbulent flow separation was observed. This result is in agreement with the separation theory formulated elsewhere in this report, which shows that the generated pressure rise, lower than obtained for Model C, is not great enough to induce boundary layer separation for the relatively high profile parameter cold wall boundary layer generated on the Model C ramp.

Laminar separation was achieved with the  $6^\circ$  vane setting. Erdos and Pallone theory predicts the correct plateau pressure level. The separation region in this case is longer due to cross flow than that observed on Model C for a similar downstream pressure rise.

Profile data taken downstream of the swept vane shock "X" wave location indicate that future formulation of techniques for analyzing inlet compression systems of this type should provide for mass addition across the shock system resulting from mixing rates associated with profile distortion as well as that due to effective origin shift and change in boundary layer edge unit Reynolds number.

#### c. Model E-3

##### (1) No-Cowl Configuration

The Model E-3 cowl-off test data was analyzed in the same manner as that of Model C with the following exception. As pointed out in Section IV-C variable static pressure normal to the ramp surface was used in reducing the boundary layer profile data compared to the use of constant static pressure in the Model C data reduction. In Figures 125 to 127 the measured



static pressure variations normal to the wall at each of the three probe stations is compared with a Method of Characteristics solution obtained using the inviscid ramp coordinates. As can be seen from these figures, a significant normal pressure gradient existed at the aft probing station. The theoretical and measured gradients at all three probe stations are in reasonable agreement, suggesting the applicability of such an analytical approach in the absence of measured normal pressure gradients.

Pressure Distributions - A typical measured ramp pressure distribution for the cowl-off configuration at Mach 10.5 is compared to the pre-test estimates and also to the post-test Method of Characteristics solution in Figure 128. As can be seen from the figure, excellent agreement is obtained in the three-way comparison. A slight waviness in the model wall, consistent with manufacturing tolerances, is evident in the pressure data and also in the Method of Characteristics solution which is based on the actual model coordinates.

Boundary Layer Integral Properties - Results of Model E-3 profile data reduction are tabulated in Table III for both the Mach 10.5 and 7.3 test conditions, including data obtained with the cowl installed. The latter represent profile measurements taken only upstream of the cowl shock impingement point in that model internal geometry constraints precluded measurements of flow profiles downstream of the shock interaction. A series of comparisons of these boundary layer integral properties are shown in Figures 129 to 131. In Figure 129, experimentally determined momentum thickness versus  $Re_x$  is compared against the theories of Van Driest and Cohen and Reshotko for flat plate skin friction. As would be expected on the basis of the Model C results, there is a very favorable comparison between the theories and the laminar boundary layer data. The turbulent data, however, deviates from the theoretical curve as would be expected because of the difference between turbulent and laminar skin friction. An interesting feature of this comparison is that the laminar flat plate theories agree well with the experimental data obtained in the mild adverse pressure gradient field of Model E-3. It should be noted, however, that  $Re_x$  was calculated from the local Reynolds number and the length to the leading edge of the plate. Actually, a more appropriate value of  $Re_x$  could be obtained by using the integrated value along the plate. This would tend to reduce the local value of  $Re_x$  compared to that reflected in Figure 129, causing the data to rotate in a clockwise manner; indicating somewhat lower skin friction as a result of the adverse pressure gradient.

In Figure 130 a similar comparison is shown for  $\delta^*/x$  versus  $Re_x$ . As can be seen in this figure, both the measured and theoretical boundary layer displacement thickness growth rate decrease due to the adverse pressure gradient.

Shown in Figure 131 is the rate of change of the shape factor with  $Re_x$ . The indicated shape factor decrease is primarily caused by the boundary layer edge Mach number reduction since there is no significant observable distortion in the measured profiles due to the adverse pressure gradient. This is consistent with the rate of growth of the momentum thickness.

$\dot{m}_{BL}$  Versus  $x$  for Cowl-Off Data - The mass flow in the boundary layer is plotted in Figures 132 and 133 versus the axial station. These figures exhibit a significant increase in mass flow rate over that expected for zero pressure gradient flow as indicated by the theoretical curves superimposed on Figure 132. Figure 132 also indicates that the trip configuration used for the Model E-3 test at Mach 10.5 did not introduce a significant additional mass flux into the boundary layer as evidenced by the agreement of the tripped and untripped data.

Cowl-Off Boundary Layer Edge Mach Number Comparison - Theoretical and experimental comparisons of the boundary layer edge Mach number distribution along the ramp are shown in Figure 134 for the Mach 10.5 and 7.3 test conditions. The boundary layer edge Mach numbers measured during the E-3 test were somewhat lower than both the inviscid and viscous theoretical estimates. Each data point represents results from a different run, representing slightly different test conditions and thus, is also a source of data scatter. Additional scatter is not doubt caused by the fact that both the static pressure at the boundary layer edge and the absolute boundary layer height are difficult to establish more precisely from the data due to the normal static pressure gradient. For example, for the low pressure Mach 10.5 data, an error of .005 psi in the static pressure measurement represents an error of .5 in the boundary layer Mach number. (The repeatability of the pressure calibration and measuring system used during the test was equivalent to .005 psi.)

Transition Study - To aid in the boundary layer data reduction, the power law parameters " $n$ " (compressible) and " $N$ " (incompressible) were computed by the method of least squares. The power law parameter was again used for appraising the state of the boundary layer; laminar, transitional or turbulent.

The results of this analysis are also tabulated in Table III. As can be seen from this table, for the high Reynolds number run, the boundary layer transitioned at approximately the same station as the Model C data. This is not unusual in that at these test conditions transition occurred in a very weak pressure gradient field. For the low pressure runs, however, transition occurred earlier for the Model E-3 data compared to that for Model C. Transition for this case occurred in the stronger adverse pressure gradient field which promoted the earlier transition.

The transition Reynolds number based upon momentum thickness was calculated for several of the transitional Model E-3 runs. Since boundary layer profiles were measured at the three discrete probing stations, the beginning and end of transition is not precisely defined. The Reynolds number at these probe stations, however, was calculated and plotted on Figure 55. To indicate the degree of transition, the value of the power law profile parameter (" $n$ ") is also tabulated on this figure. Also shown in the figure are the data from the Model A and E-1 tests. From the Model C data, the transitional data is shown bracketed by the laminar and turbulent cases to indicate the limits for boundary layer transition. In general, the

Model E-3 transition data agrees with the Model E-1 data when transition occurred on the aft portion of the model in the strong adverse pressure gradient field. When transition occurred in the mild pressure gradient field near the leading edge of the model, the data more closely agreed with the Model A and C flat plate data. The Model E-3 trip data indicates that the trips used with this model were less effective in promoting earlier transition than those trips generally employed on Model C.

In general, no significant distortion of the profiles was observed for the Model E-3 data due to the continuous adverse pressure gradient. A slight distortion was indicated earlier in Figure 58 for the laminar boundary layer when compared to the Blasius incompressible profile. In Figure 136 the Model E-3 turbulent boundary layer is compared against Model C profiles at comparable conditions. As can be seen from this figure, no significant distortion can be noted. Several profiles in the shock induced separation region for the extremely low Reynolds number conditions were more distorted as would be expected, but much more difficult to interpret because of severe gradients in measured flow properties.

Boundary Layer Edge Determination From Schlieren Pictures - As a check on the interpretation of schlieren pictures of the boundary layer, composites of the boundary layer data superimposed on schlieren pictures were constructed. These composites are shown in Figures 136 and 137 respectively for typical laminar and turbulent boundary layer cases. The outer boundary of the apparent boundary layer edge in the schlieren pictures for both the laminar and turbulent cases corresponds to the real boundary layer edge based on the profile measurements. The differences between the laminar and turbulent boundary layer become very apparent when the density profile is plotted on the schlieren. The laminar profile is characterized by a sharp density gradient near the outer edge of the profile which corresponds to the light line in the schlieren picture. The outer edge of this line defines the boundary layer edge. The turbulent layer has a more gradual density gradient from the wall to the outer edge of the boundary layer thickness. The relationship of  $\delta^*$  to the outer edge of the boundary layer is also shown in the figures. It should be noted that the light areas in the schlieren could be changed by adjusting the position of the knife edge used in the schlieren system, but the same observations could be made, the only difference being the light areas would be dark and vice versa. This procedure for determining the boundary layer edge was used in establishing the boundary layer thickness ratio across the interaction region for Model C in the absence of desired profile traverse data.

## (2) Cowl-On Configuration

Comparison of Theory/Data Maximum Pressure Rise - The maximum theoretical pressure rise for Model E-3 cowl-on testing was computed (neglecting viscous effects) as a function of cowl angle for pre-test purposes. The procedure for calculating this pressure rise was to assume that the turning angle through the shock from the cowl remained constant through the compression field generated by the Model E-3 surface. The pressure rise across the shock reflection was then calculated using local flow conditions at the

impingement point on the curved ramp. Comparisons of the data and these predictions are shown in Figure 138 and 139 for the Mach 7.3 and 10.5 test conditions respectively. The data compares very well with these estimates for the low cowl angles. At the high cowl angles, however, the data is significantly lower than the predicted levels. This is caused by the expansion off the trailing edge of the cowl which keeps the pressure rise from achieving its full value. (The Model E-3 cowl was not originally designed for the high cowl angles subsequently used during this program. During testing, the cowl was set at these high angles to achieve otherwise unobtainable increased shock strengths.)

Composite Comparison of Pressure Distribution as a Function of Cowl Angle - A set of composite pressure distributions is shown for the high and low Reynolds number runs for Mach 7.3 and 10.5 in Figures 140 to 143. A set of schlieren pictures (Figures 144 to 147) is also shown for typical interaction regions for both laminar and turbulent boundary layer at  $M = 7.3$  and 10.5. As can be seen from this set of figures, no recognizable separation plateaus were observed at Mach 10.5 and 7.3 for test conditions corresponding to those at which separation was observed with Model C. Separation was, however, observed at an extra low Reynolds number test condition at Mach 7.3 ( $Re_0 = 2 \times 10^5 \text{ Ft}^{-1}$ ). This boundary layer stability trend is believed due to the fact that even at moderately low Reynolds number runs, the boundary layer transitioned on Model E-3 before the shock interaction as a result of the extreme aft position of the impingement and the fact that the upstream adverse pressure gradient promoted earlier transition. Consequently, subsequent testing was conducted at extremely low Reynolds number test conditions as stated above.

Examination of the pressure data for Runs 65 and 88 (Figure 148) indicates significant differences in spite of comparable shock strength, cowl position with only a 30% difference in Reynolds number. Correspondingly, studies of the schlieren photograph for Run 88 (Figure 149) conform the extensive separation region evident in the pressure distribution, whereas the schlieren picture for Run 65 also shown in Figure 149 exhibits what appears to be a precompression shock ahead of the interaction region. The pressure distribution, however, does not indicate a typical pressure plateau. The mechanism responsible for this apparent discrepancy between the two otherwise reasonably comparable runs is not evident from the data obtained.

Separation Data - As previously mentioned no laminar separation was experienced on Model E-3 at test conditions comparable to the Model C test conditions. However, at Mach 7.3 an extra low Reynolds number test was conducted to achieve laminar separation. Very distinct and extensive separation plateaus were observed at these conditions. The plateau pressure levels for these conditions are compared to predictions based on the method of Erdos and Pallone in Figures 150 and 151.

The spread shown in the Erdos and Pallone prediction is due to the uncertainty in the boundary layer edge Mach number which is due to a possible static pressure error of .005 psi. In general, the prediction of Erdos and Pallone is slightly lower than the measured pressure plateau pressure for

the separation data taken during the Model E-3 test.

At the highest cowl angle ( $18^{\circ}$ ), turbulent boundary layer separation was detected during Mach 7.3 as indicated in the schlieren and pressure data of Figures 152 and 153. Although the pressure data alone might be inadequate for positively confirming the existence of a separation plateau, the pre-compression generated by the separated flow region is quite evident in the schlieren photograph.

Summary - The mild adverse pressure gradient field had only a minor effect on the boundary layer properties as borne out by direct comparison with similar Model C flat plate profile data. In general, a slight distortion of the laminar profile was noted, however, there was no appreciable distortion of the turbulent boundary layer profile. There was also a slight decrease in the measured laminar skin friction compared to Model C as determined from momentum thickness data, while the displacement thickness and shape factor decrease was consistent with the Mach number distribution for the model. The boundary layer transition results are consistent with the Models A, E-1 and C data. The flow field, pressure distribution and overall shock pressure ratio were consistent with theory. No laminar boundary layer separation was observed on Model E-3 at conditions comparable to Model C. This is believed due to the fact that the boundary layer transitioned before the shock interaction as a result of the extreme aft position of the shock impingement and the fact that the upstream adverse pressure gradient promoted the earlier transition. Consequently, test Reynolds numbers were further reduced and laminar separation was then achieved. The measured plateau levels were slightly higher than predicted based on conditions existing just upstream of the interaction. Turbulent boundary layer separation was noted at the higher shock strengths.

## E. CONCLUSIONS

As a result of the final phase of this hypersonic incident shock-wave boundary layer interaction program, the following is concluded:

1. The modifications made to the Laminar-Shock/Boundary Layer Interaction program represent extended capability in obtaining solutions for both nonadiabatic wall and adiabatic wall laminar boundary layer incident shock problems. Future effort in this area should be directed at the use of non-similar profiles and methods of analytically handling downstream transition.
2. The data from the tests conducted with the 3 incident shock models generally correlated well with existing theories for boundary layer characteristics in zero and continuous adverse pressure gradients. The shock induced laminar separation pressure plateau levels were in excellent agreement with the theory of Erdos and Pallone. The laminar boundary layer separation lengths were found to increase with increasing shock strength, and exhibited an apparent Mach number dependence not predicted by the Erdos and Pallone formulation. The hypersonic turbulent boundary layer did not separate

2. (Continued) at conditions originally predicted on the basis of lower Mach number theory.
3. Analysis of the test data aided in the formulation of a flow model for shock impingements on a turbulent boundary layer. Solutions subsequently obtained across the immediate region of the interaction, based on the formulated flow model, were found to be in general agreement with the test data in terms of boundary layer thickness change and the prediction of imminent separation. The strong effect of upstream profile shape and wall to total temperature ratio on the separation characteristics predicted by the solutions obtained, delineate the importance of these two parameters with respect to future experimental programs.
4. The technique developed for estimating the change in turbulent boundary layer properties across the immediate region of a shock impingement is adequate for use in current engineering estimates associated with the design and analysis of hypersonic inlets. Subsequent effort in this area should be directed at extending the analysis to include downstream constant pressure mixing, considering the effects of initial flow profile distortion.
5. For these hypersonic inlet applications where the laminar boundary layer has not transitioned by the first shock impingement point, shock induced transition should be expected shortly downstream. For shock strengths in excess of  $4^\circ$  turning, laminar separation should be expected. Heat transfer estimates downstream of the shock impingement point should reflect appropriate turbulent boundary layer heating rates.
6. Reduced wall to total temperature ratios associated with full scale inlet operation at flight enthalpy levels represent a potential source of increased turbulent boundary layer stability compared to separation characteristics at higher wall to total temperature ratios. This should be considered in the interpretation of inlet component test data commonly obtained in ground test facilities at higher wall to total temperature ratios when full scale enthalpy levels are not simulated. Assuming attendant thermal protection requirements can be met, flight enthalpy hypersonic inlet boundary layer separation problems may be alleviated through the use of appropriately designed boundary layer trips.

## SECTION IV APPENDIX I

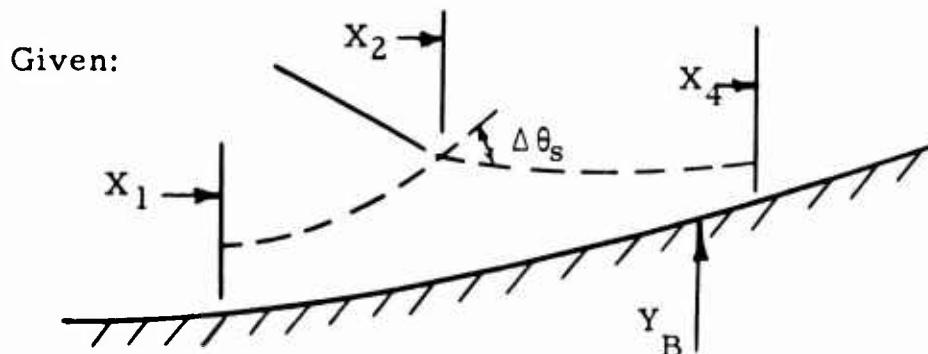
### Laminar-Shock/Boundary Layer Interaction Program Users' Manual

#### a. Program Description

The Laminar-Shock/Boundary Layer Interaction Program is intended to calculate the wall pressure distribution, the boundary layer growth, and the wall shear in a region of sudden pressure rise and possible boundary layer separation. The principal application is that of a shock wave, induced by a secondary surface, impinging on a flat plate or wedge in uniform supersonic flow. A second application is the boundary layer inviscid flow interaction in a concave corner, as formed by a double wedge. The concave corner (with an exterior angle of  $2\Delta\theta$ ) produces an effect similar to an impinging shock wave (with flow deflection  $\Delta\theta$ ). The program is limited to small surface inclinations, to a laminar boundary layer, and to a single right running (impinging) shock wave. Right characteristics (exclusive of the shock wave) must be of zero strength. The program has some limited capability for handling curved flow boundaries.

The calculation procedure is based on a single analytical model in which the separated and attached boundary layer flows are treated without distinction. In both regions the boundary layer equations are integrated simultaneously with the Prandtl-Meyer inviscid flow relations. A concise statement of the problem, the formulated equations, and a brief description of the solution procedure is presented in this User's Manual.

#### b. Outline of Shock-Boundary Layer Interaction Calculation



1. Surface coordinates,  $Y_B$
2. Shock wave incidence point,  $X_2 = X_{SK}$

3. Shock wave strength, i. e. , flow deflection through shock wave  $\Delta \theta_s$
4. Starting conditions at  $X_1$   
 $\theta_1, M_{e1}, n_1$ , and  $H_{tr1}$
5. Conditions at  $X_4$   
 $M_{e4}, n_4$ , and  $H_{tr4}$  ( $M_{e4}$  is determined by  $M_{e1}$  and the shock strength)

Major Assumptions:

1. Perfect gas with constant  $C_p$ .
2. Viscosity proportional to temperature
3. Unity Prandtl number
4. Two-dimensional flow
5. Prandtl-Meyer inviscid flow up to and downstream of the shock incidence point,  $X_2$ .
6. The incident shock wave is reflected from the boundary layer edge as from a constant pressure boundary.
7. Zero Pressure gradient across the boundary layer,

$$\frac{dP}{dY} = 0$$

Unknowns:

The unknowns are divided into three categories as follows:

1.  $X_1$
2.  $X_4$  and  $\theta_4$
3.  $\theta, M_e, n$  and  $H_{tr}$  between  $X_1$  and  $X_4$

( $X_1$  is the extent of forward feed of the shock induced pressure rise,  $X_4$ , denotes the termination point of the interaction zone)

Method for Integration of Boundary Layer Equations  
 (Solution for unknowns in category 3):



Trial values of  $X_1$ ,  $X_4$  and  $\theta_4$  are assigned. Then the boundary layer equations are integrated between the calculation starting point,  $X_1$  or  $X_4$ , and the shock incidence point,  $X_2$ . Compatibility between the boundary layer growth and the Prandtl-Meyer inviscid flow is enforced.

Isentropic flow is assumed so that the boundary layer edge conditions (namely the quantities  $a_e P$  and  $\rho_e a_e / \mu_e$ ) and the Prandtl-Meyer angle are functions of the boundary layer edge Mach number  $M_e$ . The boundary layer parameters  $\ell$ ,  $E/\theta$ ,  $G$ ,  $(\delta - \delta^*)/\theta$ , and  $\varphi$  are functions of  $H_{tr}$ . The equations are:

1. Von Karman momentum integral

$$\frac{d}{dx} \left[ (a_e P) \left( \frac{\rho_e a_e \theta^2}{\mu_e} \right) \right] = 2 \frac{a_e P}{M_e} \left[ \ell + n (H_{tr} + 2) \right] \quad (A1)$$

2. Equation defining pressure gradient parameter

$$\frac{dM_e}{dx} = - \left( \frac{n}{\frac{\rho_e a_e \theta^2}{\mu_e}} \right) \quad (A2)$$

3. Kinetic energy/momentum integral

$$n = \frac{-M_e \left( \frac{\rho_e a_e \theta^2}{\mu_e} \right) \frac{dG}{dx} + 2\varphi - G \ell}{G (H_{tr} - 1) - \frac{2E}{\theta}} \quad (A3)$$

4. Boundary layer growth-inviscid flow compatibility ( $v_{ref}$  is determined by initial conditions at  $X_1$  or  $X_4$ ).

$$\delta^* = \theta \left[ (H_{tr} + 1) \left( 1 + \frac{\gamma-1}{2} M_e^2 \right) - 1 \right] \quad (A4)$$

$$D = \frac{\delta - \delta^*}{\theta} = \frac{M_e^2 - 1}{1 + \frac{\gamma-1}{2} M_e^2} \left( \frac{n}{\frac{\rho_e u_e \theta}{\mu_e}} \right) \quad (A5)$$

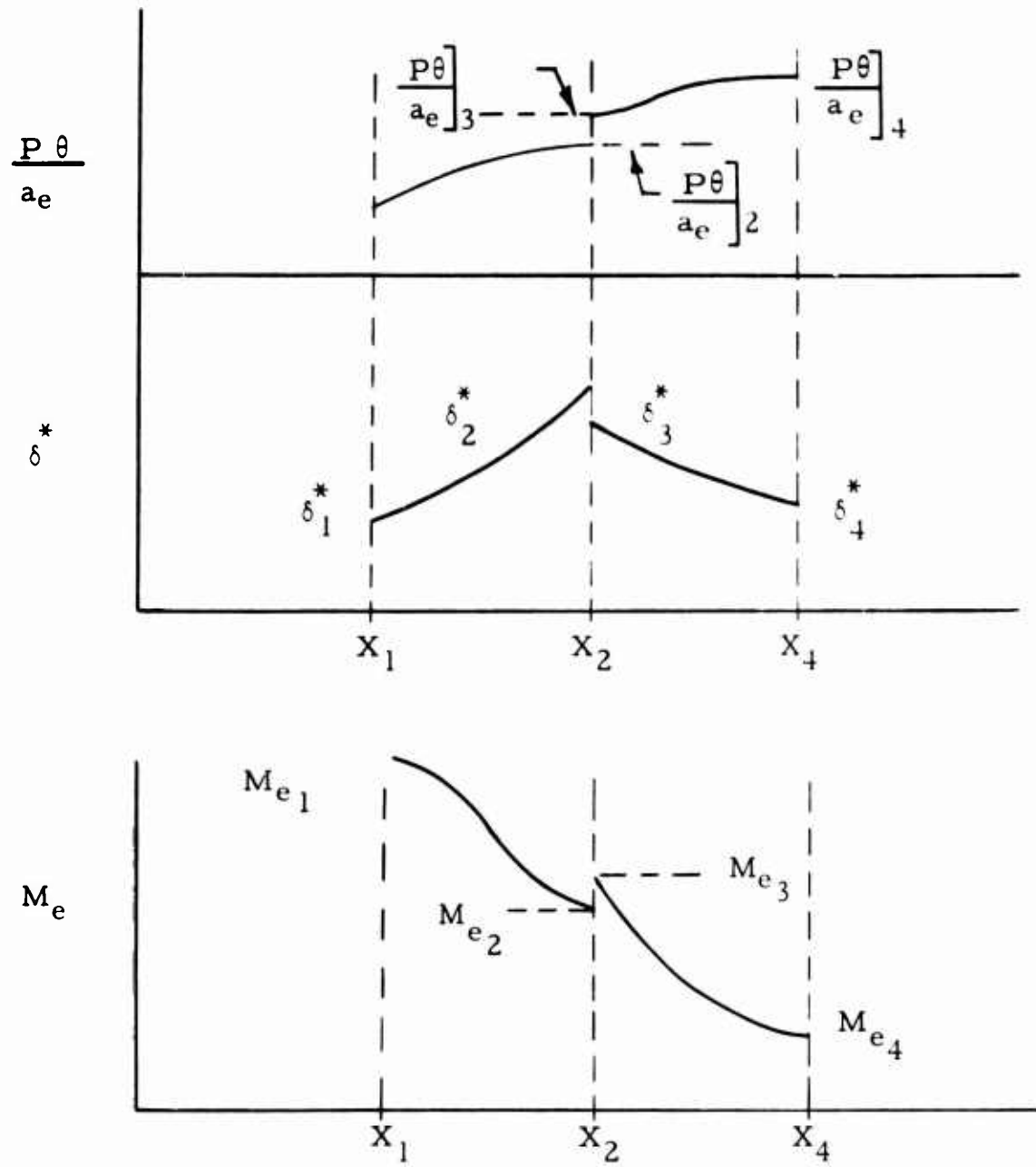
$$\Delta \left[ Y_B + \delta^* \right] - \int_{X_{i-1}}^{X_i} D dX = \int_{X_{i-1}}^{X_i} \tan ( \nu_{ref} - \nu ) dX \quad (A6)$$

The above equations are numerically integrated by employing the trapezoidal rule over a small interval defined by  $\Delta X = X_i - X_{i-1}$ . The integration proceeds as follows:

1. Assume values of  $H_{tr_i}$ ,  $n_i$  and  $M_{e_i}$  at  $X_i$ , the end of the interval.
2. Determine  $\frac{\rho_e a_e \theta^2}{\mu_e}$  by integration of Equation (A1).  
Notice that  $a_e P$  is a function of  $M_e$
3. Determine  $M_{e_i}$  by integration of Equation (A2).
4. Repeat steps 2 and 3 until agreement is obtained between the assumed and calculated  $M_{e_i}$ .
5. Calculate  $n_i$  by Equation (A3). Note that  $dG/dX$  is based on the assumed variation of  $H_{tr}$  over the interval.
6. Repeat steps 2 through 5 until agreement is obtained between the assumed and calculated  $n_i$ .
7. Evaluate both sides of equation (A6). If agreement is not obtained, assume a new value of  $H_{tr_i}$  and repeat steps 2 through 6.

Iteration Procedure for  $X_1$ ,  $X_4$  and  $\theta_4$ :

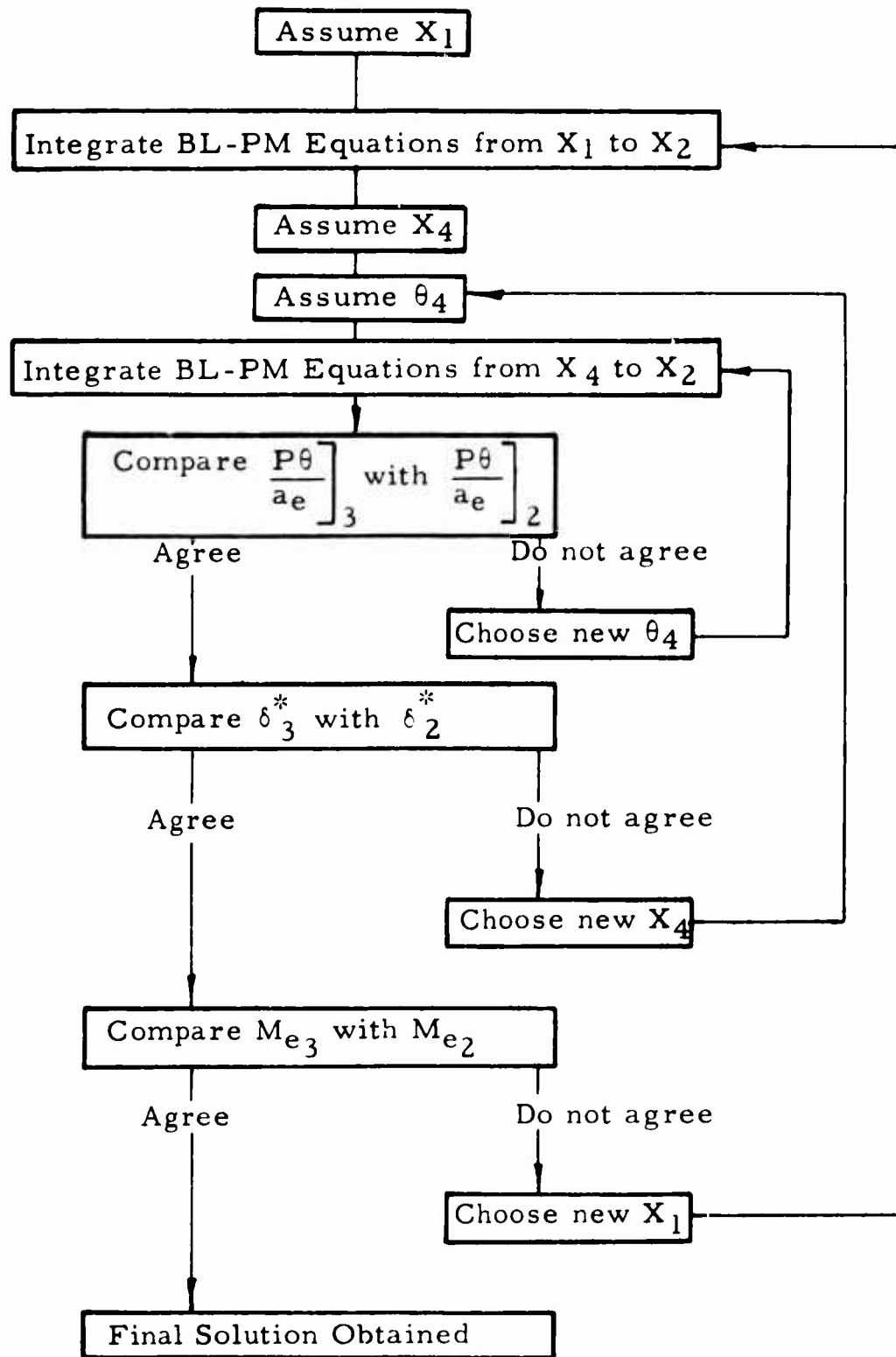
Typical results from the integration of the BL-PM equations using trial values of  $X_1$ ,  $X_4$  and  $\theta_4$  appear as follows:



The values of  $X_1$ ,  $X_4$  and  $\theta_4$  are then adjusted until the curves meet at  $X_2$ . Thus the criteria that

$$\begin{aligned} \left[ \frac{P\theta}{a_e} \right]_3 &= \left[ \frac{P\theta}{a_e} \right]_2 \\ \delta_3^* &= \delta_2^* \\ M_{e3} &= M_{e2} \end{aligned}$$

are used to confirm the solution values of  $\theta_4$ , and  $X_4$  and  $X_1$  respectively. The following block diagrams illustrate the iteration procedure.



### c. Input

A table of boundary layer properties is first read into the program under the NAMELIST name NSSBL; presently tables are available for two wall temperature ratios. Any number of sets of input for specific problems are then read under the NAMELIST name SHOCKB. The input can be prepared and keypunched from input sheets as illustrated by the example on page 61. The input quantities are defined on page 59. Additional comments regarding the input items are as follows:

The Mach number and Reynolds number are input for flow conditions parallel to the x-axis. For example, if the flow surface is a 3° wedge we would let AA=CC=0 and BB=tan 3°. For a first approximation the free stream Mach number and Reynolds number could be used for Q and RE1. However, by reference to Figures 154 and 155 Q and RE1 can be easily corrected to account for the (average) pressure recovery across the leading edge shock wave. In these Figures the Mach number and Reynolds Number ratios are plotted vs. total pressure recovery assuming the flow is re-expanded to the axial direction.

The impinging shock wave strength is input by specifying the flow deflection through the wave, DθS. DθS is zero for the concave corner problem.

The integration step size is determined by DXX. For most conditions the following relation may be used to estimate an appropriate value of DXX.

$$DXX = .25 \left[ \left( 2.59 \frac{T_{Te}}{T_W} + 1 \right) \left( 1 + \frac{\gamma-1}{2} M^2 \right) - 1 \right] \frac{X}{\left( \frac{\rho_{\infty}}{\mu} \right)^{1/4} (\theta)^{1/2}}$$

BN, B1 and B4 are pressure gradient parameters. BN is only used in the calculation of momentum thickness at the upstream boundary X1. Normally this value would be zero; it may be input to duplicate the value of BN obtained from a leading edge interaction calculation.

$$BN = \frac{X}{P} \frac{dP}{dx}$$

B1 and B4 are actual initial conditions of the parameter n (for the boundary layer integrations) at the upstream and downstream stations 1 and 4 where n is defined as:

$$n = - \frac{\rho_e a_e \theta^2}{\mu_e} \frac{dM_e}{dx}$$

The relation between BN and n is shown in Figure 156. However, in order to obtain a meaningful interaction solution, the value of B1 must be arbitrarily set to a value greater (more positive) than the precise value obtained from Figure 156 for known values of BN. Thus, B1 is usually set to zero, although BN and the corresponding n are slightly negative.

Similar rules must be followed at the downstream boundary, station 4. Here a value B4 = .01 is often used to artificially reduce the distance to the terminal point X4; the results in the immediate vicinity of the shock incidence are only very slightly affected.

A sample input sheet, prepared for the problem of Figure 3, is presented on page 61. The input sheet itself is that currently used with the computer program.

#### d. Sample Output

A sample output is shown in Figure 157 (see corresponding plot in Figure 3). Parameters relating to the boundary layer growth and external pressure distribution are printed. A list of the output symbols follows:

#### Input

AA, BB, & CC	Coefficients for quadratic surface. See input sheet.
BN, B1 & B4	Defined in Section 3.
FSN	Weighting factor; see input sheet.
X (SHOCK)	Axial position of shock wave impingement or convex corner.
H(W)/H(TOT)	Input wall to stagnation enthalpy ratio.
DEL THETA	Flow deflection through shock wave, deg.
REY	Effective unit Reynolds number corresponding to Mach number, MACH.
MACH	Mach number of flow in axial direction.

GAMMA

Ratio of specific heats

Output

DDSDX

Station 1 value of  $\frac{d \delta^*}{dx}$

X

Axial coordinate

N (HAT)

Second derivation parameter

$$\hat{n} = \frac{\theta^2}{\mu_e u_e} - \frac{H_e}{h_e} \left[ \frac{\partial \Gamma}{\partial Y} \right]_w$$

MACH

Boundary layer edge Mach number

P/P1

Pressure ratio; P1 pressure corresponding to the input MACH number.

N

Pressure gradient parameter

$$n = - \frac{\rho_e \theta^2}{\mu_e} \frac{H_e}{h_e} \frac{du_e}{dx}$$

$$= \frac{\theta^2}{\mu_e u_e} \frac{H_e}{h_e} \frac{dp}{dx}$$

HTR

Low speed form factor,  $H_{tr}$

L

Shear parameter,

PHI

Kinetic energy dissipation function,  $\Phi$

THETA

Momentum thickness,  $\theta$

DELTA\*

Displacement thickness,  $\delta^*$

INV. Y

Ordinate of boundary layer edge.

WBL

Boundary layer flow parameter

$$(\delta - \delta^*) \frac{\rho_e u_e}{(\rho_e u_e)_o}$$

Subscript "o" refers to conditions at the input MACH number.

SHOCK-BOUNDARY LAYER INTERACTION

FO988A

SHOCK-BL

NAMELIST

Plus signs may be omitted. Use exponents for long numbers.  
 Enter  $30 \times 10^6$  as 30E6. Enter  $.15 \times 10^6$  as .15E6. Do not use  
 commas within field, i.e., enter 3,800 as 3800.

required input

2

\$

\$ SHOCKB

IDENT =60H ① STRONG ① SHOCK ① CONVERGENCE

Q= 10.4 , RE1= 6.32E4 , XSK= 24 , D0S= 5 , GAMMA=

surface specificationsoption A

DXX= 1 , X= 12 , AA= 0 , BB= .05241 , CC= 0 ,

option B

X= \_\_\_\_\_ , \_\_\_\_\_ , \_\_\_\_\_ , \_\_\_\_\_ , \_\_\_\_\_ , \_\_\_\_\_ , \_\_\_\_\_ , \_\_\_\_\_ ,

\_\_\_\_\_ , \_\_\_\_\_ , \_\_\_\_\_ , \_\_\_\_\_ , \_\_\_\_\_ , \_\_\_\_\_ , \_\_\_\_\_ , \_\_\_\_\_ ,

Y= \_\_\_\_\_ , \_\_\_\_\_ , \_\_\_\_\_ , \_\_\_\_\_ , \_\_\_\_\_ , \_\_\_\_\_ , \_\_\_\_\_ , \_\_\_\_\_ ,

\_\_\_\_\_ , \_\_\_\_\_ , \_\_\_\_\_ , \_\_\_\_\_ , \_\_\_\_\_ , \_\_\_\_\_ , \_\_\_\_\_ , \_\_\_\_\_ ,

K= \_\_\_\_\_ , NK = \_\_\_\_\_ ,

optional input

X4I= \_\_\_\_\_ , 04I= \_\_\_\_\_ , D03D04= \_\_\_\_\_ ,

BN= -.2 , BI= 0 , B4= .01 ,

FNS= \_\_\_\_\_ ,

STOP= \_\_\_\_\_ ,



NOTE: Input also includes a table of boundary layer properties for the appropriate wall to stagnation temperature ratio. Tables are presently available for  $T_W/T_T = 0.2$  and  $1.0$ .

## SHOCK - BL EXPLANATION OF TERMS

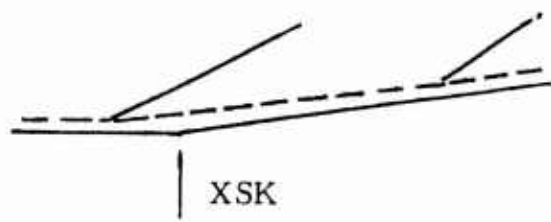
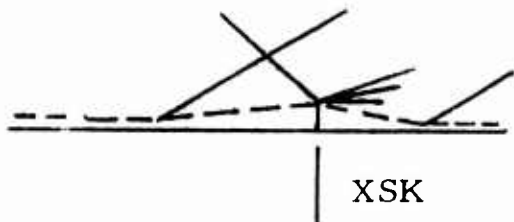
### 1. Required Input:

Q Mach number of flow achieved by isentropic expansion (or compression) to the axial direction.

RE1 Effective unit Reynolds number corresponding to Mach number Q (including non-linear viscosity correction),  $RE1 = \frac{\rho_o u_o}{C\mu_o}$

$$C = \frac{\mu_w}{\mu_o} \frac{T_o}{T_w}$$

XSK Axial position of shock wave impingement or convex corner



DθS Flow deflection through the shock wave, deg.

GAMMA Presently, the deck is limited to either  $\gamma = 1.4$  or  $\gamma = 1.667$ . If not specified,  $\gamma = 1.4$  will be assumed.

### 2. Surface Specification:

#### Option A

DXX Axial interval of the integration steps times four

X First guess of X1, the beginning of the interaction region

AA, BB, CC, Coefficients for quadratic surface

$$y_B = AA + BB \cdot X + CC \cdot X^2$$

to be omitted or set equal to zero for nominal horizontal surface.

Option B

X, Y List of surface coordinates - maximum of 100. Note that the integration interval is  $(X_n - X_{n-1}) / 4$ . Note that for an arbitrary curved boundary, the coordinates must be specified close together with great accuracy.

K First guess of X1 (beginning of interaction region) is Kth value of X.

NK Number of X-Y pairs input

3. Optional Input for Iteration

X41 First guess of axial position of station 4, the terminal point of the interaction zone.

041 First guess of momentum thickness at station 4.

4. Optional Input - Unless other wise specified, zero is used for the following parameters.

BN Power law exponent for pressure variation upstream of X1  
 $\left[ P \propto X^{BN} \right]$  used in the calculation of momentum thickness at X1. The boundary layer is assumed to start at  $X = 0$ .

B1, B4 Boundary conditions on  $n$  at stations 1 and 4.

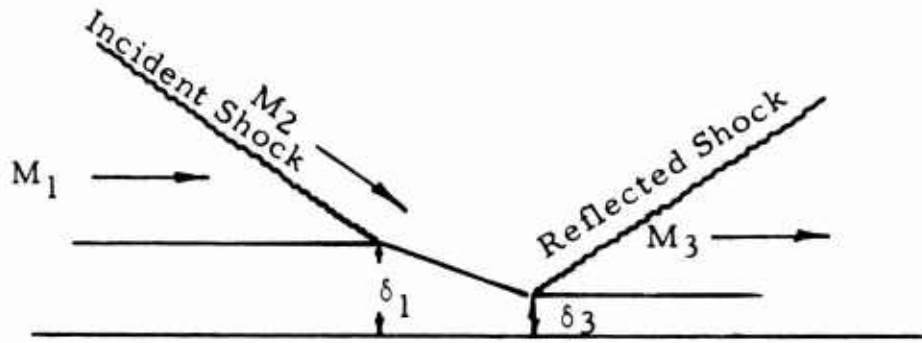
FSN Weighting factor on the use of wall momentum condition (FSN = 1) or K.E. equation (FSN = 0)

STOP Specify STOP = 2 for trial solution without iteration for X1, X4 & 04. Specify STOP = 2 for upstream free interaction calculation only.

D03D04 Rate of change of  $\theta$  at 3 compared to rate of change of  $\theta$  at 4.

## APPENDIX II

Using the computational procedure for estimating the change in turbulent boundary layer thickness across an impinging shock wave using the equations formulated in Reference 5, the boundary layer thickness change across a turbulent boundary layer-shock wave interaction:



can be estimated as follows:

1. Given  $M_1$ ,  $M_3$ ,  $\frac{T_W}{T_{Te}}$ ,  $\frac{P_3}{P_1}$  and upstream profile properties (compressible)
2. Compute upstream incompressible profile parameter:

$$N_1 = \frac{2 \left( \frac{T_W}{T_{Te}} \right) \left( 1 + \frac{\gamma-1}{2} M_e^2 \right)}{H - \frac{\gamma-1}{2} M_e^2 - \left( \frac{T_W}{T_{Te}} \right) \left( 1 + \frac{\gamma-1}{2} M_e^2 \right)}$$

$$3. \quad (H_i)_1 = \frac{N_1 + 2}{N_1}$$

$$4. \quad f(H_i)_1 = \int_{1.04}^{(H_i)_1} \frac{-2dH_i}{H_i (H_i^2 - 1) (H_i + 1) \left[ 1 - \left( 1 - \frac{T_W}{T_{Te}} \right) \frac{(H_i^2 + 4H_i - 1)}{(H_i + 1)(H_i + 3)} \right]} \quad \text{or from}$$

curves of Figure 158.

$$5. \quad f(H_i)_3 = \ln \frac{M_3}{M_1} + f(H_i)_1$$

$$6. \quad \text{Solve (4) for } (H_i)_3 \longrightarrow \text{if } (H_i)_3 > 3 \longrightarrow \text{SEPARATION}$$

$$7. \quad N_3 = \frac{2}{(H_i)_3 - 1}$$

$$8. \quad \text{At } M_1, N_1 \text{ and } M_3, N_3 \text{ compute } \left(\frac{\delta^*}{\delta}\right)_1 \text{ and } \left(\frac{\delta^*}{\delta}\right)_3$$

$$\frac{\delta^*}{\delta} = \frac{\frac{T_W}{T_{T_e}} \left(\frac{1}{N+1}\right) + \frac{\frac{\gamma-1}{2} M_e^2}{1 + \frac{\gamma-1}{2} M_e^2} \frac{N}{(N+1)(N+2)}}{\frac{T_W}{T_{T_e}} + \left(1 - \frac{T_W}{T_{T_e}}\right) \frac{N}{N+1} - \frac{\frac{\gamma-1}{2} M_e^2}{1 + \frac{\gamma-1}{2} M_e^2} \frac{N}{N+2}}$$

$$9. \quad \frac{\delta_1}{\delta_3} = \frac{1 - (\delta^*/\delta)_3}{1 - (\delta^*/\delta)_1} \frac{M_3}{M_1} \frac{P_3}{P_1} \sqrt{\frac{1 + \frac{\gamma-1}{2} M_3^2}{1 + \frac{\gamma-1}{2} M_1^2}} \quad (\text{Continuity Equation})$$

$$10. \quad \frac{\delta^*_3}{\delta^*_1} = \frac{(\delta^*/\delta)_3}{(\delta^*/\delta)_1} \frac{1}{(\delta_1/\delta_3)}$$

## APPENDIX III

### Data Reduction Techniques

#### a. Boundary Layer Data Reduction

##### Introduction

To expedite the analysis of the large amount of profile data obtained during the Model C, D and E-3 testing program, a computer program was utilized which would take as input the measured boundary layer data as tabulated in Reference 11 and Reference 12, which are the Model C, D and E-3 data reports.

The computer data reduction program can be run with any of four options on the selection of input data. The difference between these four options is as follows:

1. Option I - All the measured boundary layer data: probe location, pitot pressure, static pressure and total temperature are used in evaluating the boundary layer flow properties.
2. Option II - Use is made of an assumed constant static pressure across the boundary layer rather than measured values.
3. Option III - A Crocco temperature profile is used instead of the measured temperature distribution, however, either the measured static pressure or a constant static pressure can be used. In either case, the boundary layer edge velocity is assumed equal to freestream value in the iteration required for determining the velocity distribution within the boundary layer.
4. Option IV - This option is similar to Option III with the exception that the boundary layer edge velocity as determined from a previous pass using Option III is used in the total temperature calculations instead of the free-stream velocity.

The equations, assumptions and procedures used in calculating the boundary layer properties with these different options are described in the next subsection.

For nearly all of the wedge Model C-D data reduction, Option IV was used with constant static pressure assumed across the boundary layer. For the curved surface Model E-3 data reduction, Option IV was used with variable static pressure across the boundary layer.

#### b. Data Reduction Procedure

Boundary layer surveys were made using the NASA boundary layer probe of Figure 31. The probe and its drive unit are described in Section III-A which also identifies the location of the probing stations on each of the three test models. Pitot pressure, static pressure, and total temperature measurements were made across the boundary layer.

The flow properties in the boundary layer were then calculated on the IBM 7094 computer using the selected Option and the probe measurements as described in the following paragraphs.

The Mach number at a point in the boundary layer was computed from the pitot and static pressure using the Rayleigh pitot formula for perfect gas. Initially this equation was corrected for caloric imperfections using the correction factor given in Chart 17 (supersonic) and Chart 12 (subsonic) of NACA Report 1135. Since this corresponded to a one percent or less correction to the Mach number at the Ames testing conditions; this correction was subsequently neglected.

From the Mach number and the total temperature, the static temperature was determined using the following perfect gas relation.

$$T = T_T / (1 + \frac{\gamma-1}{2} M^2)$$

Where:

T = static temperature

T<sub>T</sub> = total temperature

M = Mach number

γ = ratio specific heats = 1.4

This equation was corrected by the correction factor given in Chart 10 of NACA Report 1135. The procedure for using the NACA 1135 correction factors in the computer program was to carpet-plot the charts from NACA 1135 and then construct two-dimensional tables of the correction factors versus Mach number and total temperature. A two-dimensional table-lookup method, which initially used parabolic interpolation, was used to determine the correction factor given the Mach number and total temperature. The parabolic interpolation routine was later replaced with a linear interpolation routine to save on computer time.

From the static temperature and Mach number, the velocity was computed using the definitions of Mach number and speed of sound as indicated by the following relation:

$$u = \sqrt{\gamma R T} M$$

Where:

- u = velocity, ft/sec
- R = universal gas constant
- T = static temperature, °R
- M = Mach number
- $\gamma$  = ratio of specific heats at T

At this static temperature the ratio of specific heats ( $\gamma$ ) was calculated from a curve fit of temperature versus  $\gamma$  as determined from Keenan and Kaye Gas Tables.

The density was then calculated from the equation of state using the static pressure and temperature. The unit mass flow could then be determined from the product of density and velocity.

Using these fluid properties, the boundary layer integral properties were then calculated by numerical integration across the boundary layer using the trapezoidal rule. The displacement, momentum and energy thicknesses were thus computed using numerical integration and the following relations:

$$\delta^* = \int_0^\delta \left(1 - \frac{\rho u}{\rho_e u_e}\right) dy$$

$$\theta = \int_0^{\delta} \frac{\rho u}{\rho_e u_e} \left(1 - \frac{u}{u_e}\right) dy$$

$$\delta^{***} = \int_0^{\delta} \frac{\rho u}{\rho_e u_e} \left(1 - \frac{u^2}{u_e^2}\right) dy$$

Where:

- $\delta^*$  = displacement thickness
- $\theta$  = momentum thickness
- $\delta^{***}$  = energy thickness
- $\rho$  = local density
- $\rho_e$  = boundary layer edge density
- $u$  = local velocity
- $u_e$  = boundary layer edge velocity

The boundary layer mass flow and transformed y coordinate across the boundary layer are also computed. The transformed y coordinate ( $\eta$ ) is evaluated using the Stewartson's transformation:

$$\eta = \int_0^{\delta} \frac{\rho}{\rho_e} dy$$

$\eta$  is subsequently used to determine the incompressible form factor for the boundary layer.

For the turbulent boundary layer the incompressible form factor was determined by plotting the velocity versus  $\eta$  and measuring the value of the slope. This slope corresponds to  $N$  (the power-law profile parameter) which is related to the incompressible shape factor by the following relation:

$$H_i = 1 + \frac{2}{N}$$

Where:

- $H_i$  = incompressible shape factor
- $N$  = incompressible power law profile parameter  
in the expression  $\frac{U}{U_e} = \left(\frac{\eta}{\Delta}\right)^{\frac{1}{N}}$



For the laminar cases, the  $\eta$  transformation allows the data to be compared directly to the various theoretical results. (For example, see Figure 159 for a typical comparison of the experimental data to the theory of Cohen and Reshotko).

All of the computed flow properties are tabulated at each input point along with the integral properties, mass flow and  $\eta$ . Also tabulated are the integrands of the various integral properties; the freestream and boundary layer edge flow conditions. Several options are also available for printing out the data. One option prints the boundary layer flow properties, another the flow properties and all the integral properties, while a third prints the flow properties, selected integral properties, mass flow and  $\eta$ . A typical print out is presented in Figure 160.

The normal calculational procedure was to make a pass through the data using Option III (See Section IV-B) to determine the boundary layer edge conditions. Re-inputting this data into the computer program Option IV was then used to calculate the final boundary layer properties. The reason for using a two-pass procedure was that a check could be made on the boundary layer edge conditions before the final integration was conducted.

#### c. Model C Data Reduction

For the Model C and D boundary layer data reduction, the static pressure distribution was assumed to be constant across the boundary layer and equal to the wall static pressure at the probing station. The validity of this assumption is verified by essentially constant static pressure distributions measured across the boundary layer during the Model C and D testing program, such as the typical example of Figure 161.

The total temperature measurements for Model C appeared to never reach equilibrium because of a time lag problem and, therefore, a Crocco's total temperature distribution was used in the data reduction instead of the measured values.

#### d. Model E-3 Data Reduction

A re-examination of the boundary layer properties was conducted to determine if the following assumptions were valid for Model E-3. The assumptions are:

1. Constant static pressure across the boundary layer.
2. A Crocco total temperature distribution.

For the Model E-3 data, the static pressure did vary across the boundary layer such that the constant static pressure assumption could not be used. A typical variation of static pressure across the boundary layer at the three probing stations is shown in Figures 162 through 164. As indicated in the figures, the static pressure variation becomes more severe at the aft probing position as would be expected since these stations are in a more severe axial adverse pressure gradient field.

For the low pressure runs (Figure 165), the static pressure probe seemed to consistently give high readings when compared to the wall pressure measurements. This was possibly caused by increased boundary layer growth on the probe at the low Reynolds number test conditions. As a consequence, the static pressure distribution was determined by matching the pressure at the wall and using the pressure variation measured by the static pressure probe.

Since it is necessary to iterate between the velocity distribution and the assumed temperature distribution, a distribution where the temperature and velocity are coupled is a desirable and necessary condition. Not enough information is ordinarily obtained during a boundary layer survey to solve the momentum and energy equations at the probing station.

The Crocco distribution is expressed as

$$H = H_W - (H_e - H_W) u/u_e$$

Where:

- H = local total enthalpy-BTU/# mass
- H<sub>W</sub> = wall enthalpy-BTU/# mass
- H<sub>e</sub> = boundary layer edge total enthalpy-BTU/#mass
- u = local velocity-ft/sec
- u<sub>e</sub> = boundary layer edge velocity-ft/sec

The modified form of the Crocco distribution is given as:

$$H = H_W + (H_e - H_W) \frac{u}{u_e} + (R-1) (u - u_e - u_e^2) / 2gJ$$

Where:

R = recovery factor

R  $\approx \sqrt{Pr}$  laminar,  $\sqrt[3]{Pr}$  turbulent

g = gravitational constant -32.174 ft/sec<sup>2</sup>

J = Joule's Constant -778 ft-#/BTU

When  $Pr < 1$ , the modified Crocco distribution approximates the enthalpy distribution near the wall better than the Crocco distribution. The modified Crocco distribution, however, does not satisfy all conditions at the boundary layer edge; namely, a thicker thermal boundary layer and temperature overheat phenomena occur.

As can be seen, the modified form reduces to the standard form when  $R = 1$ . A comparison of the two theoretical distributions are shown compared with experimental data from a typical high and low pressure run in Figures 166 and 167 (Run numbers 10 and 13 respectively from the E-3 data). Also for Runs 10 and 13 a comparison was made to determine the effect, on the integral properties, of using these two temperature distributions. There was less than a one percent effect on displacement thickness and approximately a five to ten percent effect on momentum thickness,  $\theta$ . The overall effect was the Crocco distribution predicted a slightly fuller profile.

In general, the modified Crocco distribution agreed better with experimental temperature data near the wall while the Crocco distribution gave better agreement near the boundary layer edge.

It was evident that the temperature time-lag problem still existed during the E-3 test and can be illustrated in Figure 168 during the up and down traverse of the total temperature probe. In general, the total temperature probe also measured a total temperature at the boundary layer edge approximately 200-300 °R lower than the tunnel total temperature (See Figure 168). Because of this apparent time-lag problem coupled with the low readings, the experimental temperature data was not used in the E-3 data reduction, but rather the theoretical distributions were used.

During the Model C data reduction the Prandtl number was assumed equal to one and the Crocco distribution was used exclusively. For Model E-3 the data reduction program was modified so that either temperature distribution could be used by simply specifying an appropriate temperature recovery factor. However, to be consistent with the Model C data reduction, a recovery factor of one was used for most of the E-3 data.

#### e. Pressure Distribution Analysis

The data reduction for the Model C, D, and E-3 surface static pressure was done at Ames by NASA. A considerable amount of data was processed by the NASA personnel, nearly one-half million lines. In order to reduce this data to a less voluminous and more convenient form, a condensed data report was prepared for the Model C and D data and another for the Model E-3 (See References 11 and 12). The data tabulated in these reports consists of the raw data which has not been corrected for any reference pressure error, instrumentation time-lag, etc.

A thorough examination of the data indicated that a reference pressure error existed in the data. It appears that this error was caused by the calibration procedure for the pressure transducers. This procedure was to pump the test cabin pressure down to .2 psia before the test. The pressure transducers were then zeroed at this pressure level. An error of only 2 1/2% (.005 psia) in the reference pressure, which is the repeatability of the reference pressure measuring system, would cause approximately a 20% error in the surface pressure measurements at the low Reynolds number, Mach 10.5 testing conditions.

A comparison of the surface pressure data and boundary layer data against the theoretical expected values indicated that the problem was of a zero shift nature. In the absence of any better way for predicting this reference pressure error, the pressure distributions were shifted to match the G.E./Bertram prediction which from past experience, at the same testing conditions (for example earlier results obtained under this program), gives an excellent surface pressure prediction. Therefore, the procedure used in the data reduction for the Model C, D and E-3 test results was to adjust the static pressure readings by an amount equal to the difference between the leading edge pressure measurements and the G.E./Bertram pressure predictions.

## SECTION V

### REFERENCES

1. Kutschenreuter, P.H., Jr. et al, "Investigation of Hypersonic Inlet Shock-Wave Boundary Layer Interaction", General Electric Company, Technical Report AFFDL-TR-65-36, March 1965.
2. Lees, L. and Reeves, B.L., "Supersonic Separated and Re-Attaching Laminar Flows: I. General Theory and Application to Adiabatic Boundary Layer-Shock Wave Interactions", AIAA Preprint 64-4, January 1964.
3. Ginoux, J.J., "Laminar Separation in Supersonic Flow", VonKarman Institute for Fluid Dynamics, Final Report, Contract AF EOAR 64-7, October 1964.
4. Hakkinen, R.J., Greber, I., Trilling, L. and Arban, S.S., "The Interaction of an Oblique Wave with a Laminar Boundary Layer", NASA Memo 2-18-59W, March 1959.
5. Kutschenreuter, P.H., Jr., "A Moment of Momentum Integral Solution for Turbulent Boundary Layer Thickness Change Across a Shock Impingement Region", General Electric Report TIS R66FPD93, March 1966.
6. Sterrett, J.R., and Emery, J.C., "Extension of the Boundary-Layer Separation Criteria to a Mach Number of 6.5 by Utilizing Flat Plates with Forward Facing Steps, NASA TN D-618, December 1960.
7. Erdos, J. and Pallone, A., "Shock Boundary Layer Interaction and Flow Separation", From: Proceedings of the 1962 Heat Transfer and Fluid Mechanics Institute, Pages 239-254, Printed by Stanford University Press, Stanford, California, 1962.

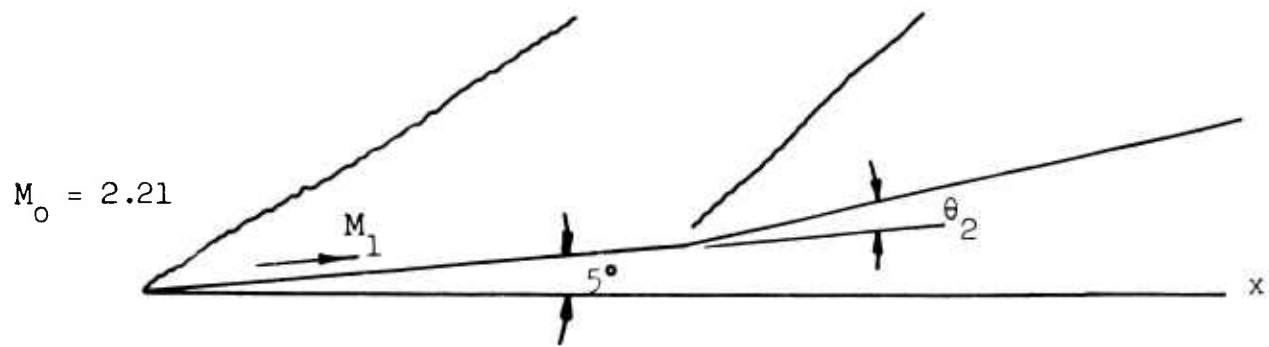
8. Spence, D. A., "Distributions of Velocity, Enthalpy and Shear Stress in the Compressible Turbulent Boundary Layer on a Flat Plate", Royal Aircraft Establishment, Ministry of Aviation, London, AERO 2631, November 1959.
9. Persh, J., "A Theoretical Investigation of Turbulent Boundary Layer Flow with Heat Transfer at Supersonic and Hypersonic Speeds", U.S. Naval Ordnance Laboratory, White Oak, Maryland, NAVORD Report 3854, Aeroballistic Research Report 258, May 1955.
10. Pinckney, S. Z., "Semiempirical Method for Predicting Effects of Incident-Reflecting Shocks on the Turbulent Boundary Layer", Langley Research Center, Hampton, Virginia, NASA TN D-3029, October 1965.
11. Nettleton, P. H., "Test Data Report - Models C and D Incident Shock Wave Boundary Layer Interaction Investigation. AF33(657)-11747, February-March 1965.
12. Nettleton, P. H., "Test Data Report - Model E-3 Incident Shock Wave Boundary Layer Interaction Investigation. AF33(657)-11747", June-July 1965.
13. Van Driest, E. R., "Investigation of Laminar Boundary Layer in Compressible Fluids Using the Crocco Method", North American Aviation, Inc., NACA TN 2597, January 1952.
14. Cohen, C. B. and Reshotko, E., "The Compressible Laminar Boundary Layer with Heat Transfer and Arbitrary Pressure Gradient", Lewis Flight Propulsion Laboratory, Cleveland, Ohio, NACA Report 1294, 1956.

15. Putnam, L.E., "Investigation of Effects of Ramp Span and Deflection Angle on Laminar Boundary-Layer Separation at Mach 10.03", NASA TN D-2838, May 1965.
16. Kutschenreuter, P.H., Jr., Zurschmeide, R.L. and Surber, L.E., "An Investigation of Shock Wave-Boundary Layer Interaction with Suction", Air Force Flight Dynamics Laboratory Report ASRMDF TM 61-30, January 1962.
17. Kuehn, D.M., "Turbulent Boundary Layer Separation Induced by Flares on Cylinders at Zero Angle of Attack", NASA TR R-117, May 1961.
18. The Boeing Company, "Monthly Technical Report No. 21", Contract AF33(615)-1202, Study of Heating in Regions of Interfering Flow Fields, September 1965.

**SECTION VI**  
**ILLUSTRATIONS**  
**TABLES**



**BLANK PAGE**



Double Wedge Model

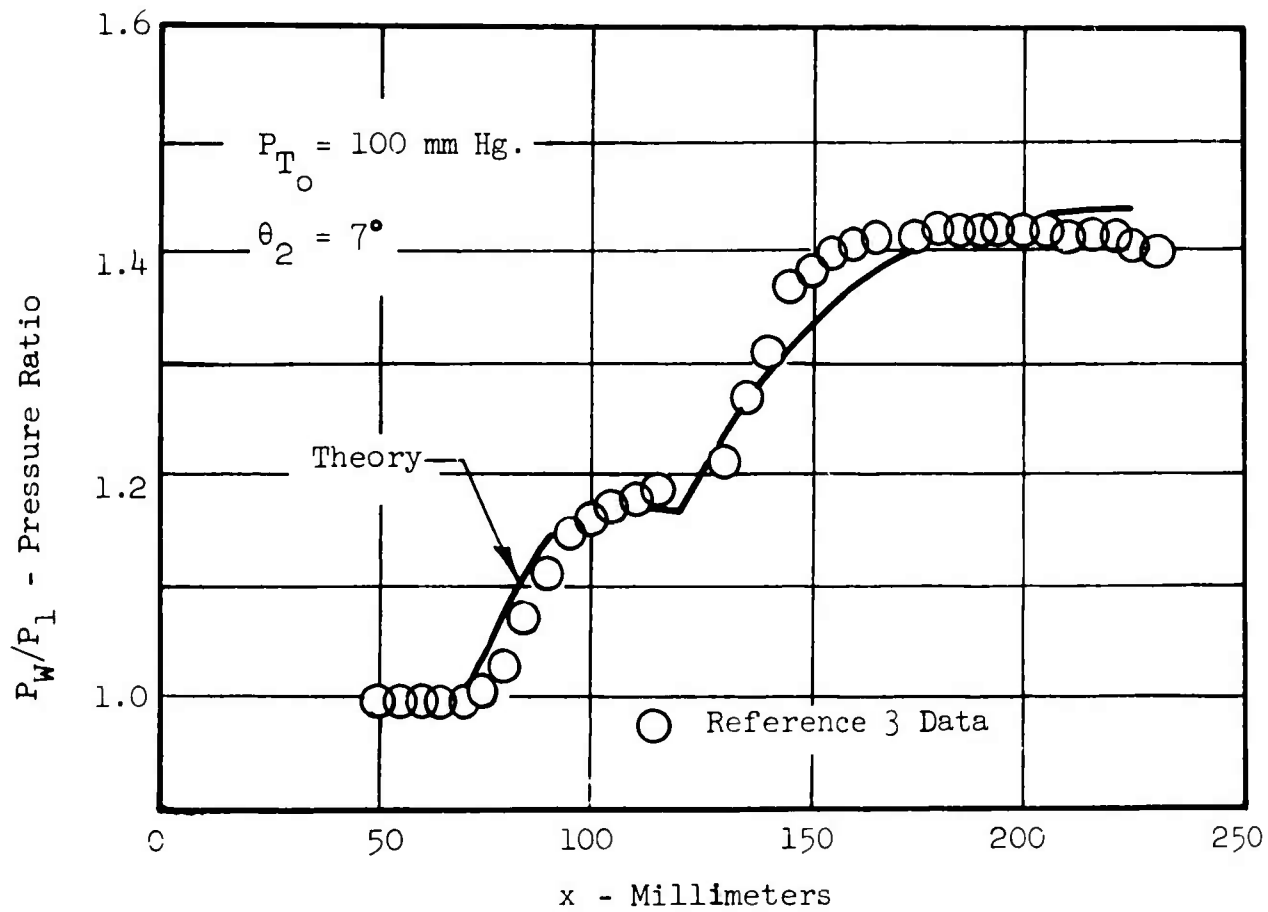


Figure 1 SUPERSONIC LAMINAR BOUNDARY LAYER  
THEORY/DATA COMPARISON

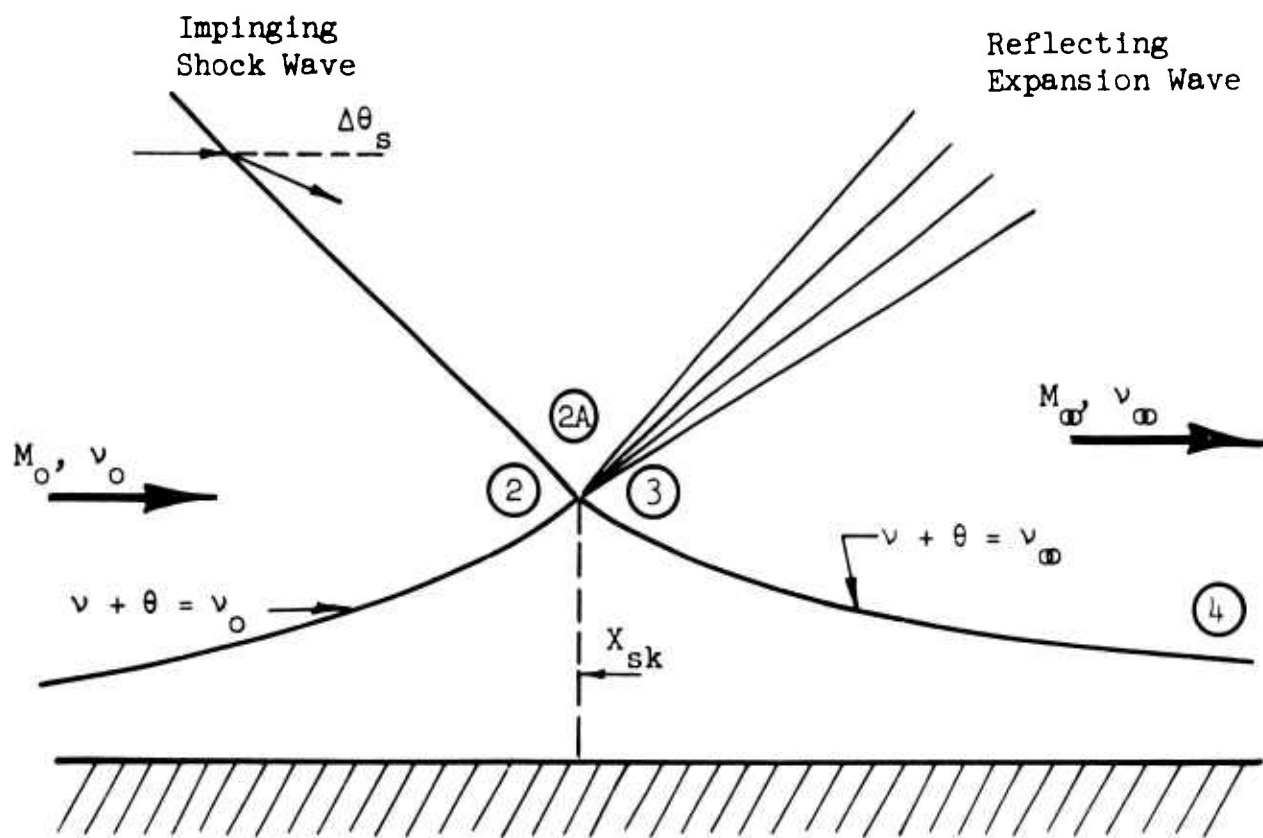


Figure 2 LAMINAR-SHOCK/BOUNDARY LAYER  
INTERACTION FLOW MODEL

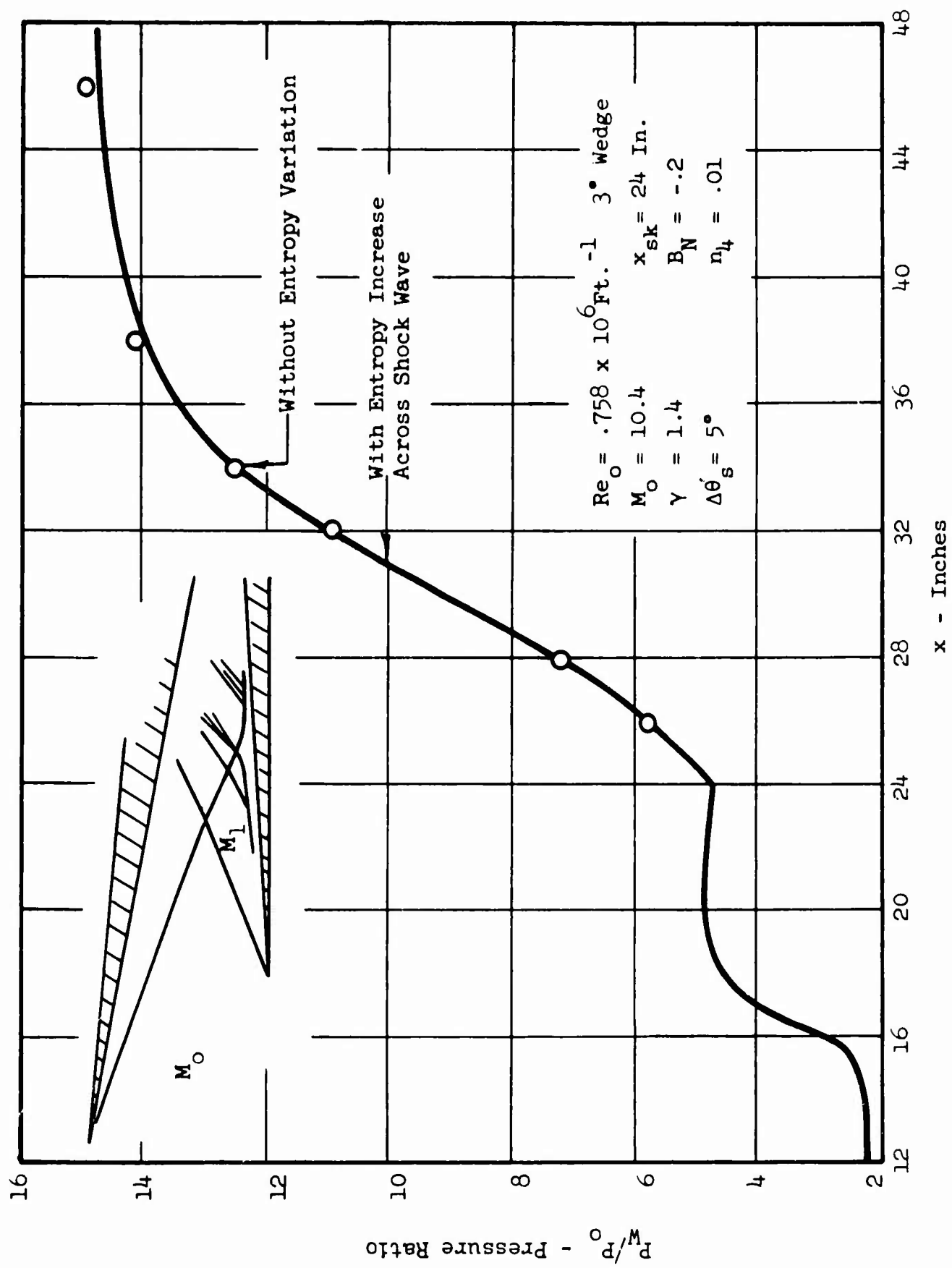


Figure 3 ENTROPY EFFECT ON WALL PRESSURE RATIO

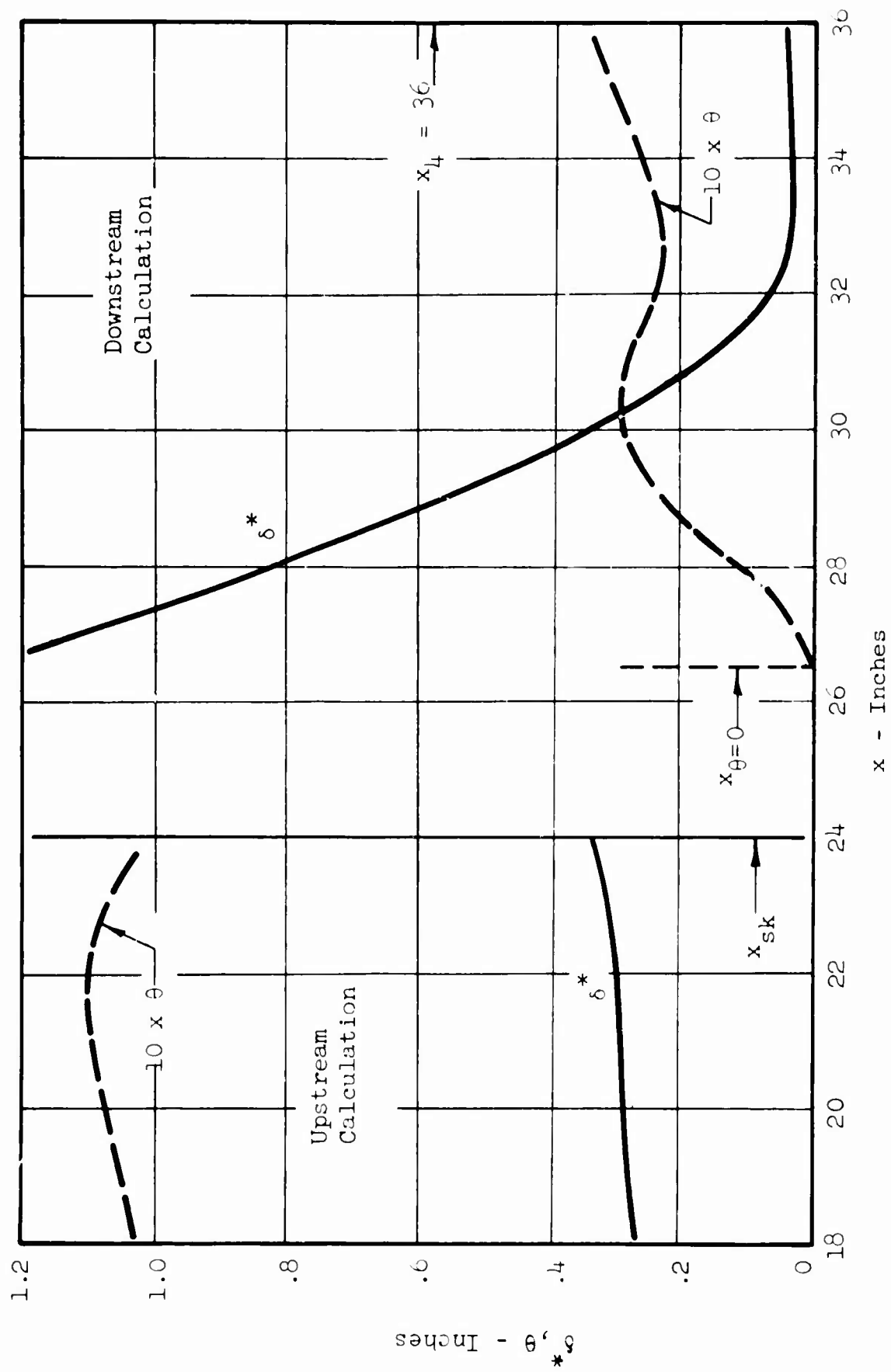


Figure 4 EXAMPLE OF LAMINAR SOLUTION ITERATION

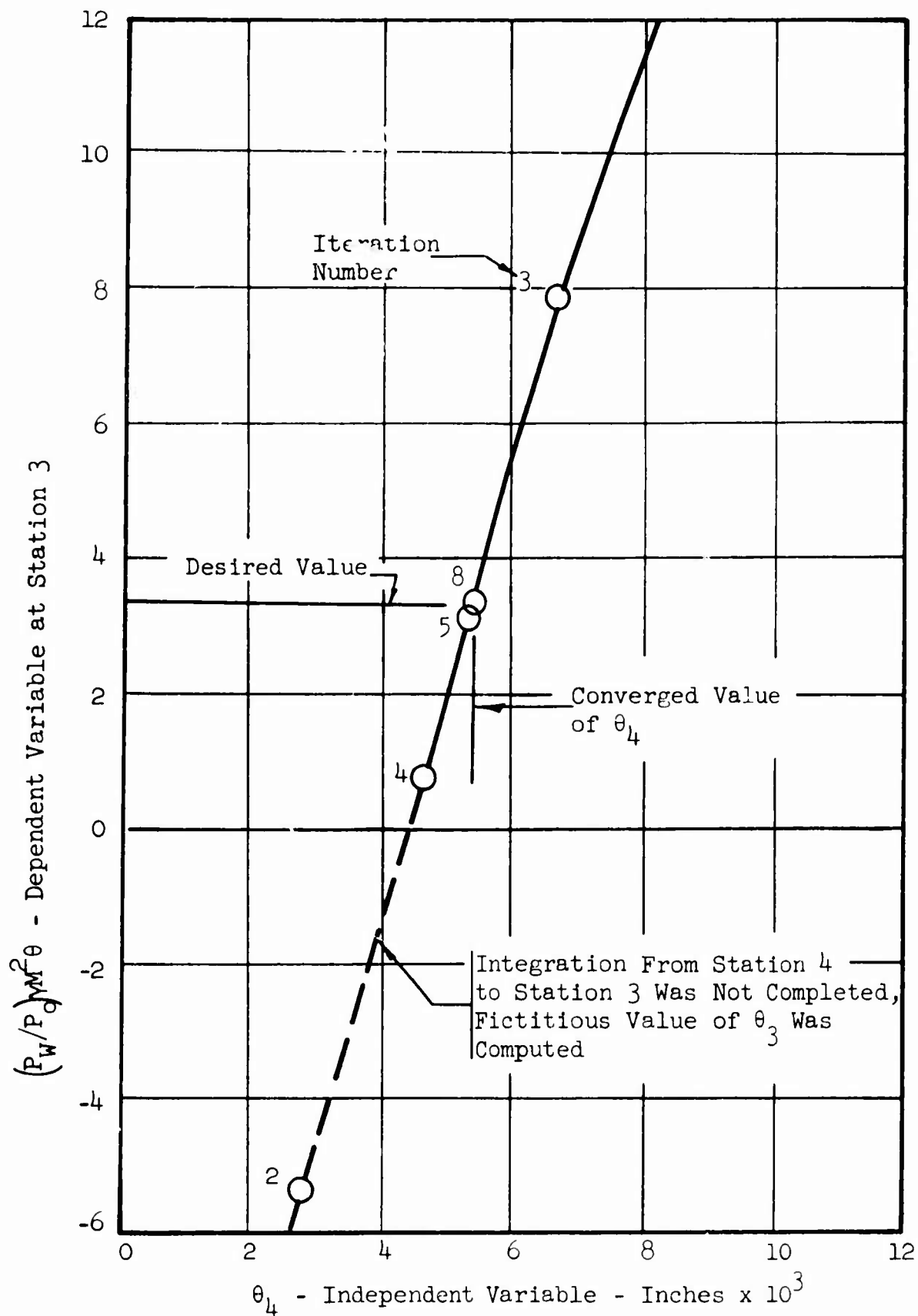


Figure 5 EXAMPLE OF LAMINAR SOLUTION CONVERGENCE

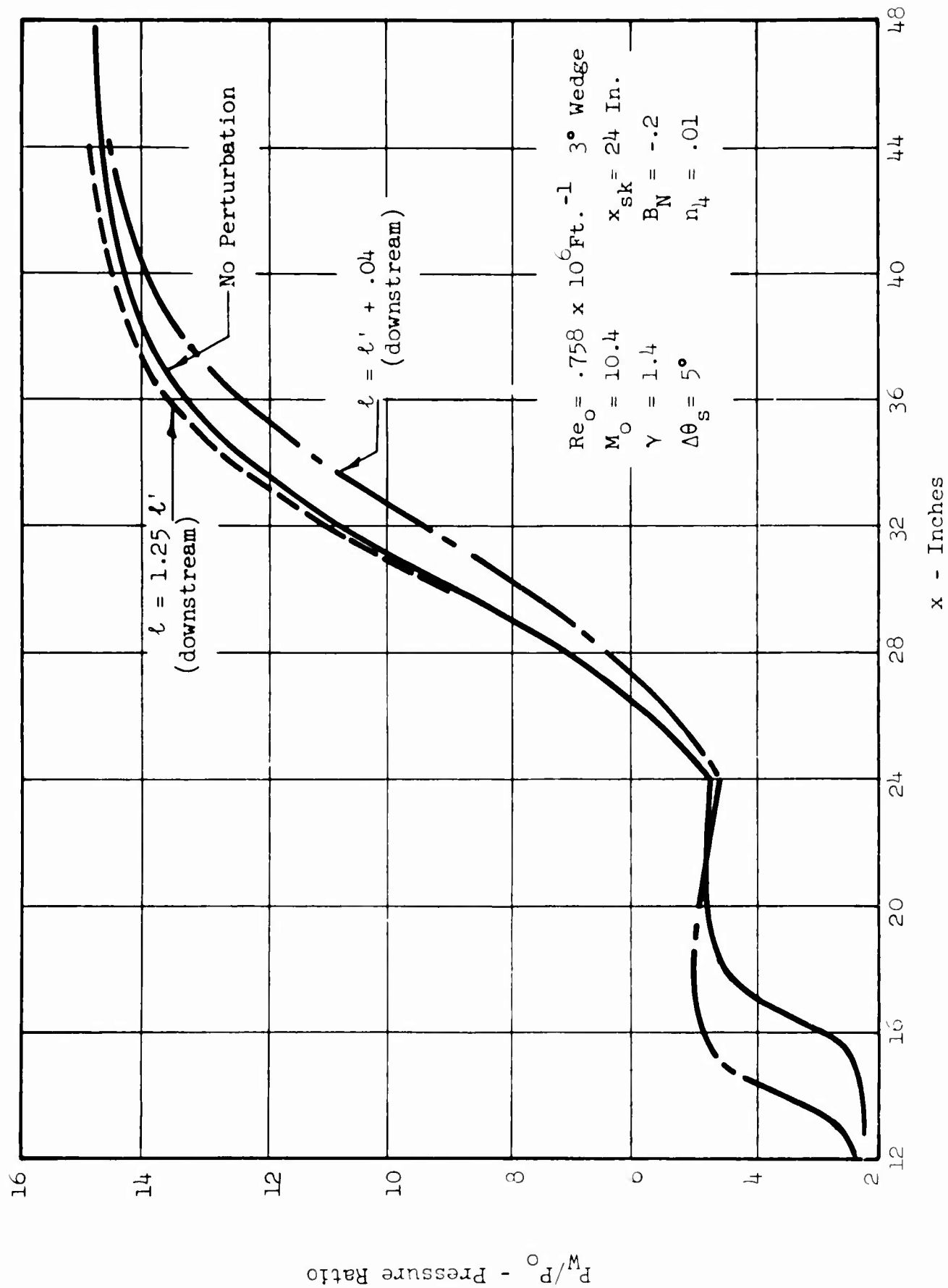


Figure 6 SHEAR PERTURBATION EFFECT ON PRESSURE DISTRIBUTION

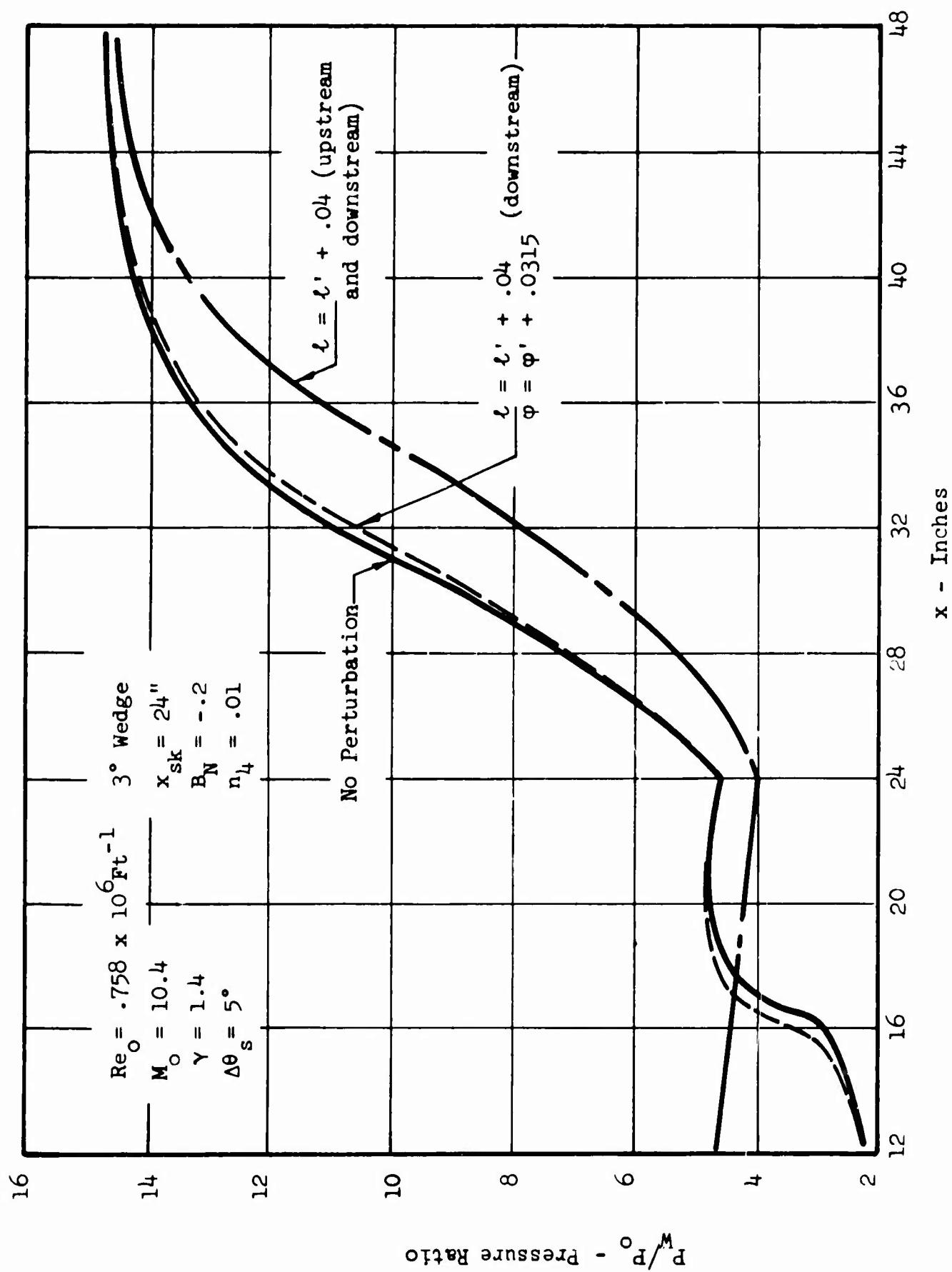


Figure 7 PERTURBATION EFFECT ON PRESSURE DISTRIBUTION



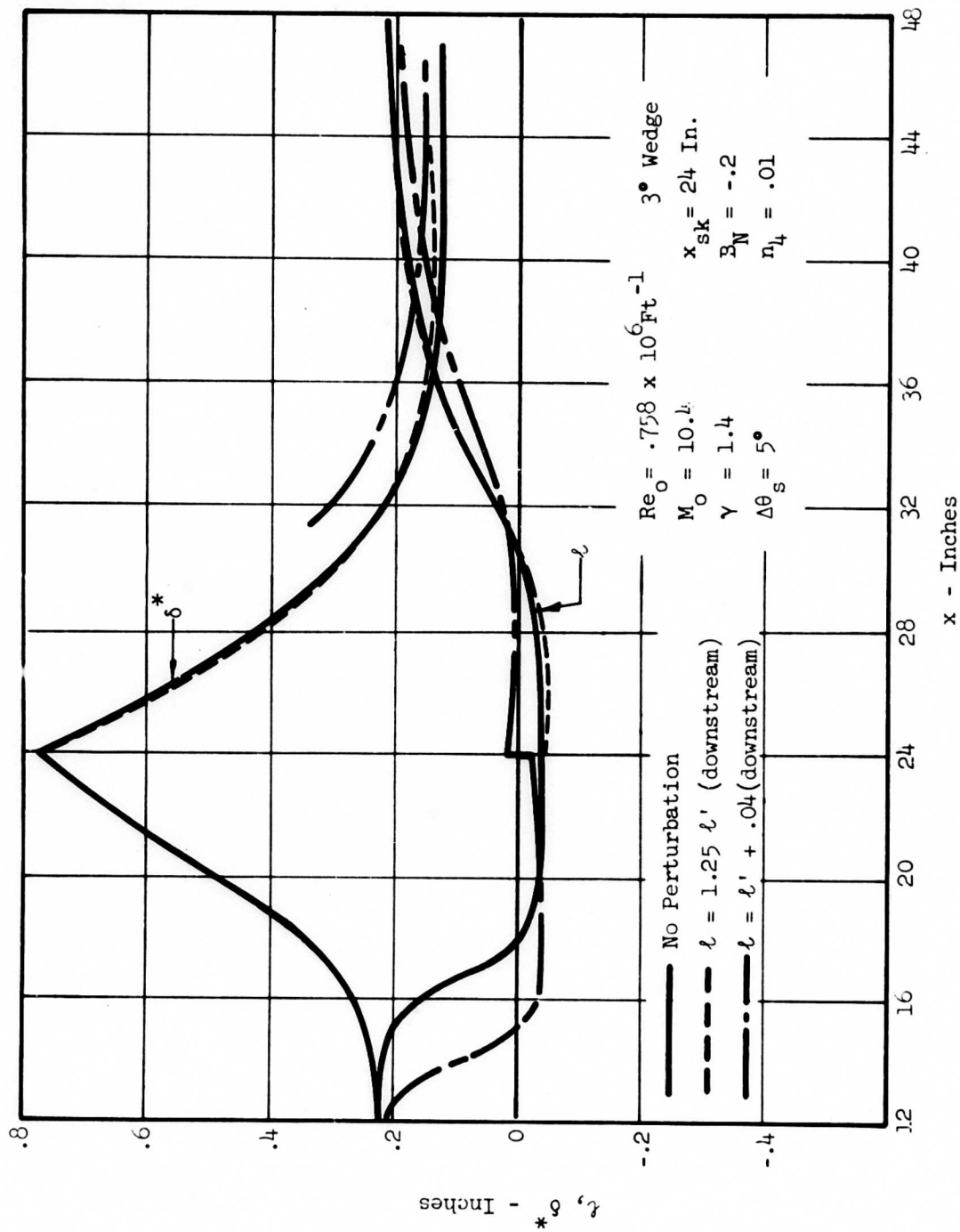


Figure 8 PERTURBATION EFFECT ON INTEGRAL PROPERTIES

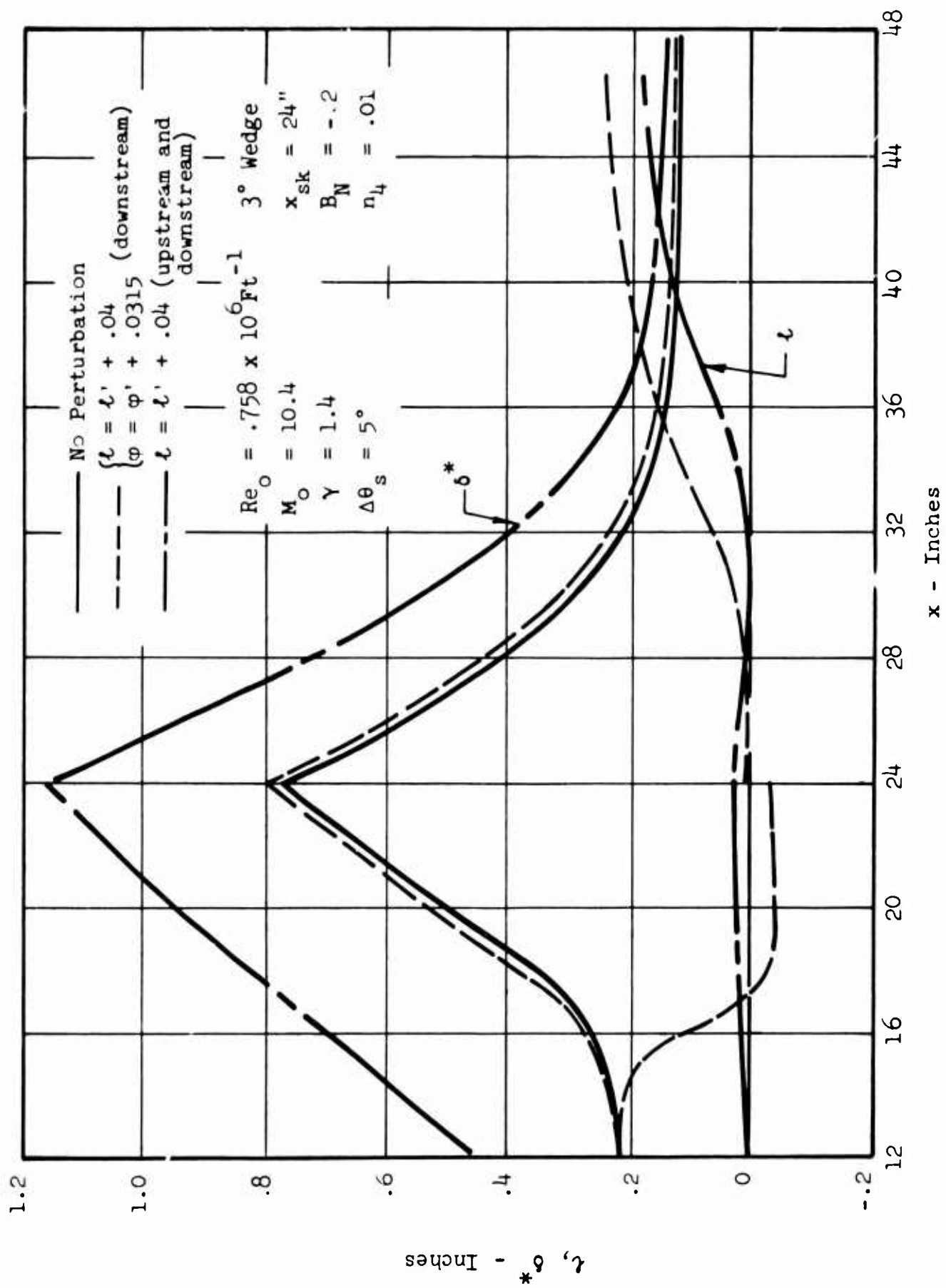


Figure 9 PERTURBATION EFFECT ON INTEGRAL PROPERTIES

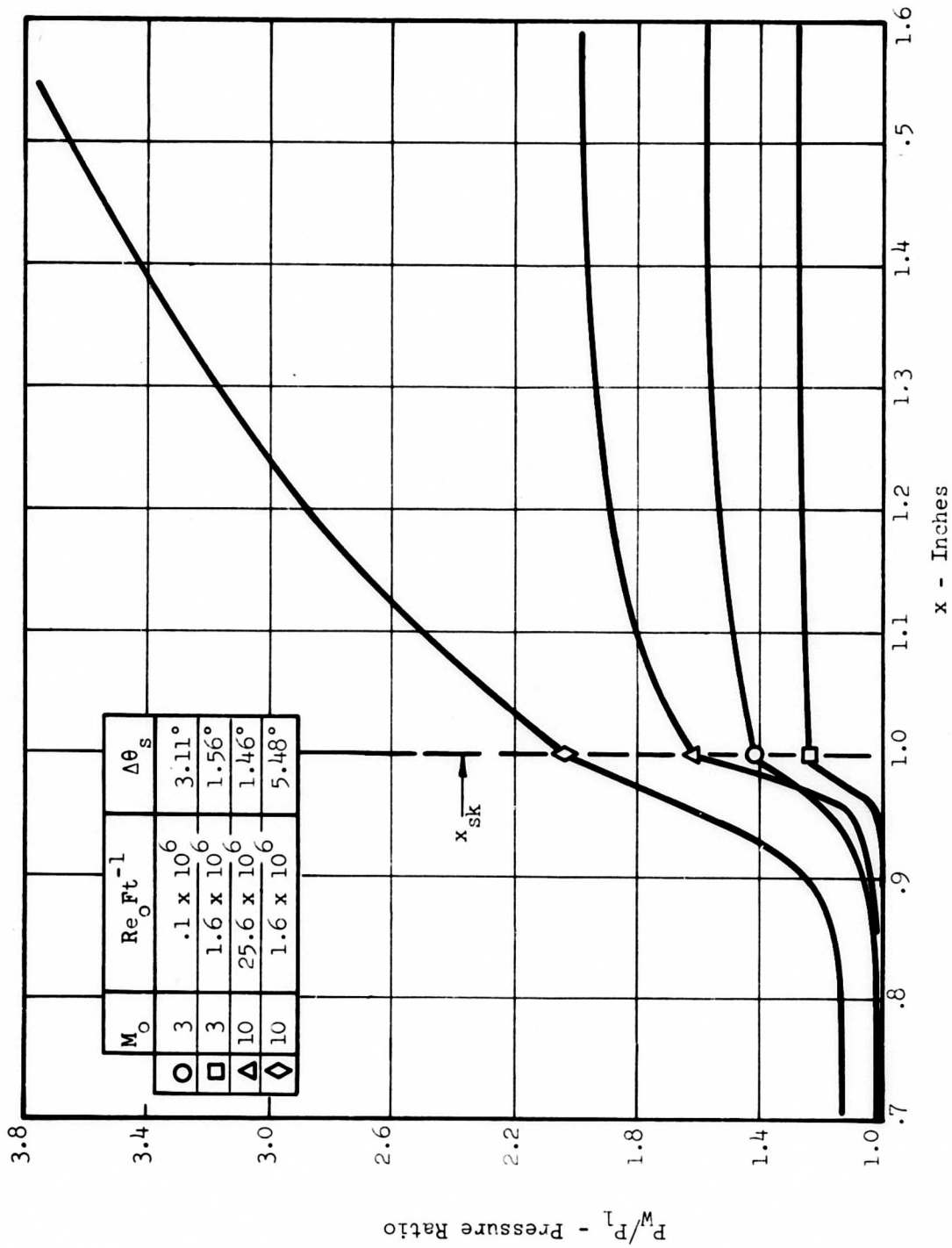


Figure 10 THEORETICAL PRESSURE DISTRIBUTIONS

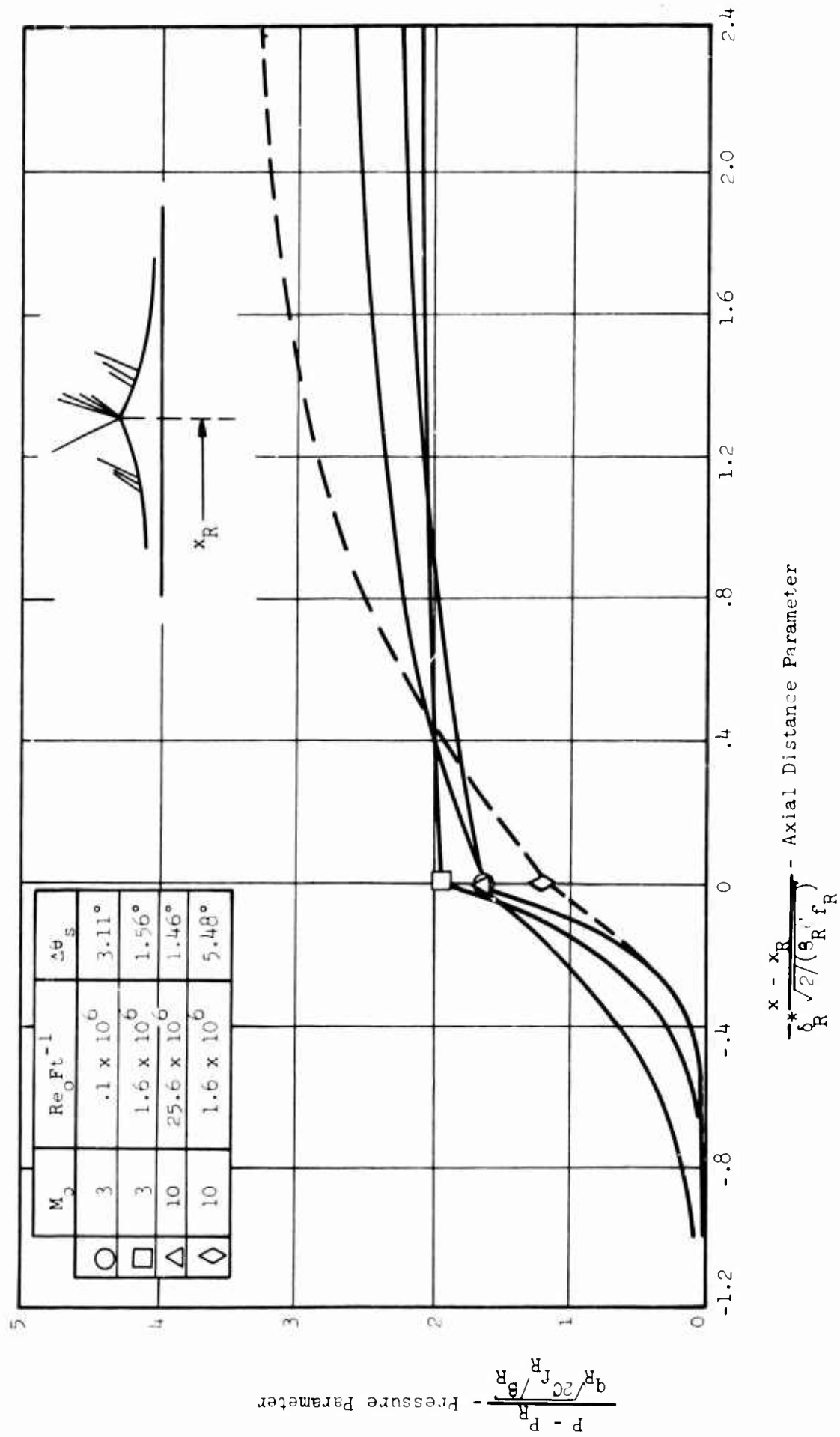


Figure 11 PRESSURE DISTRIBUTION CORRELATION

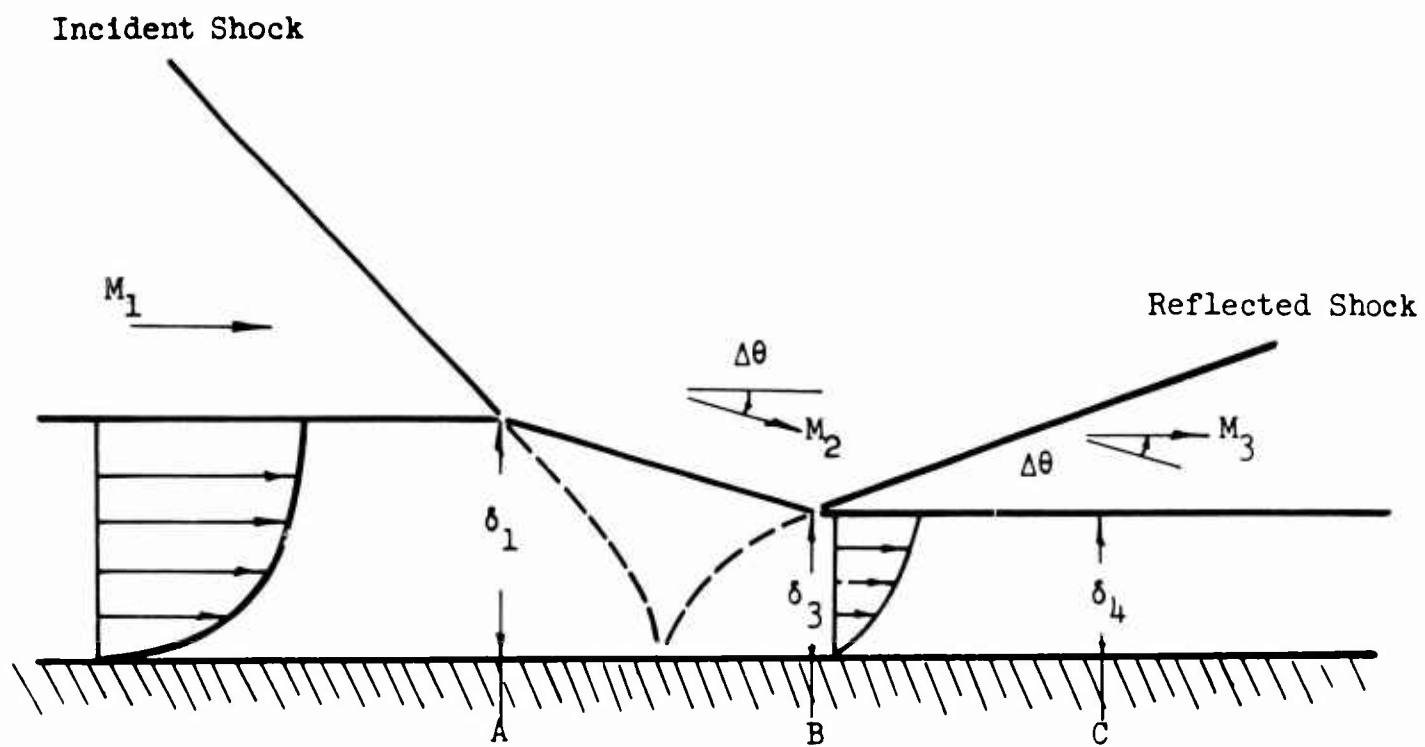


Figure 12 SCHEMATIC OF TURBULENT FLOW MODEL

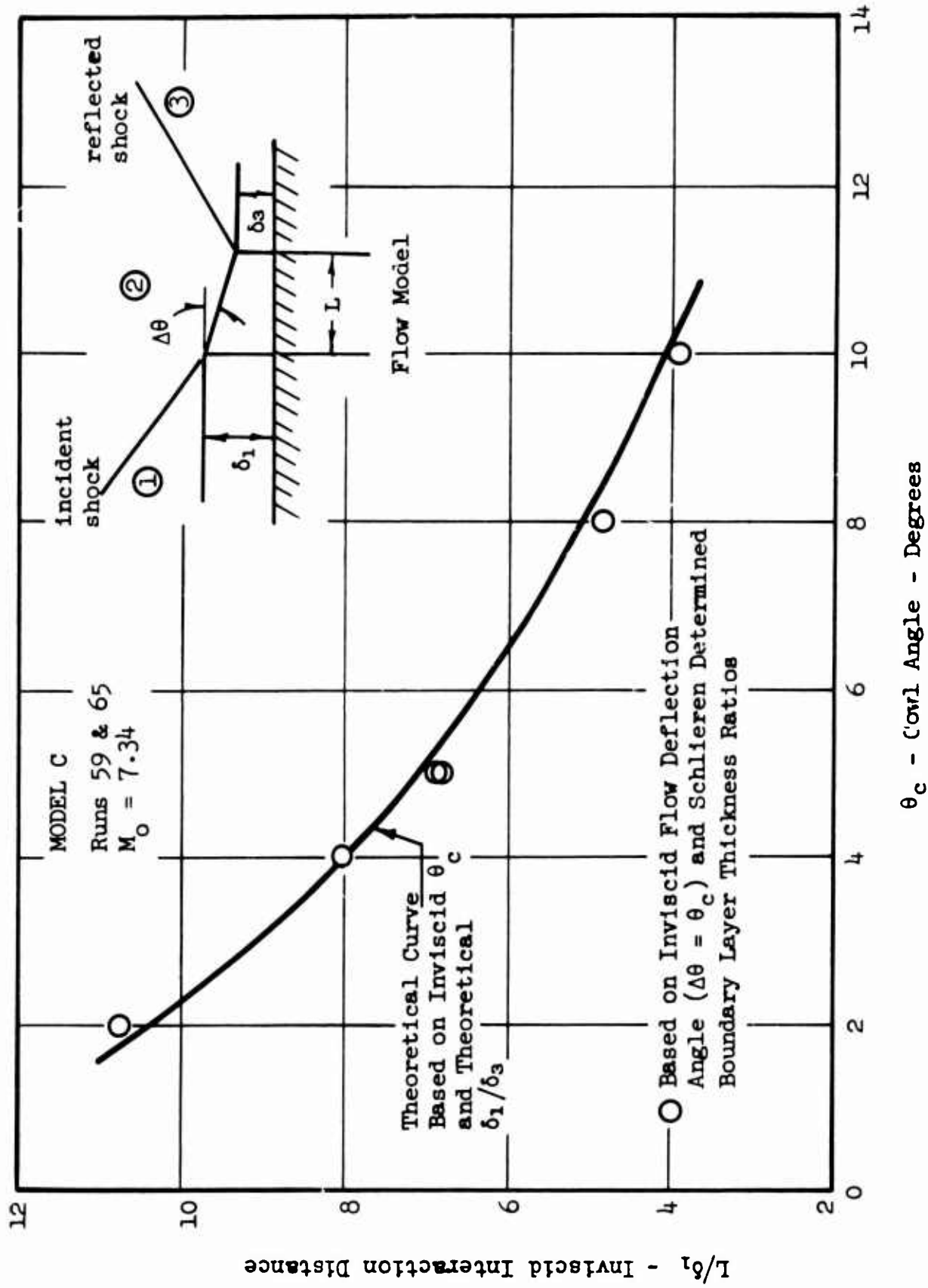


Figure 13 INVISCID INTERACTION LENGTH THEORY/DATA  
COMPARISON

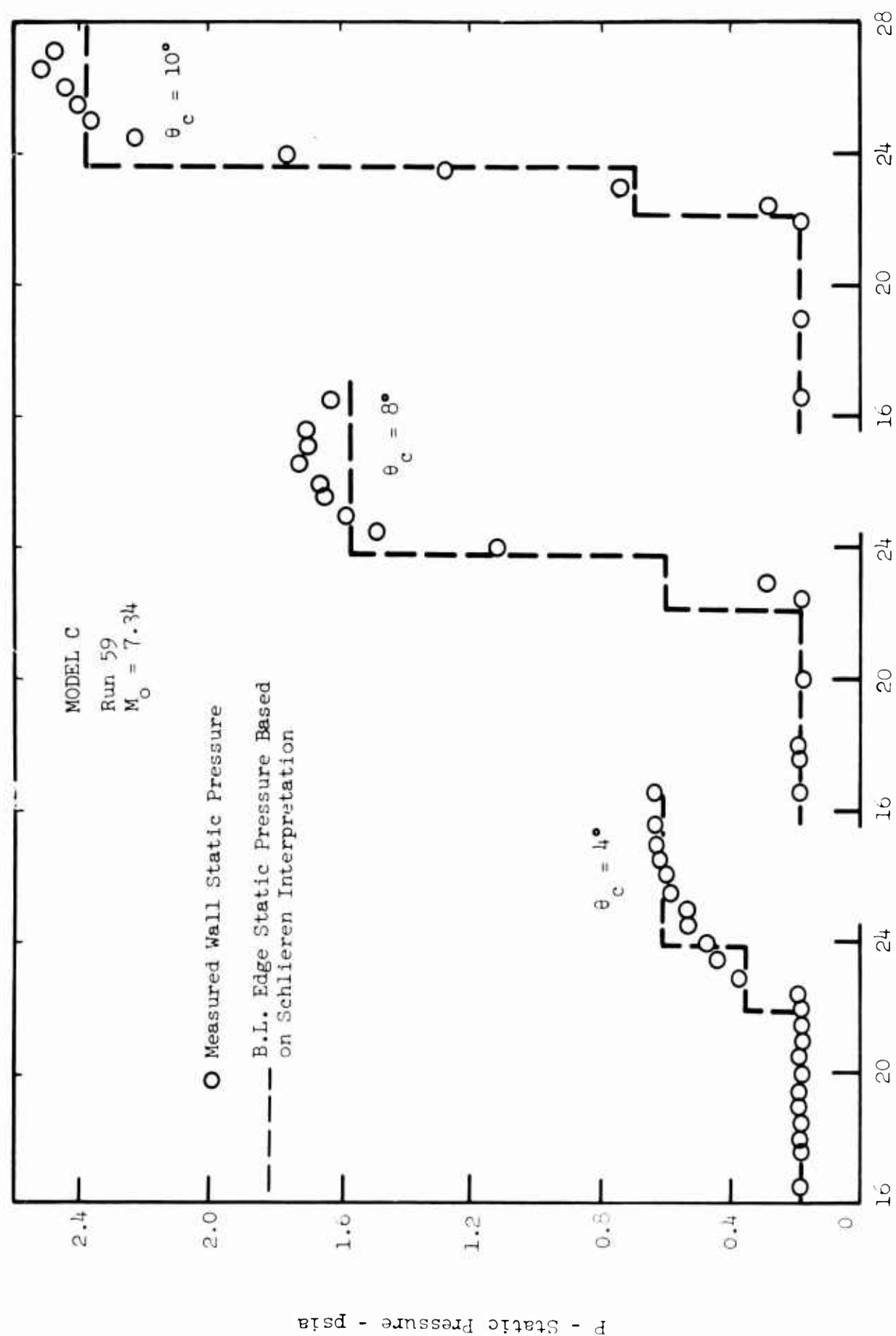


Figure 14 THEORY/DATA PRESSURE DISTRIBUTION COMPARISONS

MODEL C

Run 59

$M_o = 7.30$

$Re_o = 3.59 \times 10^6 \text{ Ft}^{-1}$

$\theta_c = 4^\circ$



Figure 15    TURBULENT BOUNDARY LAYER SHOCK  
                  IMPINGEMENT



MODEL C

Run 59

$M_o = 7.3$

$Re_o = 3.56 \times 10^6 \text{ Ft}^{-1}$

$\theta_c = 8^\circ$



Figure 16    TURBULENT BOUNDARY LAYER SHOCK  
                  IMPINGEMENT

MODEL C

Run 59

$$M_o = 7.3$$

$$Re_o = 3.56 \times 10^6 \text{ Ft}^{-1}$$

$$\theta_c = 10^\circ$$

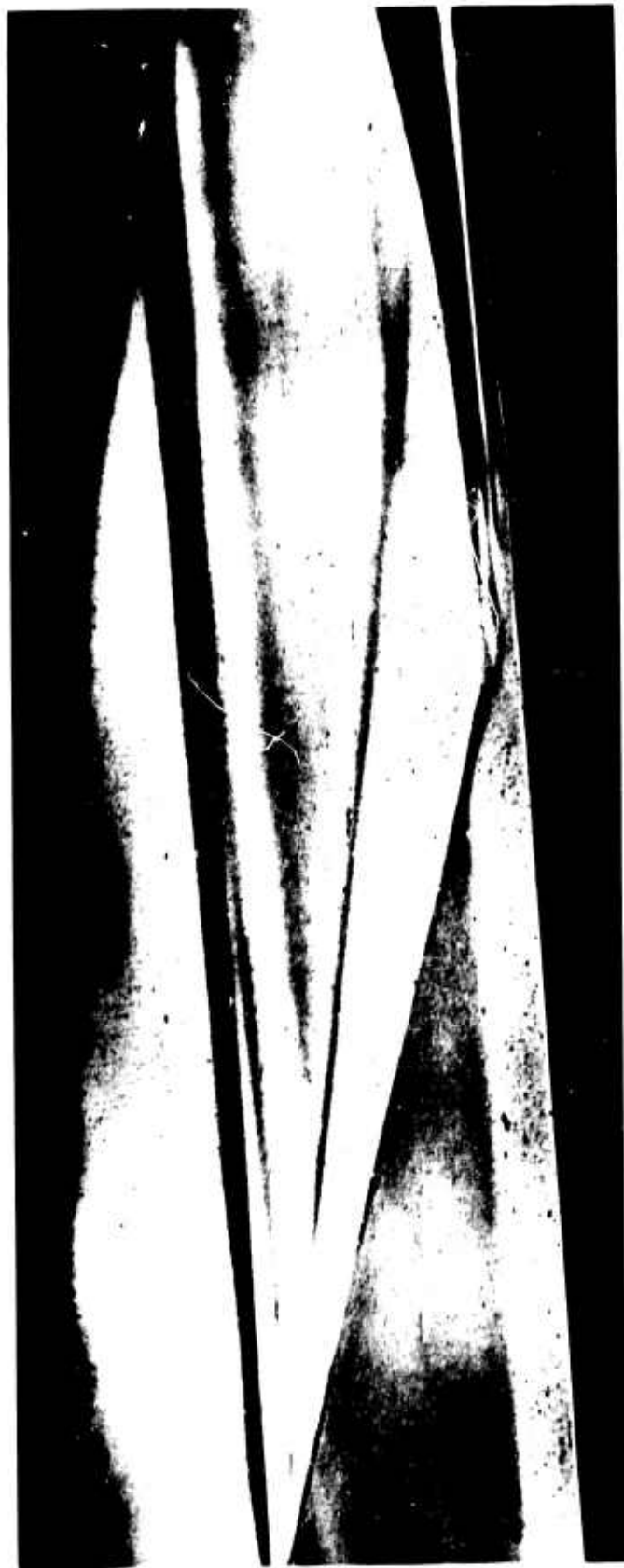


Figure 17    TURBULENT BOUNDARY LAYER SHOCK  
                  IMPINGEMENT

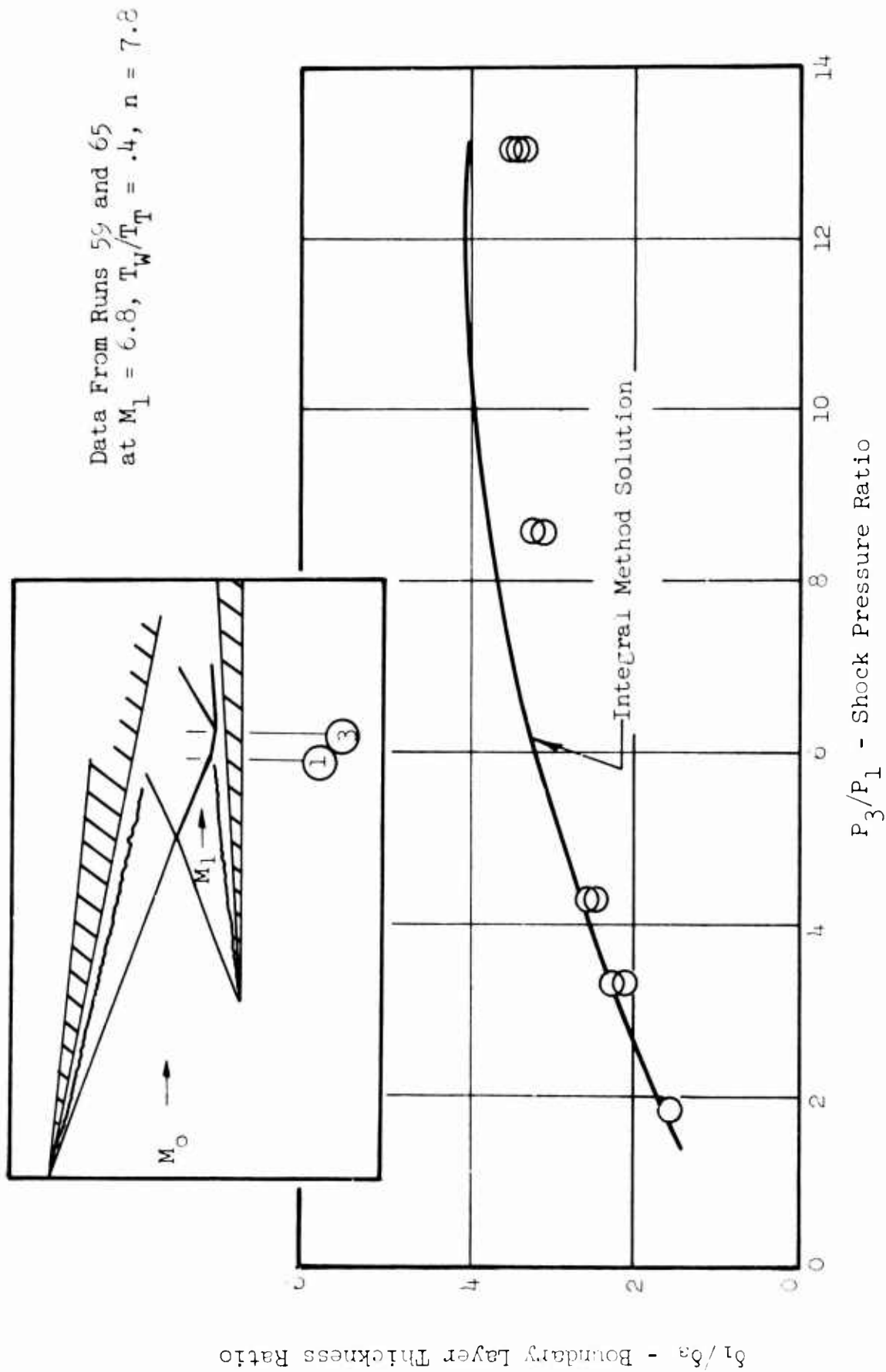


Figure 18 THEORY/DATA COMPARISON OF BOUNDARY LAYER THICKNESS RATIO

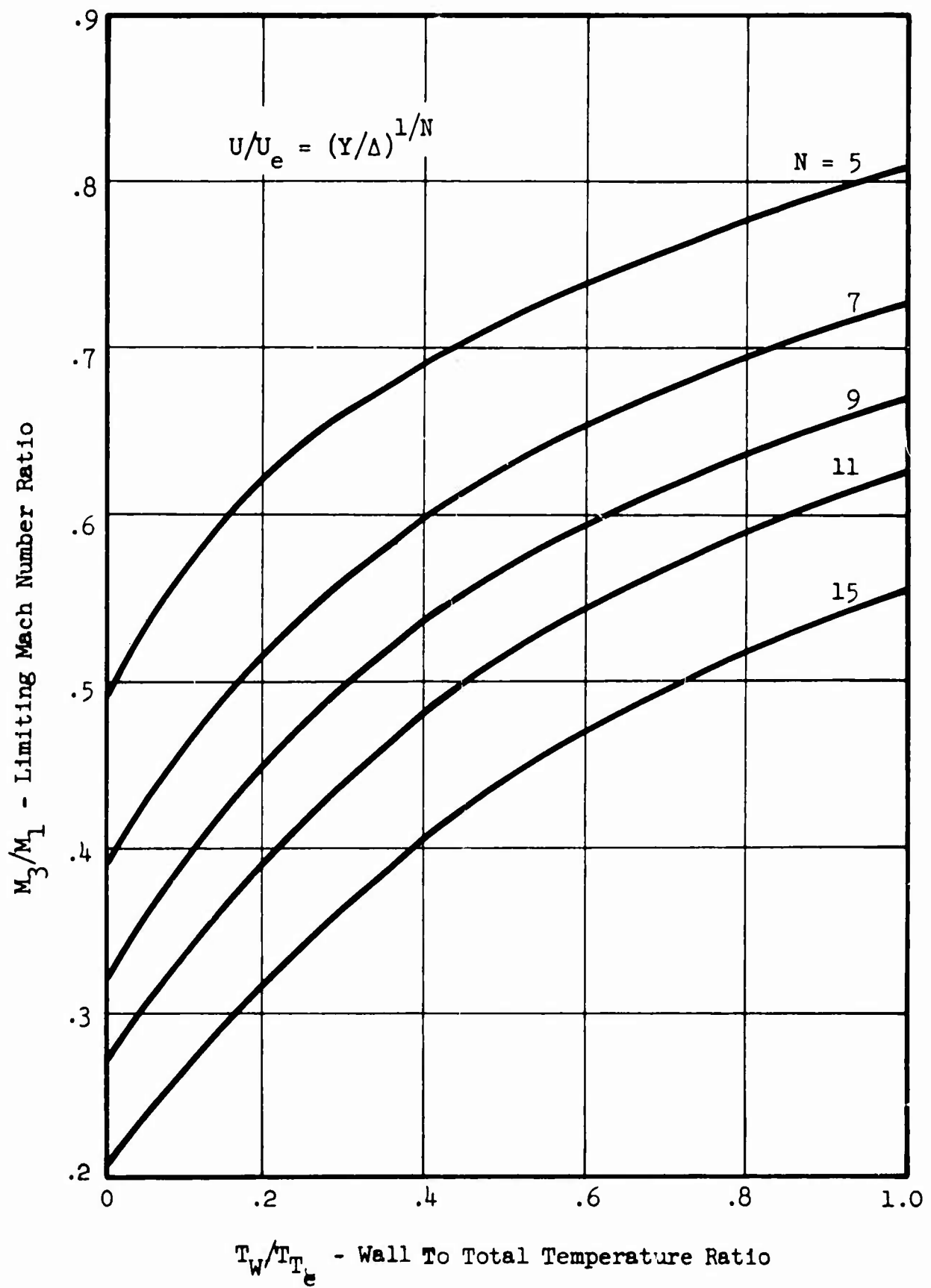


Figure 19 THEORETICAL SEPARATION LIMITED MACH  
NUMBER RATIO

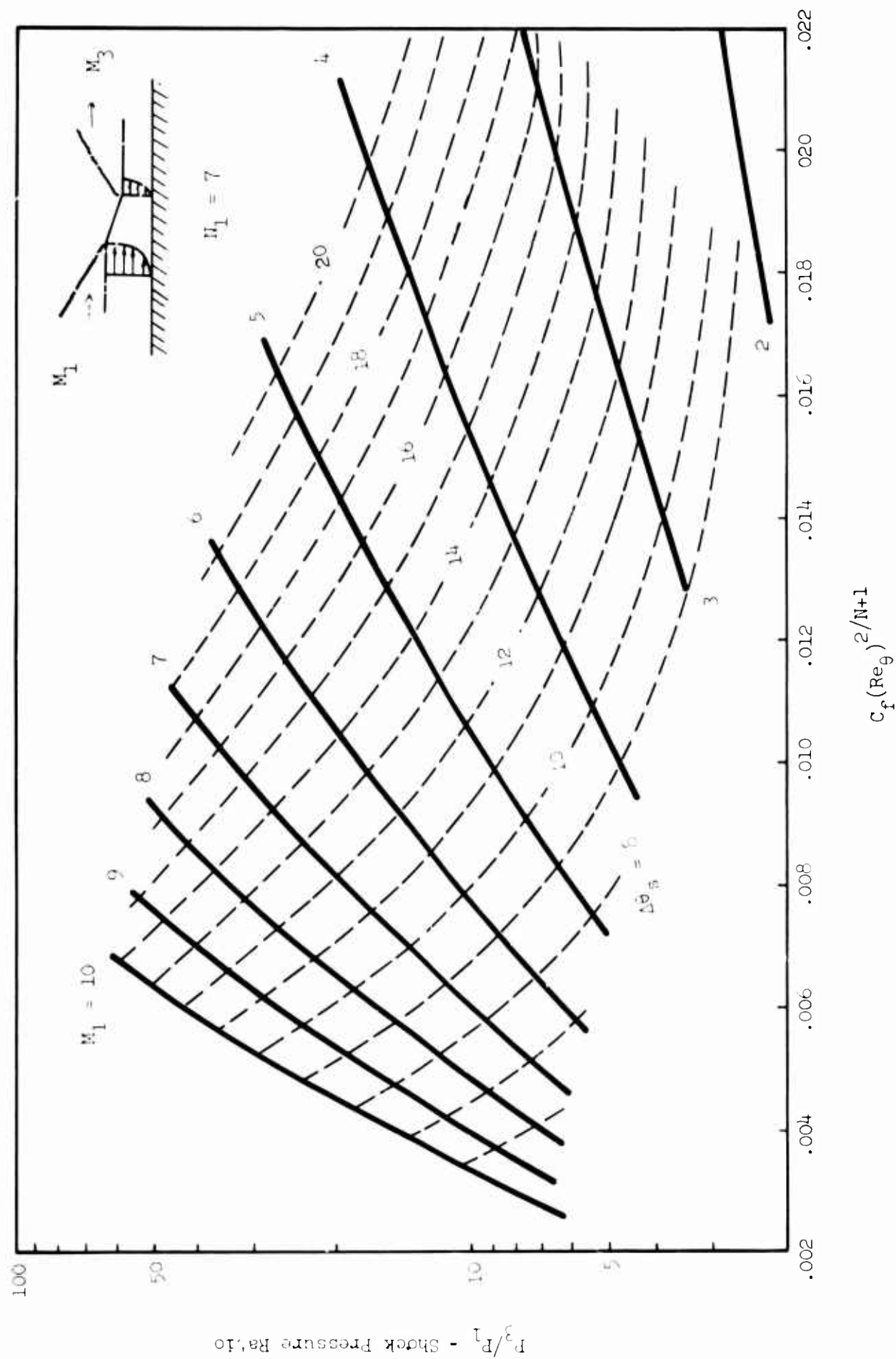


Figure 20 PREDICTED SEPARATION PRESSURE RATIO

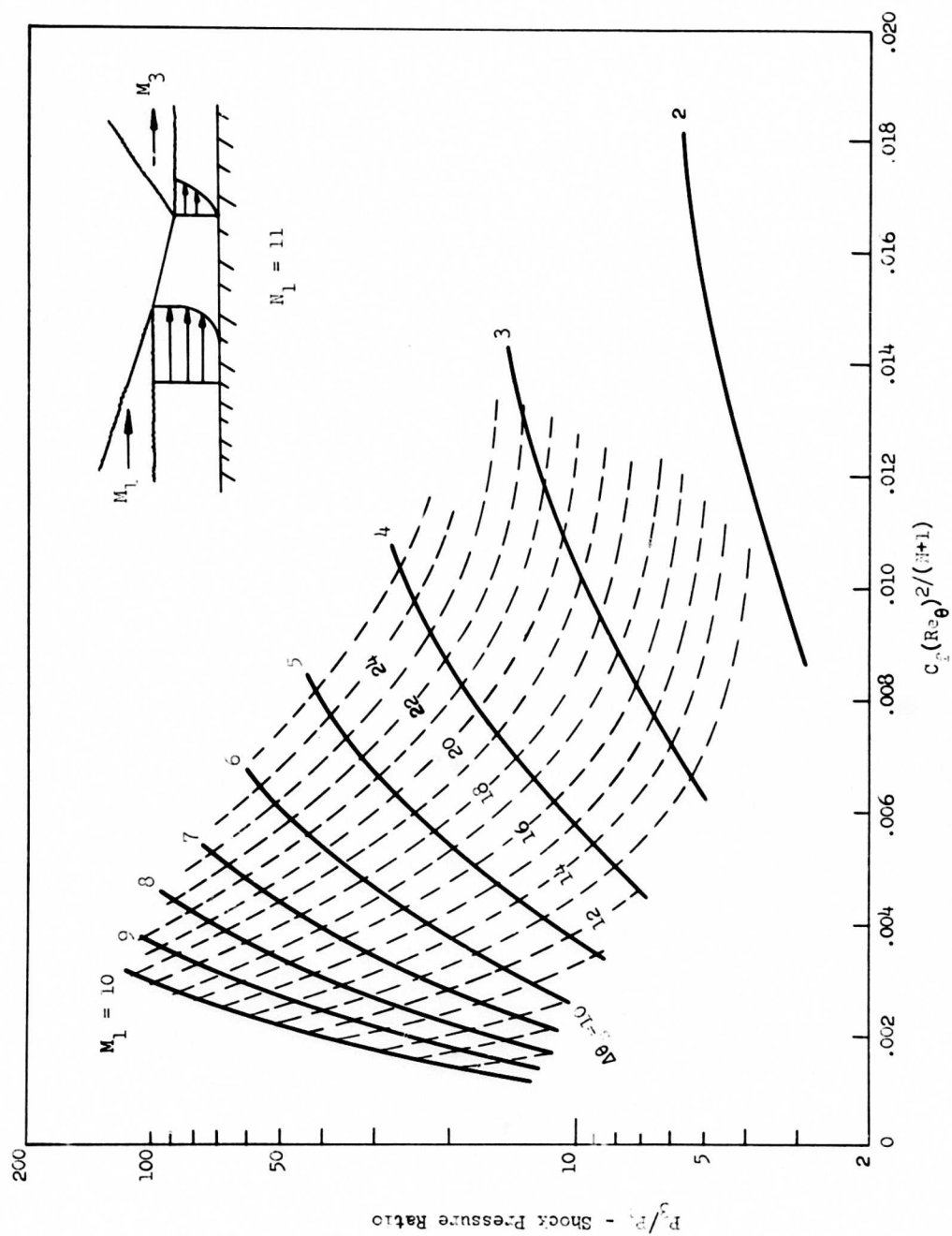


Figure 22 PREDICTED SEPARATION PRESSURE RATIO

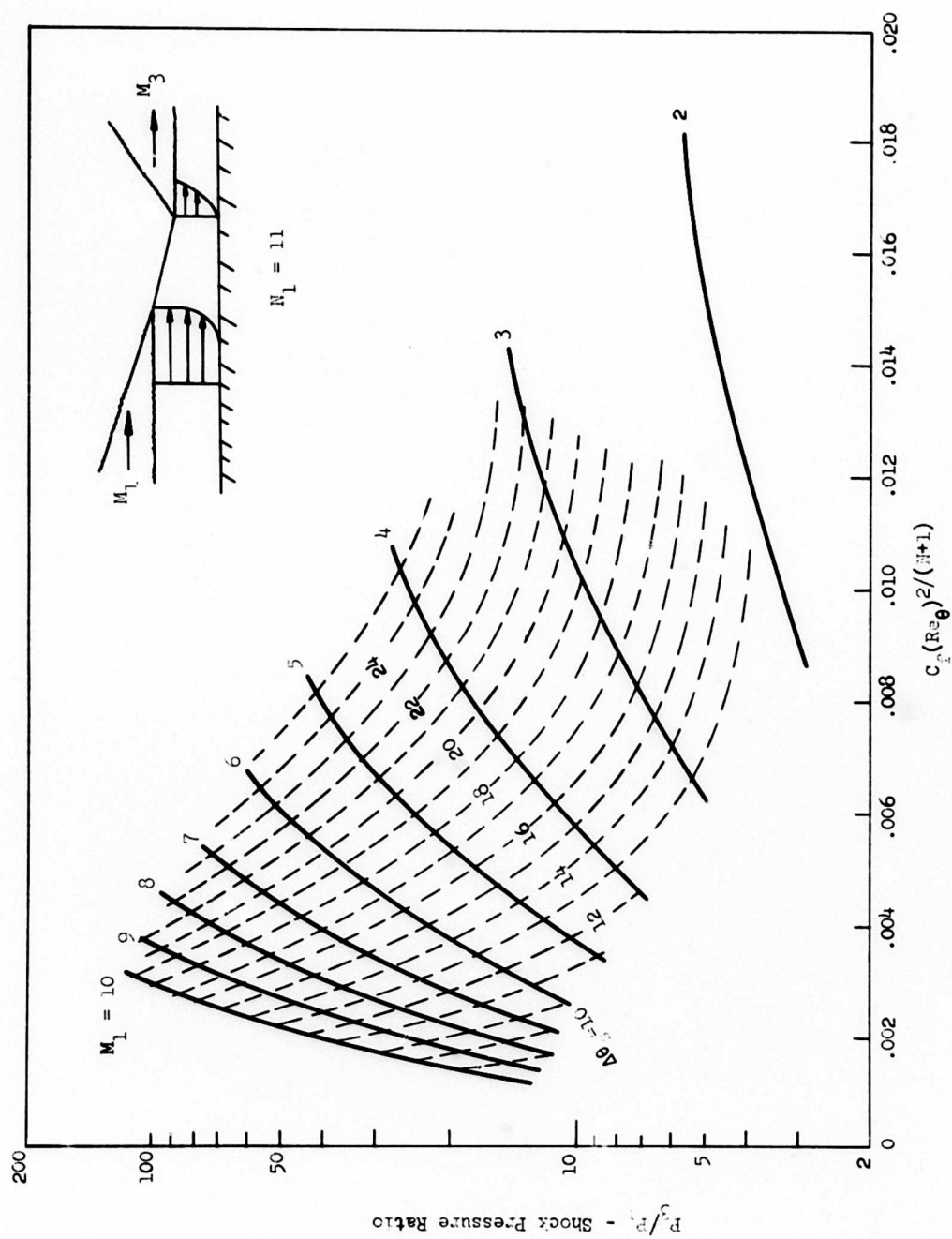


Figure 22 PREDICTED SEPARATION PRESSURE RATIO

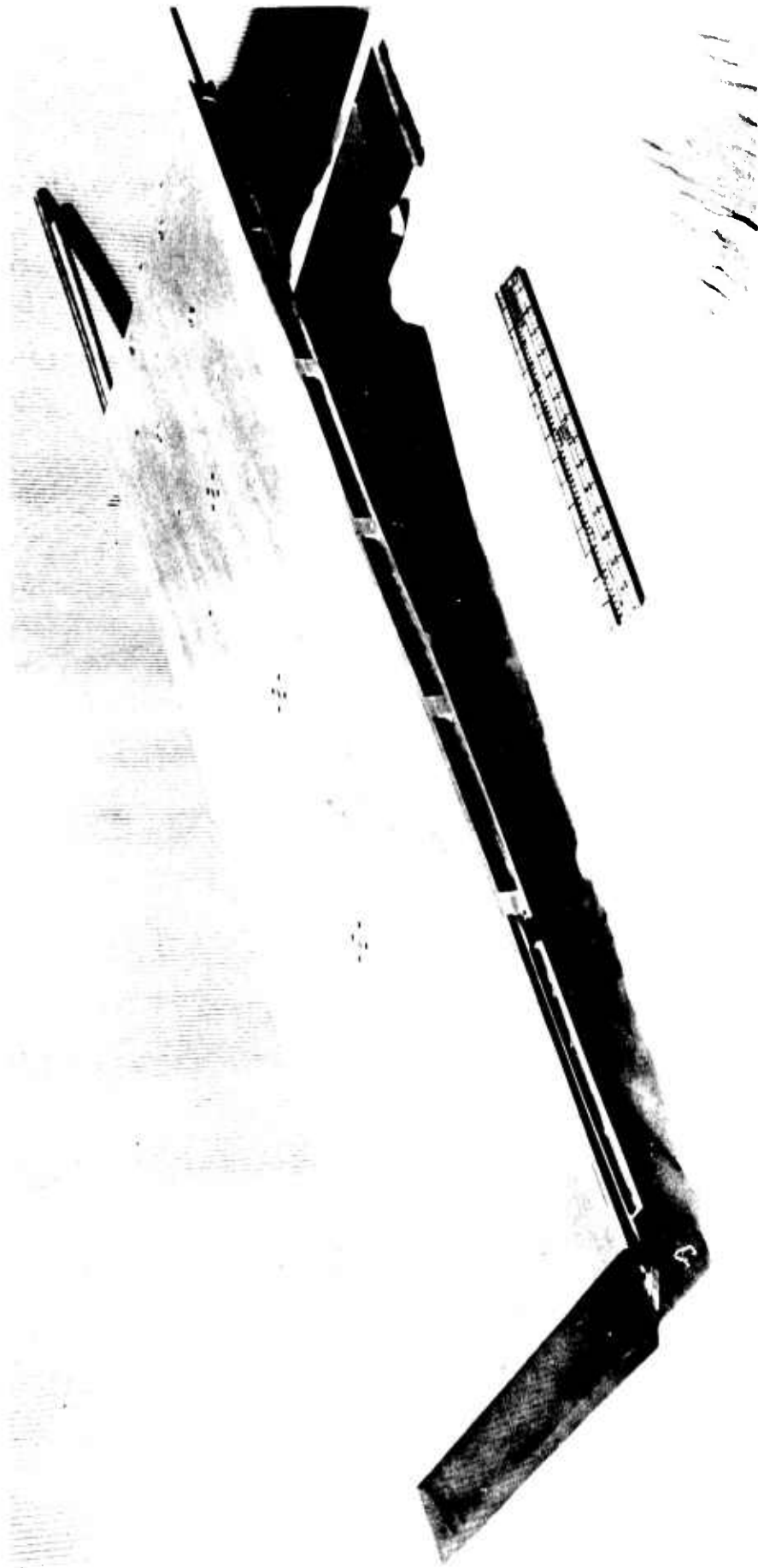


Figure 23 MODEL C RAMP



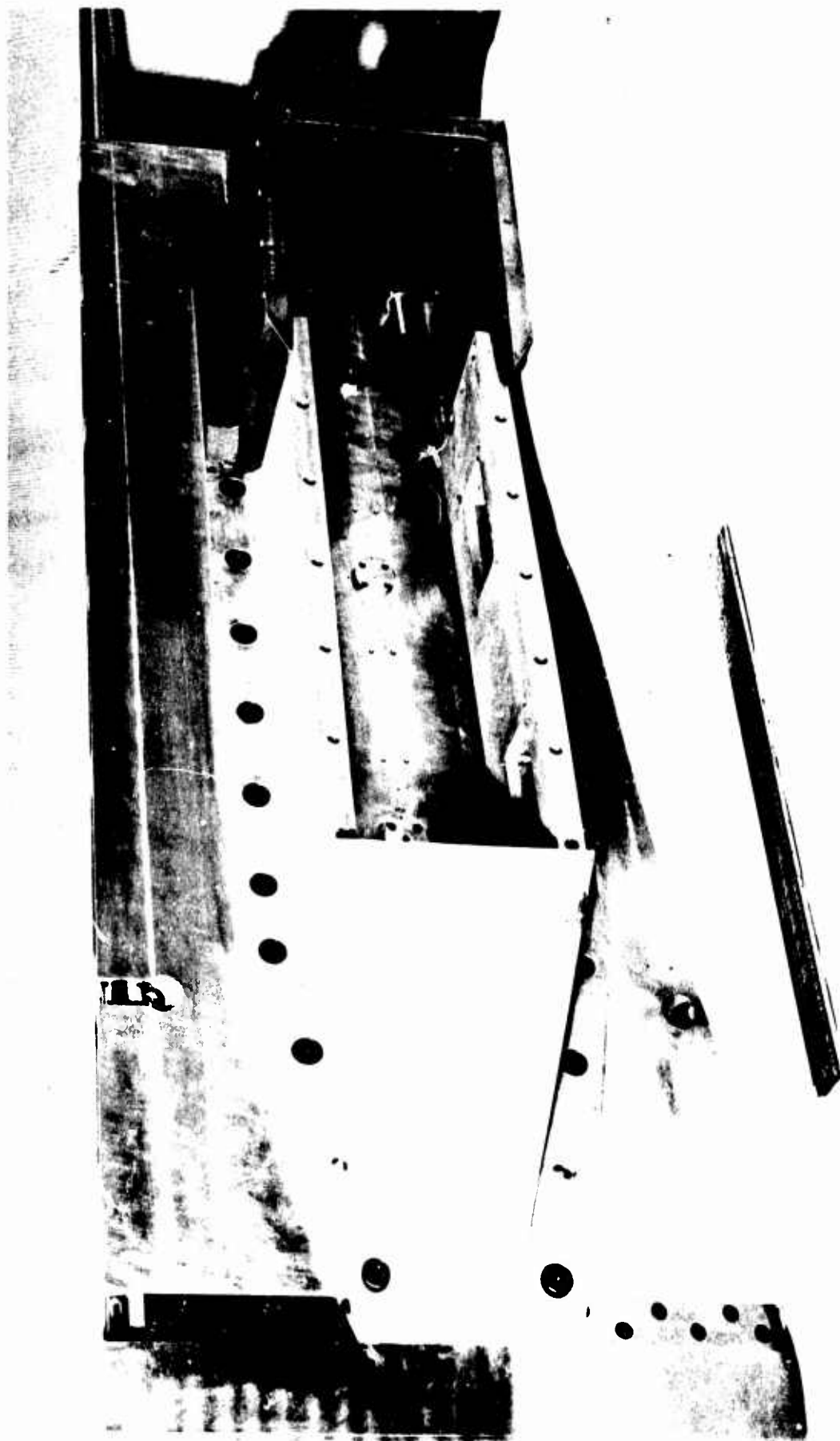


Figure 24      MODEL C RAMP UNDERCARRIAGE

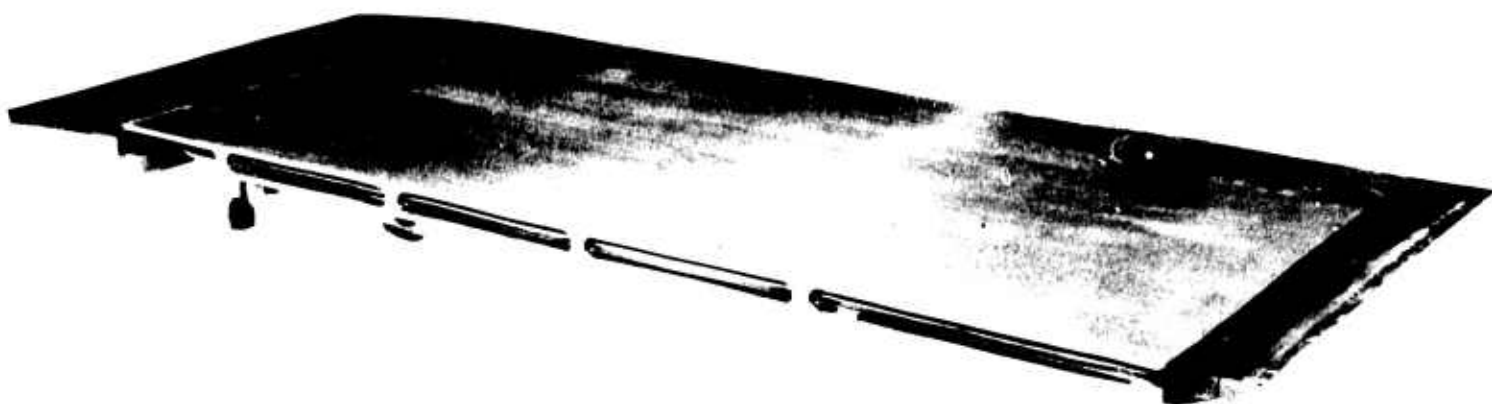


Figure 25    MODEL C COWL PLATE



Figure 26    MODEL C COWL SUPERSTRUCTURE

Ramp Static Pressure  
Tap Locations

Tap No.	X (inches)	Y (inches)
1	1.50	26.56
2	4.00	27.06
3	6.06	27.50
4	8.00	27.94
5	10.00	28.44
6	12.00	28.94
7	13.75	29.44
8	14.38	29.94
9	15.00	30.50
10	15.56	31.00
11	16.13	31.50
12	16.13	32.00
13	16.13	32.50
14	16.63	33.00
15	17.13	33.62
16	17.56	34.25
17	18.00	34.81
18	18.50	35.38
19	19.00	35.98
20	19.50	36.58
21	20.00	37.19
22	20.50	37.79
23	21.00	38.39
24	21.50	38.99
25	22.00	39.59
26	22.50	40.19
27	23.00	40.79
28	23.38	41.39
29	23.75	41.99
30	24.13	42.59
31	24.50	43.19
32	25.00	43.79
33	26.06	44.39
34	26.06	44.99
35	26.06	45.59

Ramp Thermocouple Locations											
T/C	T1	T2	T3	T4	T5	T6	T7	T8	T9	T10	T11
inches	2.44	5.25	9.50	16.50	21.00	24.00	27.00	30.00	33.00	36.00	39.00

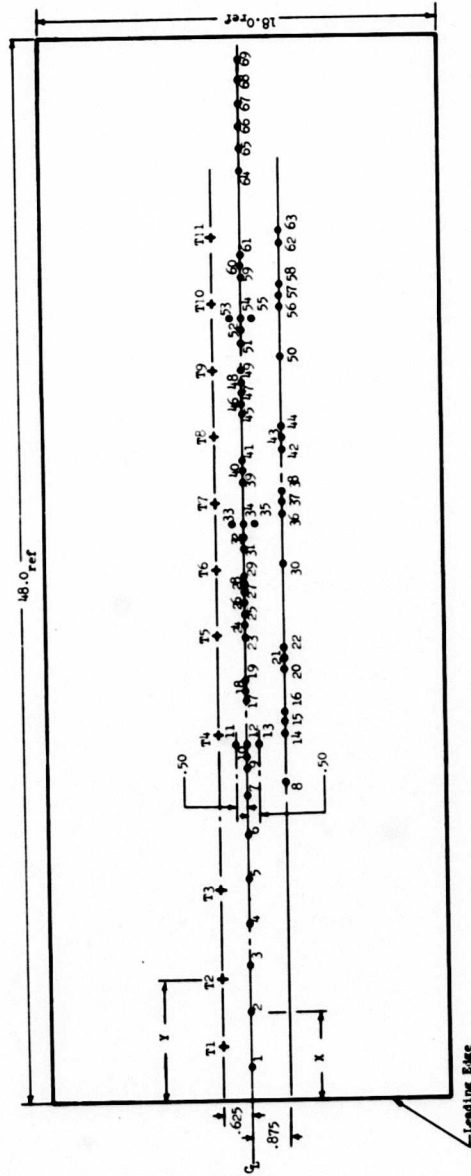
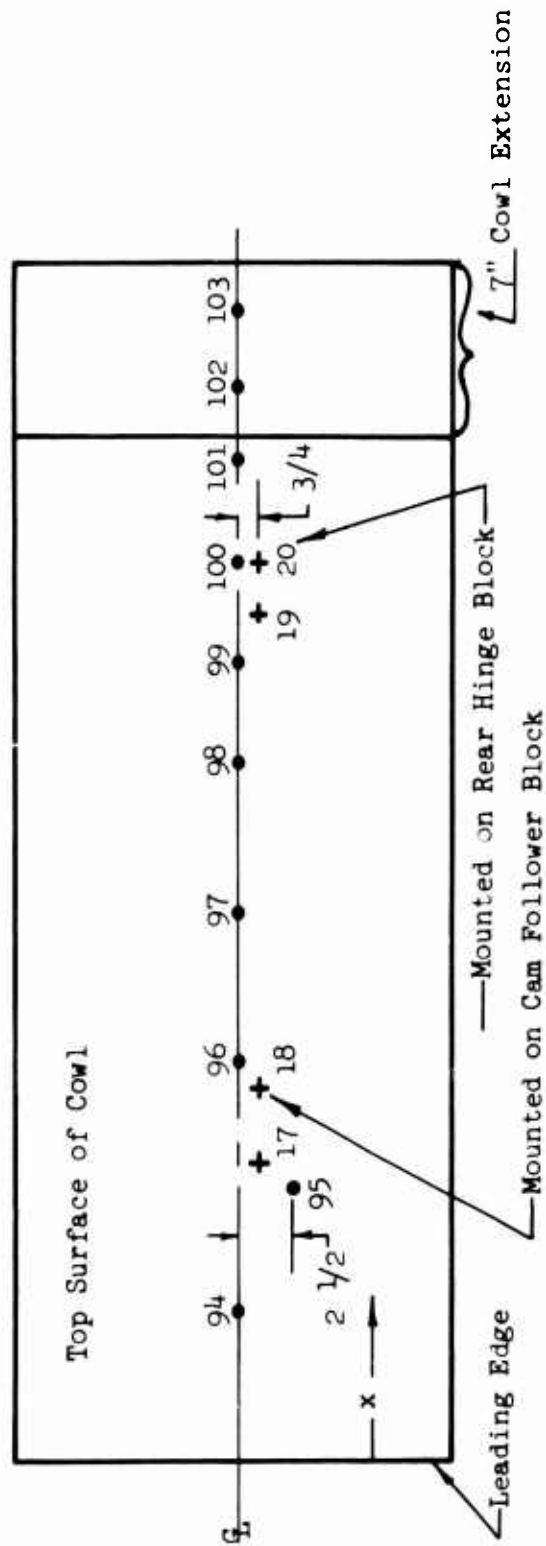


Figure 27 MODEL C RAMP INSTRUMENTATION



Figure 28 MODEL C RAMP INSTRUMENTATION  
INSTALLATION



Cowl Static Pressure Tap Locations

Tap No.	x (inches)
94	6
95	11
96	16
97	22
98	28
99	32
100	36
101	40
102	42 $\frac{7}{8}$
103	45 $\frac{7}{8}$

Cowl Thermocouple Locations

T/C	x (inches)
17	12
18	15
19	34

Figure 29 MODEL C COWL INSTRUMENTATION

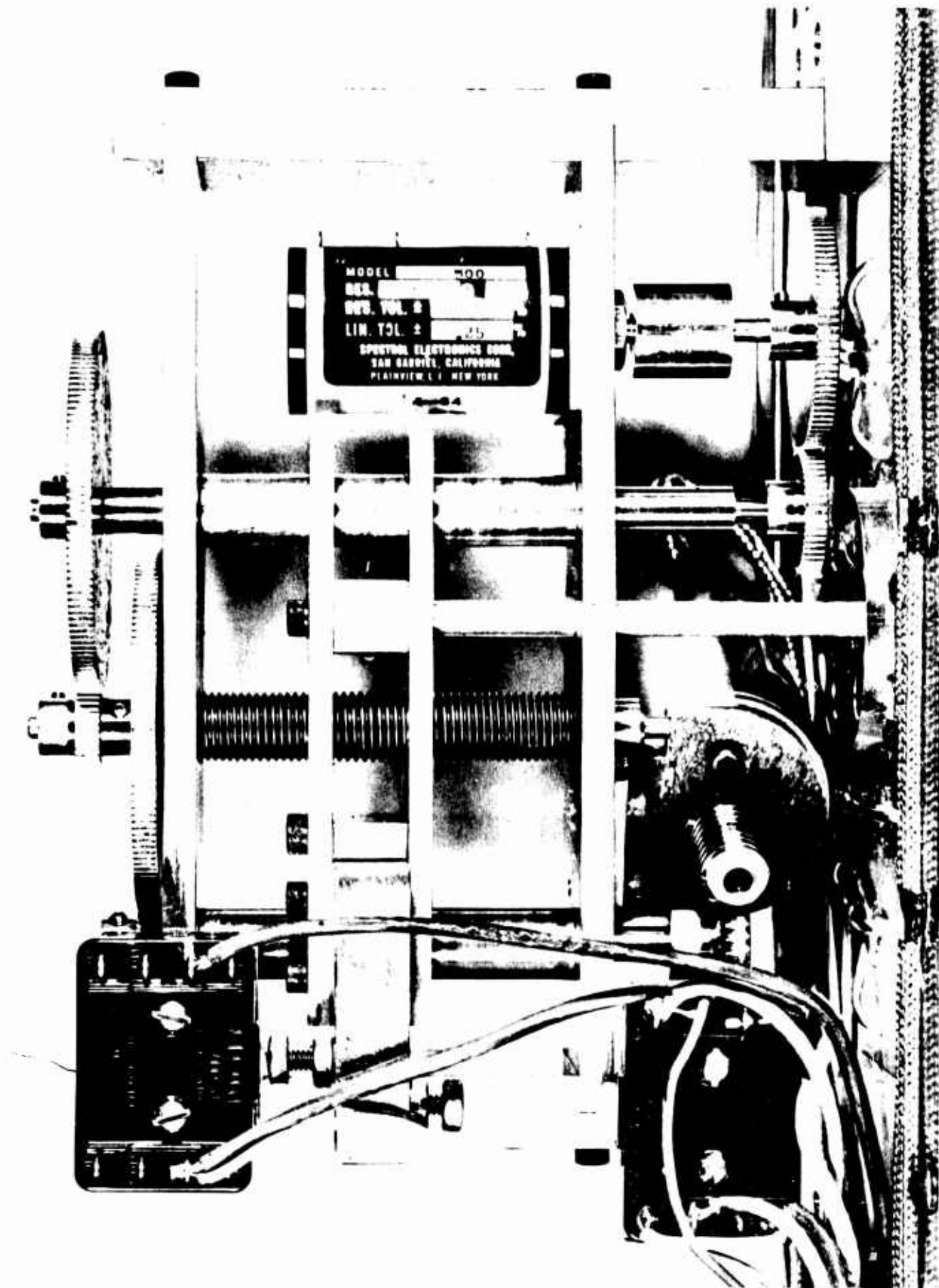


Figure 30 BOUNDARY LAYER PROBE ACTUATOR

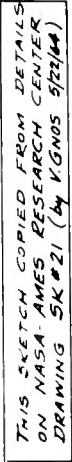


Figure 31 NASA-AMES BOUNDARY LAYER COMBINATION PROBE





Figure 32 NASA-AMES BOUNDARY LAYER COMBINATION  
PROBE AND INSTALLATION

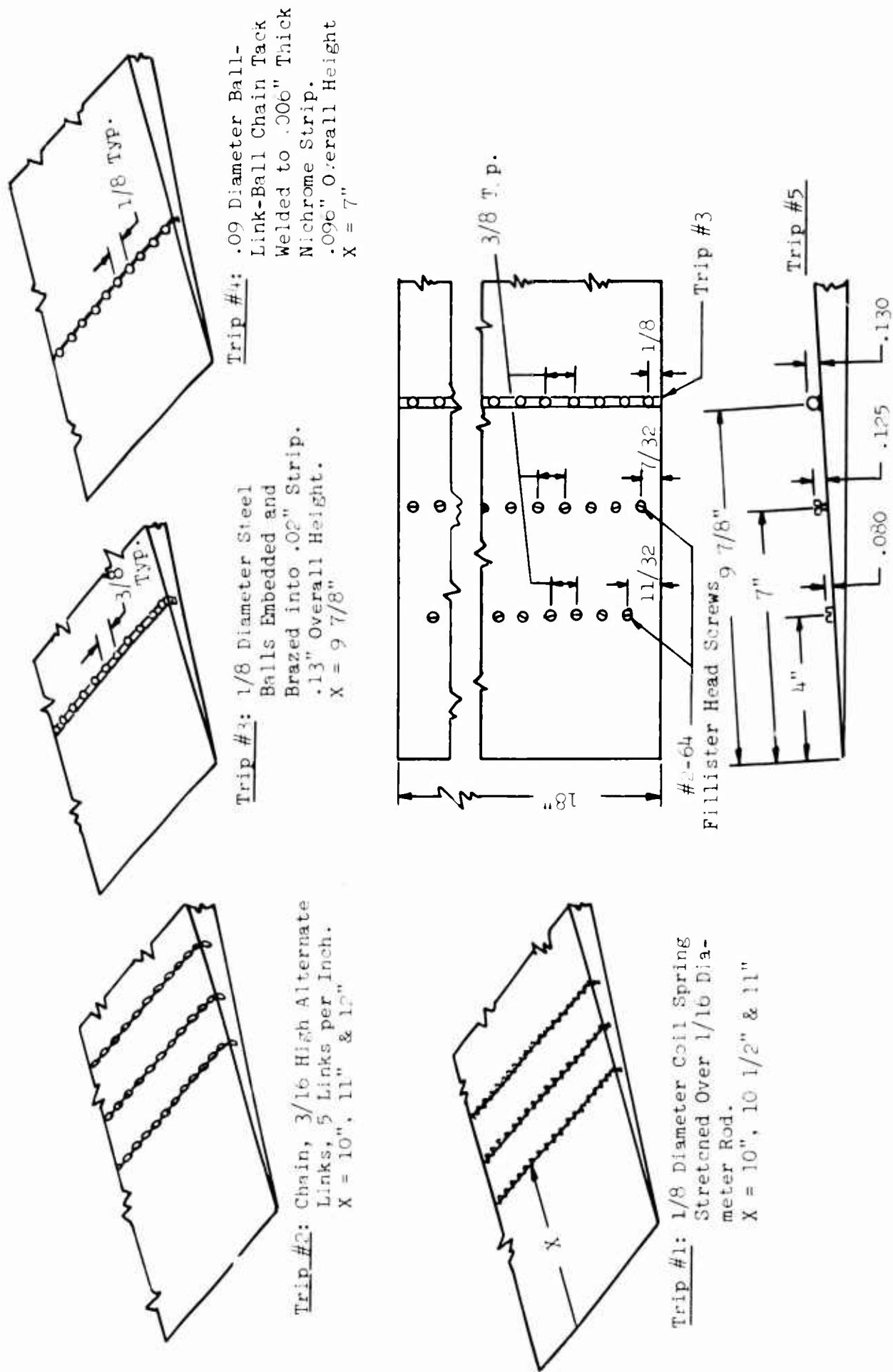
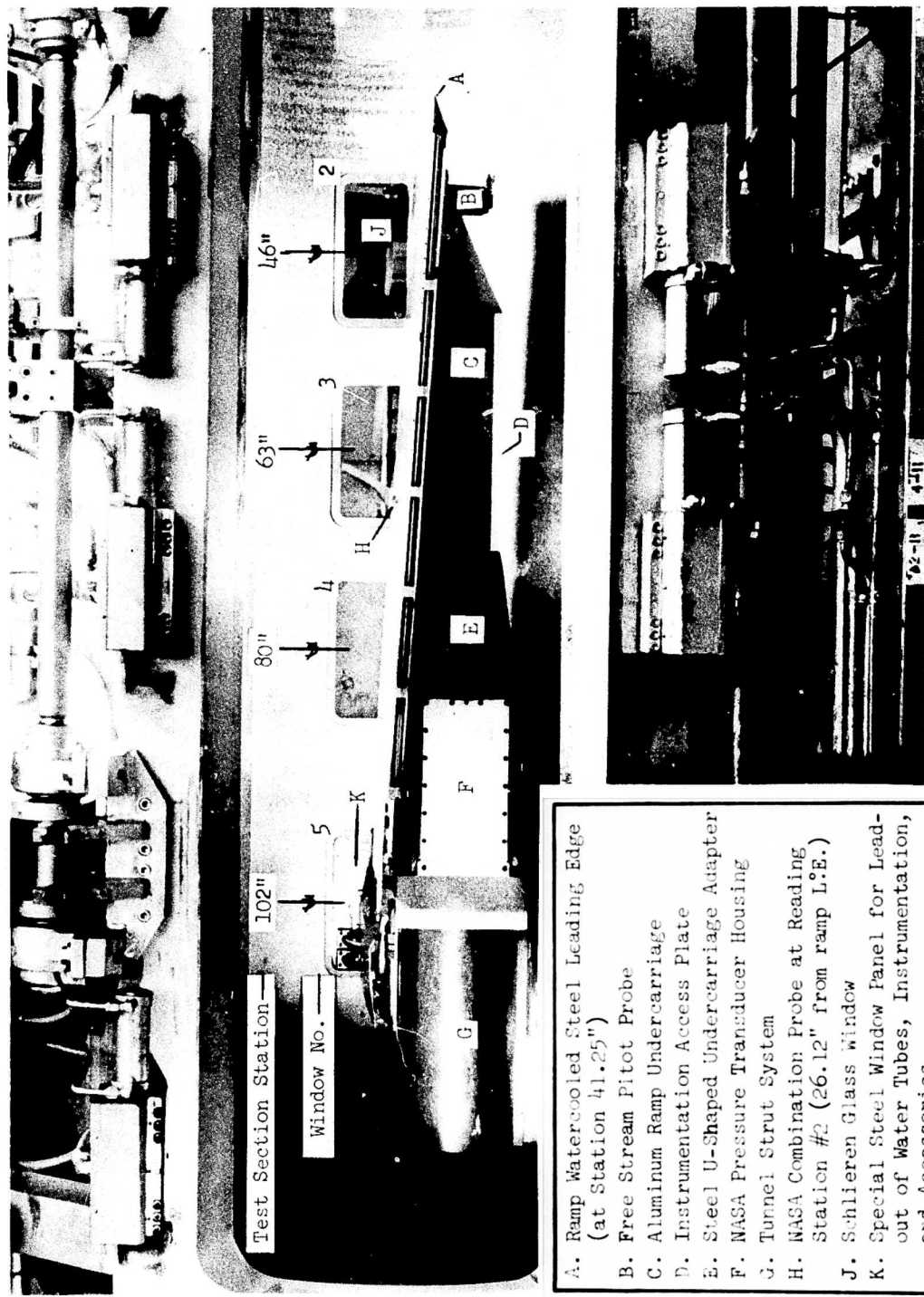
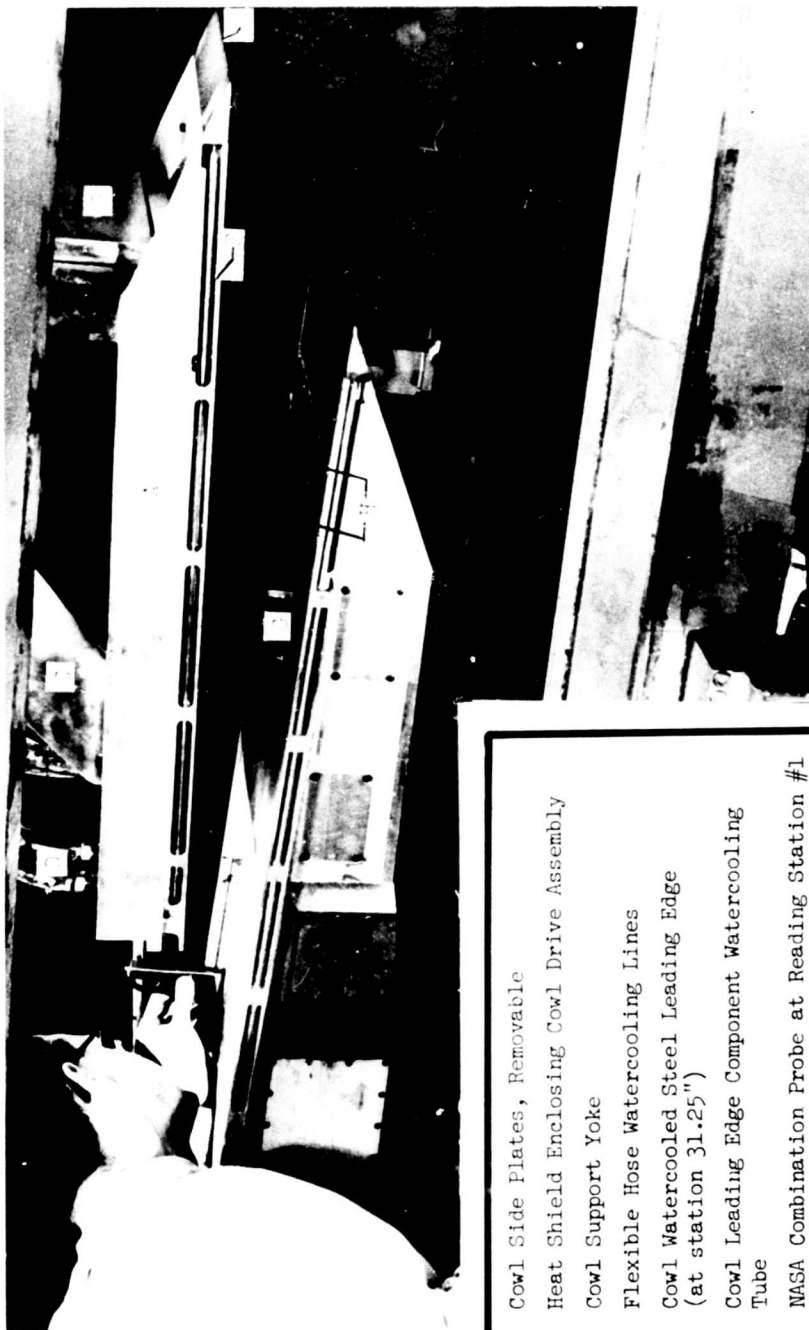


Figure 33 MODEL C BOUNDARY LAYER TRIP CONFIGURATIONS





- A. Cowl Side Plates, Removable
- B. Heat Shield Enclosing Cowl Drive Assembly
- C. Cowl Support Yoke
- D. Flexible Hose Watercooling Lines
- E. Cowl Watercooled Steel Leading Edge  
(at station 31.25")
- F. Cowl Leading Edge Component Watercooling  
Tube
- G. NASA Combination Probe at Reading Station #1  
(16.12" from ramp L.E.)
- H. Ramp Boundary Layer Trips

Figure 35 MODEL C RAMP AND COWL INSTALLATION

1. ALL DIMENSIONS ARE USED FOR MOUNTING OF TUBES TO  
 2. ALL DIMENSIONS ARE USED FOR MOUNTING OF TUBES TO  
 3. ALL DIMENSIONS ARE USED FOR MOUNTING OF TUBES TO

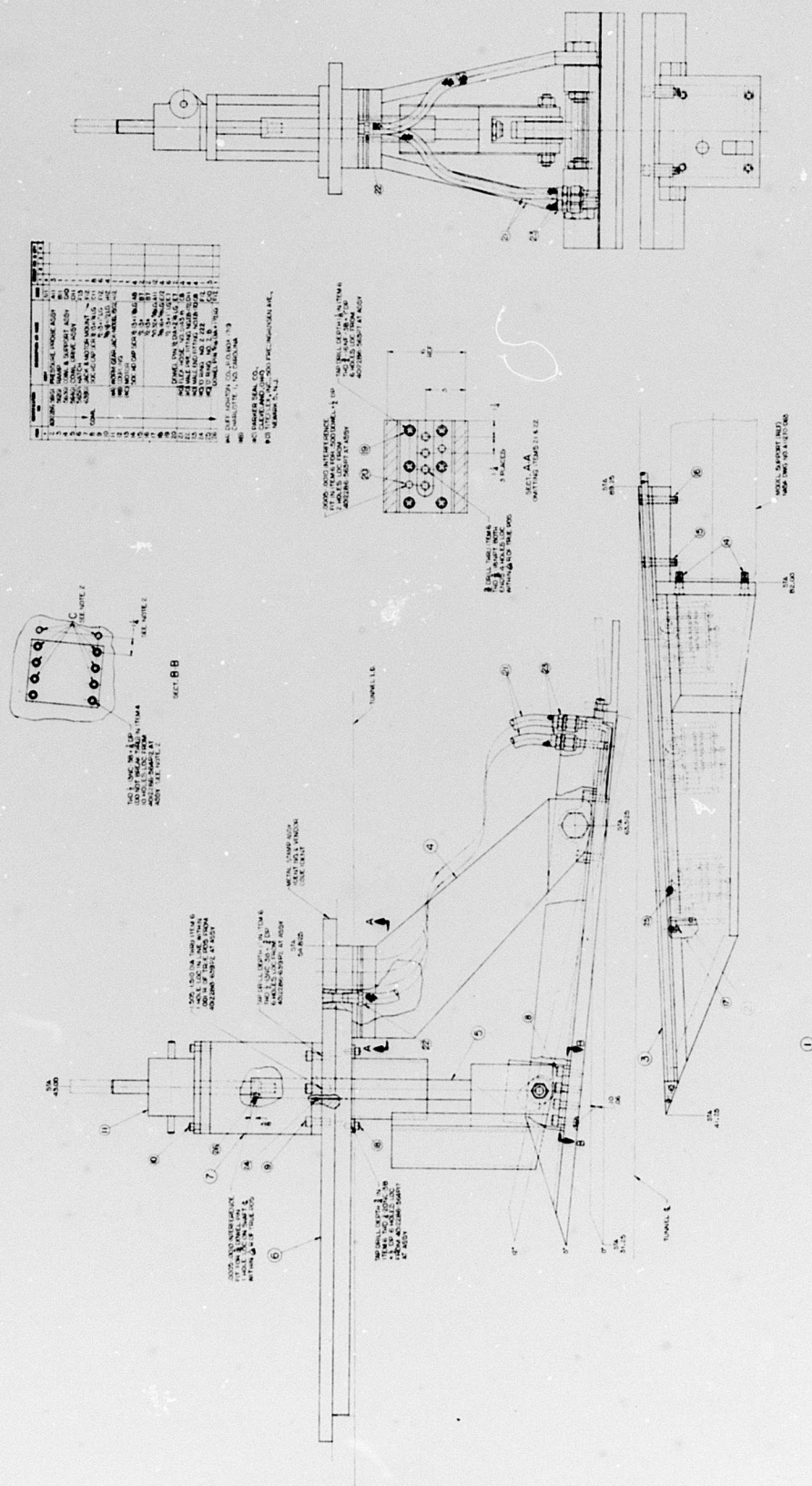


Figure 36 MODEL C ASSEMBLY DRAWING

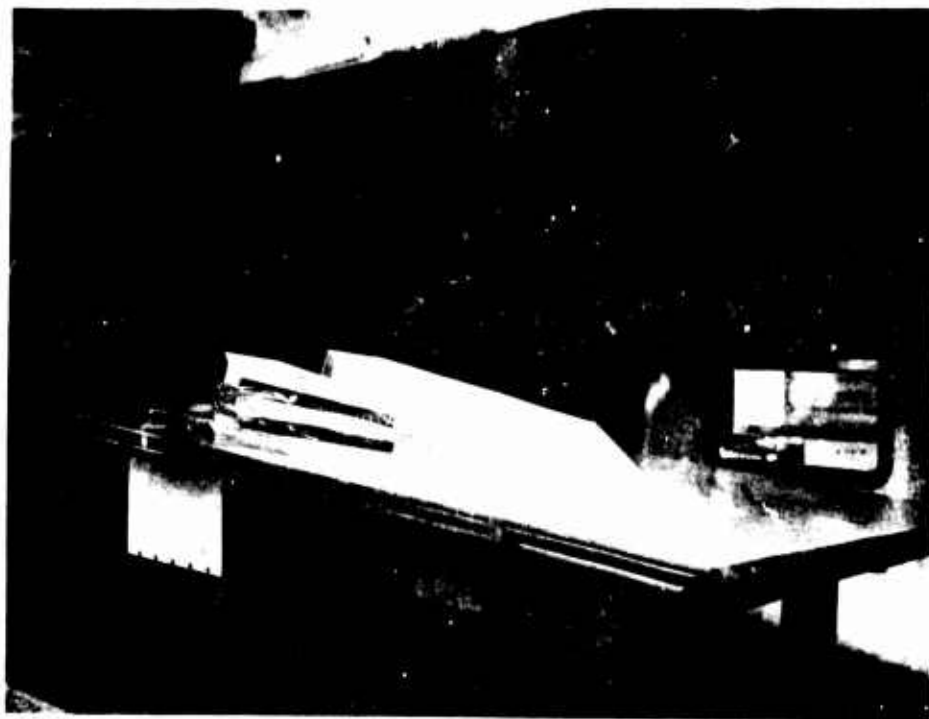
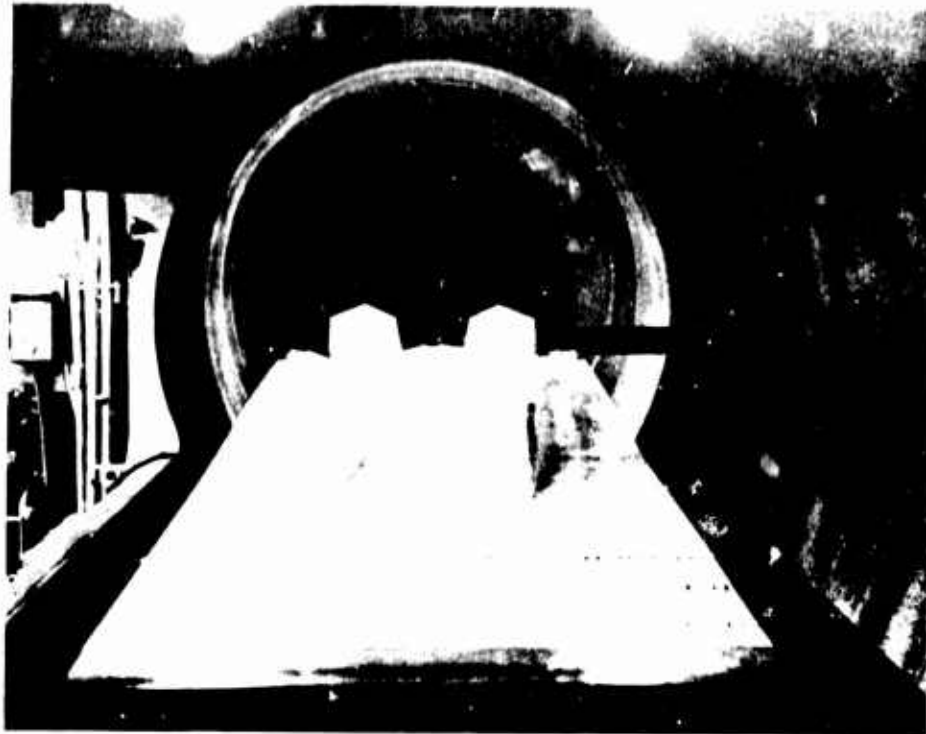


Figure 37     MODEL D VANE INSTALLATION

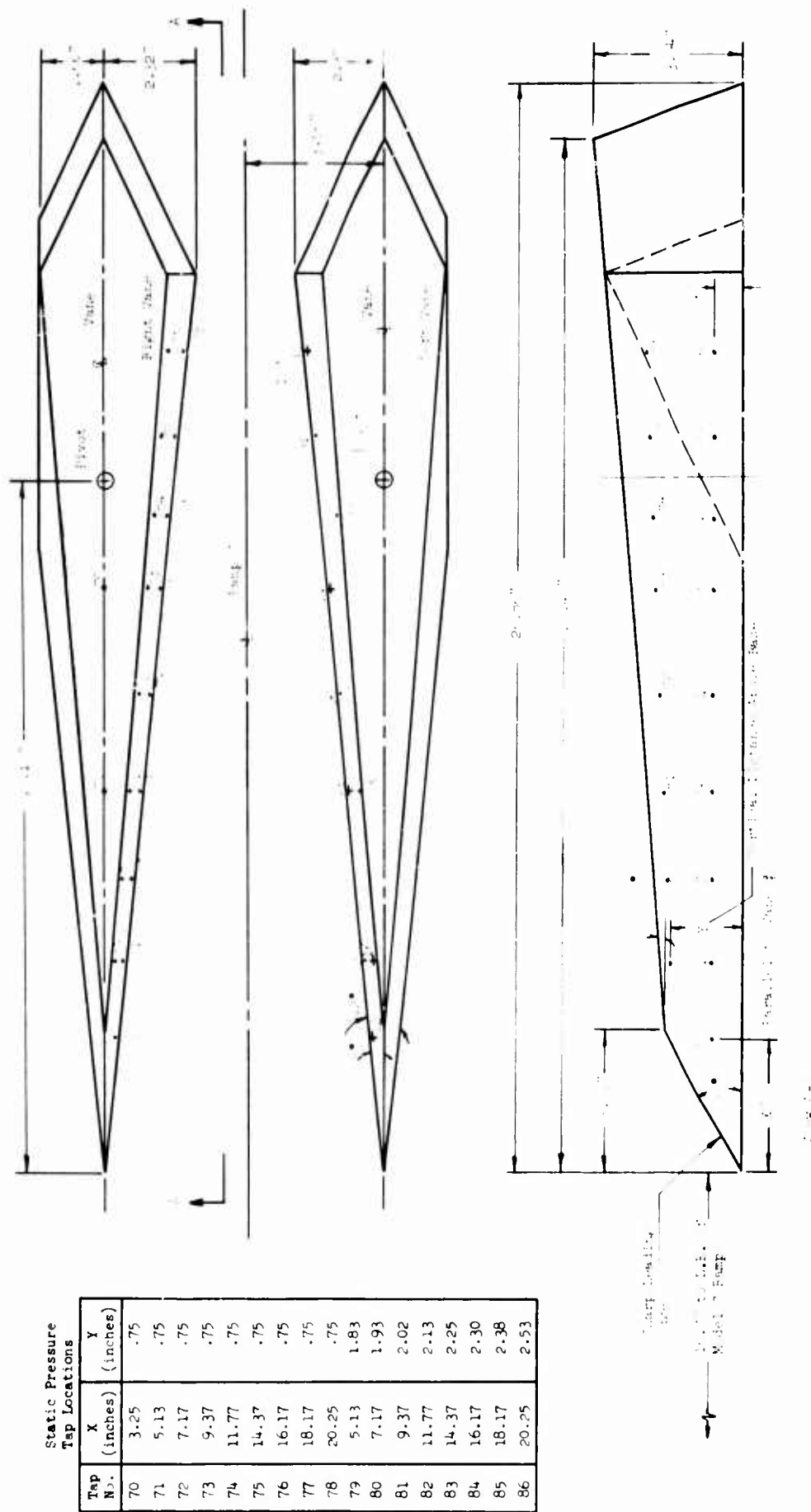


Figure 38 MODEL D VANE INSTRUMENTATION AND GEOMETRY

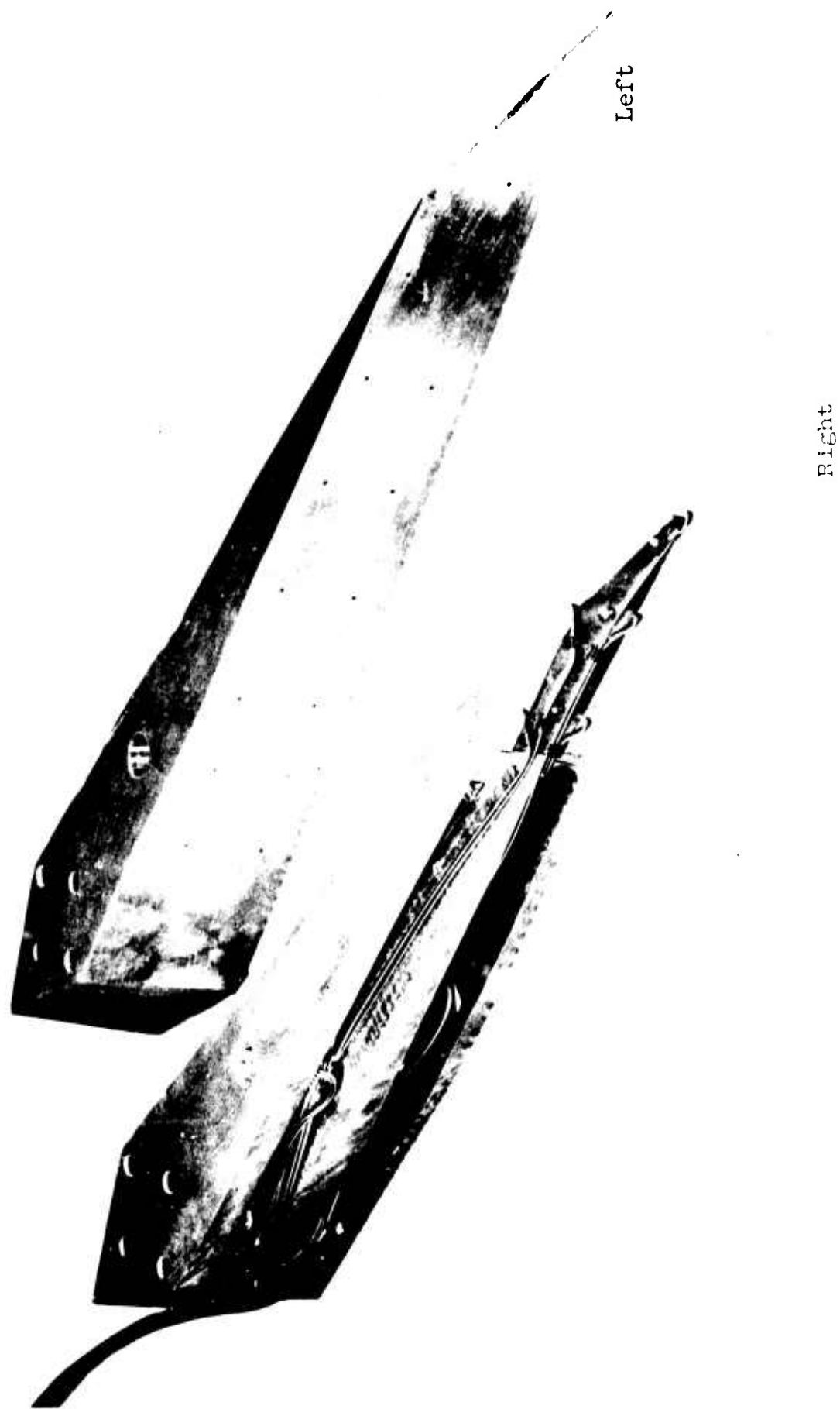


Figure 39 MODEL D VANE INSTRUMENTATION INSTALLATION





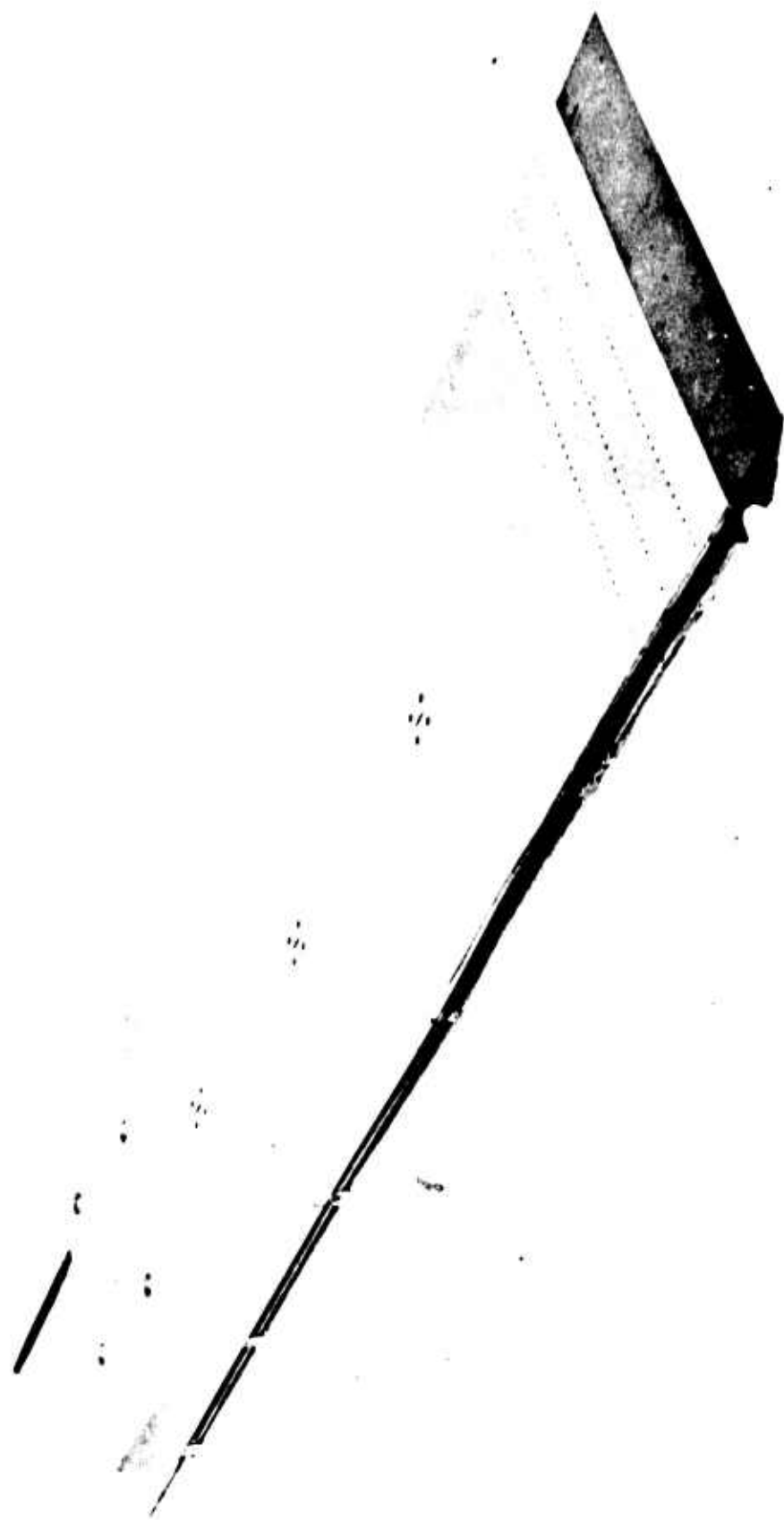
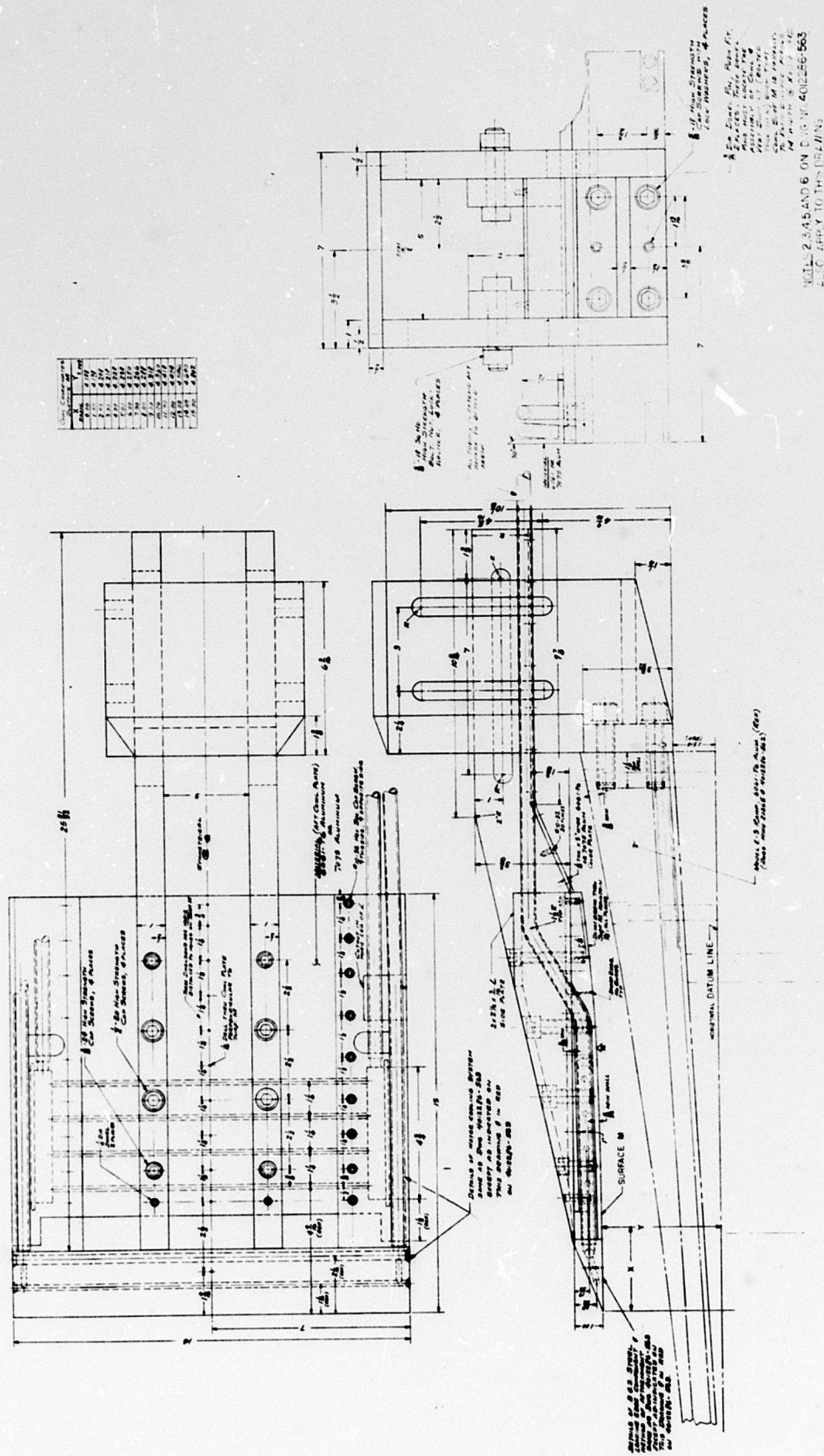
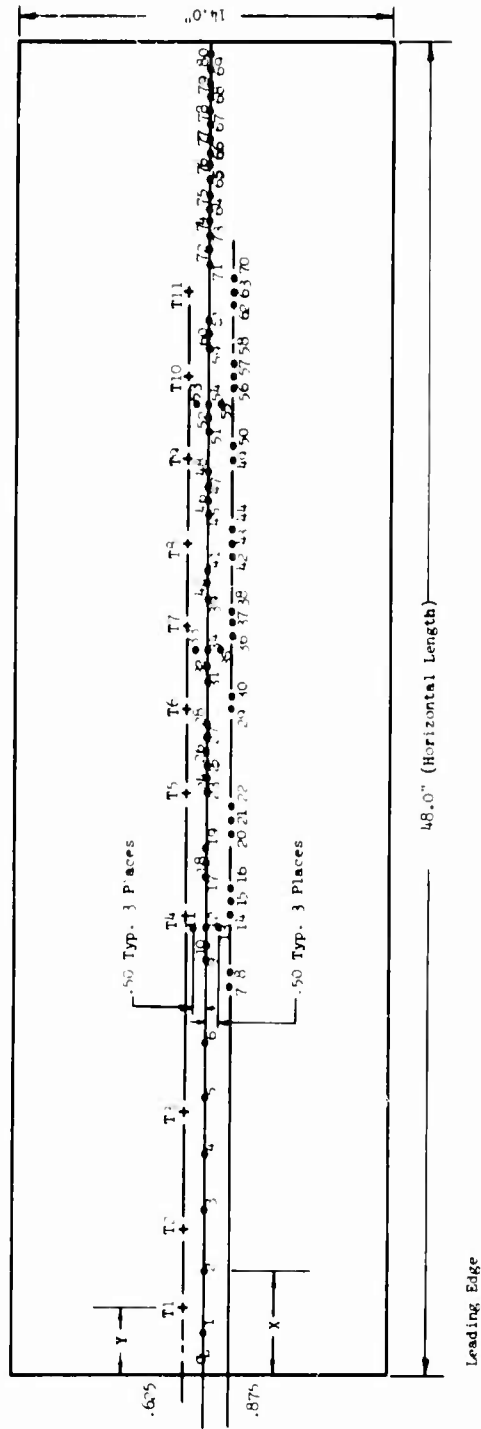


Figure 41 MODEL E-3 RAMP



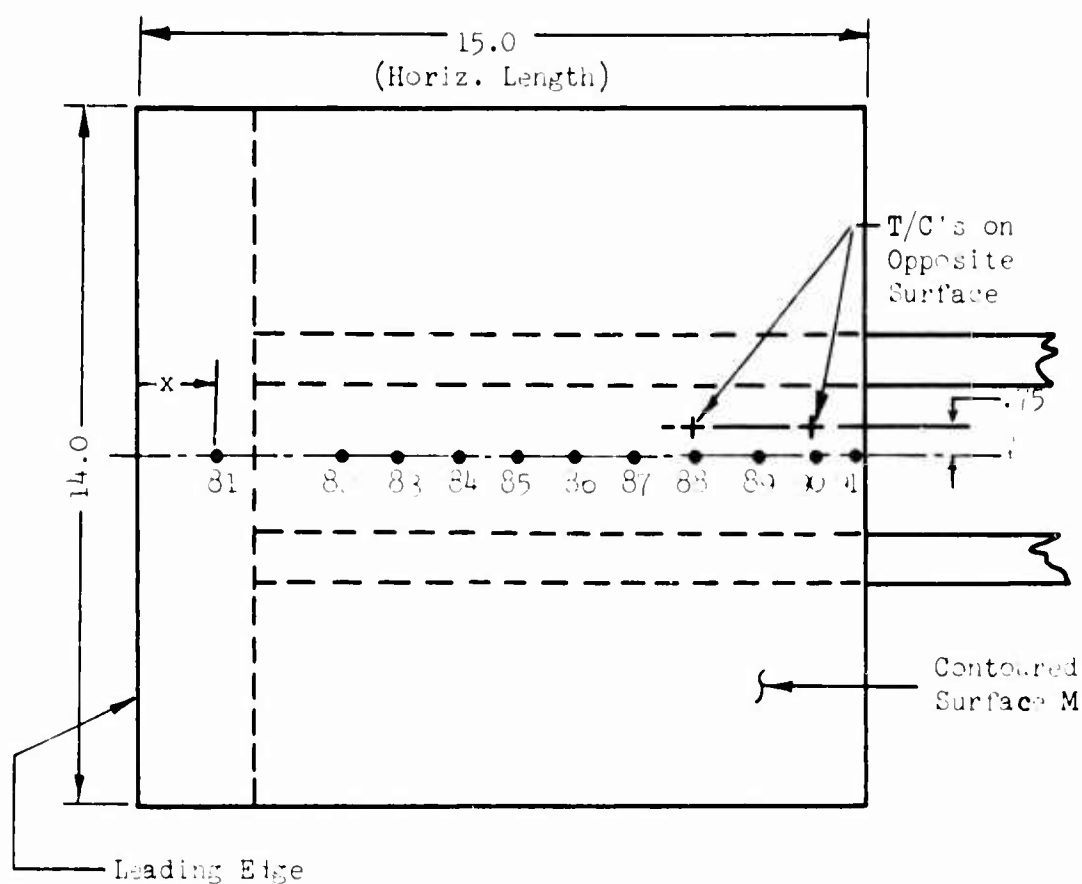
Ramp Static Pressure Tap Locations			
Tap No.	X (inches)	Tap No.	X (inches)
1	1.50	42	22.50
2	3.75	43	30.00
3	6.00	44	30.50
4	8.20	45	31.50
5	10.00	46	31.50
6	12.00	47	32.00
7	14.00	48	32.50
8	14.50	49	33.00
9	15.00	50	33.50
10	15.50	51	34.00
11, 12, 13	16.13	52	34.50
14	16.63	53, 54, 55	35.00
15	17.13	56	35.50
16	17.56	57	36.00
17	18.00	58	36.50
18	18.50	59	37.00
19	19.00	60	37.50
20	19.50	61	38.00
21	20.00	62	38.50
22	20.50	63	39.00
23	21.00	64	42.00
24	21.50	65	43.00
25	22.00	66	44.00
26	22.50	67	45.00
27	23.00	68	46.00
28	23.50	69	47.00
29	24.00	70	39.50
30	24.50	71	40.00
31	25.00	72	40.50
32	25.50	73	41.00
33, 34, 35	26.13	74	41.50
36	26.63	75	42.50
37	27.13	76	43.50
38	27.56	77	44.50
39	28.00	78	45.50
40	28.50	79	46.50
41	29.00	80	47.50

Ramp Thermocouple Locations										
T/C No.	1	2	3	4	5	6	7	8	9	10
Y (inches)	1.50	3.75	6.00	8.20	10.00	12.00	14.00	14.50	15.00	15.50



Note: X and Y Are Horizontal Distances From Ramp Leading Edge and Are Not Distances Along Ramp Surface

Figure 43 MODEL E-3 RAMP INSTRUMENTATION



Static Pressure  
Tap Locations

Tap No.	x (inches)
81	1.50
82	4.00
83	5.19
84	6.44
85	7.69
86	8.94
87	10.19
88	11.44
89	12.69
90	13.94
91	14.69

Note: x Is Horizontal Distance From Cowl Leading Edge and Is Not Distance Along Cowl Contoured Surface M

Figure 44 MODEL E-3 COWL INSTRUMENTATION



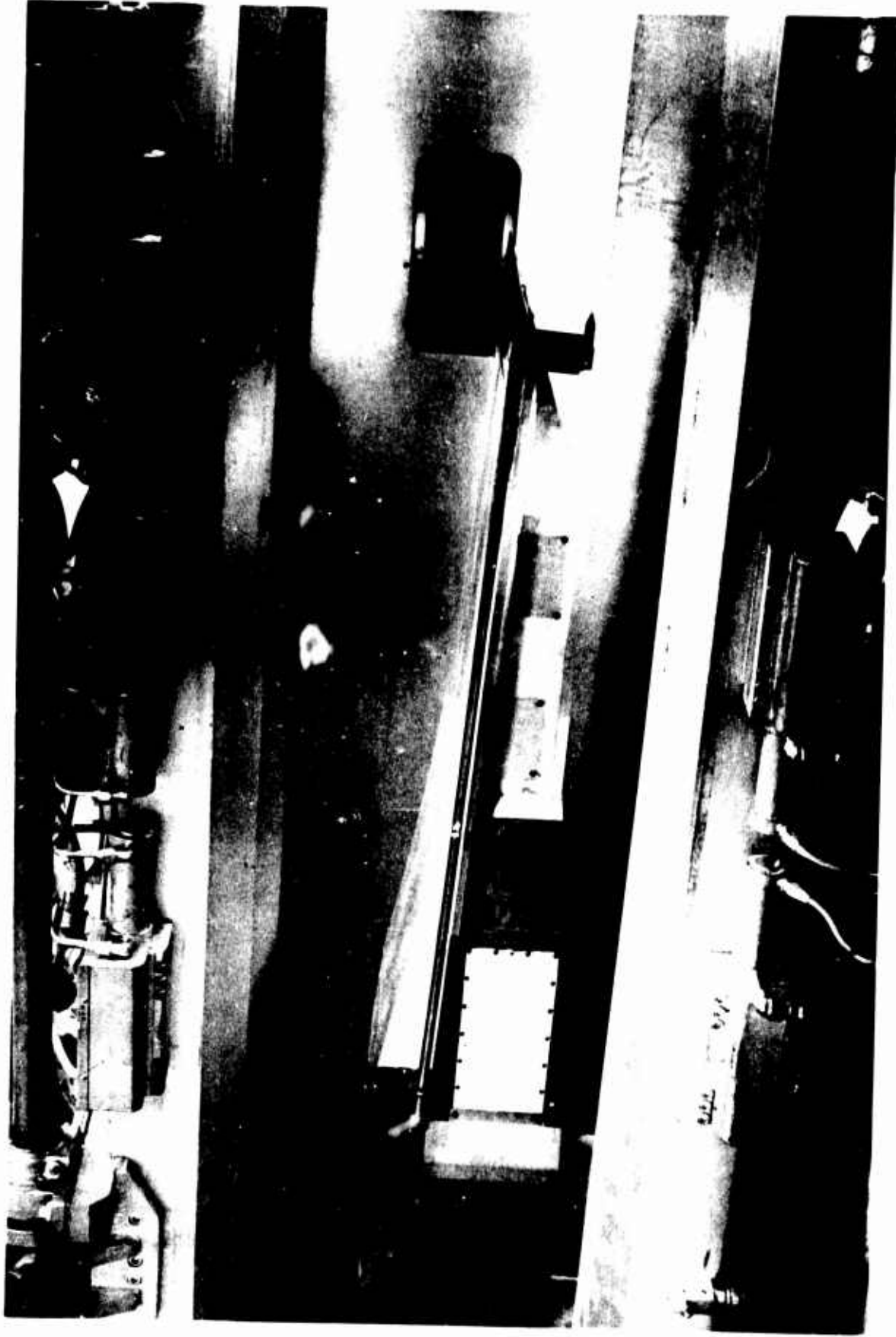


Figure 46    MODEL E-3 RAMP INSTALLATION

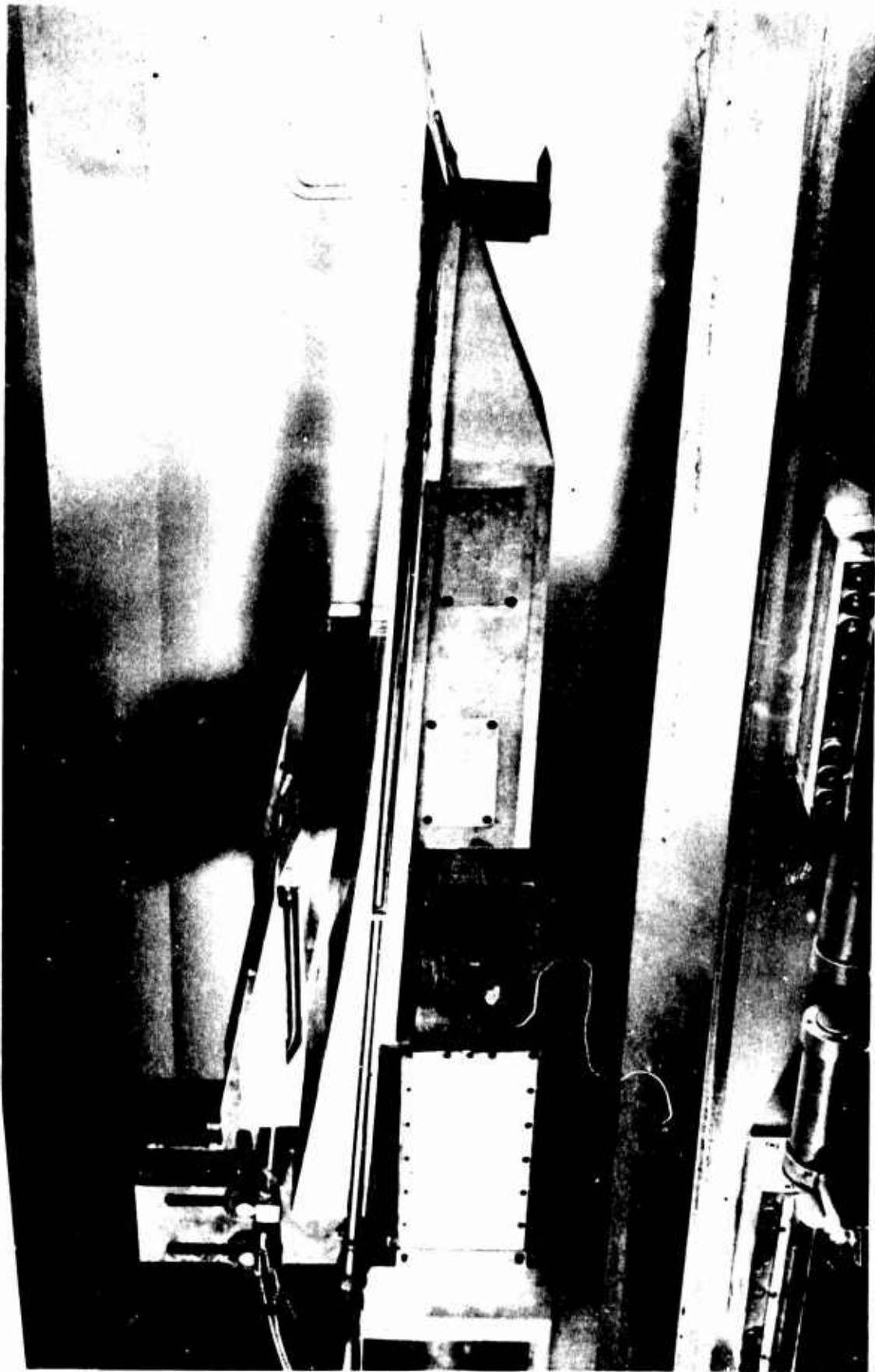


Figure 47    MODEL E-3 RAMP AND COWL INSTALLATION



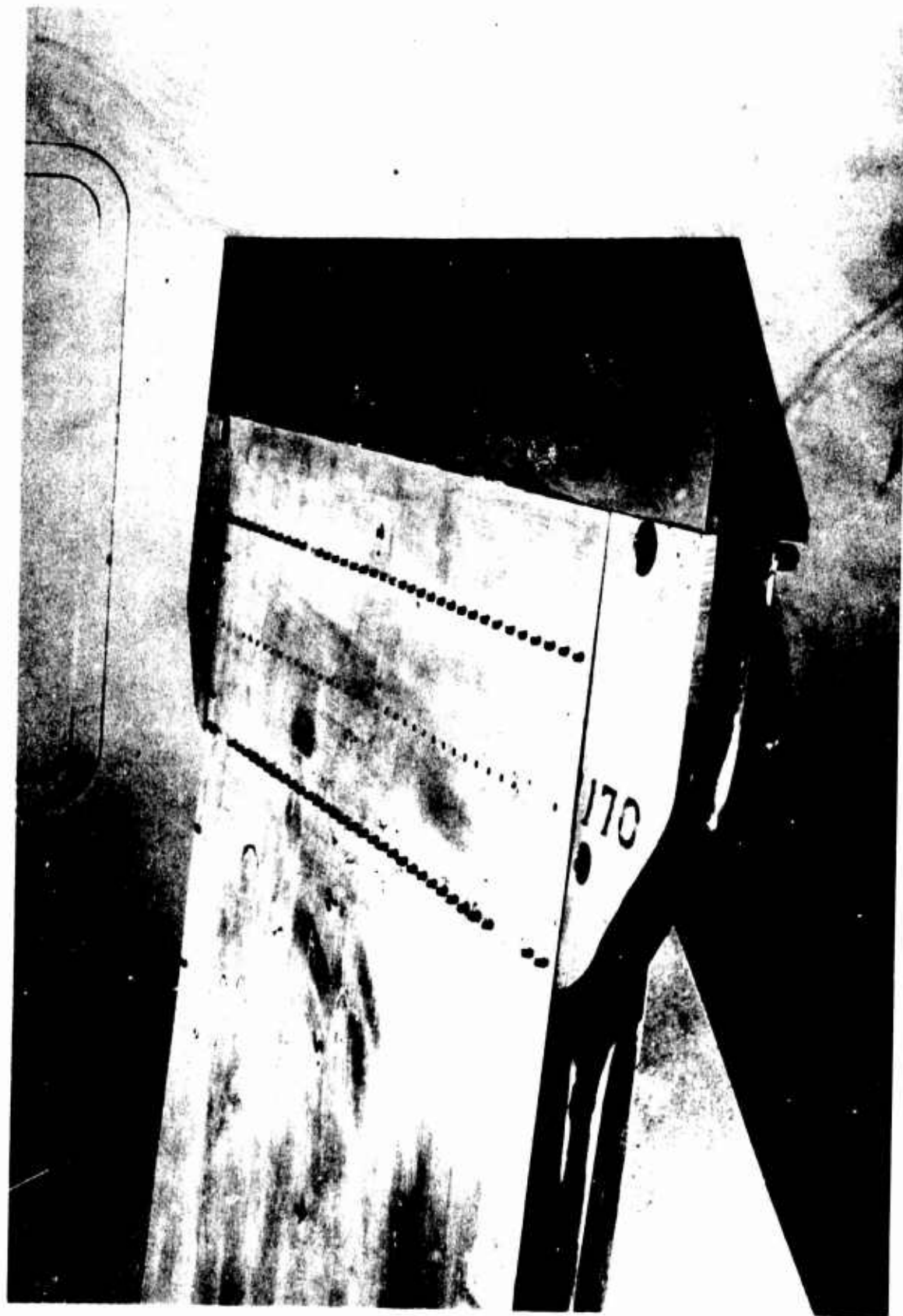


Figure 48 MODEL E-3 RAMP LEADING EDGE MODIFICATION

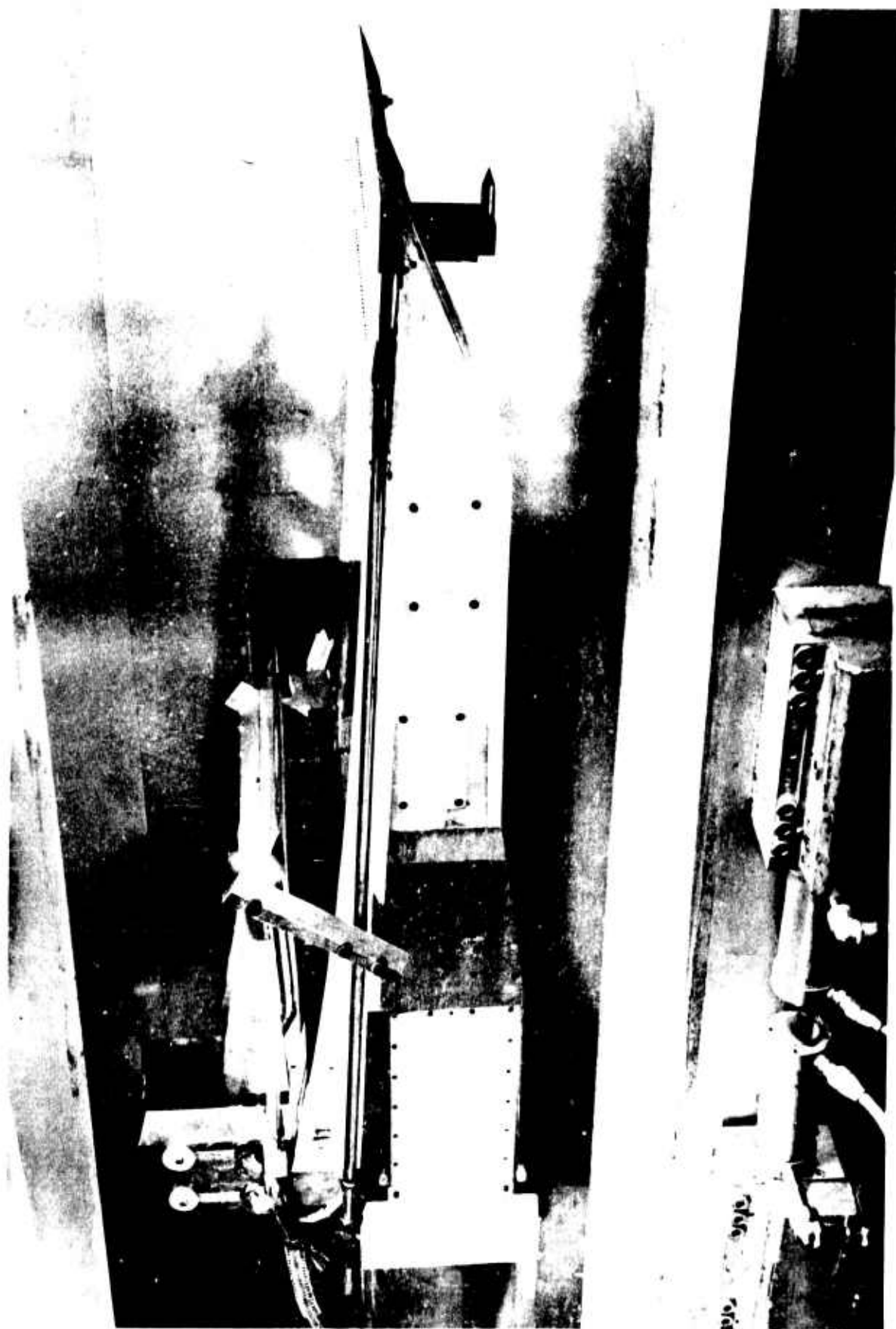


Figure 49      MODEL E-3 COWL SUPPORT STRUTS

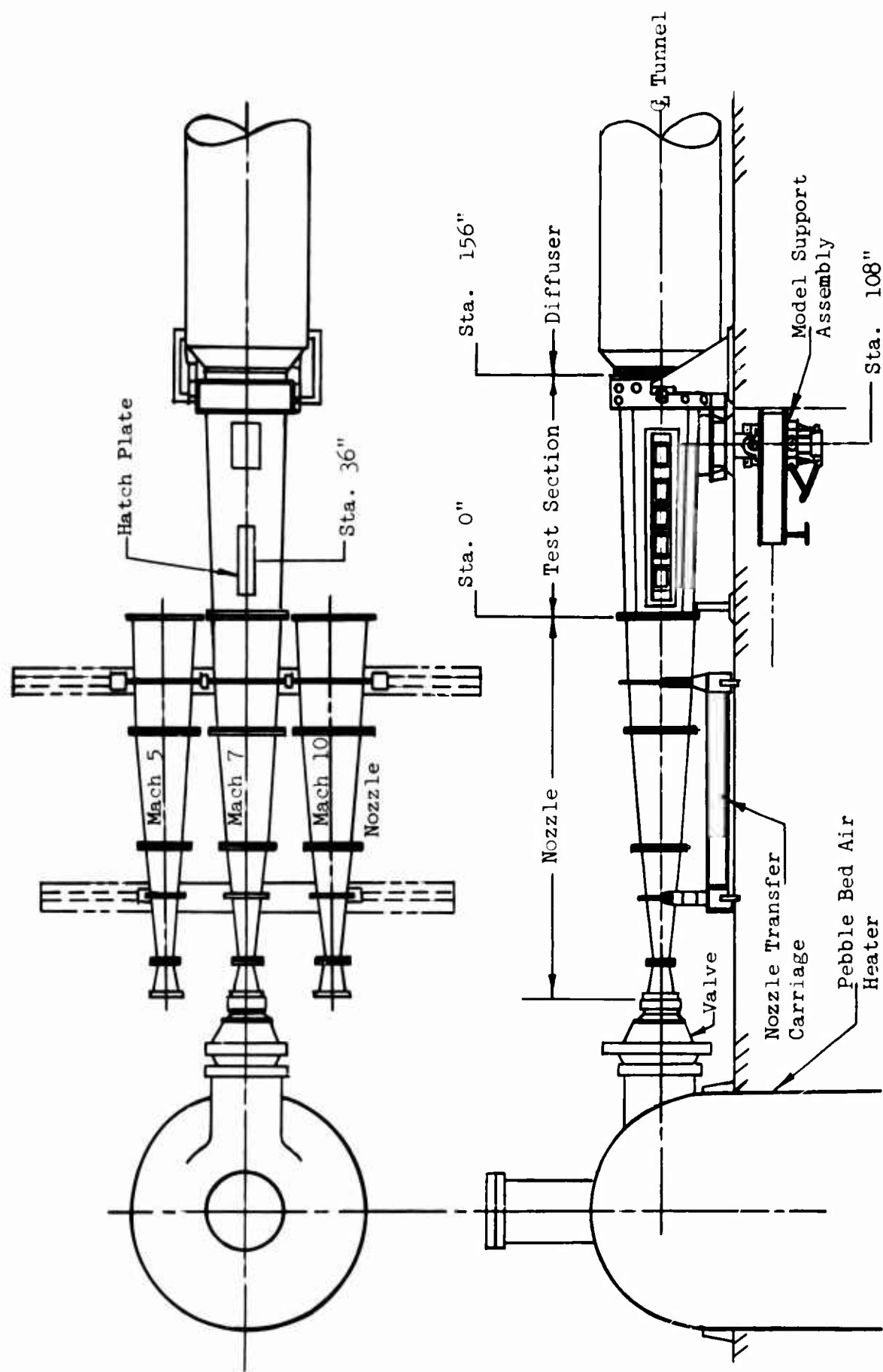


Figure 50 NASA-AMES 3.5 FOOT HYPERSONIC WIND TUNNEL

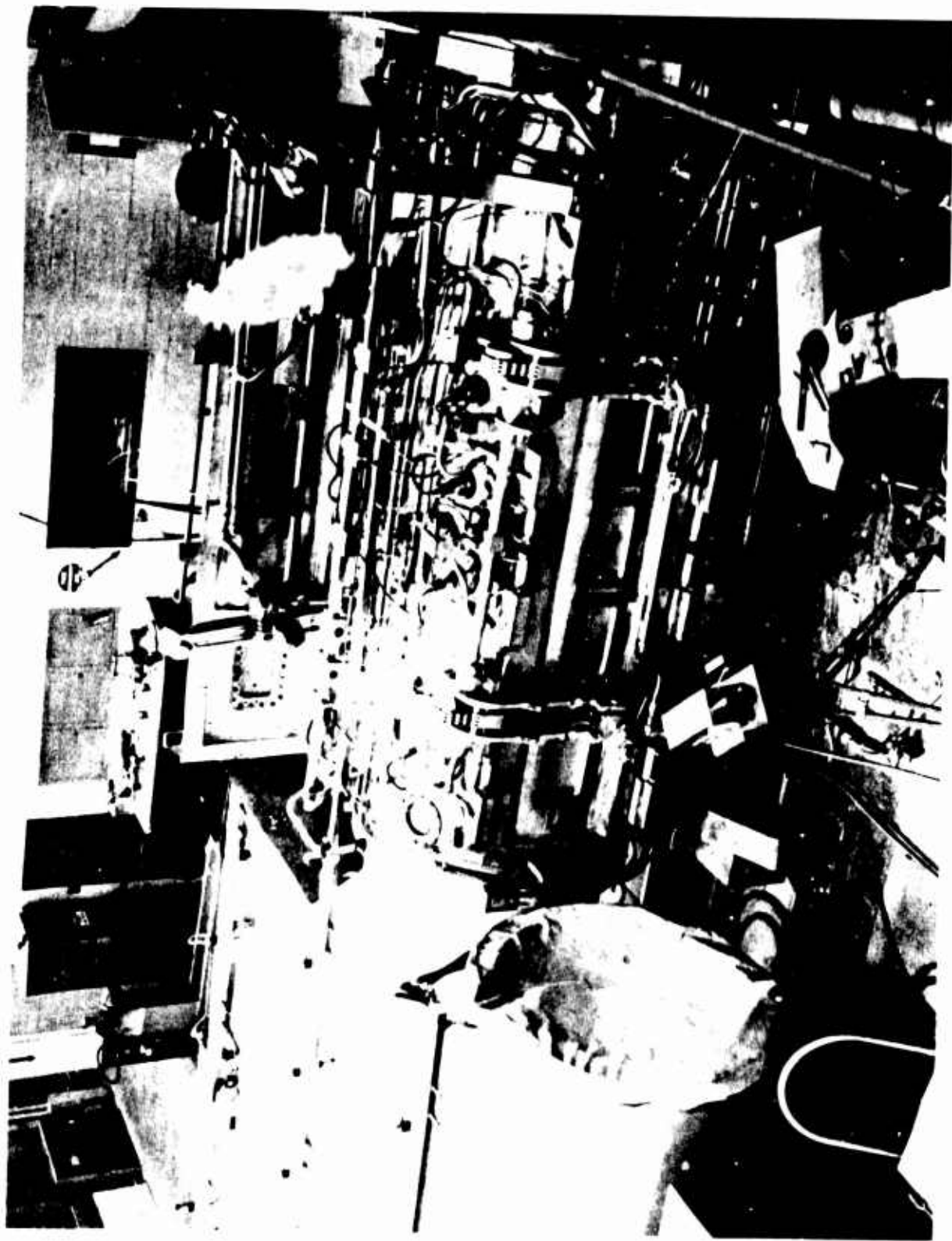
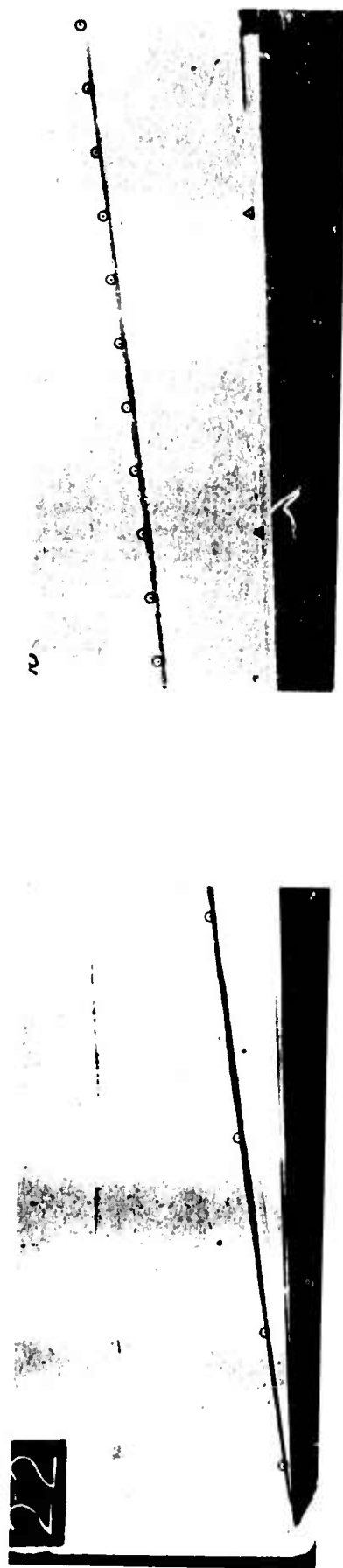


Figure 51    NASA-AMES 3.5 FOOT HYPERSONIC WIND TUNNEL  
TEST SECTION

# MODEL C

$$M_o = 10.55$$

$$Re_o = 2.0 \times 10^6 \text{ Ft}^{-1}$$



Run 22

Run 10

○ Shock Solution  
 Δ δ\* Solution

Figure 52 MODEL C SHOCK SHAPE COMPARISON

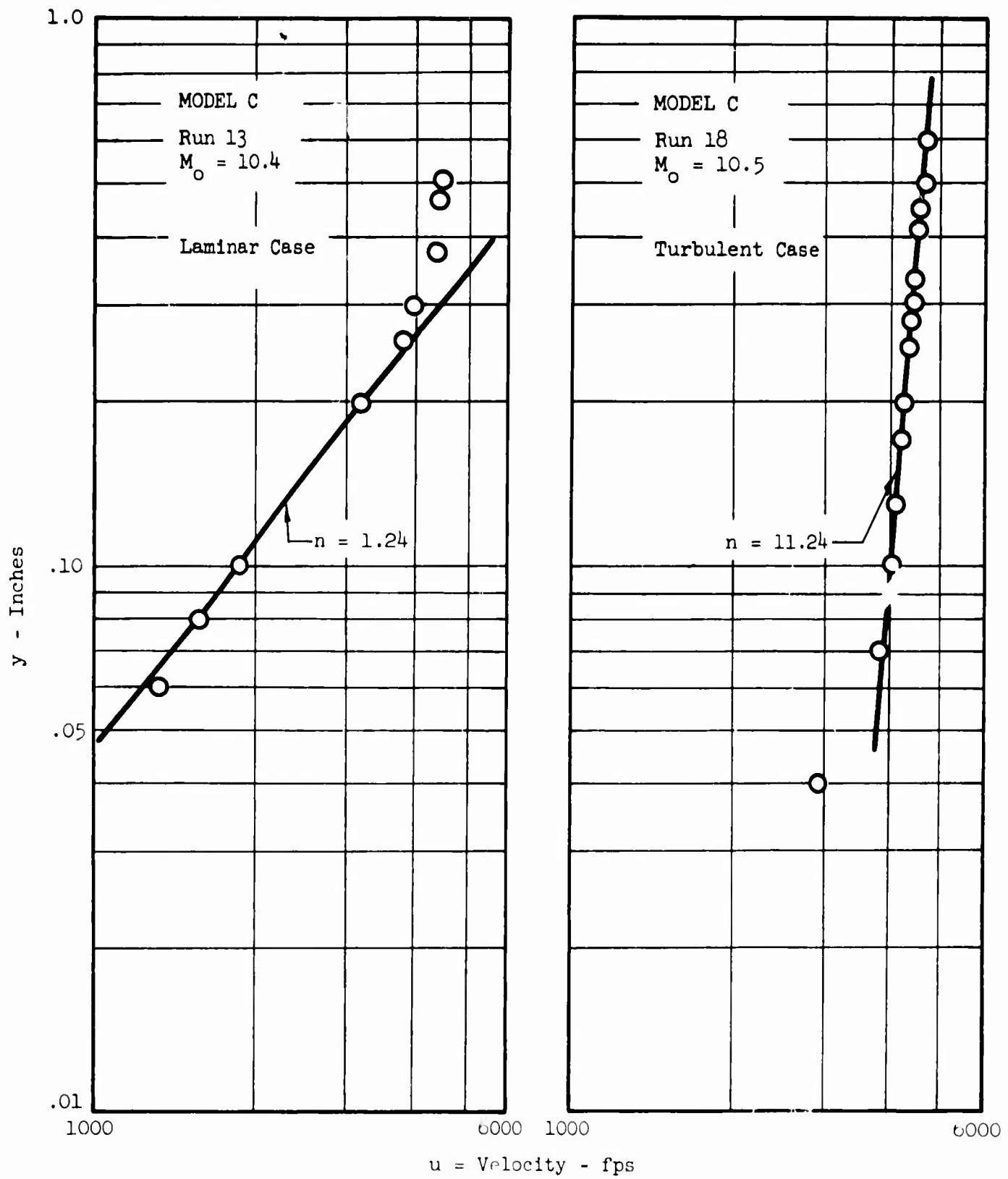


Figure 53 POWER LAW PROFILE DATA REPRESENTATION

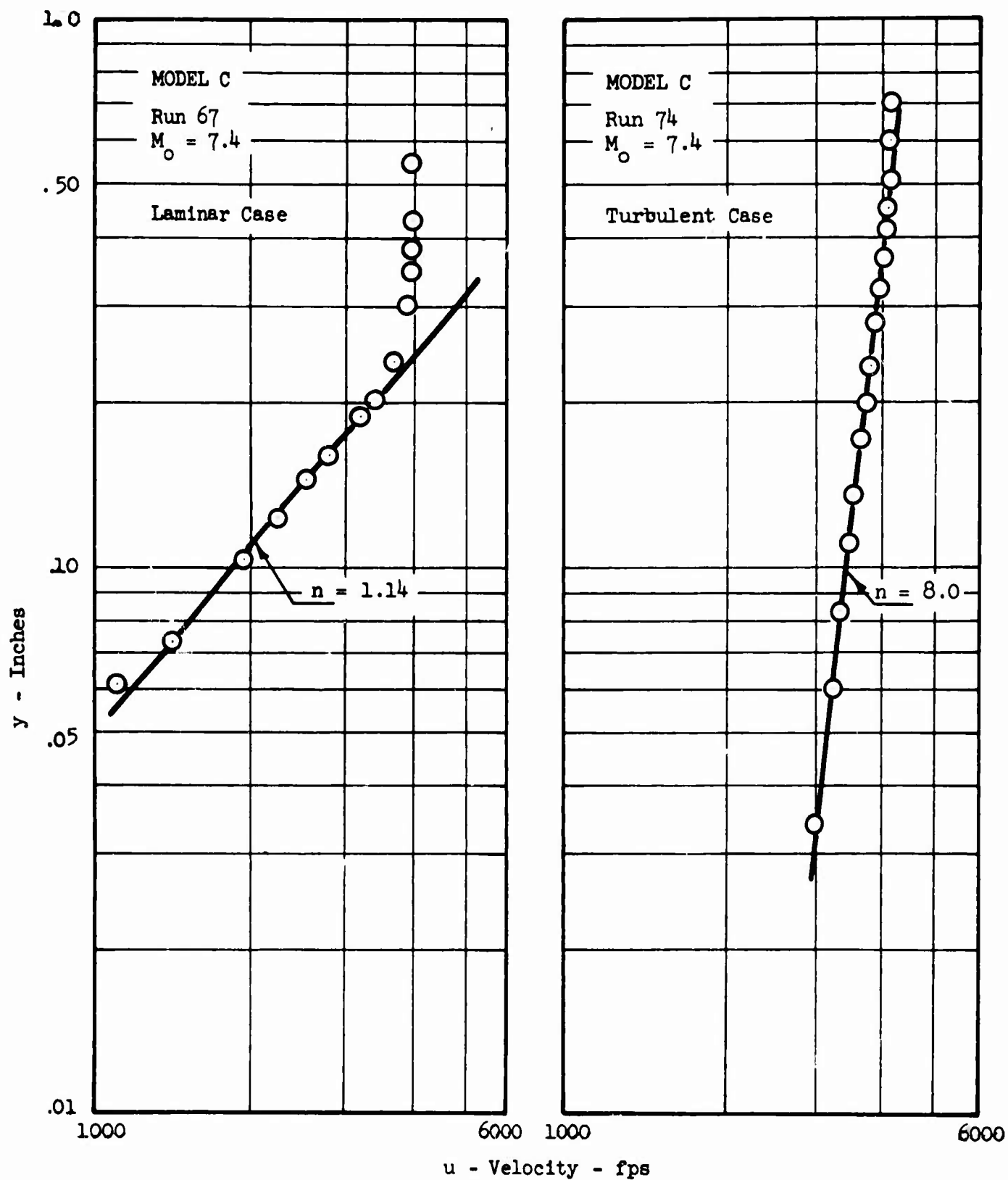


Figure 54 POWER LAW PROFILE DATA REPRESENTATION

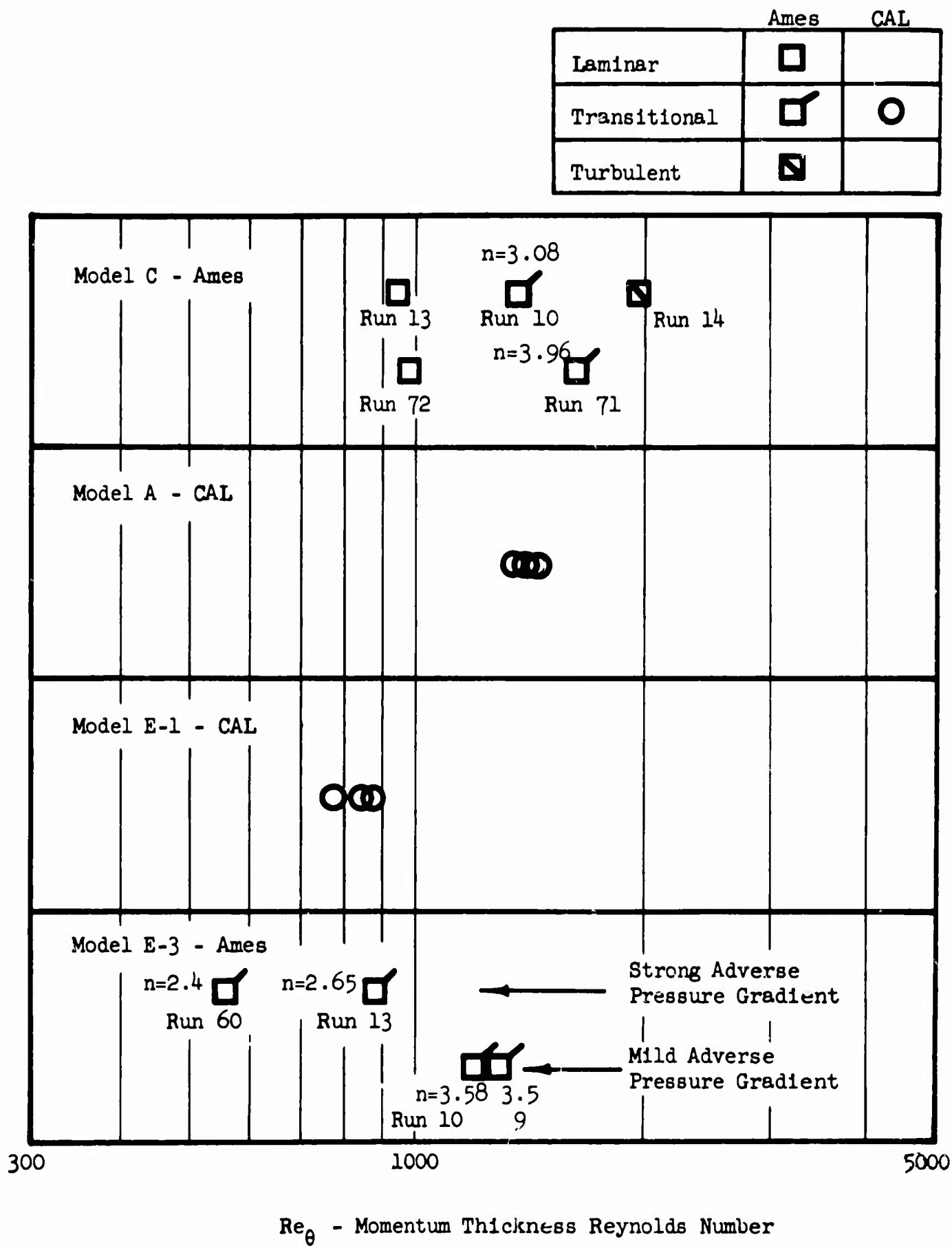


Figure 55 BOUNDARY LAYER TRANSITION CHARACTERISTICS



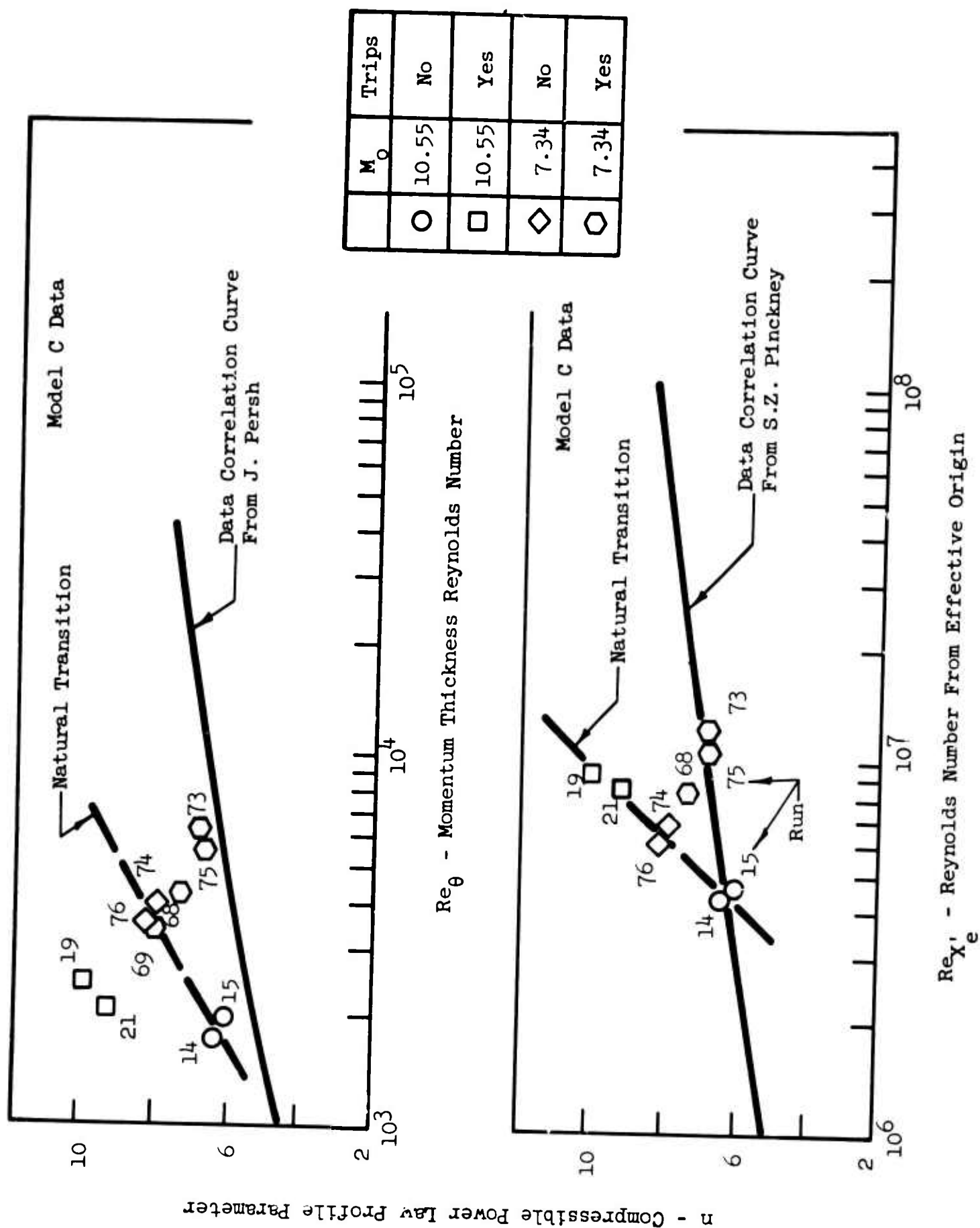
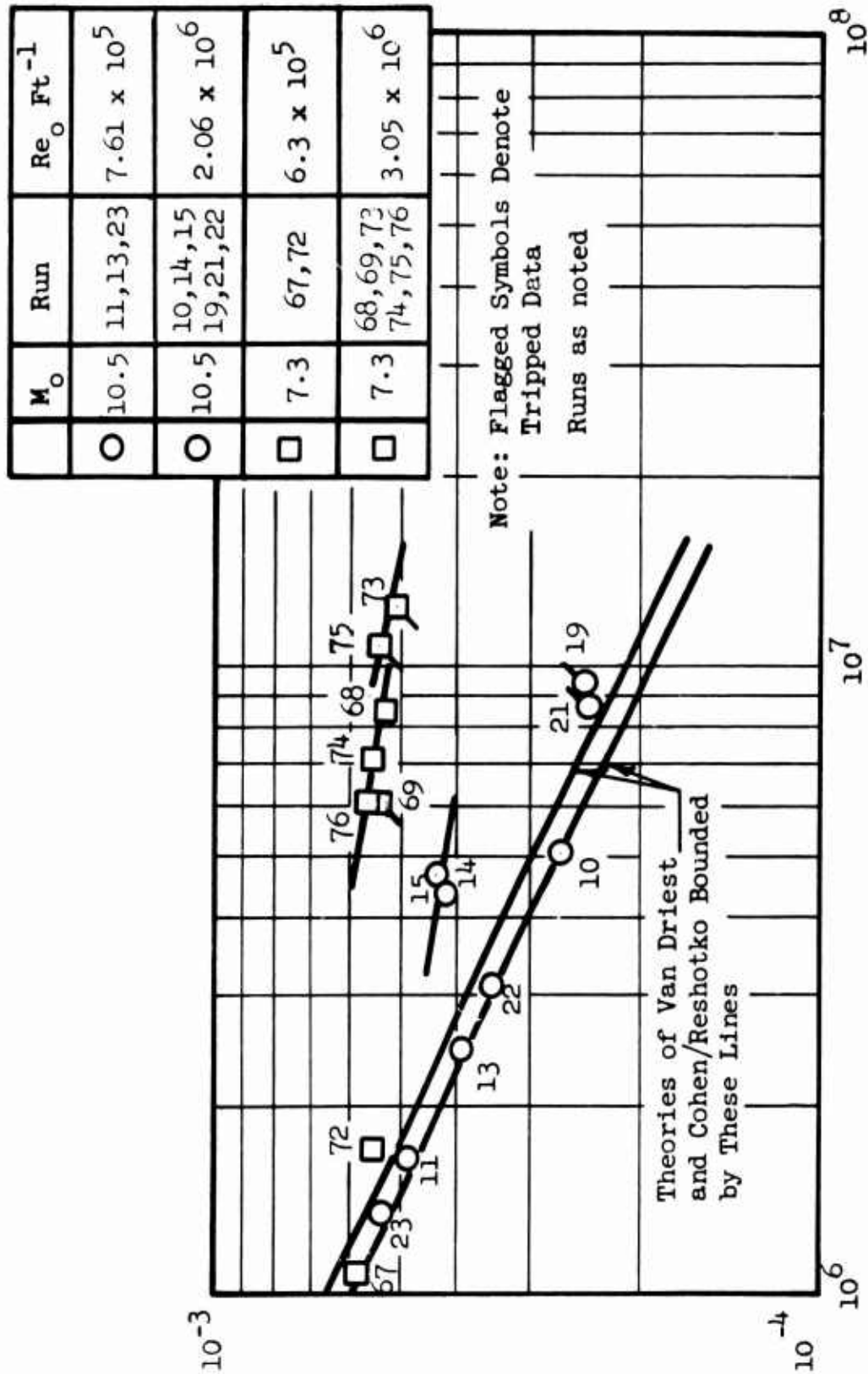


Figure 56 POWER LAW PROFILE AS A FUNCTION OF REYNOLDS NUMBER

$\theta/X'$  - Momentum Thickness/Effective Length



$Re_{X'_e}$  - Effective Reynolds Number

Figure 57 THEORY/DATA COMPARISON OF MOMENTUM THICKNESS

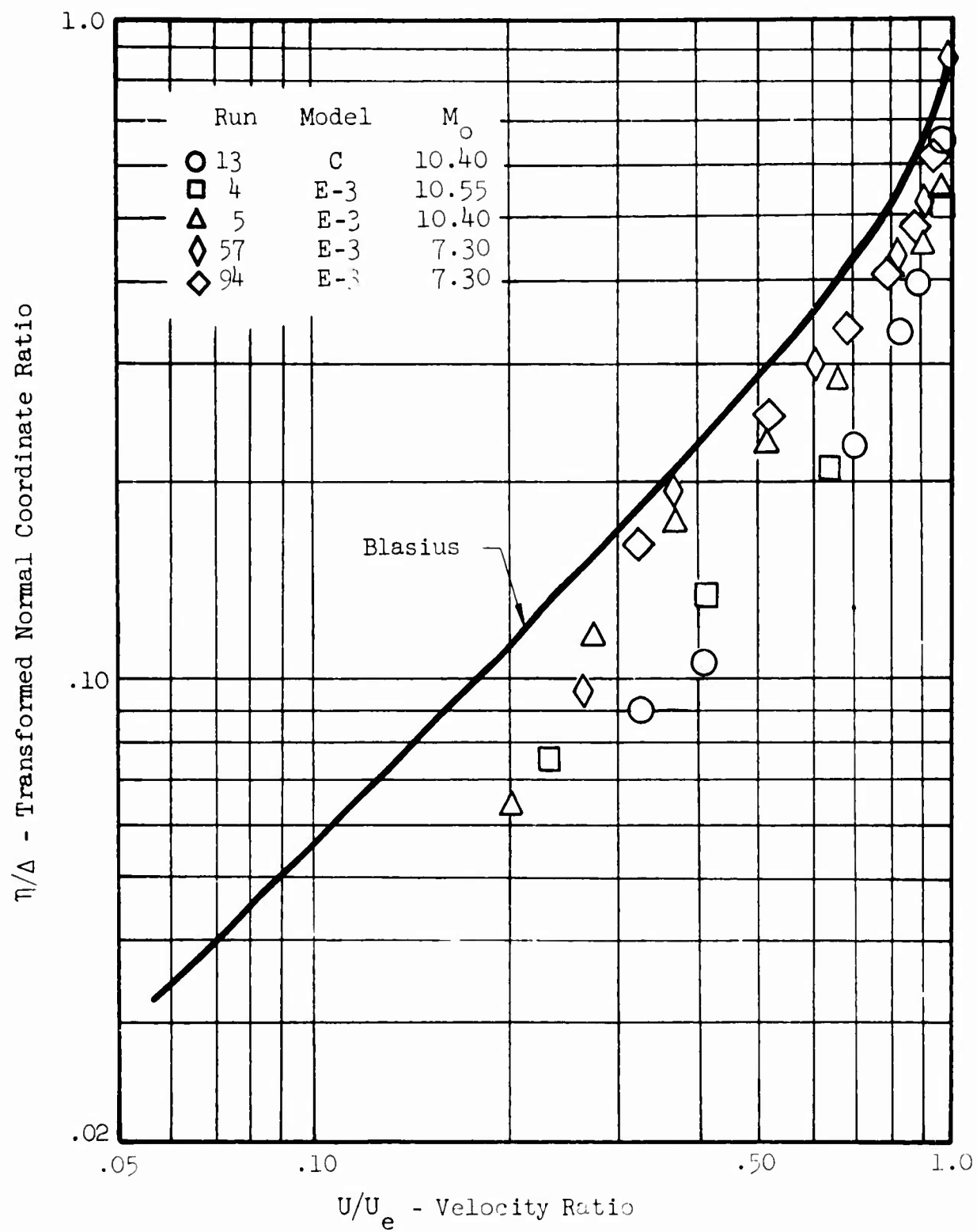


Figure 58 LAMINAR PROFILE THEORY/DATA COMPARISON

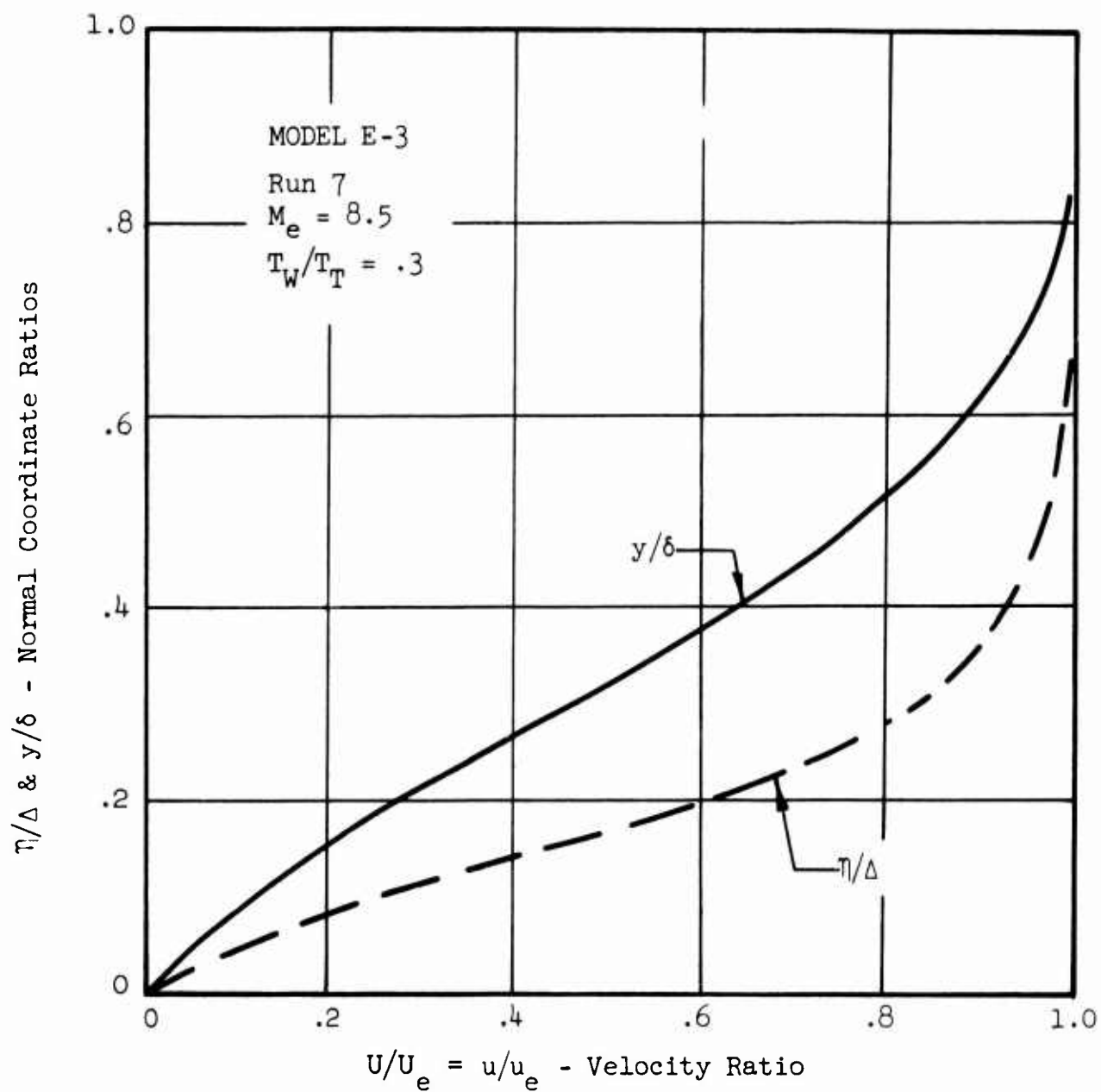


Figure 59 LAMINAR INCOMPRESSIBLE/COMPRESSIBLE  
PROFILE COMPARISON

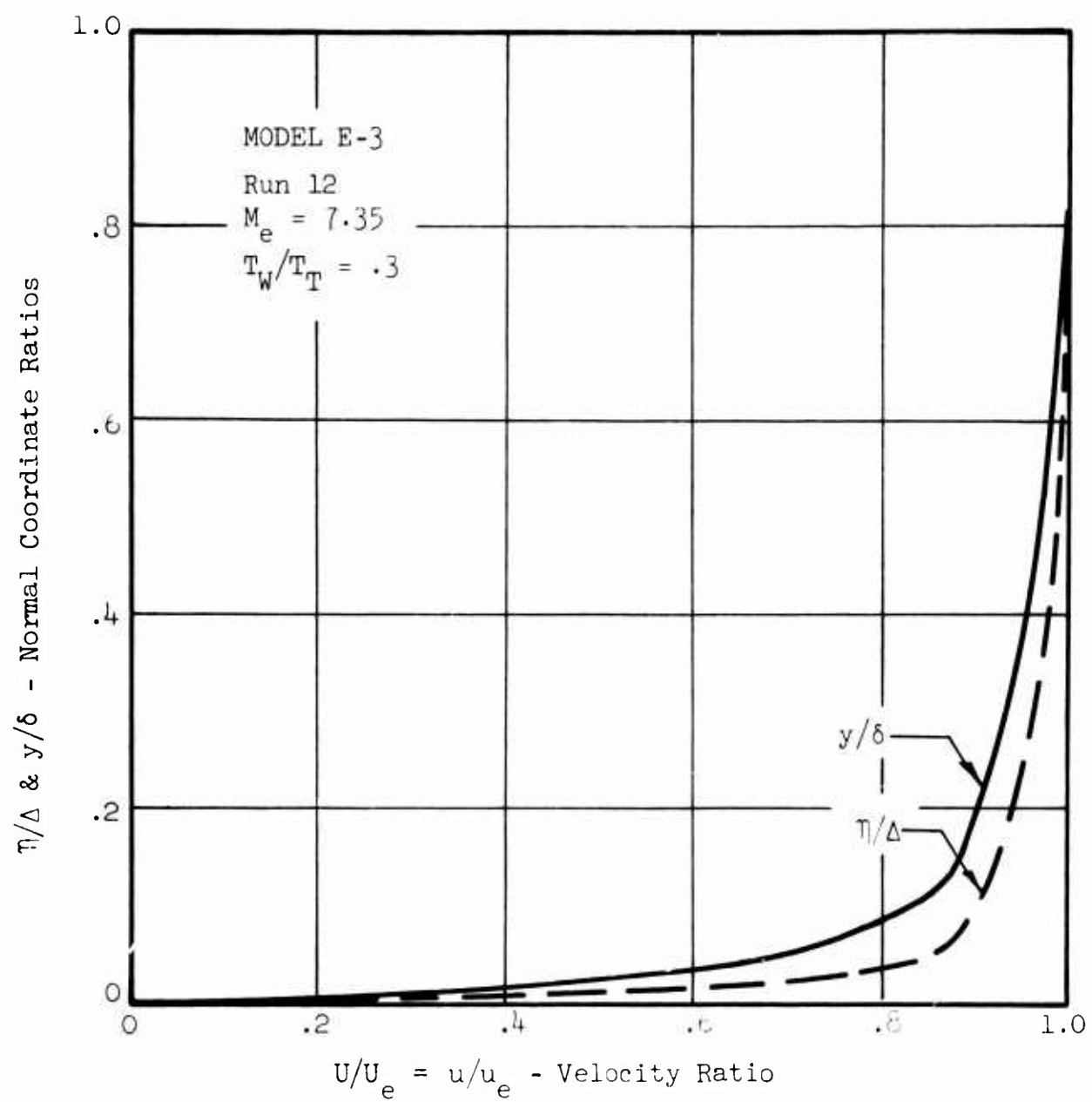


Figure 60      TURBULENT INCOMPRESSIBLE/COMPRESSIBLE  
PROFILE COMPARISON

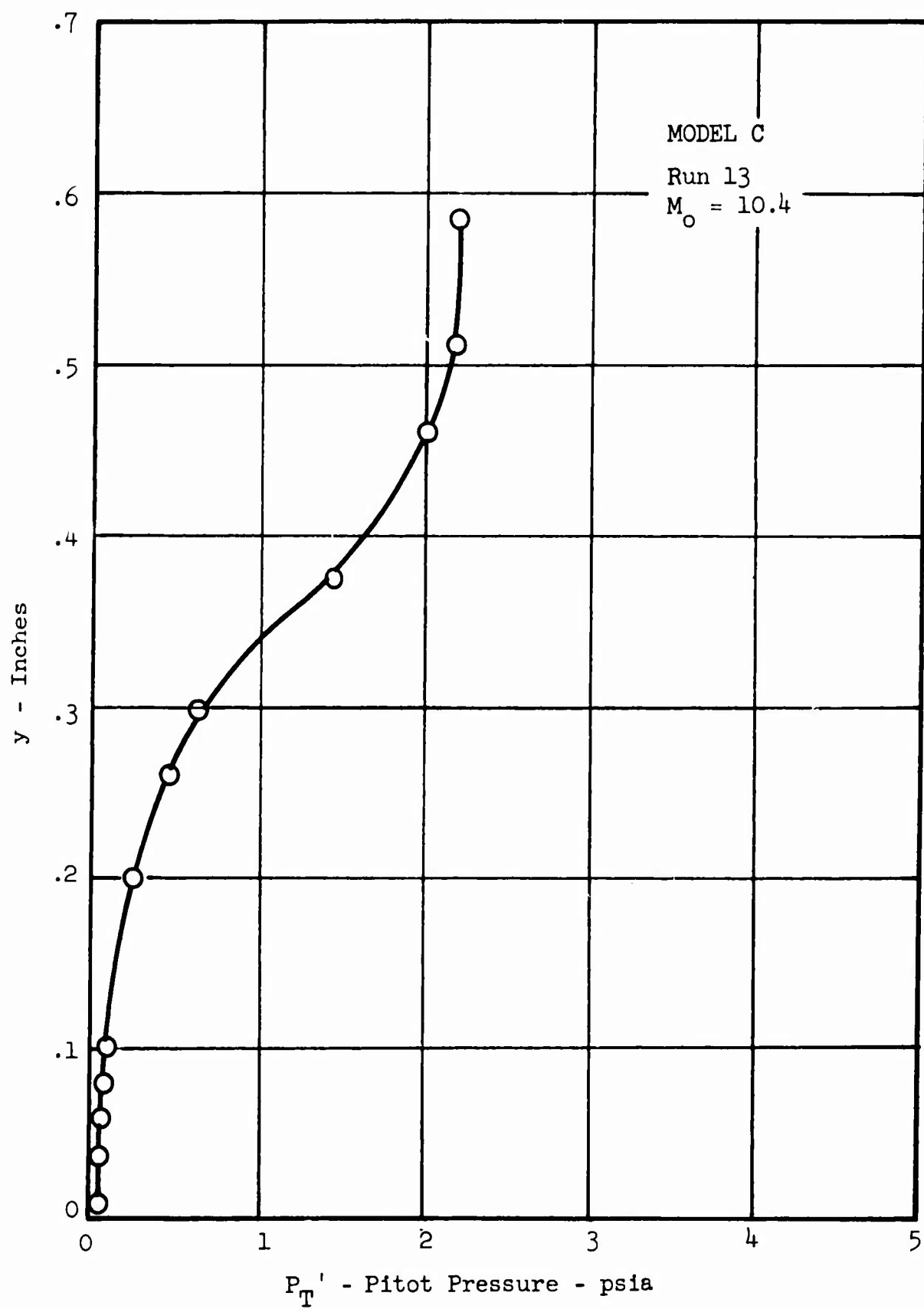


Figure 61 TYPICAL LAMINAR PITOT PRESSURE PROFILE

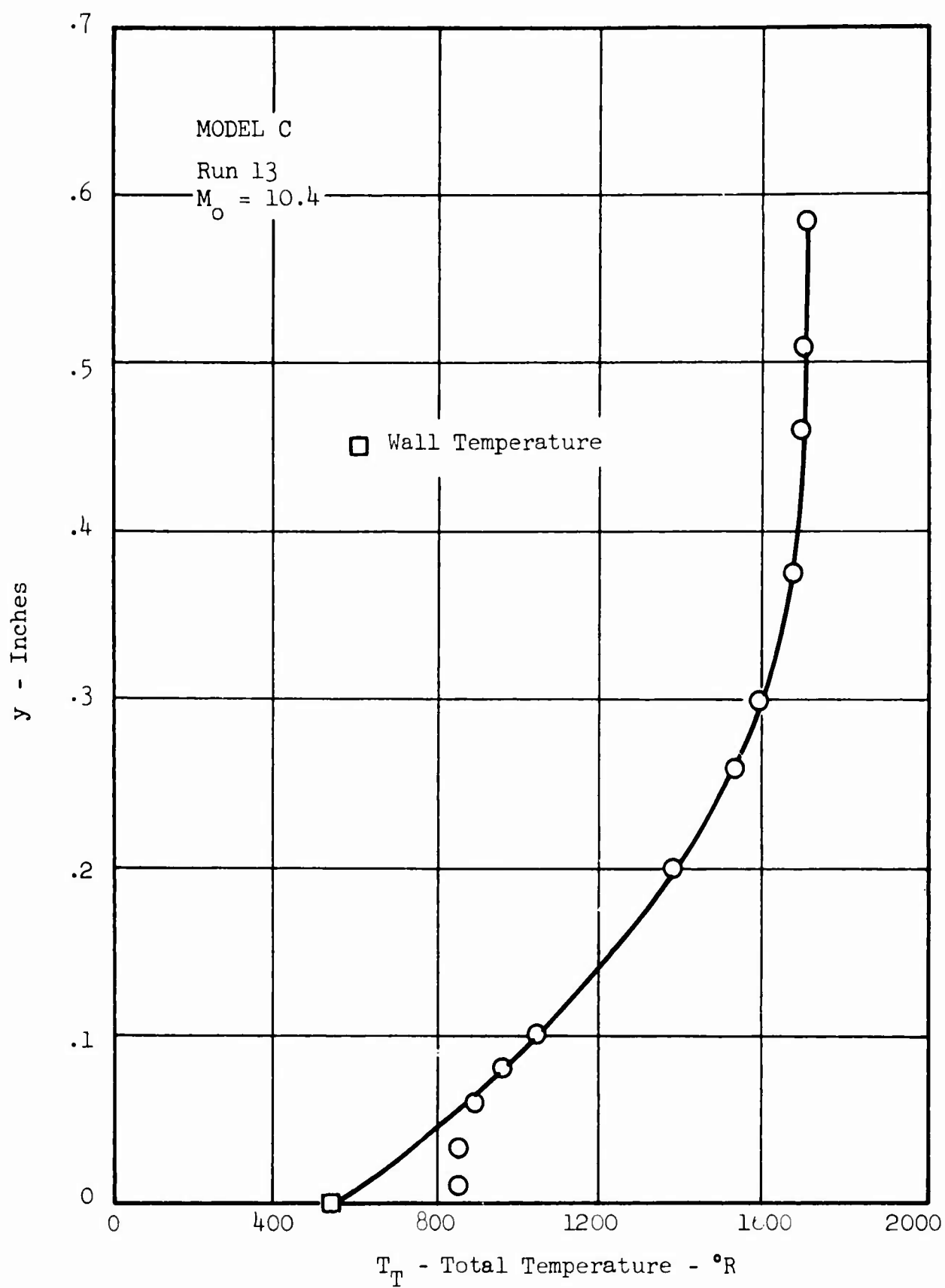


Figure 62 TYPICAL LAMINAR TOTAL TEMPERATURE PROFILE

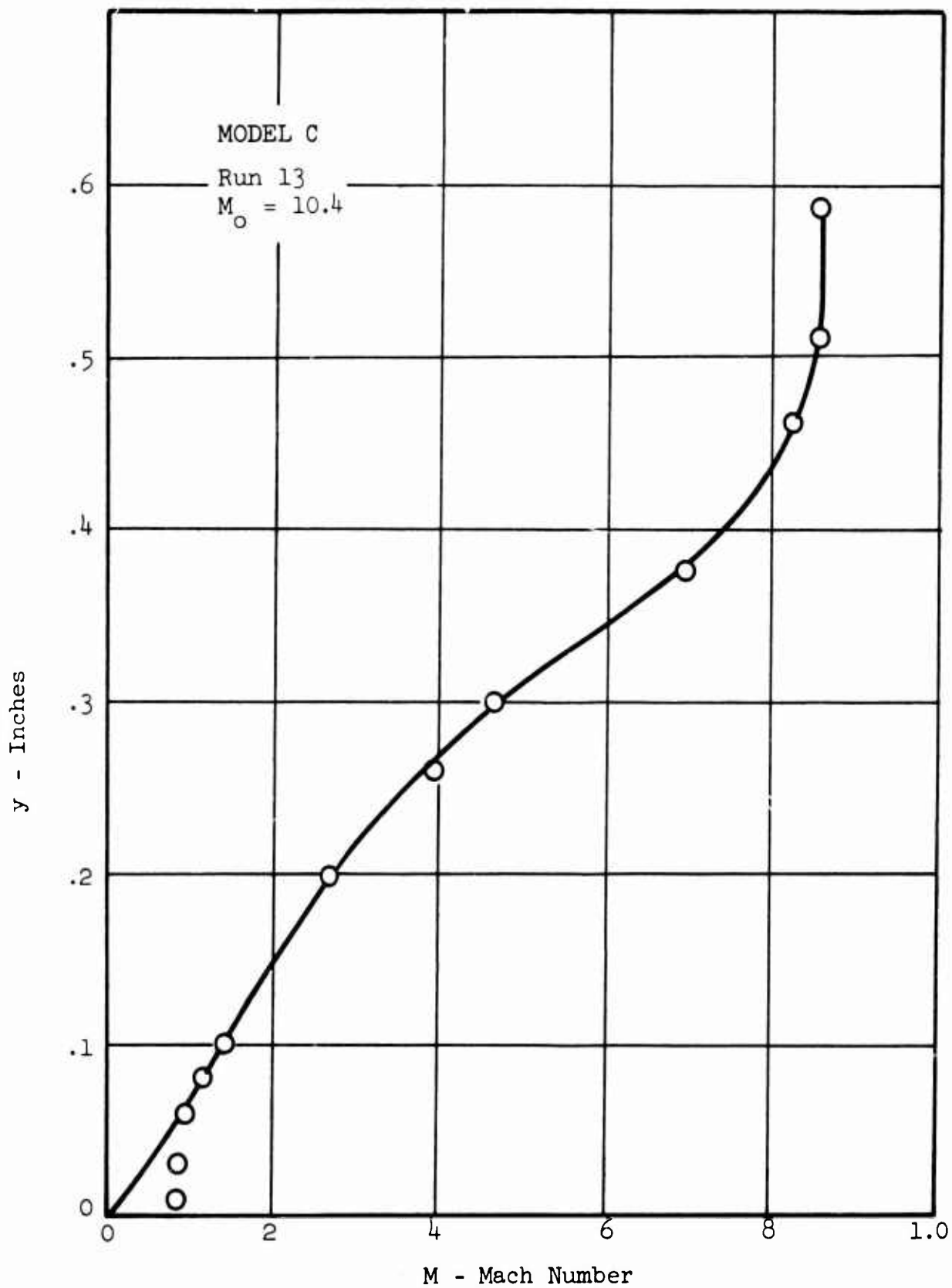


Figure 63 TYPICAL LAMINAR MACH NUMBER PROFILE



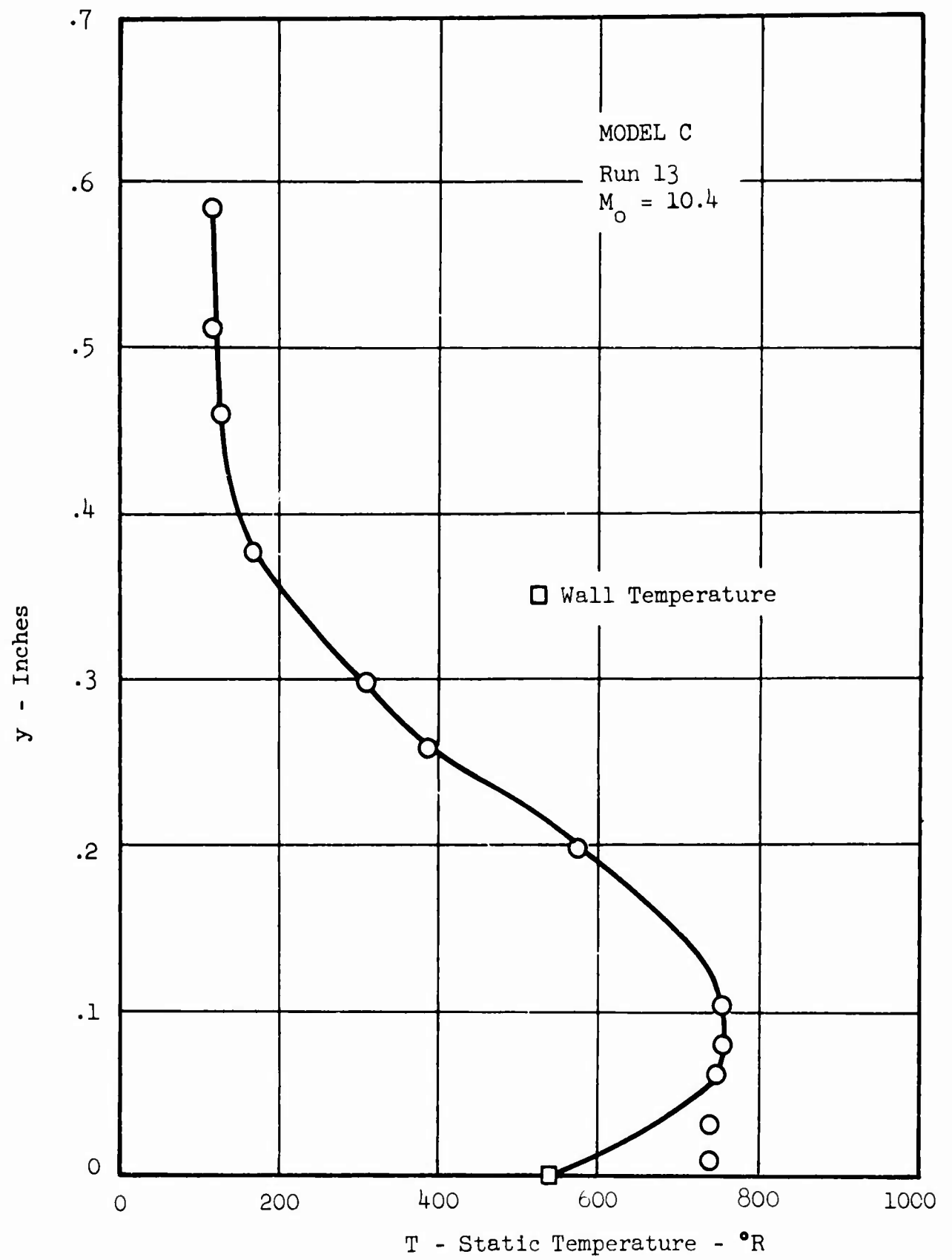


Figure 64 TYPICAL LAMINAR STATIC TEMPERATURE PROFILE

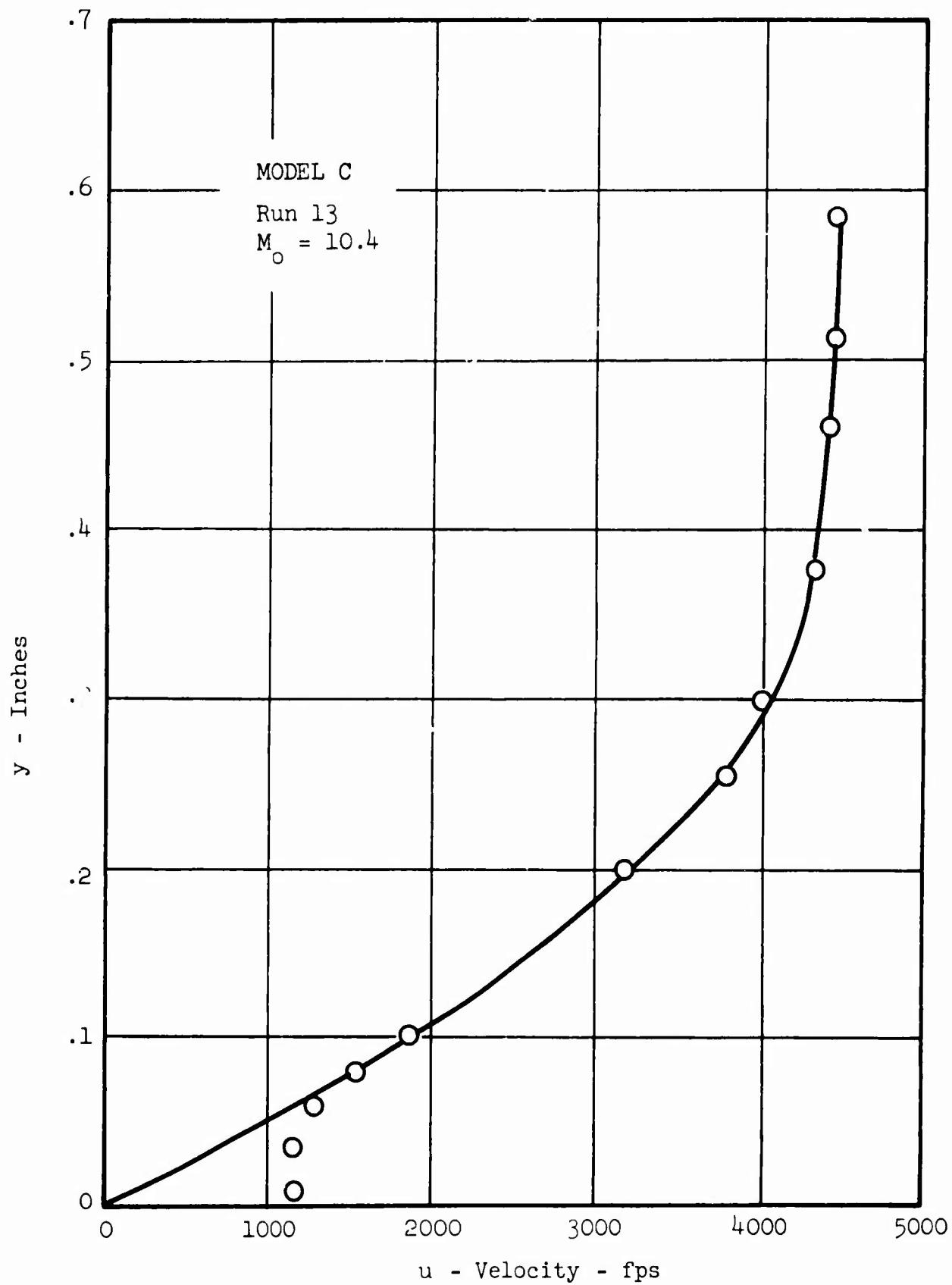


Figure 65 TYPICAL LAMINAR VELOCITY PROFILE

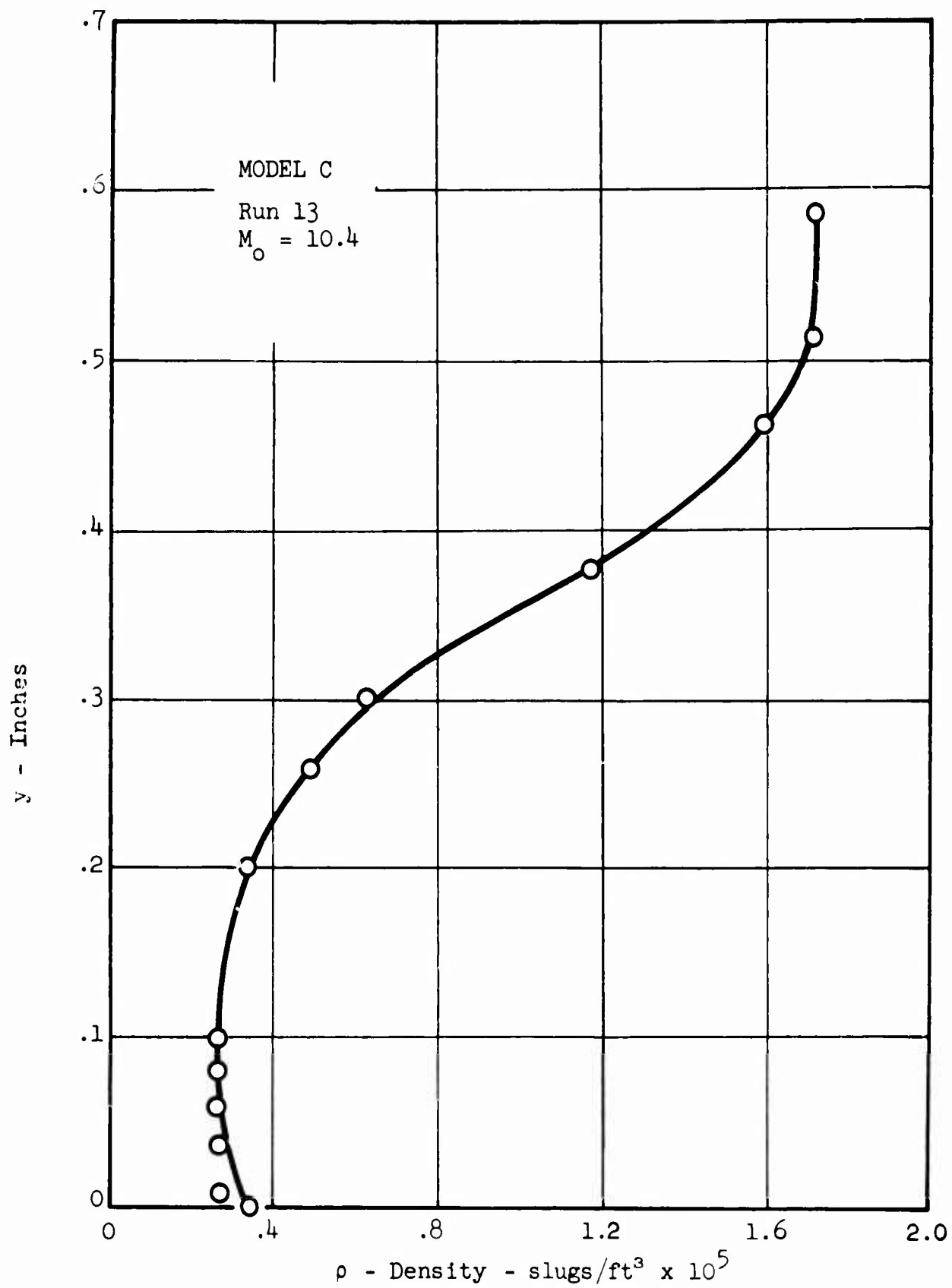


Figure 66 TYPICAL LAMINAR DENSITY PROFILE

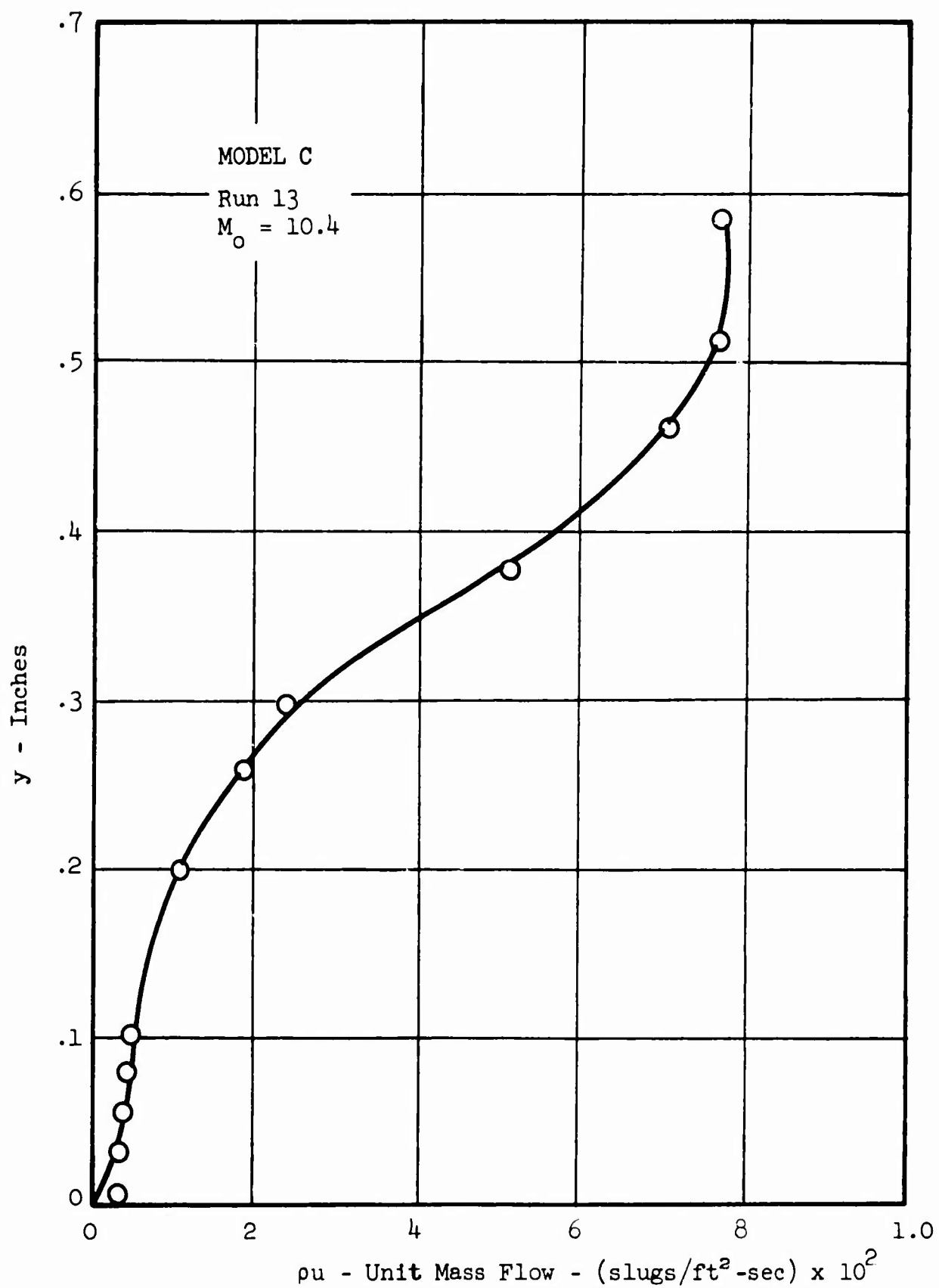


Figure 67 TYPICAL LAMINAR UNIT MASS FLOW PROFILE

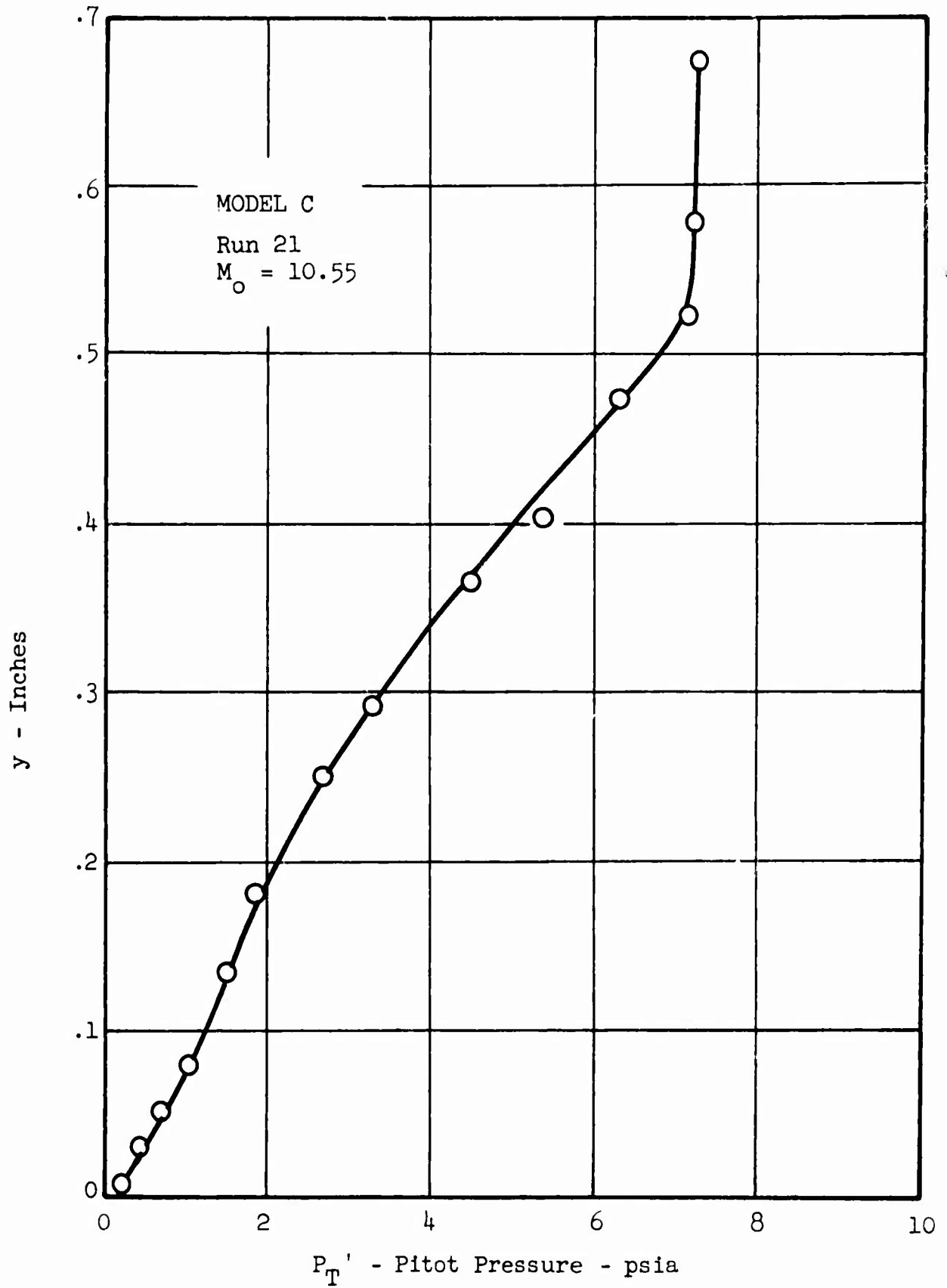


Figure 68 TYPICAL TURBULENT PITOT PRESSURE PROFILE

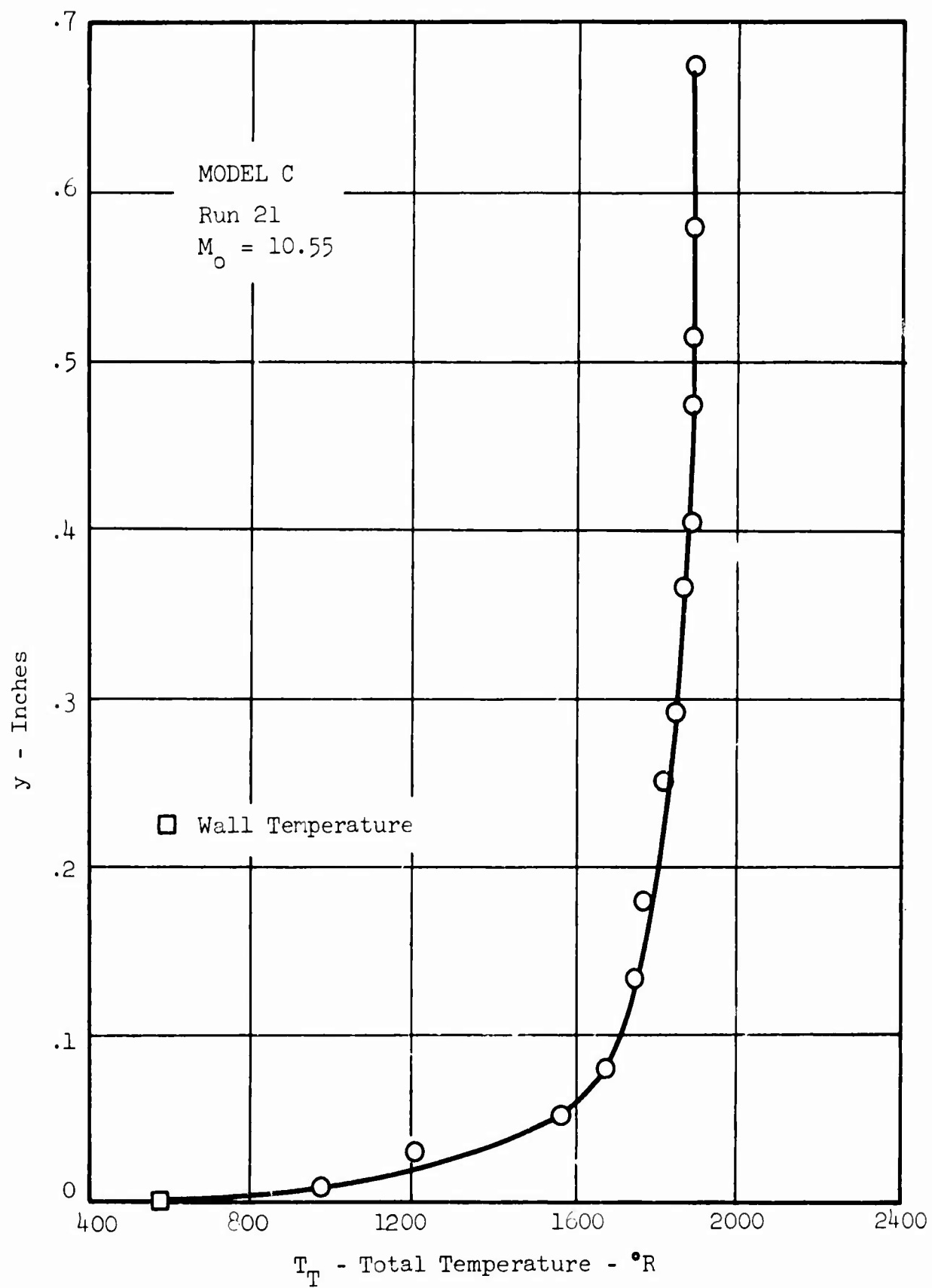


Figure 69 TYPICAL TURBULENT TOTAL TEMPERATURE PROFILE

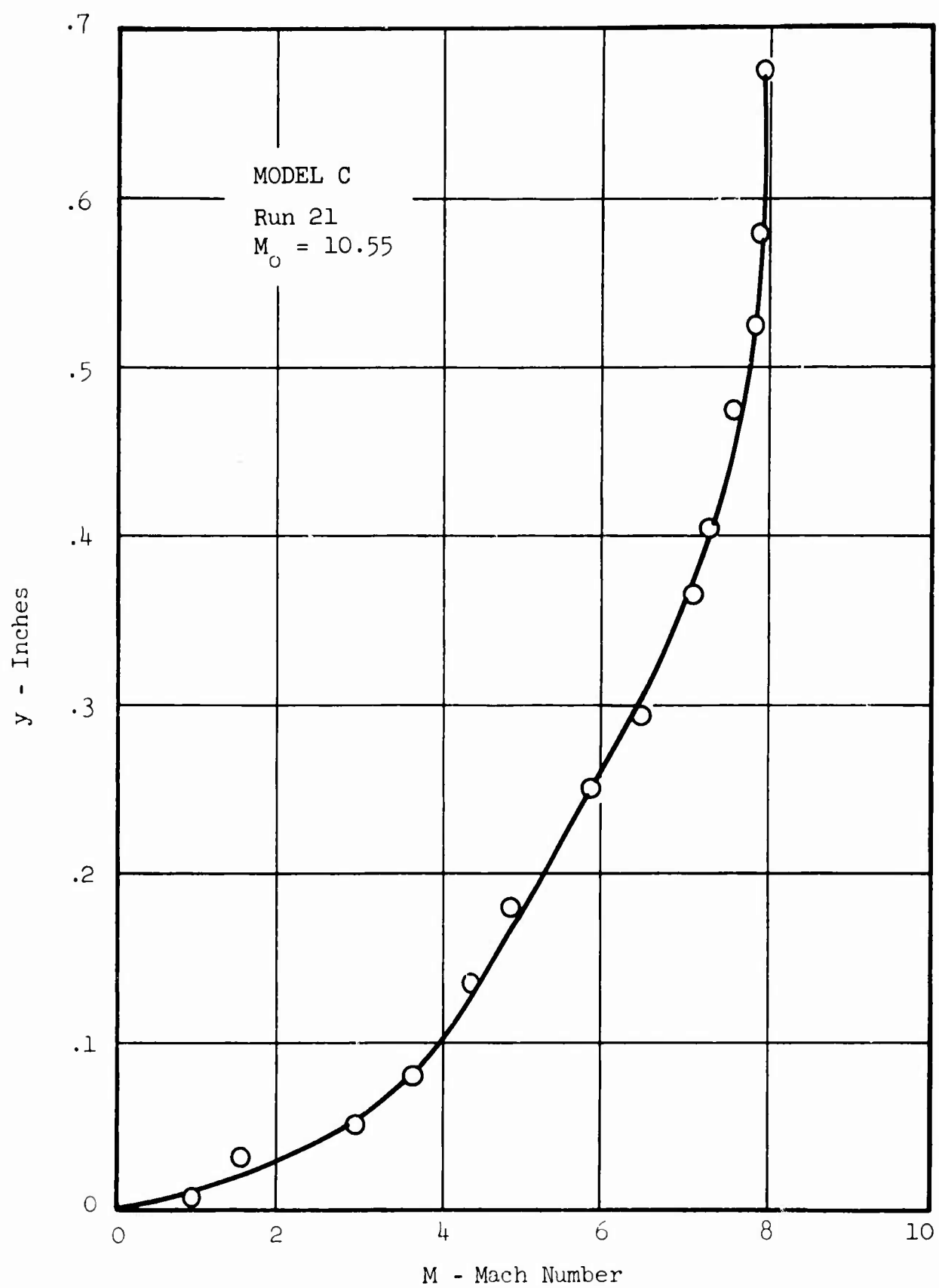


Figure 70 TYPICAL TURBULENT MACH NUMBER PROFILE

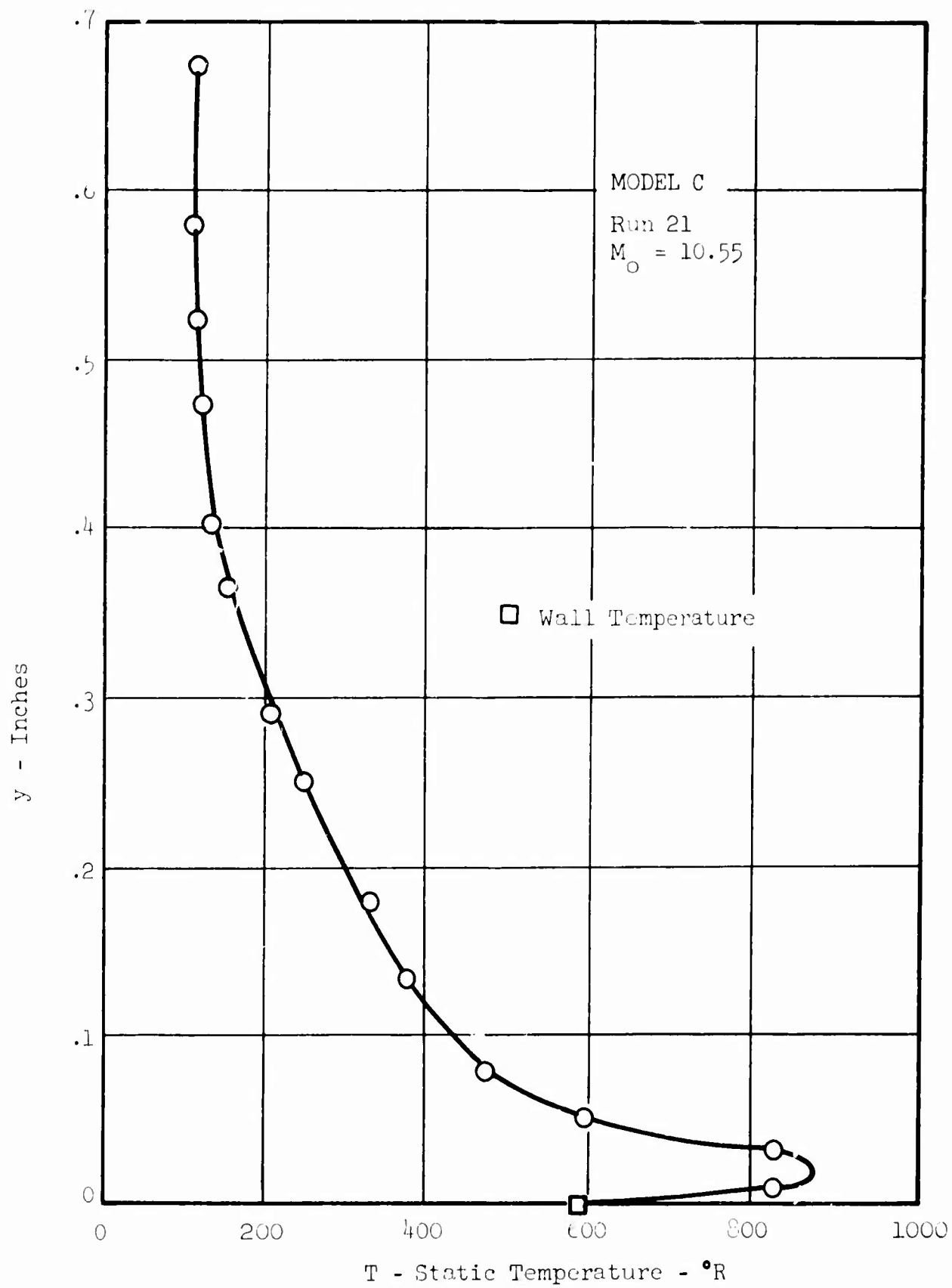


Figure 71 TYPICAL TURBULENT STATIC TEMPERATURE PROFILE



**BLANK PAGE**

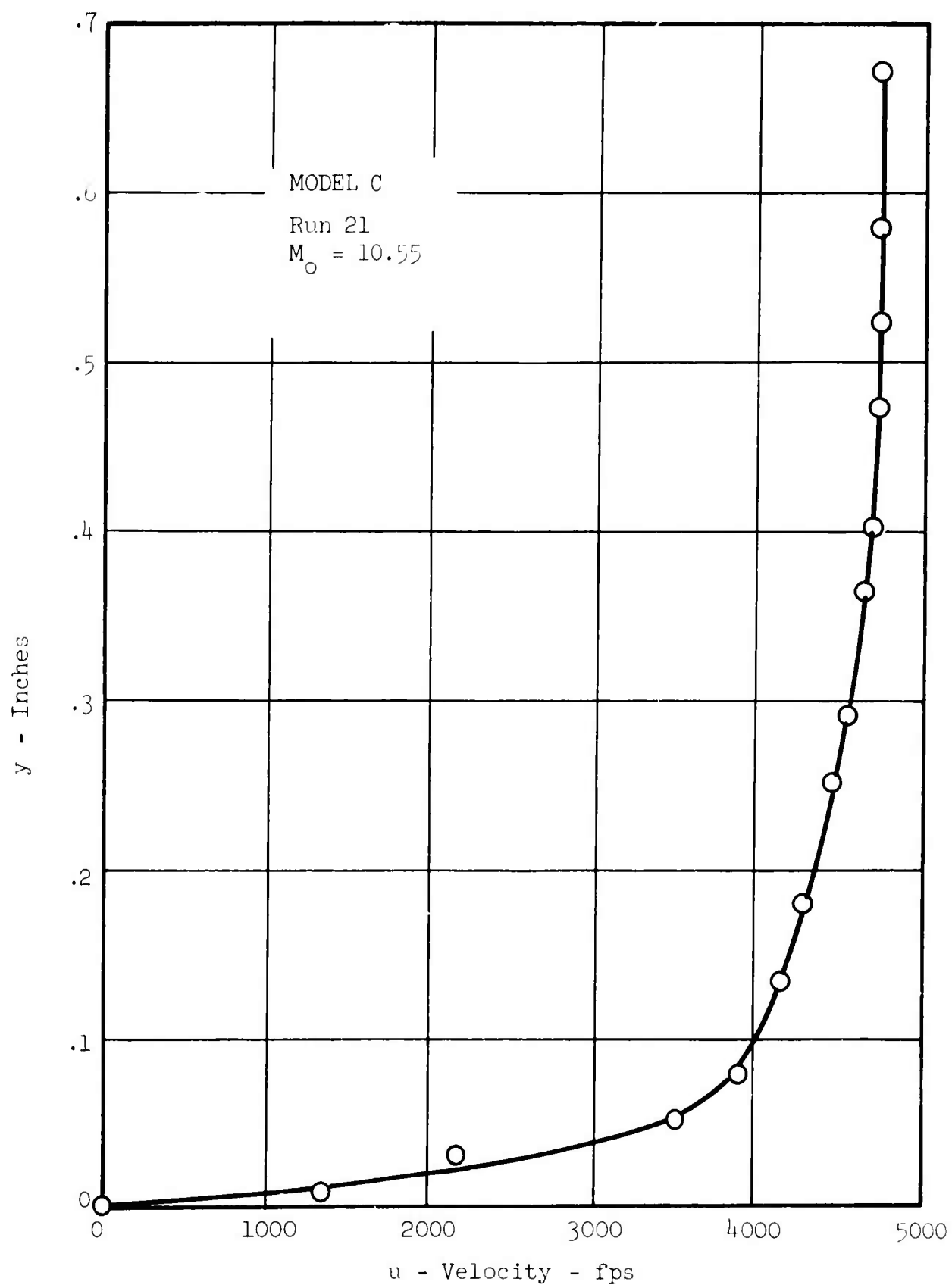


Figure 72 TYPICAL TURBULENT VELOCITY PROFILE

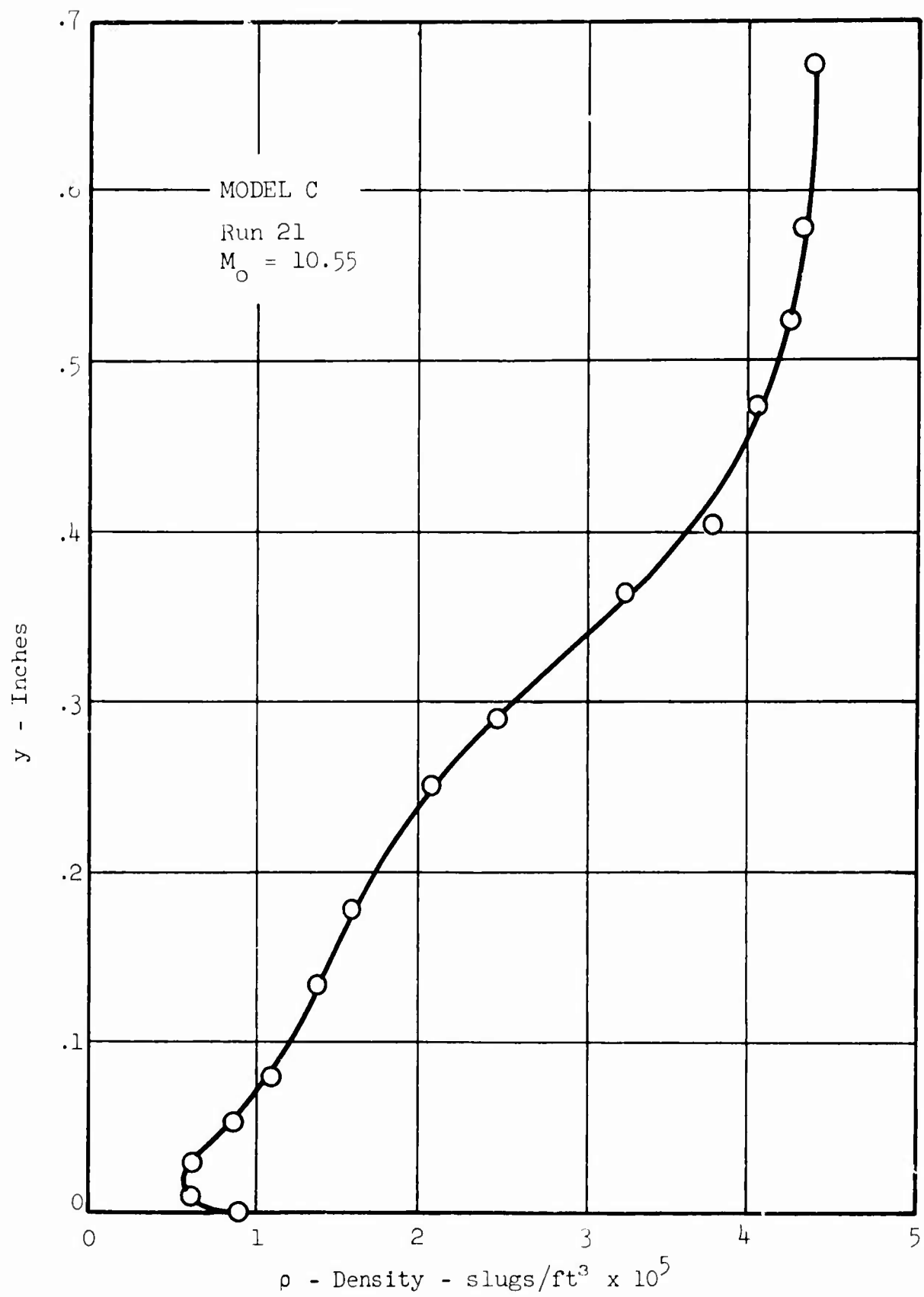


Figure 73 TYPICAL TURBULENT DENSITY PROFILE

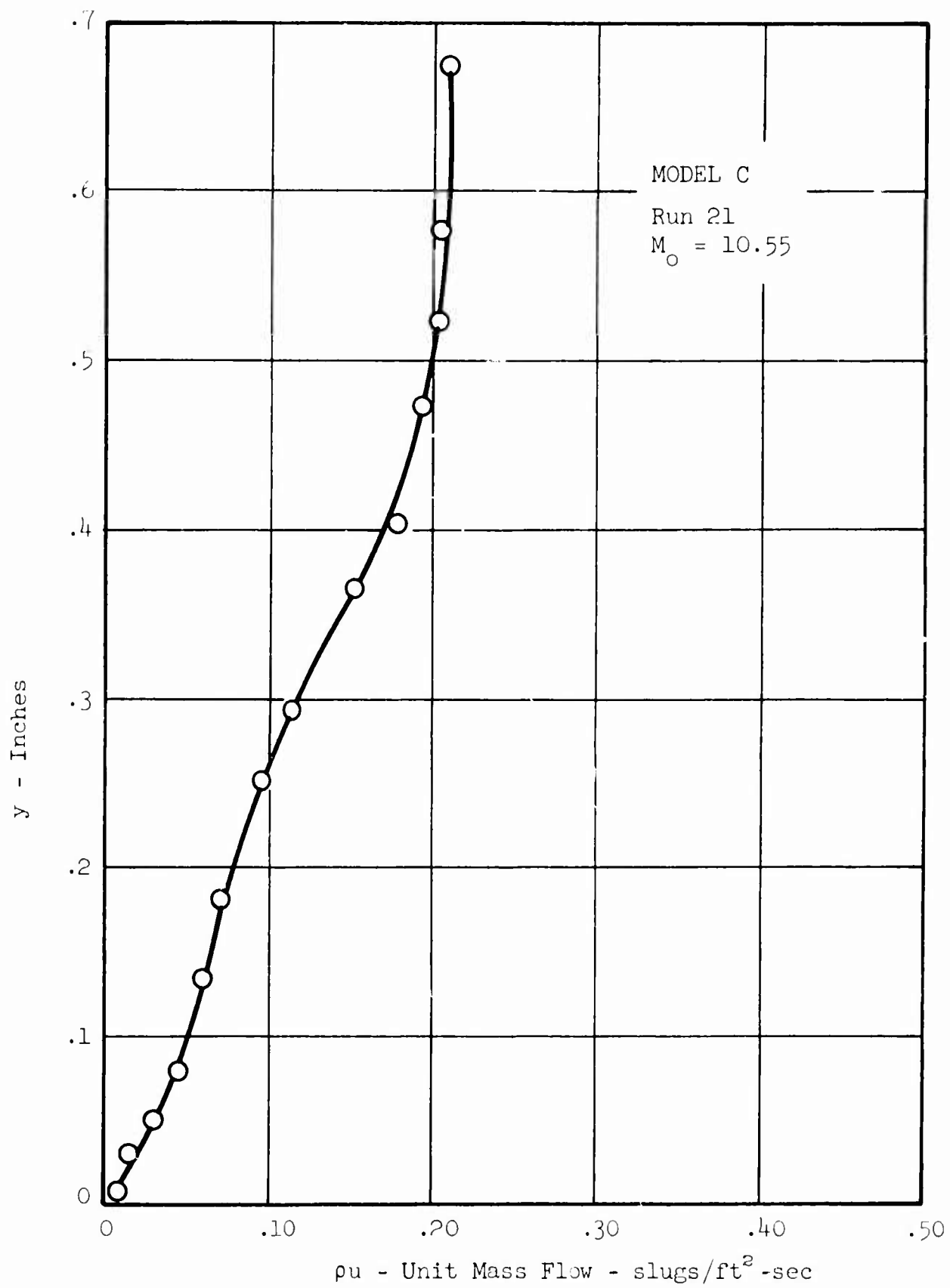


Figure 74 TYPICAL TURBULENT UNIT MASS FLOW PROFILE

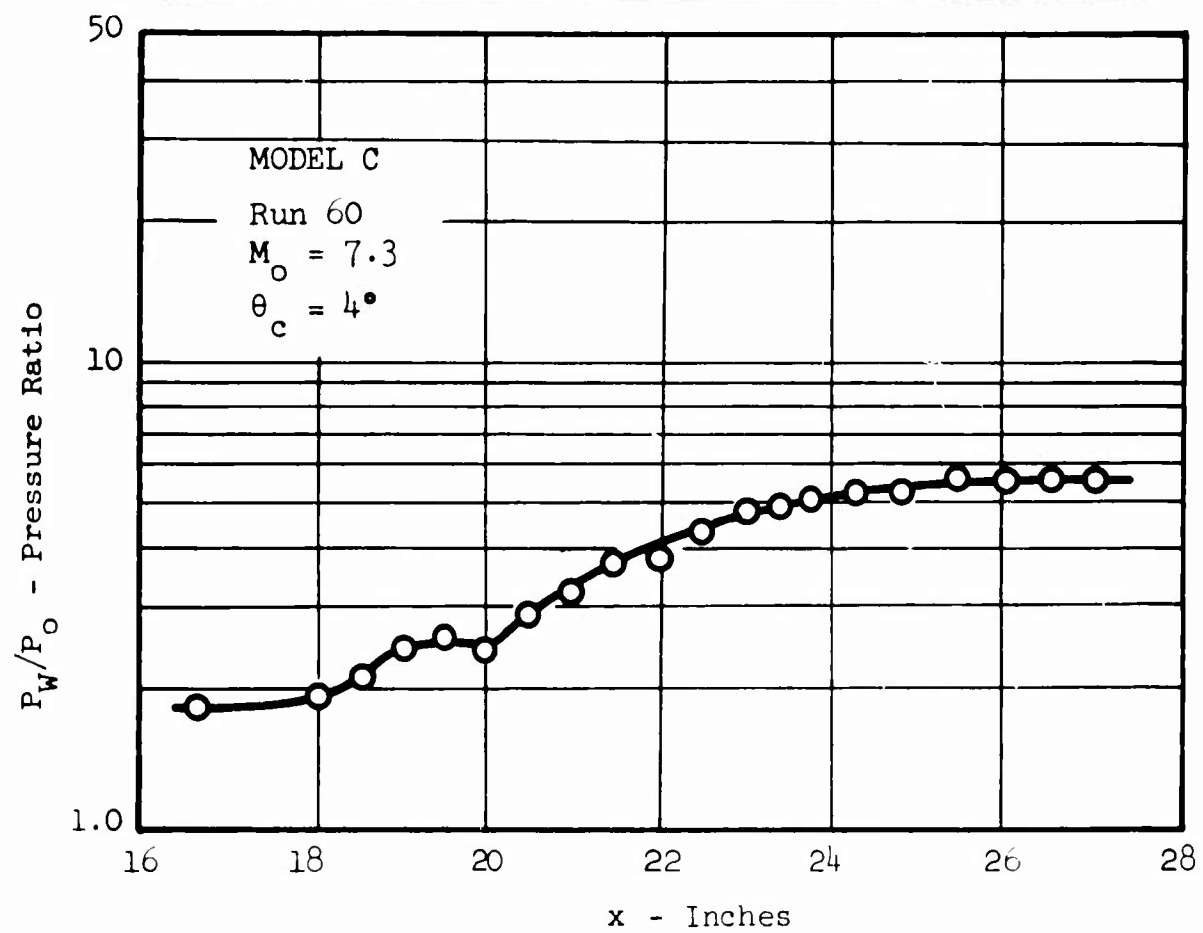


Figure 75 SCHLIEREN-PRESSURE DISTRIBUTION COMPOSITE

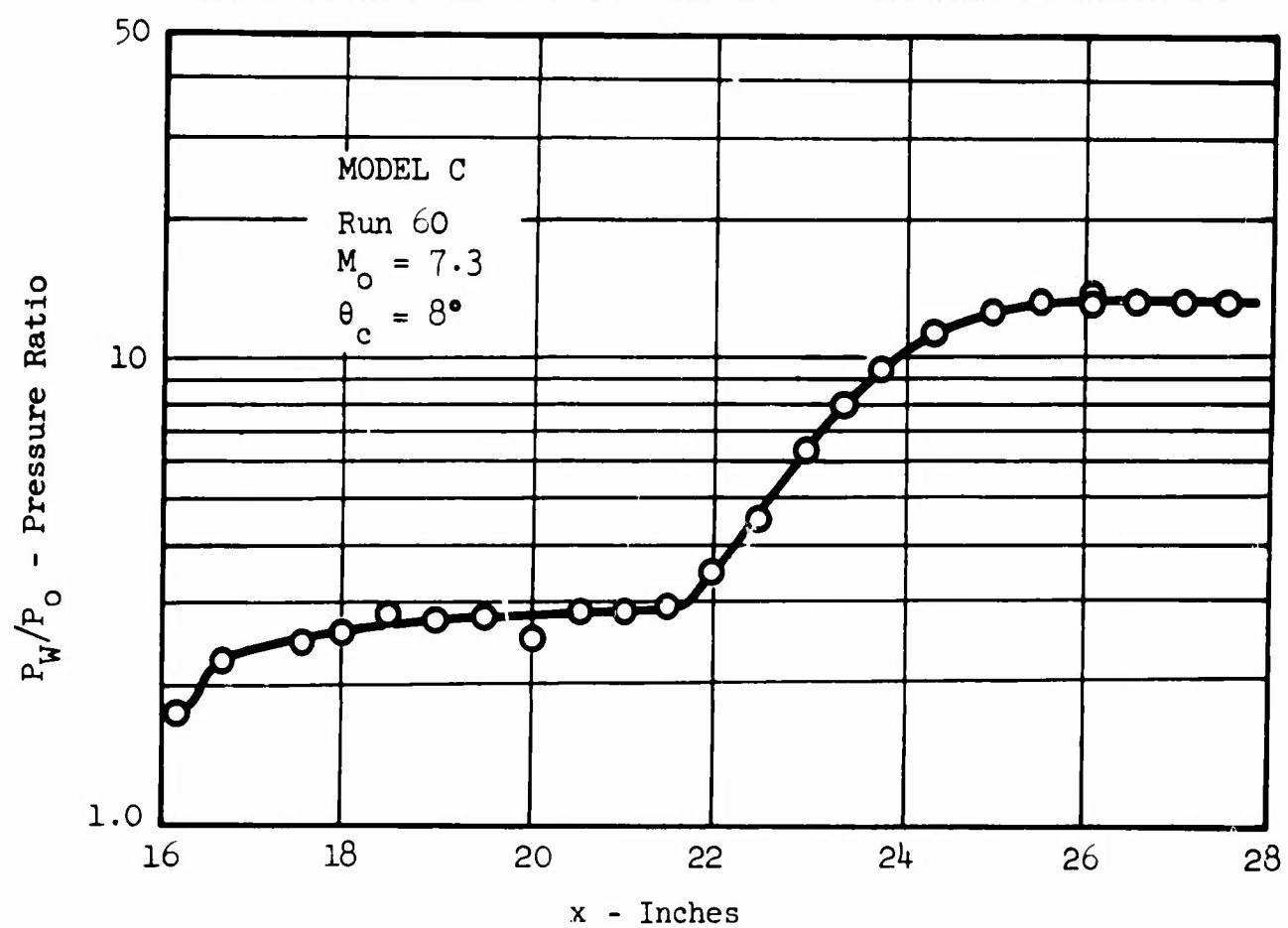


Figure 76 SCHLIEREN-PRESSURE DISTRIBUTION COMPOSITE

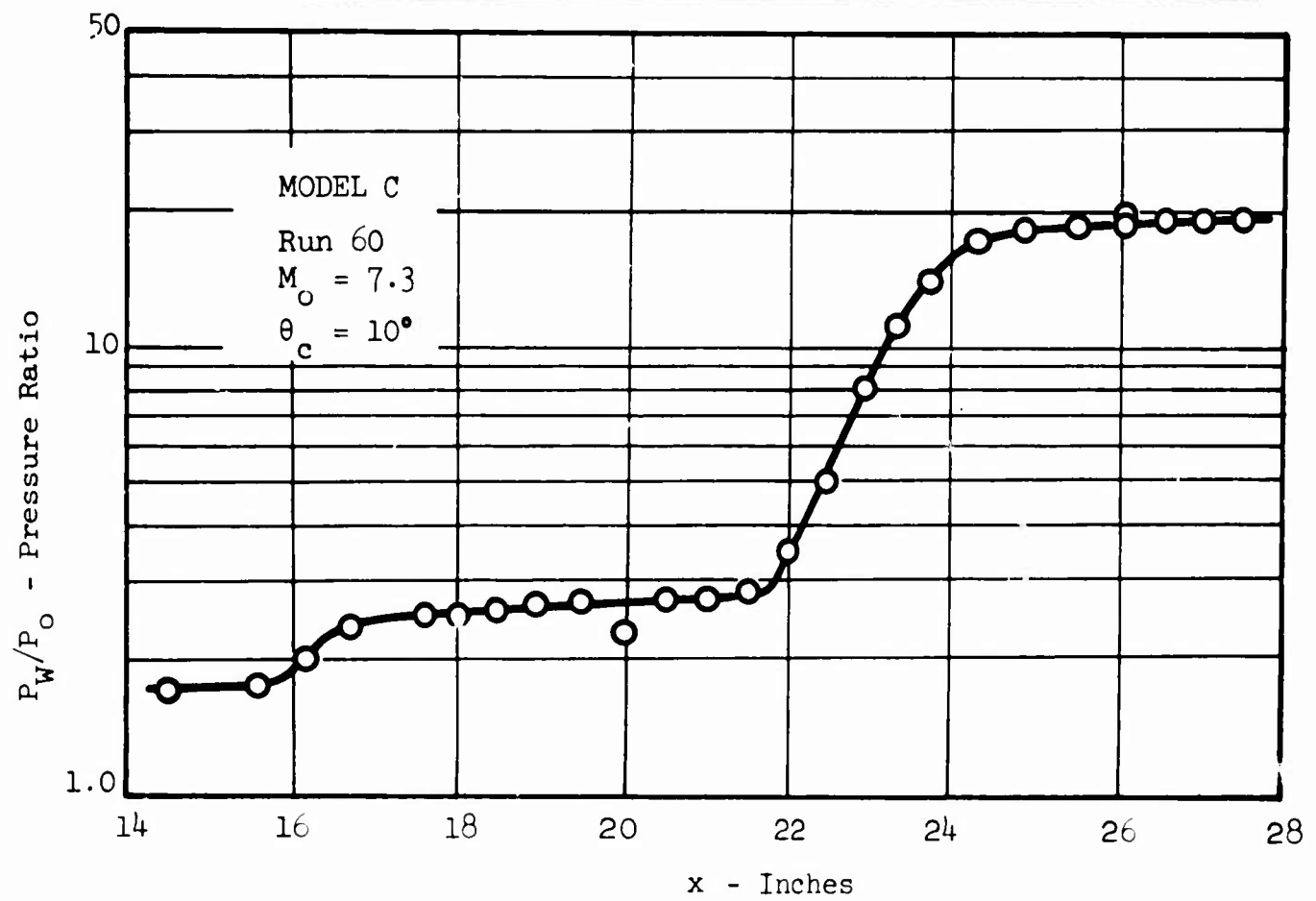


Figure 77 SCHLIEREN-PRESSURE DISTRIBUTION COMPOSITE

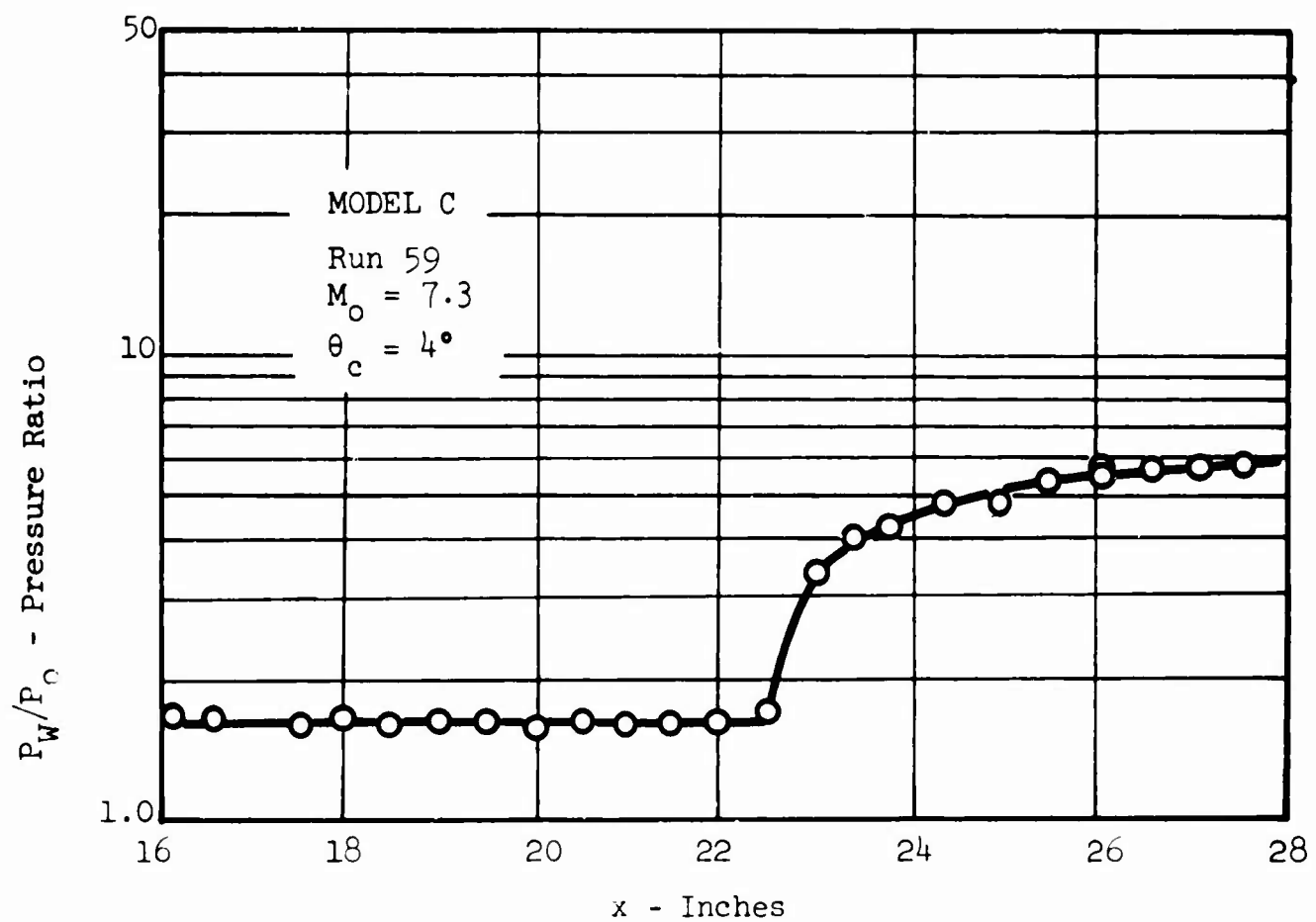
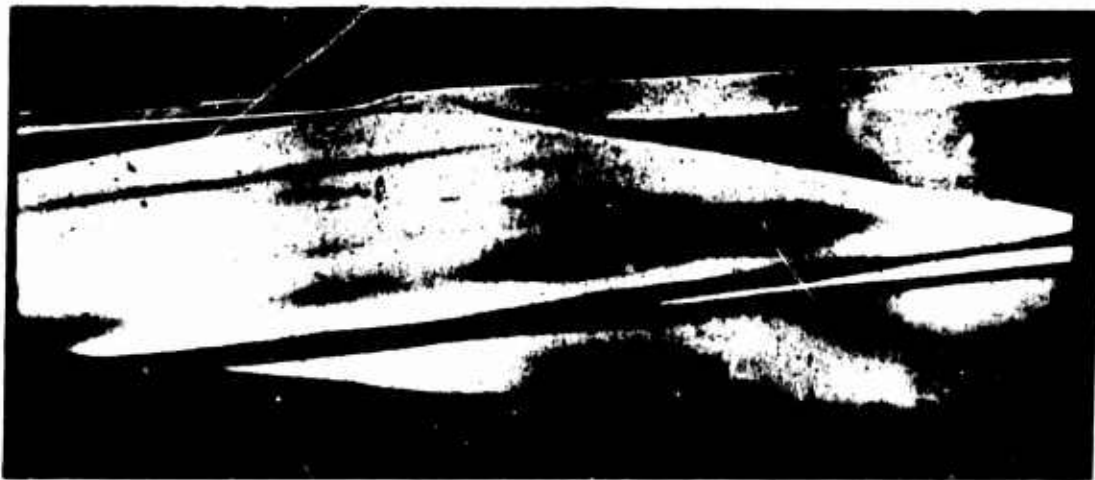


Figure 78 SCHLIEREN-PRESSURE DISTRIBUTION COMPOSITE



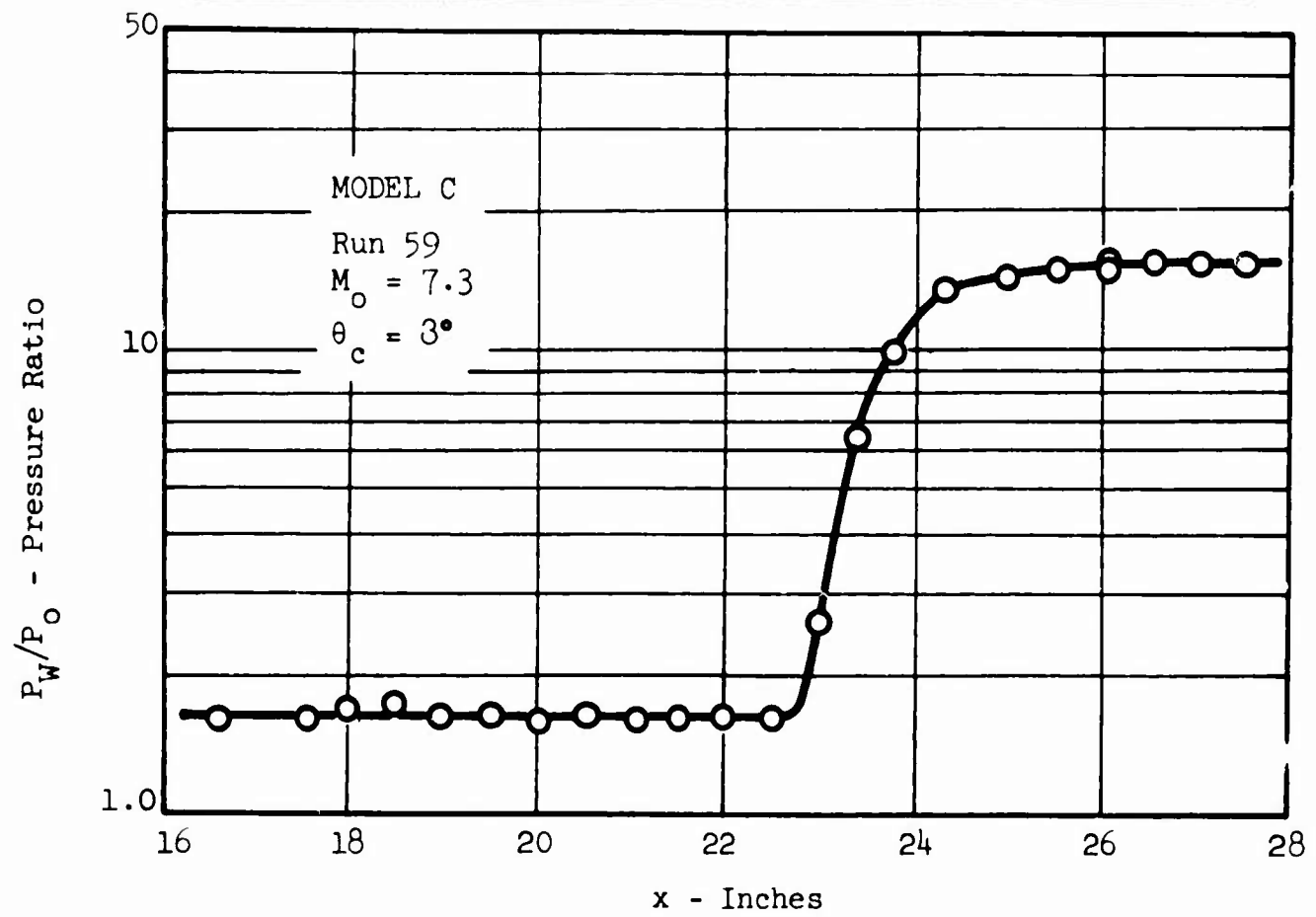


Figure 79 SCHLIEREN-PRESSURE DISTRIBUTION COMPOSITE

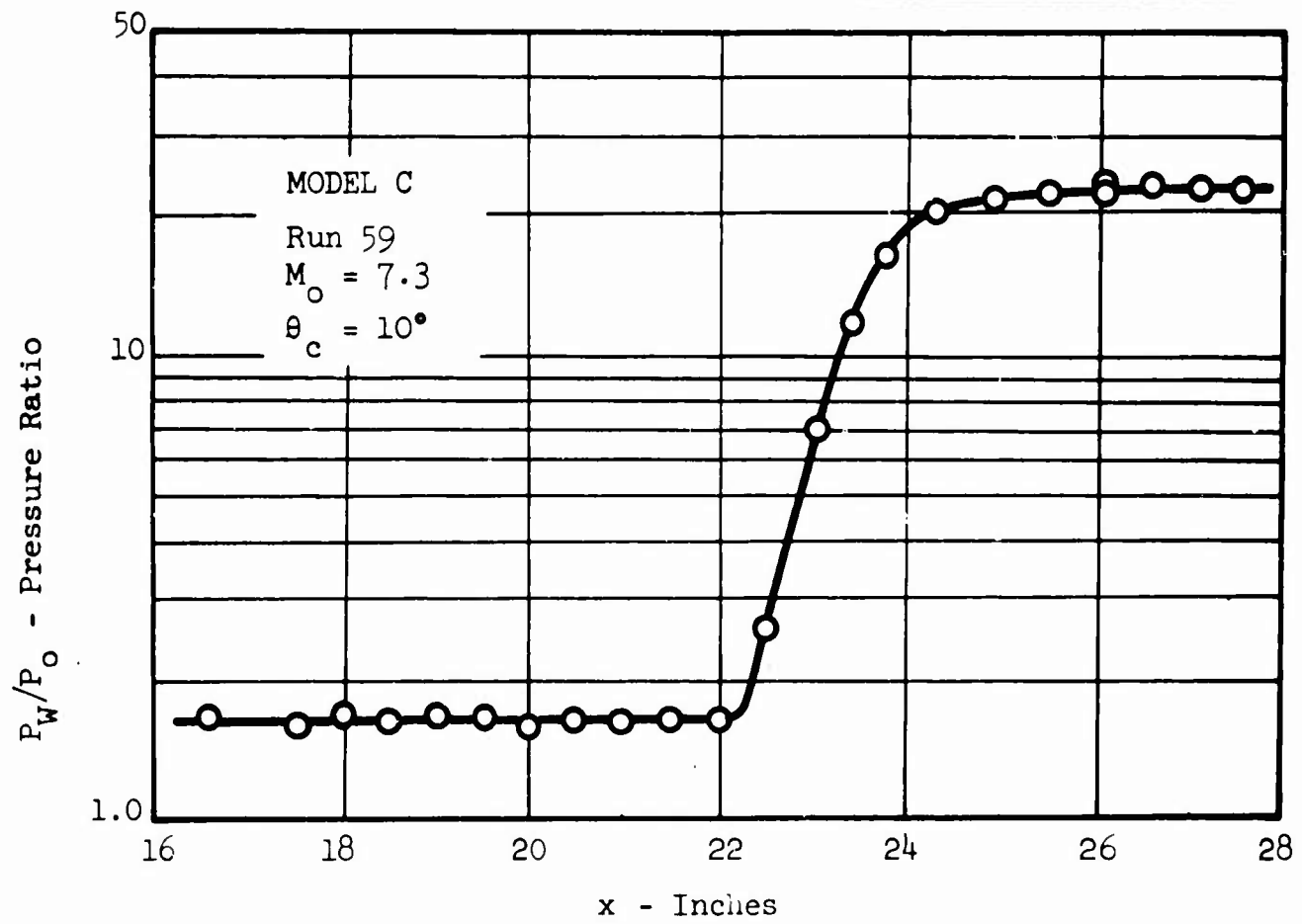
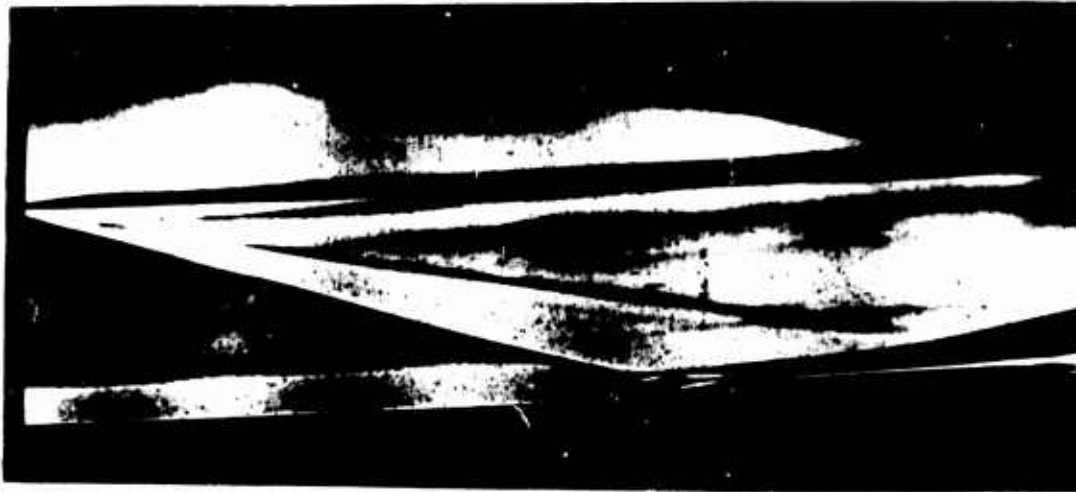


Figure 80 SCHLIEREN-PRESSURE DISTRIBUTION COMPOSITE

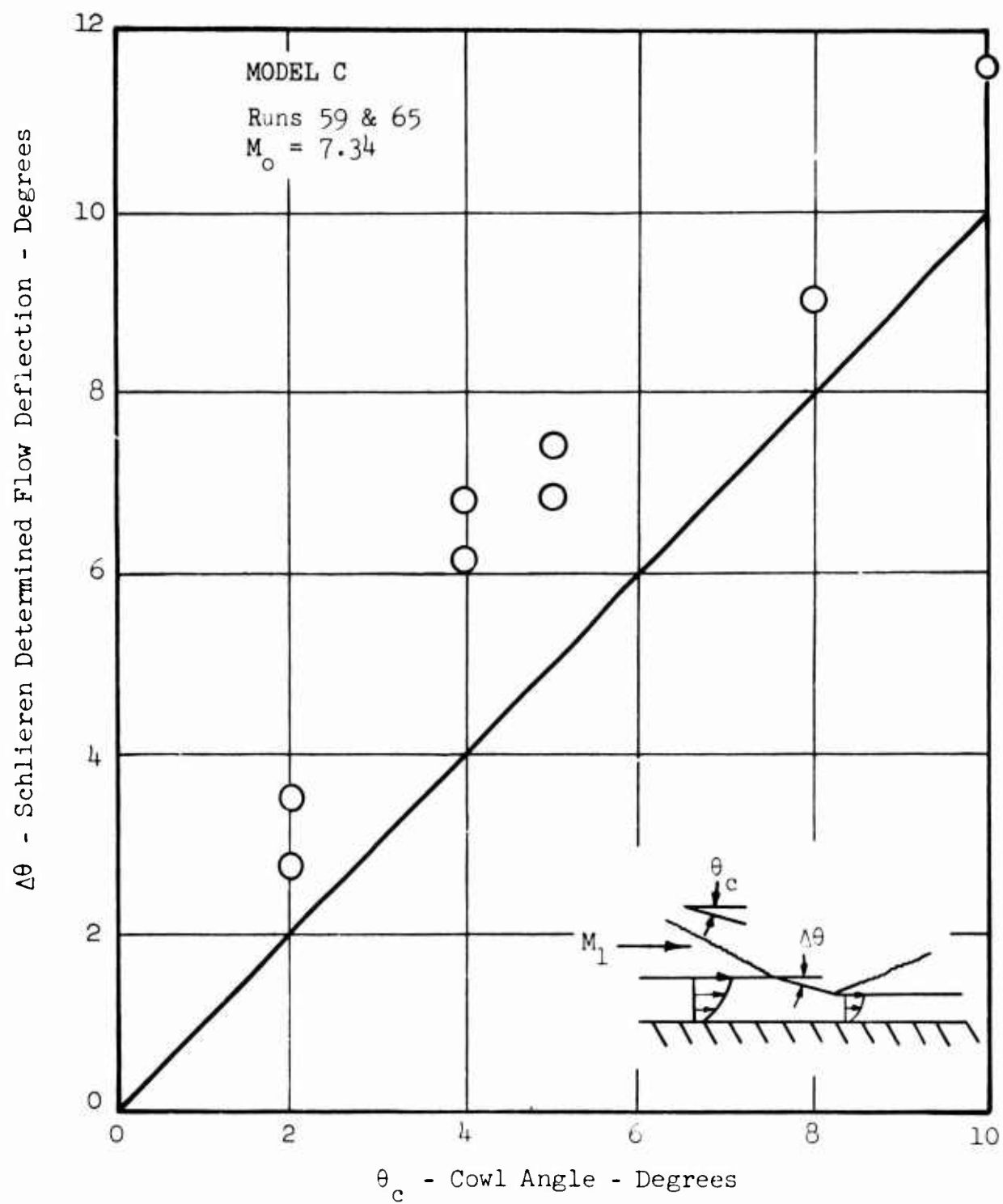


Figure 81 COMPARISON OF INVISCID SHOCK AND BOUNDARY LAYER EDGE FLOW ANGLES

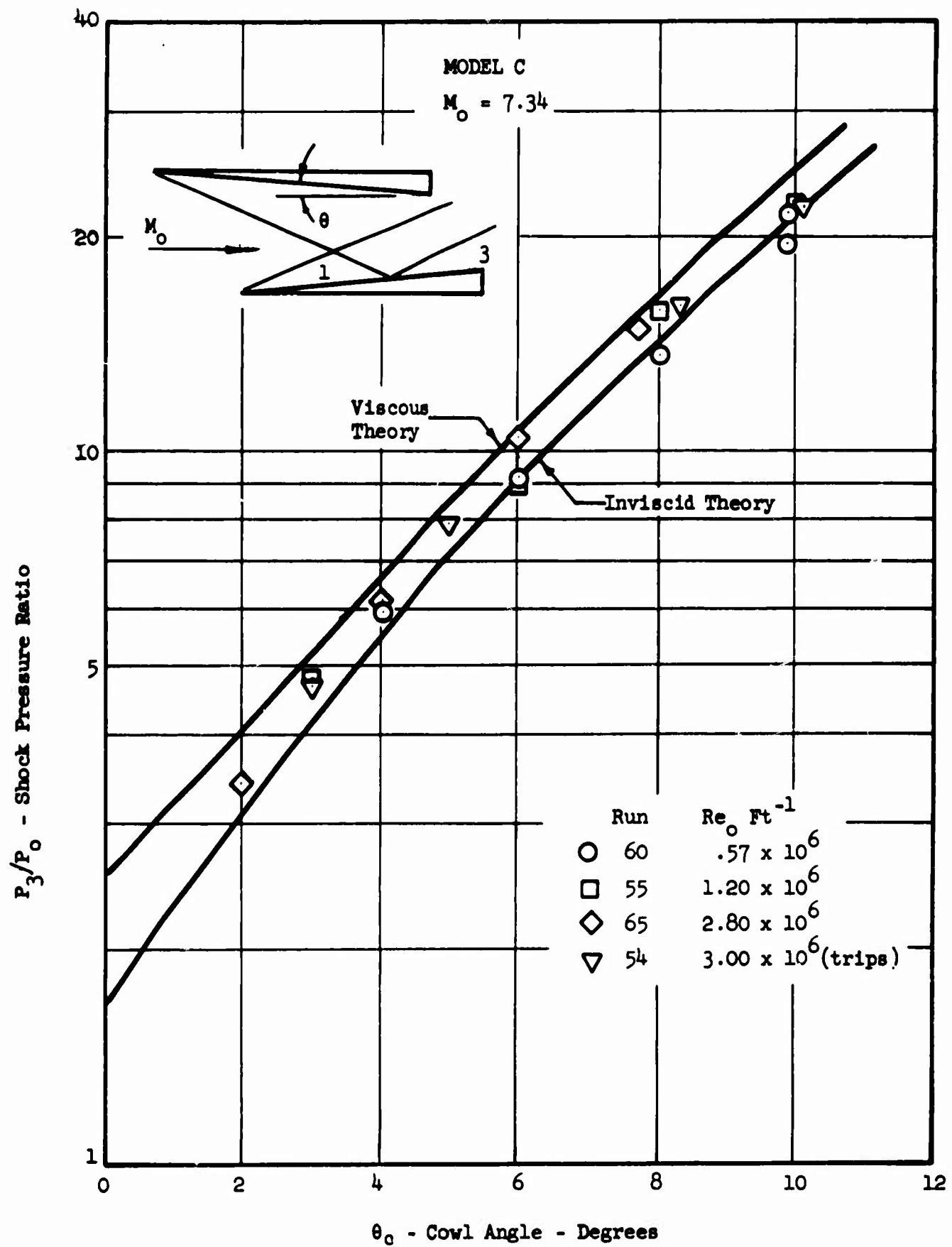


Figure 82 THEORY/DATA SHOCK PRESSURE RATIO COMPARISONS

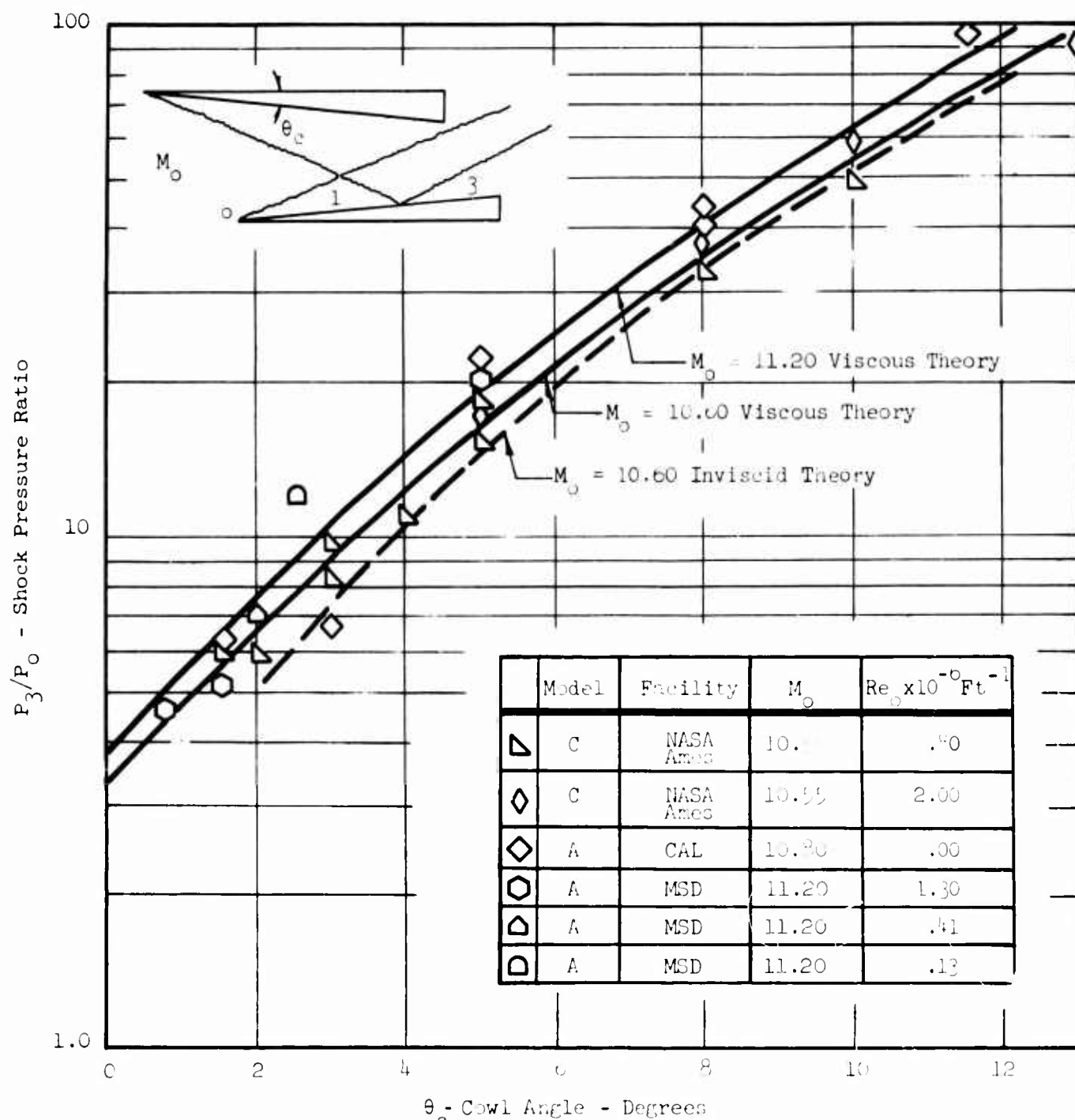


Figure 83 THEORY/DATA SHOCK PRESSURE RATIO COMPARISONS

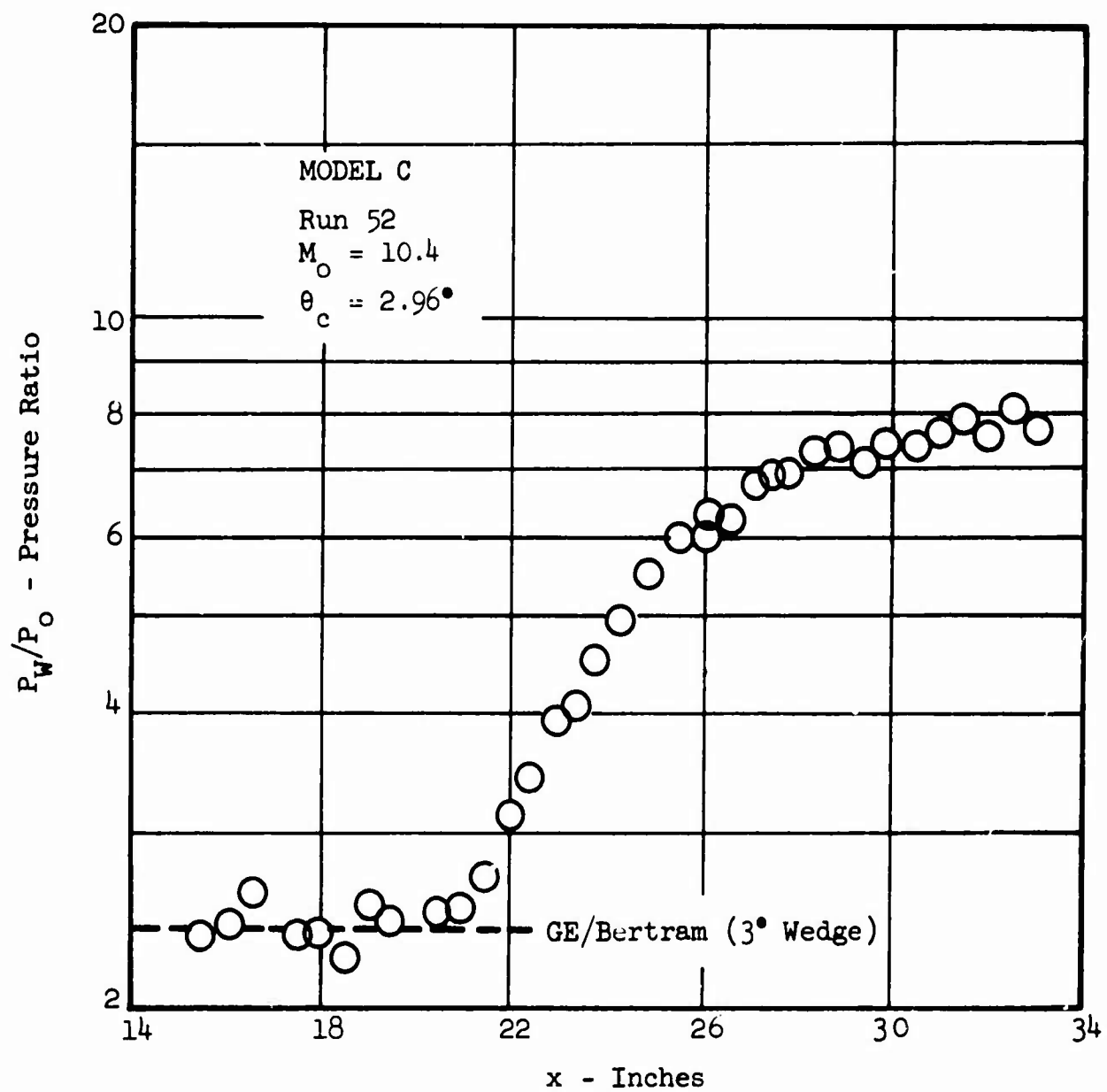


Figure 84 LAMINAR BOUNDARY LAYER INCIDENT SHOCK PRESSURE DISTRIBUTION

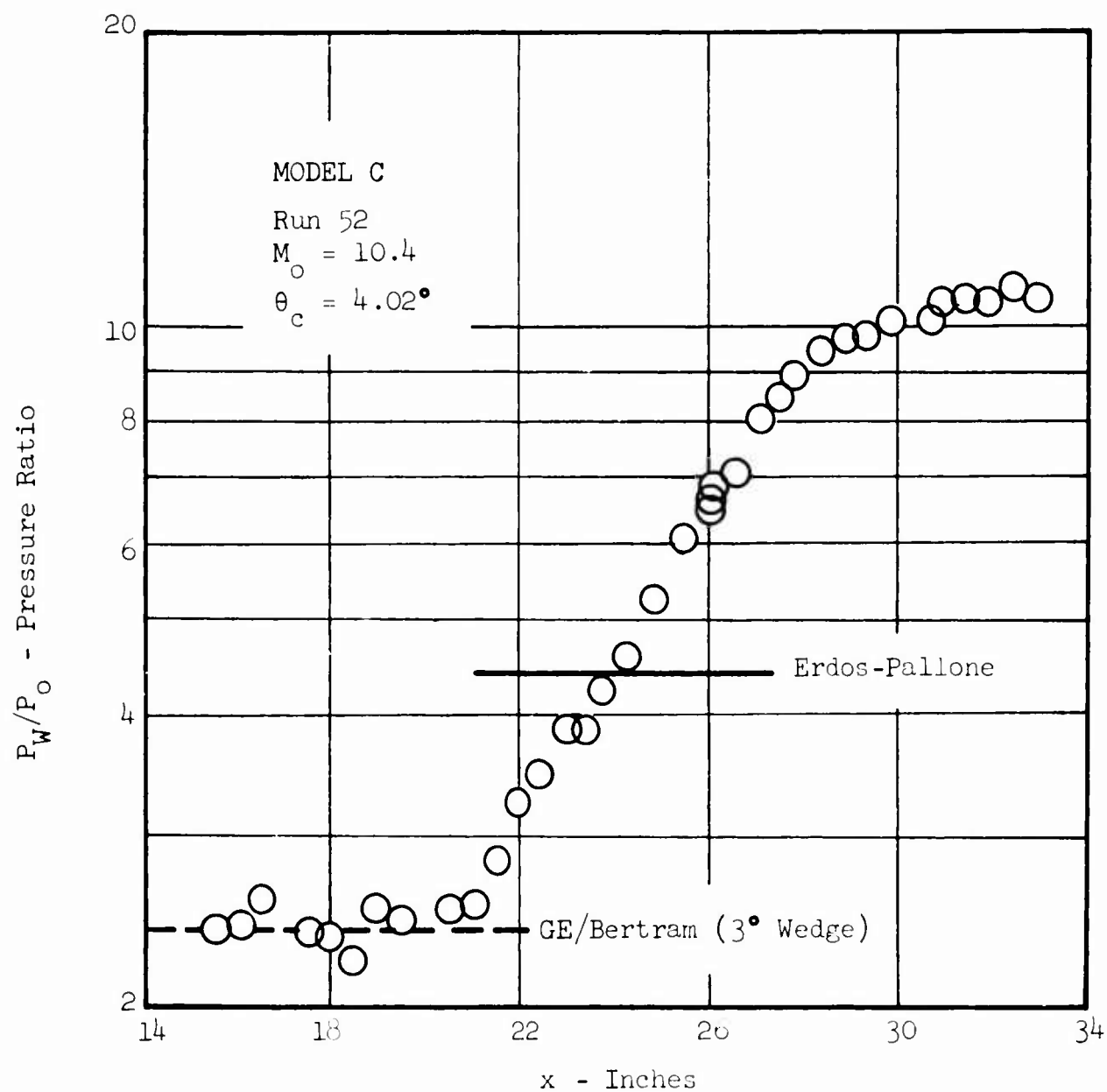


Figure 85 LAMINAR BOUNDARY LAYER INCIDENT SHOCK  
PRESSURE DISTRIBUTION

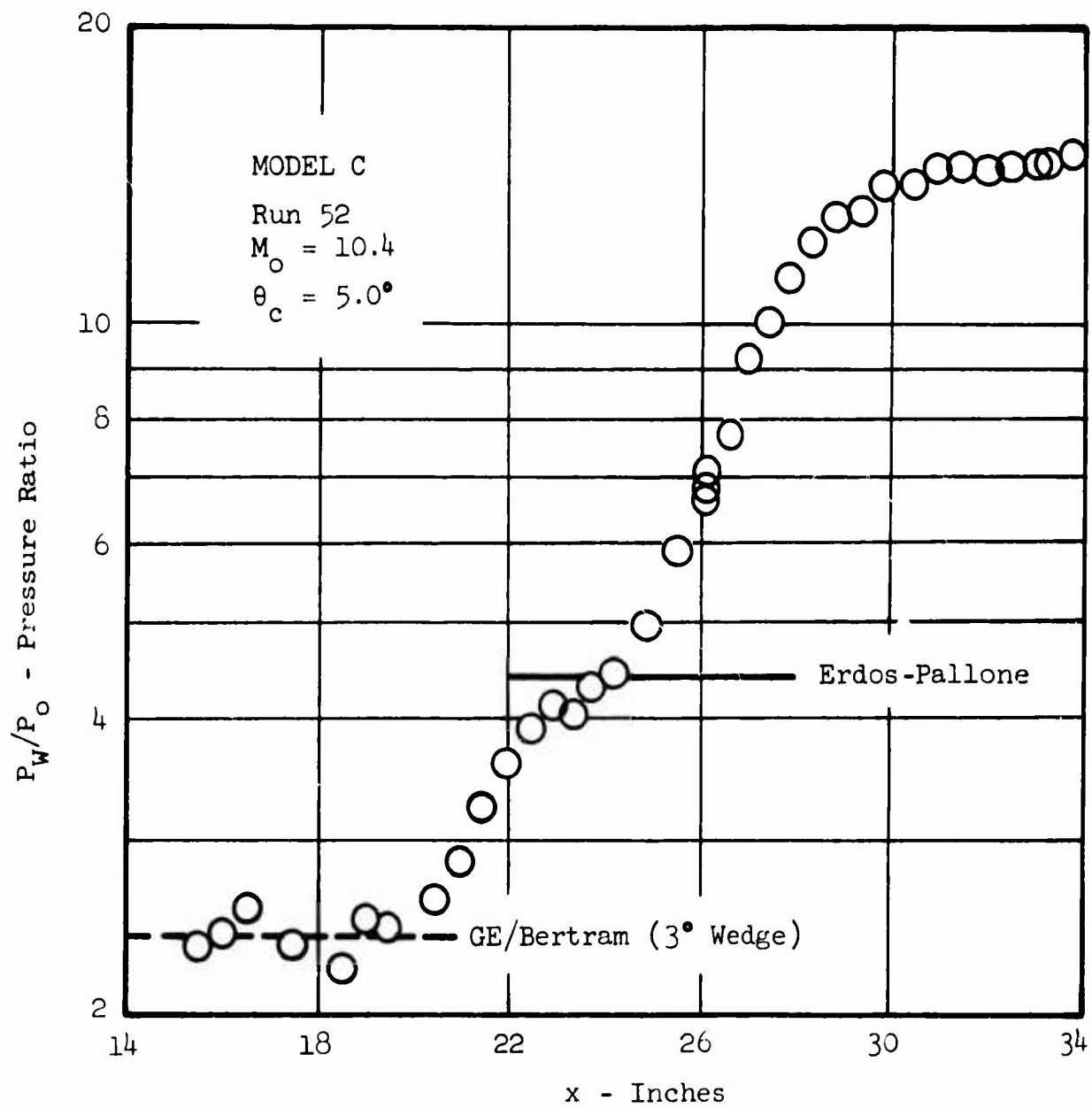


Figure 86 LAMINAR BOUNDARY LAYER INCIDENT SHOCK  
PRESSURE DISTRIBUTION



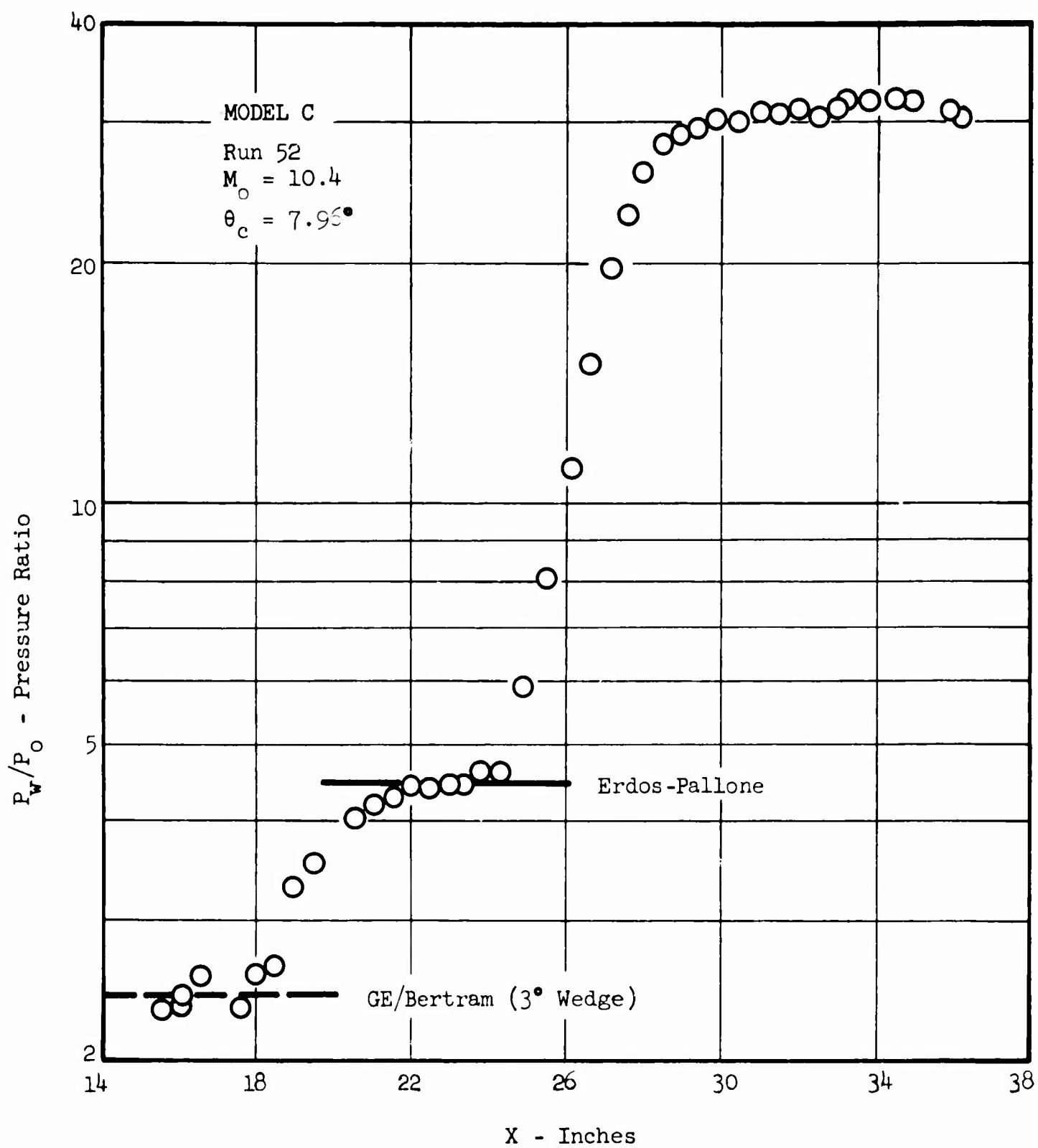


Figure 87 LAMINAR BOUNDARY LAYER INCIDENT SHOCK  
PRESSURE DISTRIBUTION

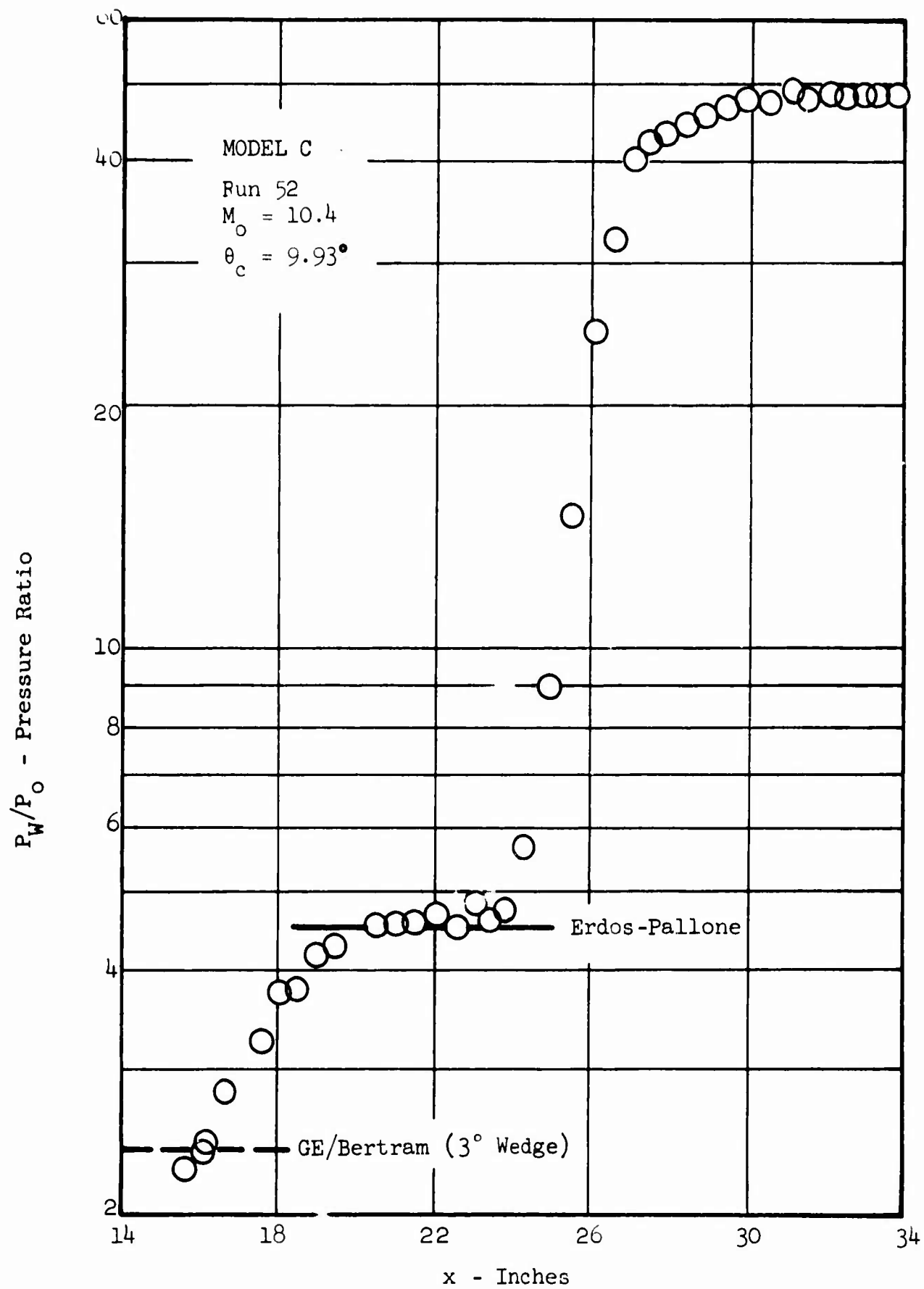


Figure 88 LAMINAR BOUNDARY LAYER INCIDENT SHOCK  
PRESSURE DISTRIBUTION

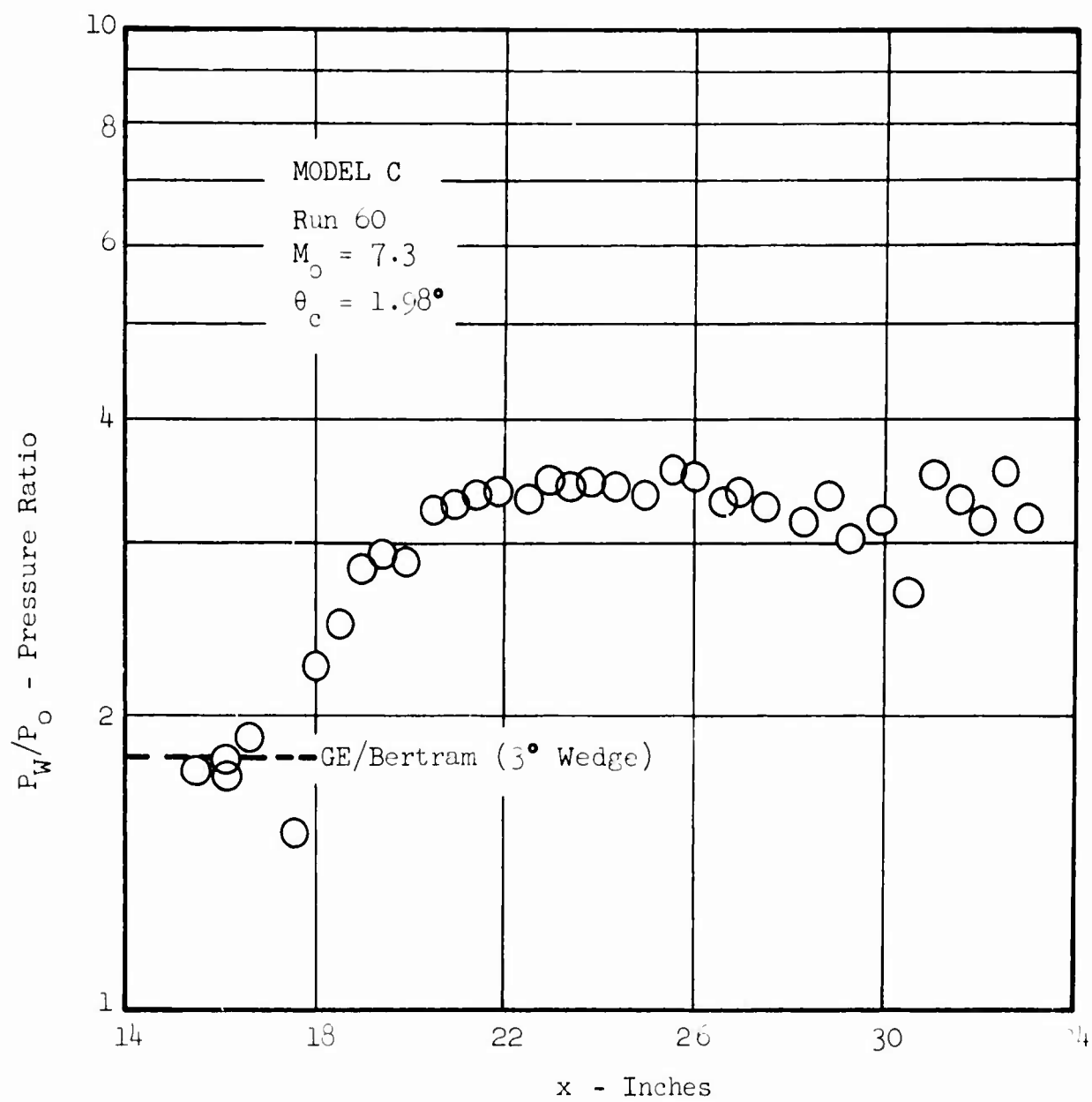


Figure 89 LAMINAR BOUNDARY LAYER INCIDENT SHOCK  
PRESSURE DISTRIBUTION

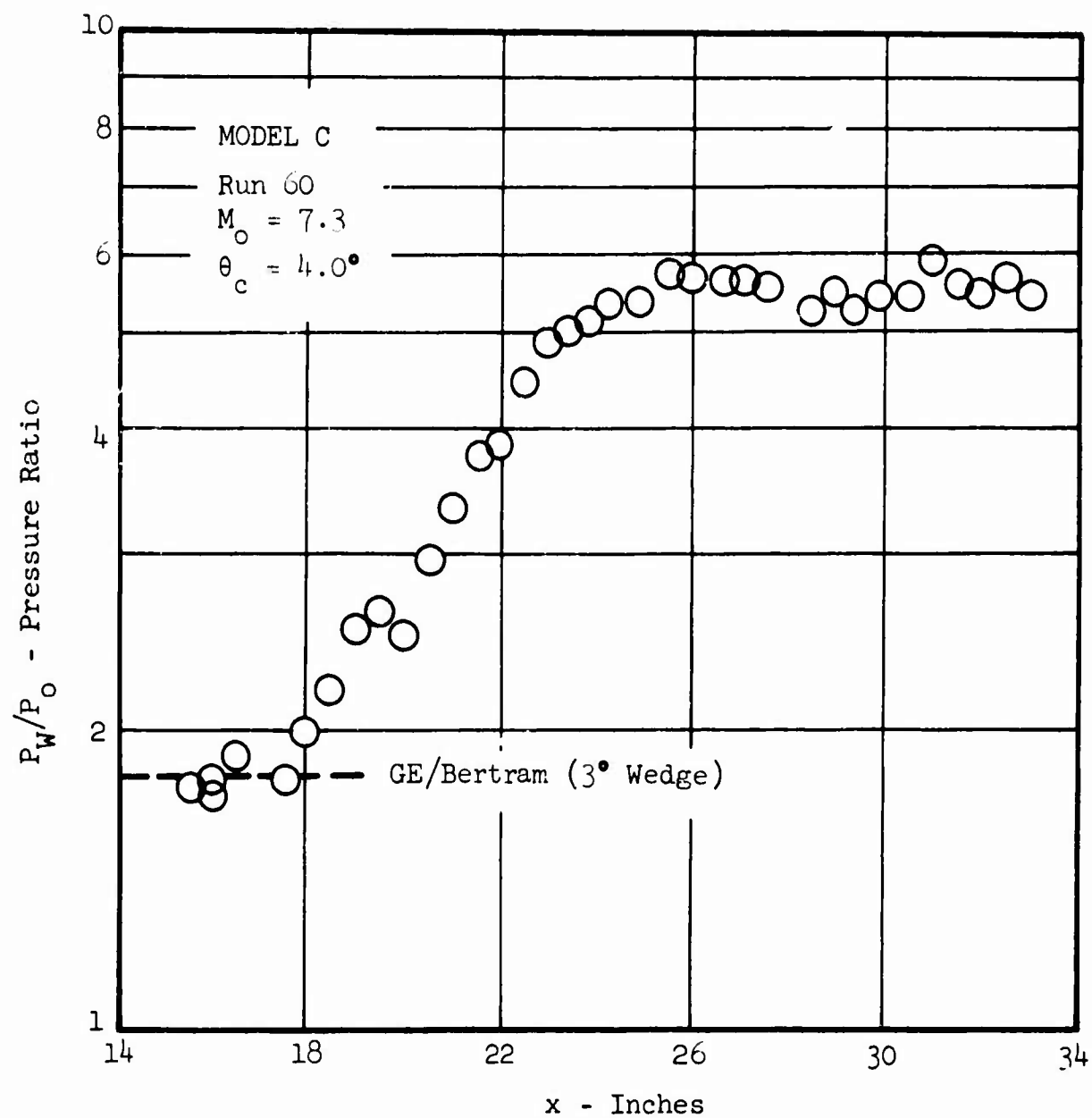


Figure 90 LAMINAR BOUNDARY LAYER INCIDENT SHOCK PRESSURE DISTRIBUTION

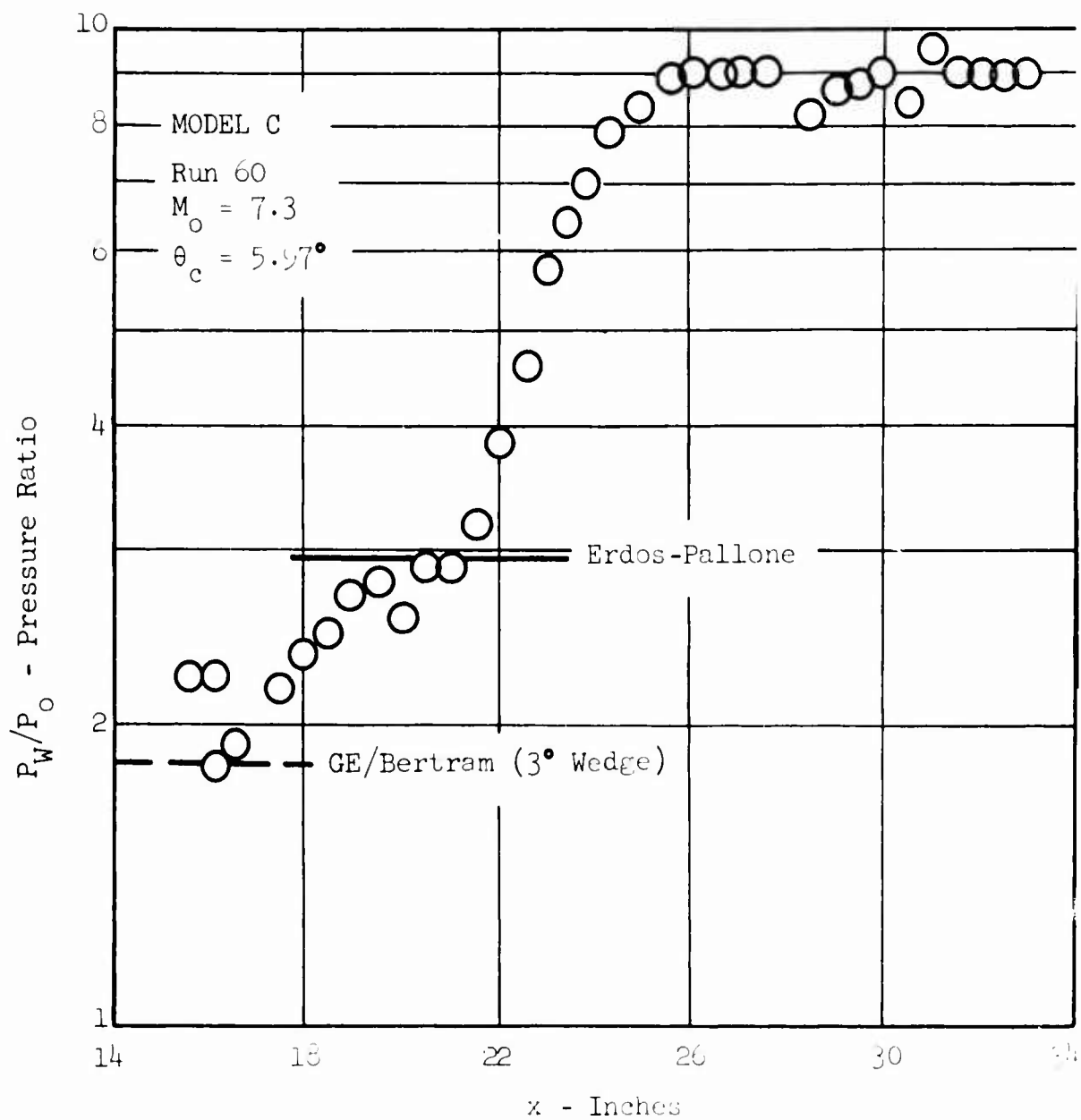


Figure 91 LAMINAR BOUNDARY LAYER INCIDENT SHOCK PRESSURE DISTRIBUTION

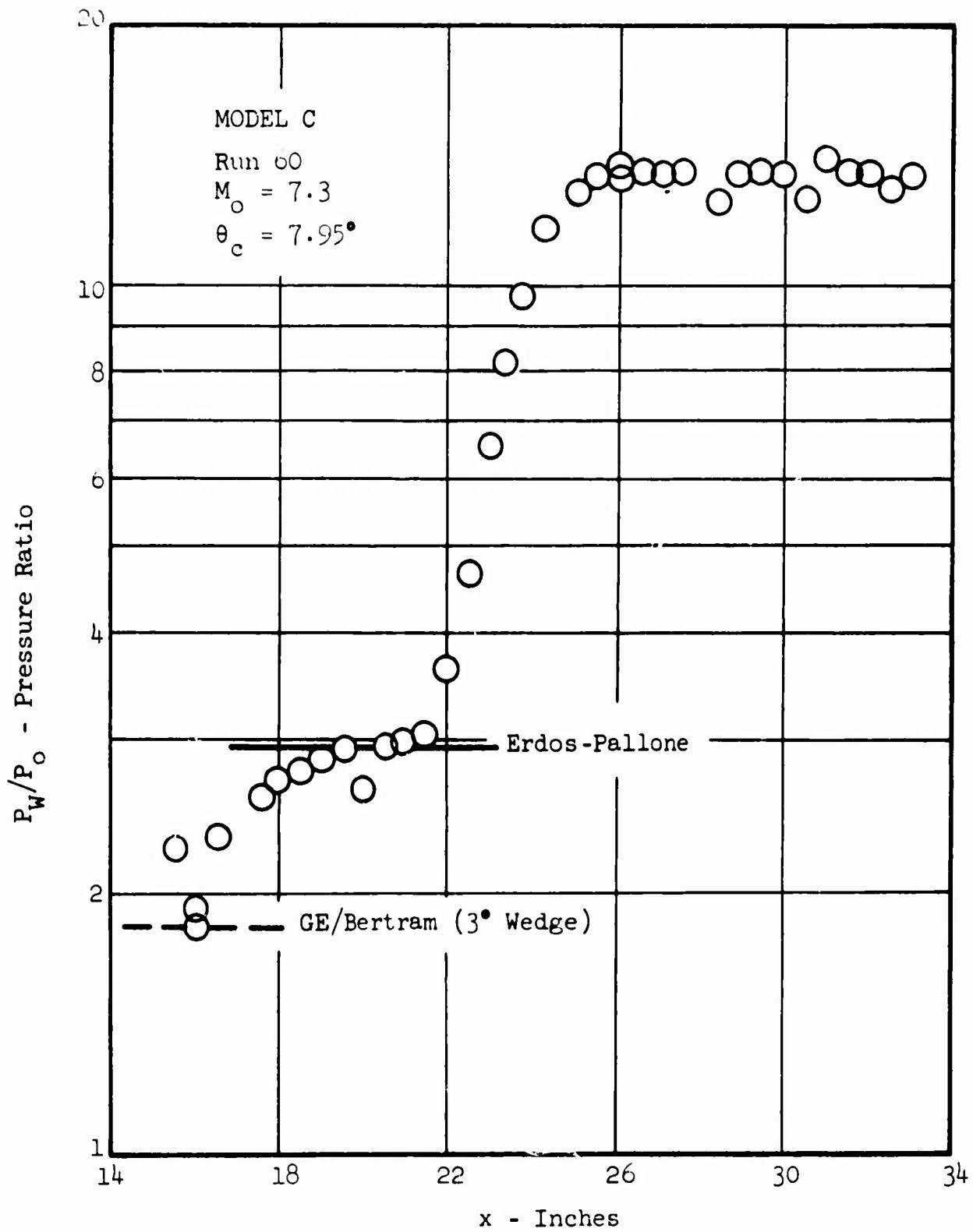


Figure 92 LAMINAR BOUNDARY LAYER INCIDENT SHOCK PRESSURE DISTRIBUTION

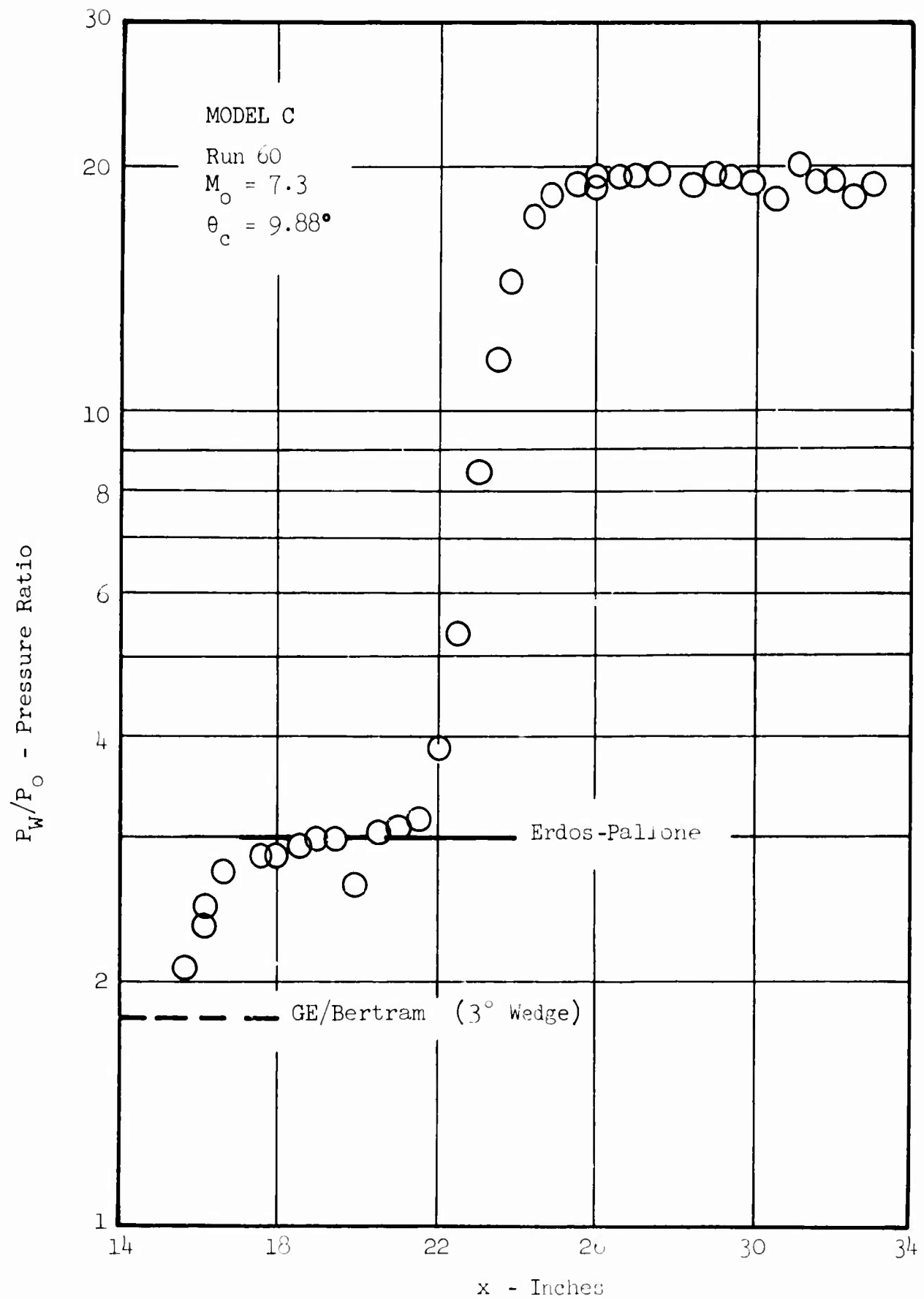


Figure 93 LAMINAR BOUNDARY LAYER INCIDENT SHOCK  
PRESSURE DISTRIBUTION

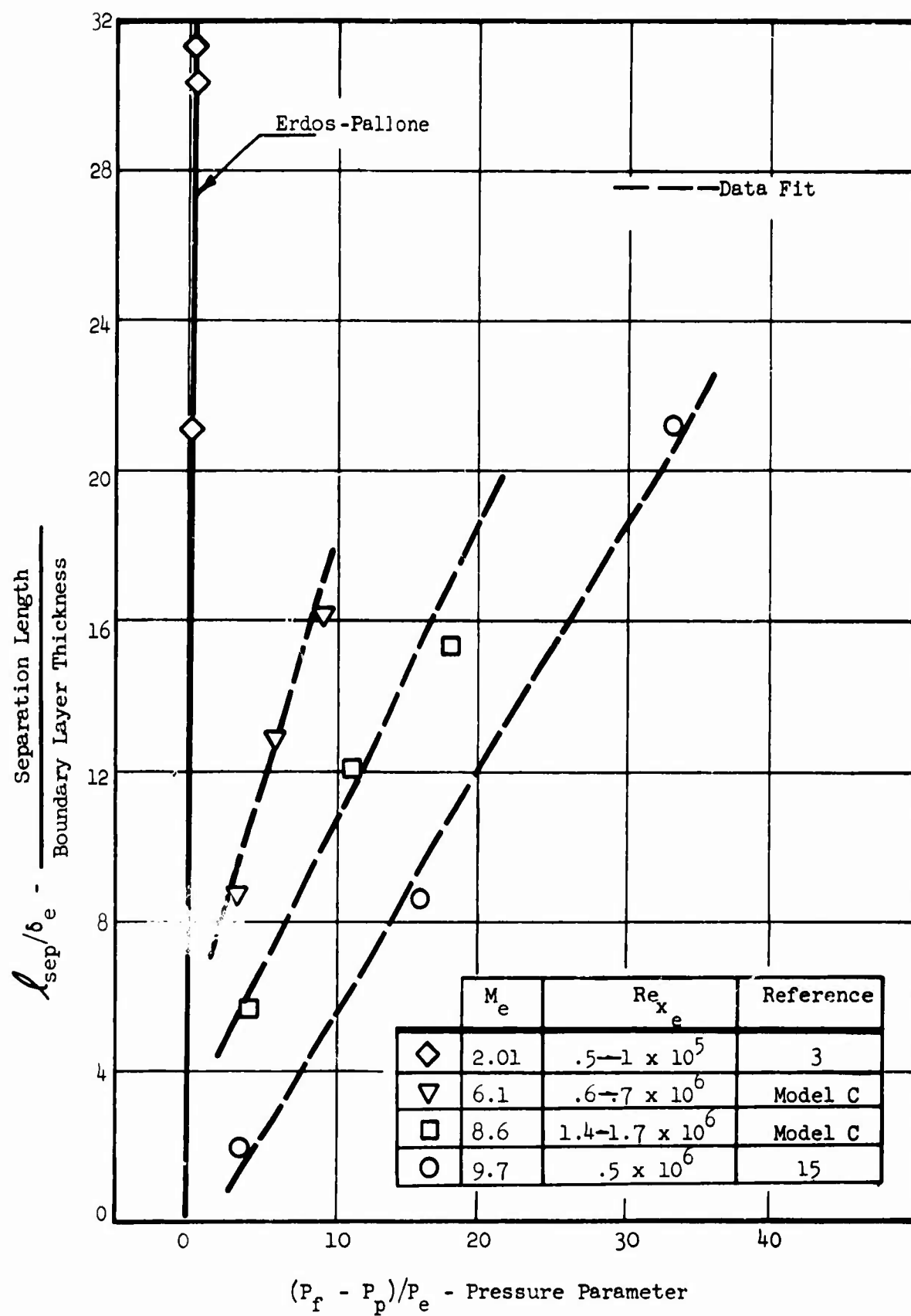


Figure 94 CORRELATION OF LAMINAR BOUNDARY LAYER SEPARATION LENGTH



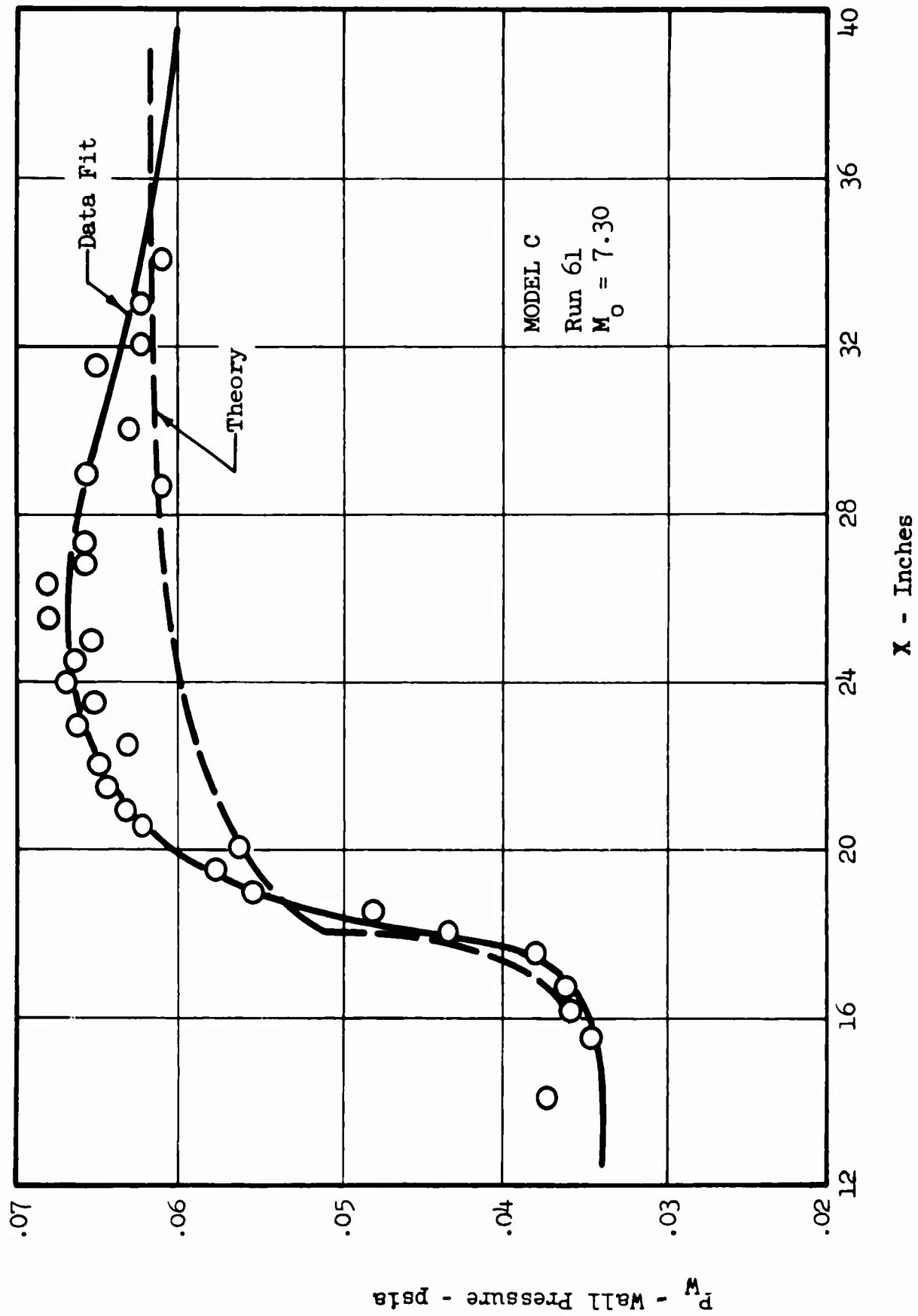


Figure 95 LAMINAR INTERACTION THEORY/DATA PRESSURE DISTRIBUTIONS

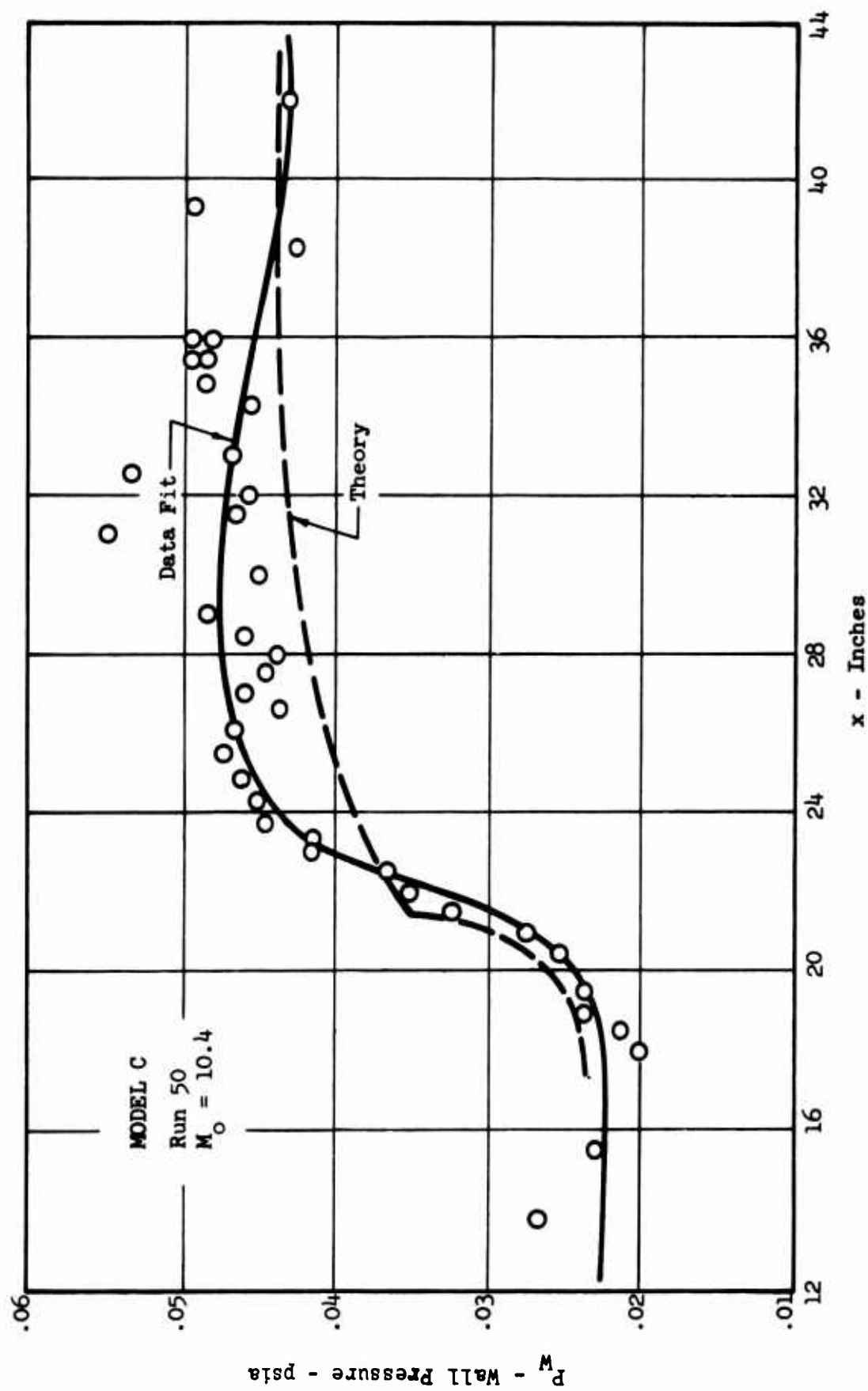


Figure 96 LAMINAR INTERACTION THEORY/DATA PRESSURE DISTRIBUTIONS

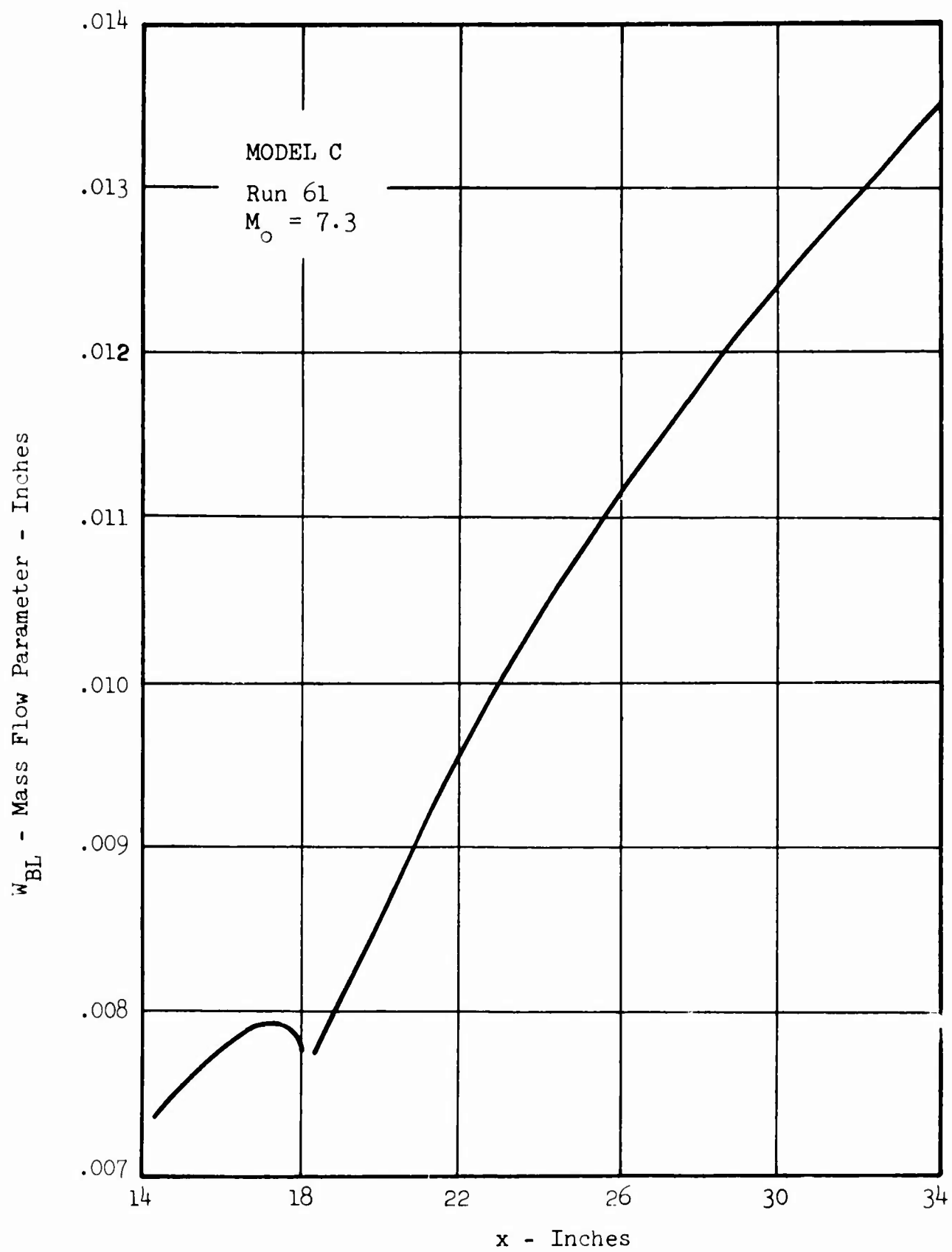


Figure 97 THEORETICAL MASS FLOW VARIATION

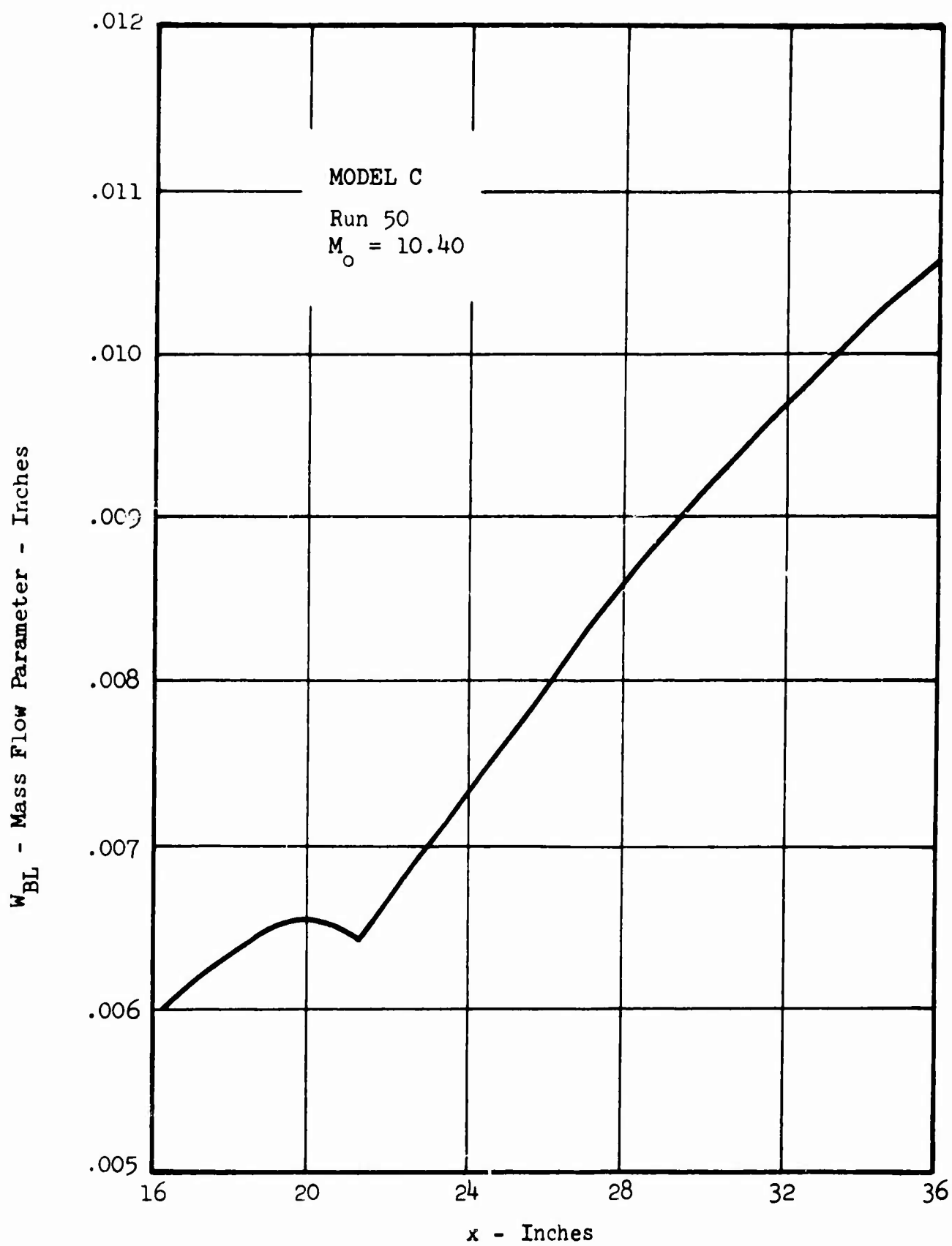


Figure 98 THEORETICAL MASS FLOW VARIATION

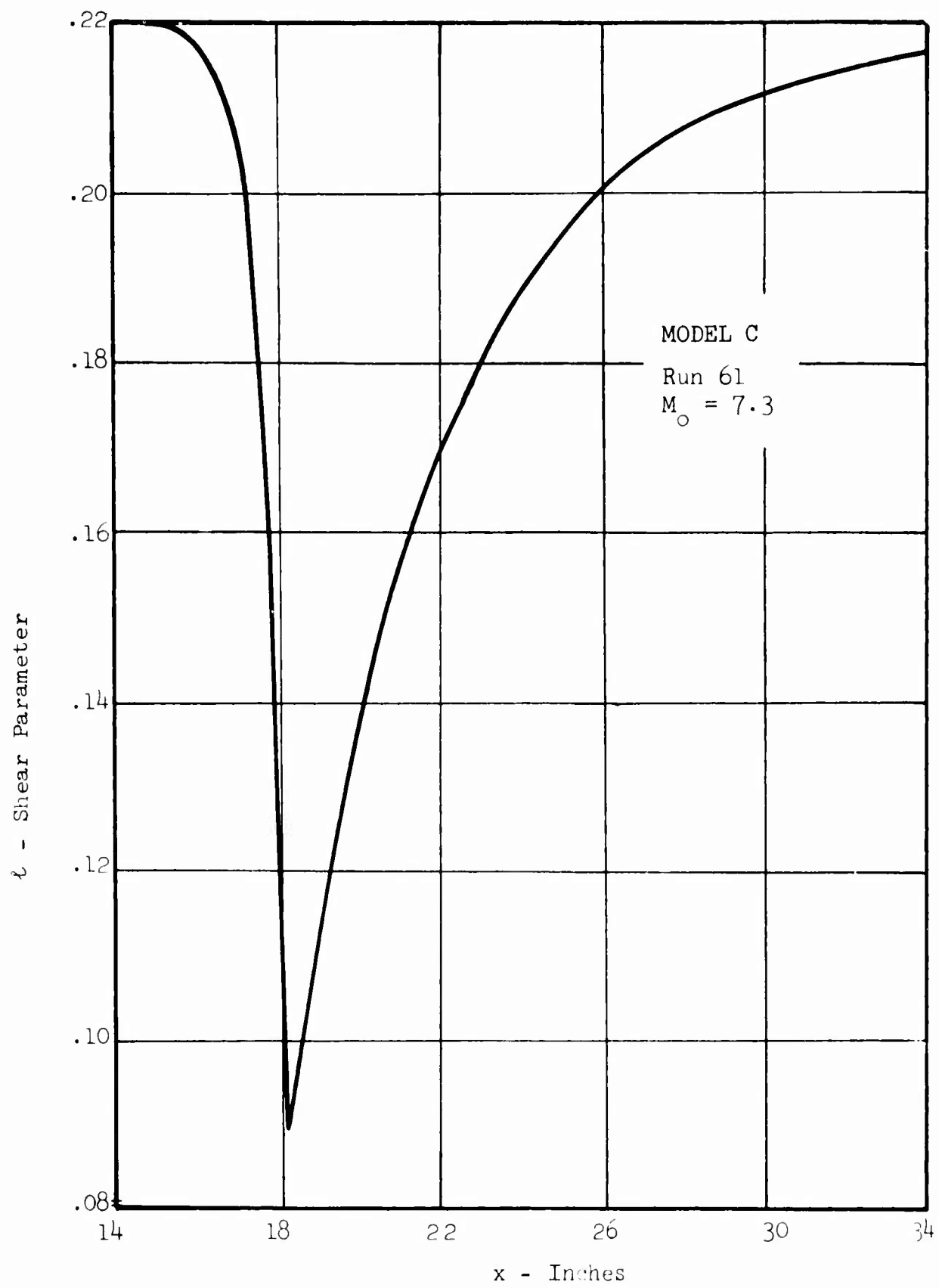


Figure 99 THEORETICAL SHEAR PARAMETER

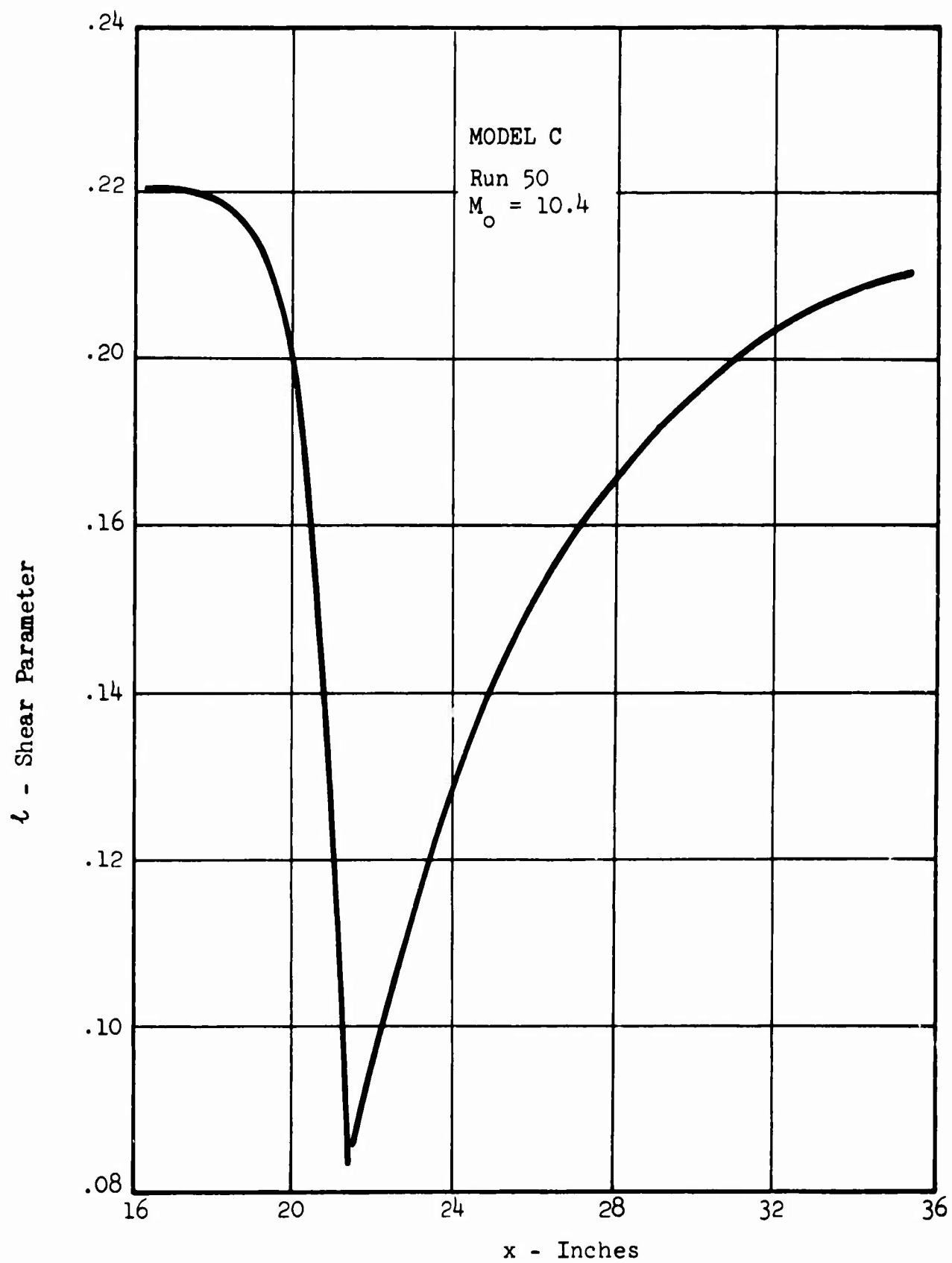
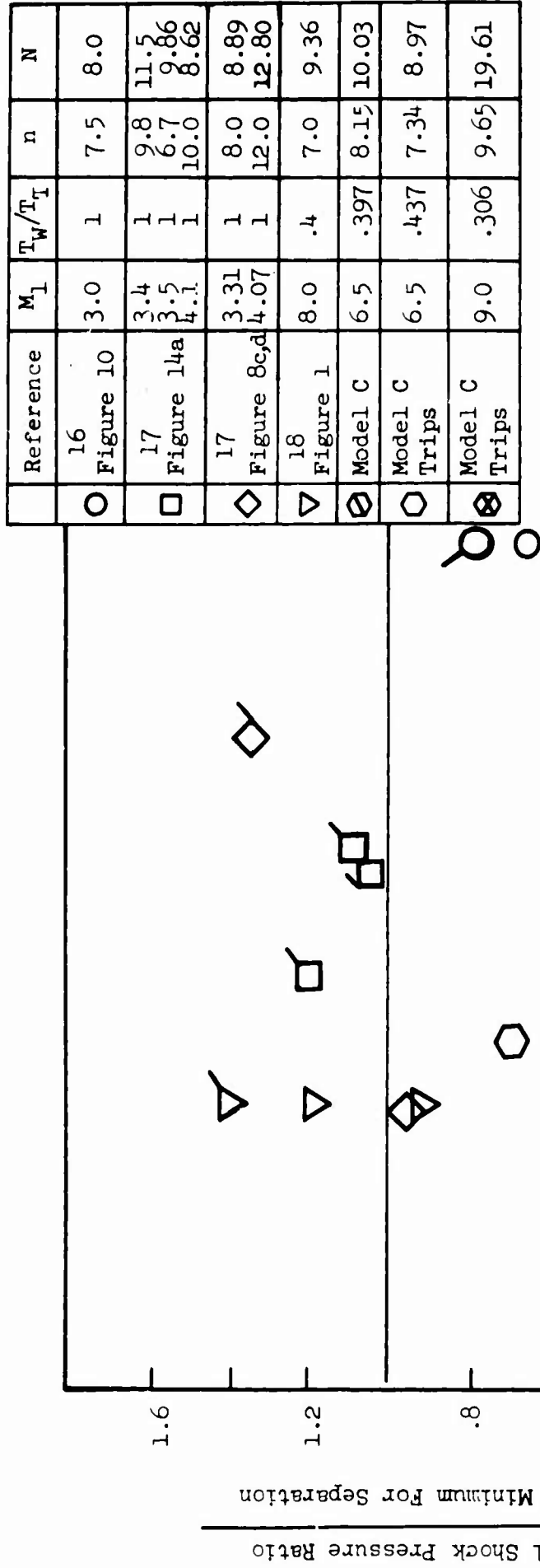


Figure 100 THEORETICAL SHEAR PARAMETER



Note: Flagged Symbols Indicate Turbulent  
Boundary Layer Separation Data

Figure 101 TURBULENT BOUNDARY LAYER SEPARATION  
THEORY/DATA COMPARISON

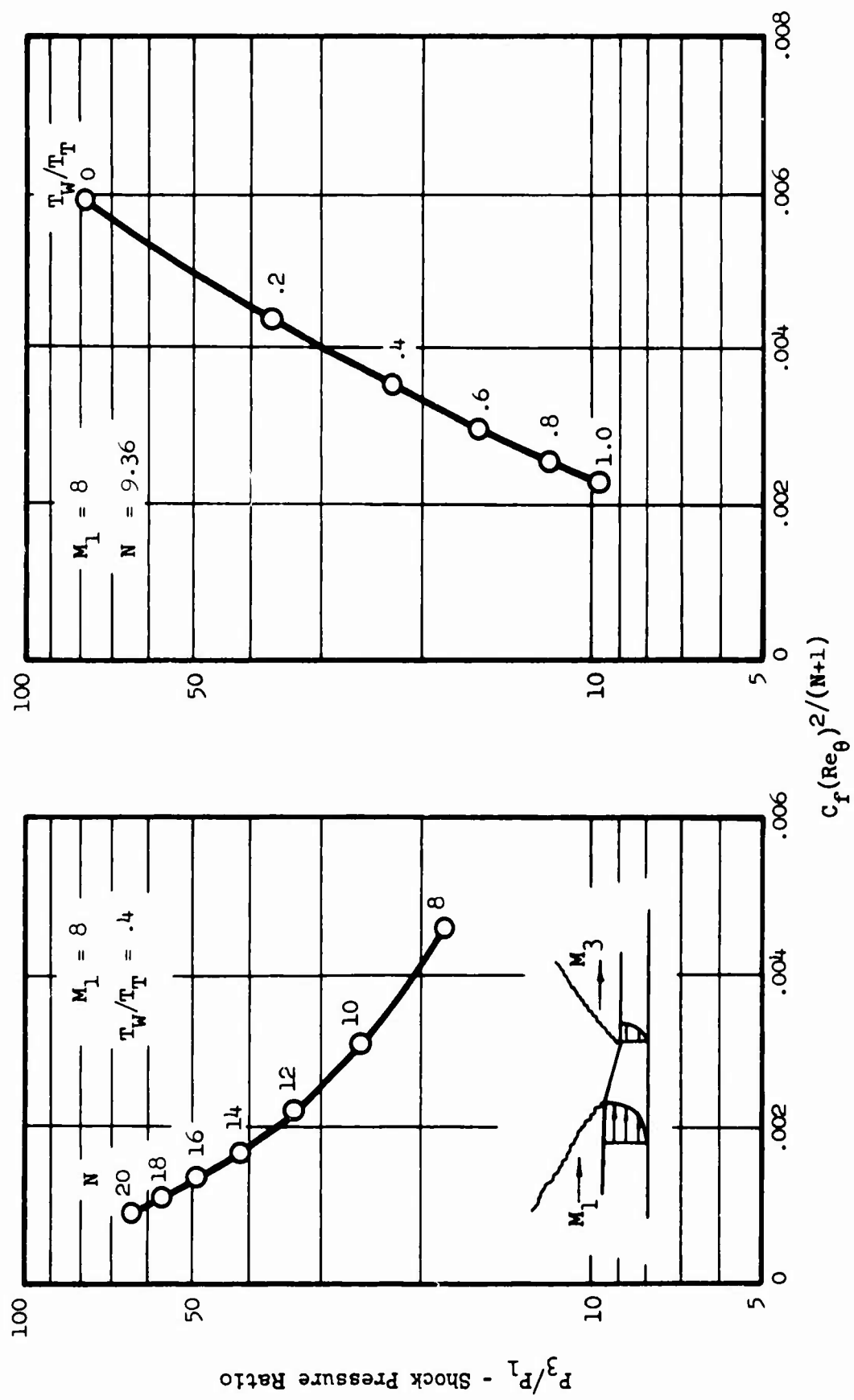


Figure 102 SEPARATION SENSITIVITY TO  $T_w/T_t$  AND  $N$



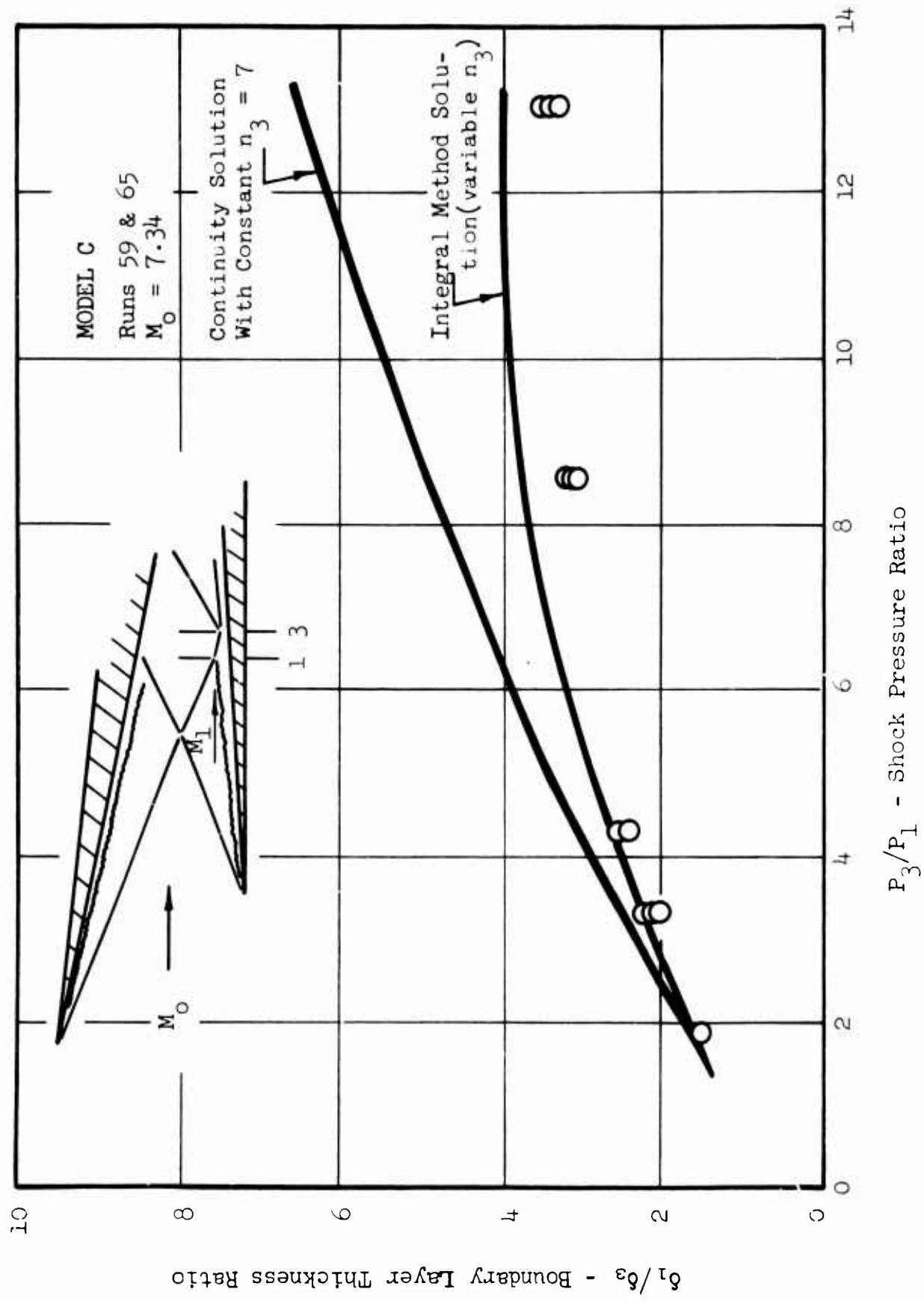


Figure 103 TURBULENT BOUNDARY LAYER THICKNESS  
RATIO THEORY/DATA COMPARISON

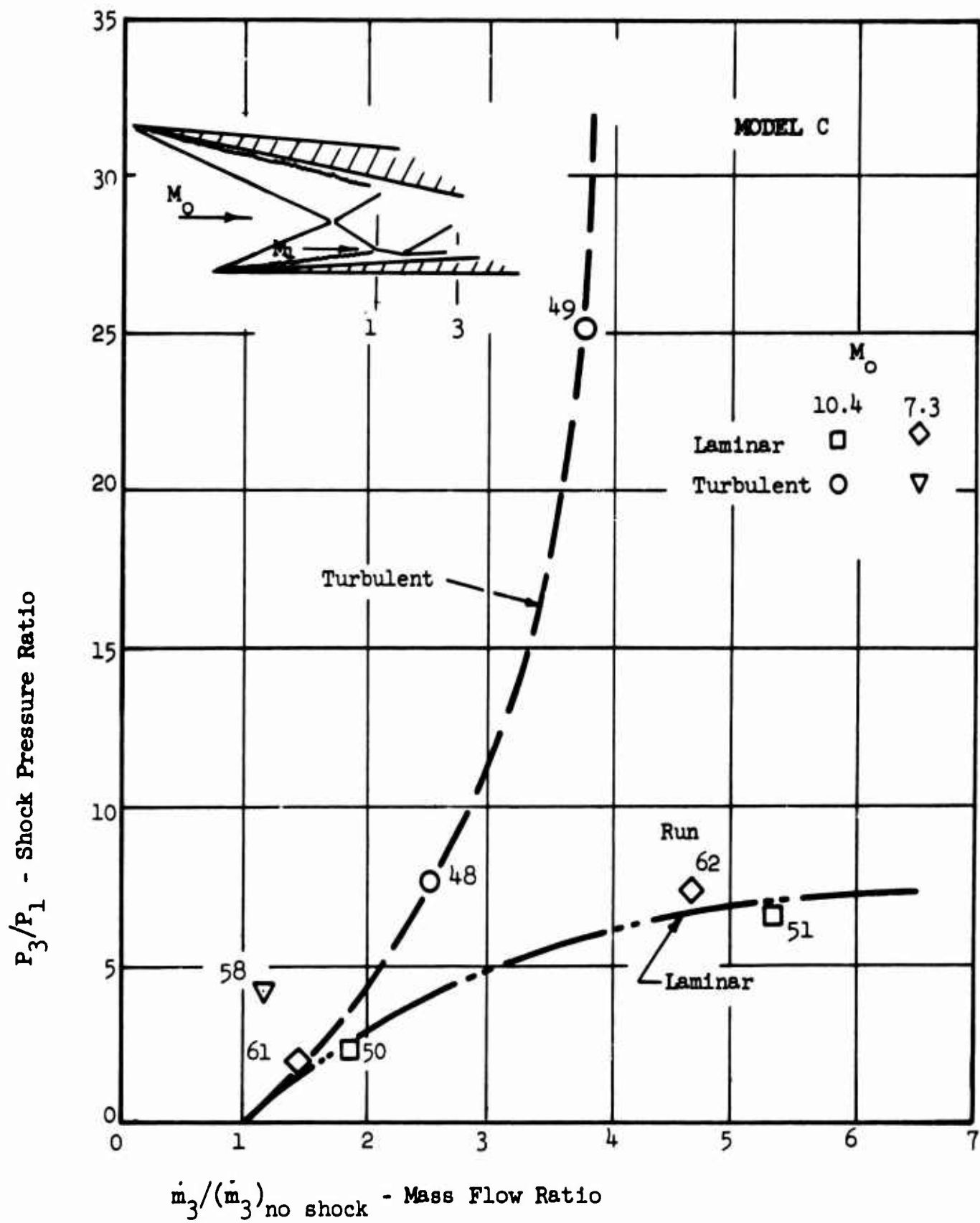


Figure 104 MASS FLOW RATIO SUMMARY

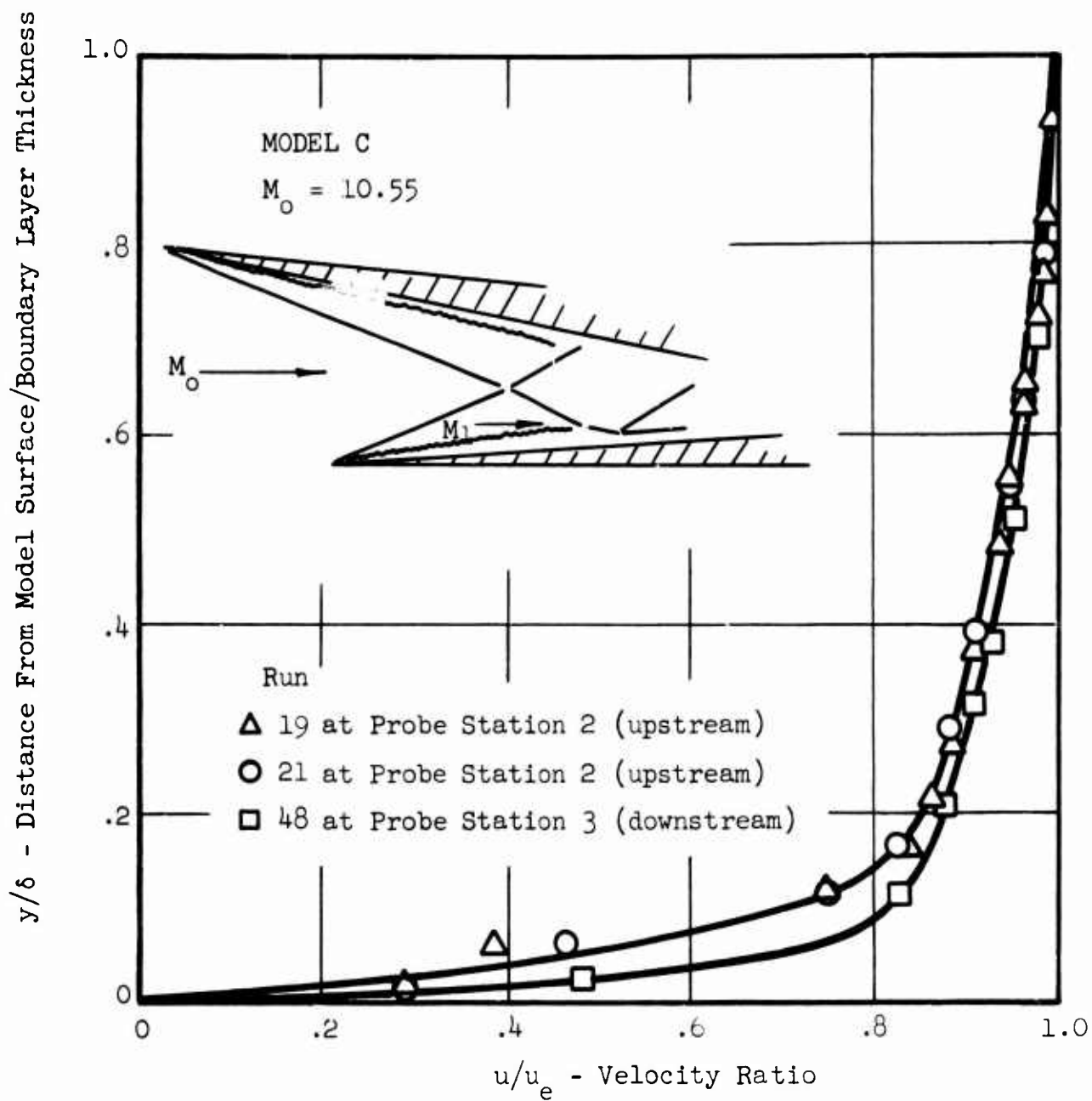


Figure 105 MEASURED PROFILE SHAPE CHANGE ACROSS INTERACTION

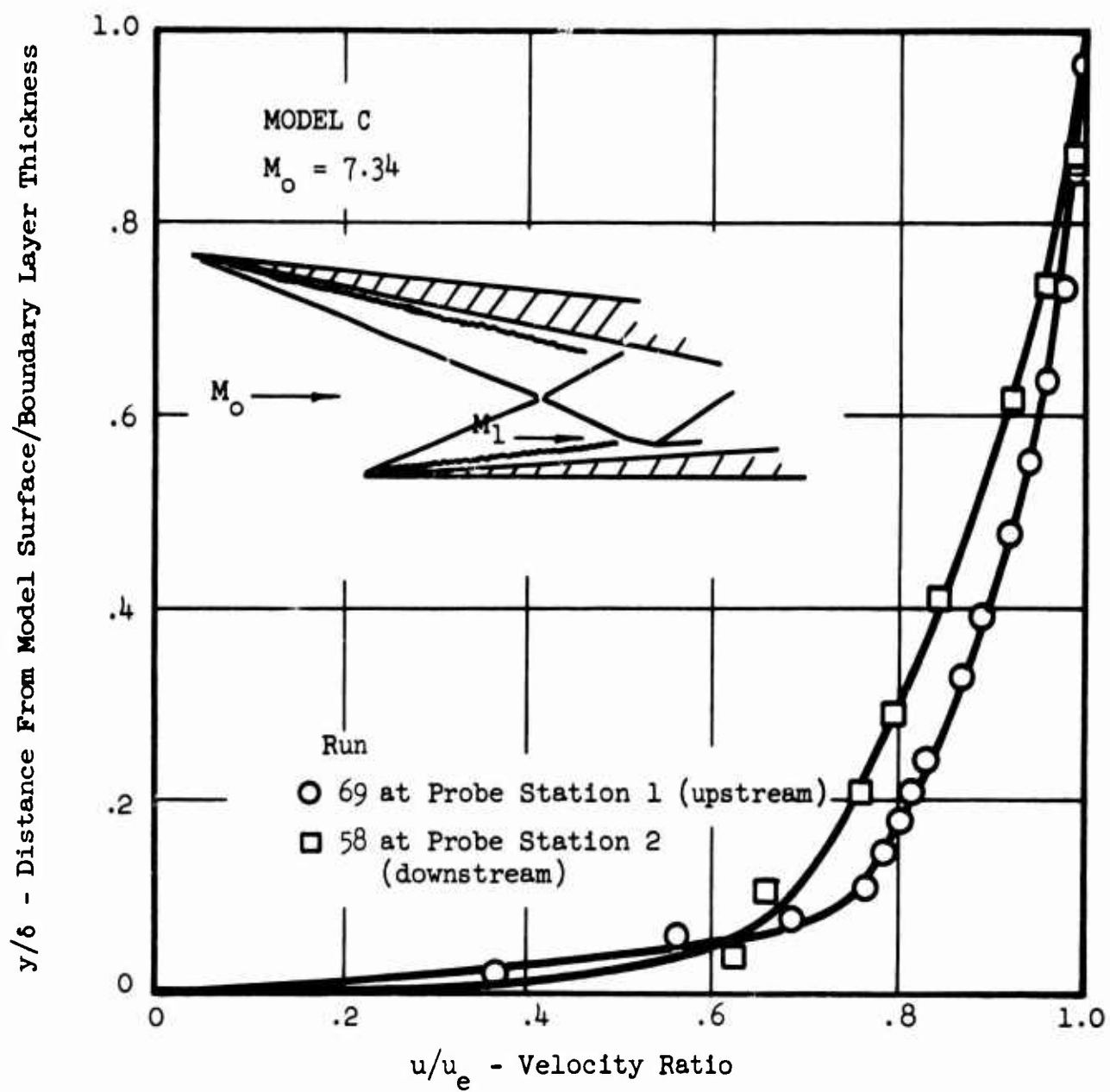


Figure 106 MEASURED PROFILE SHAPE CHANGE ACROSS INTERACTION

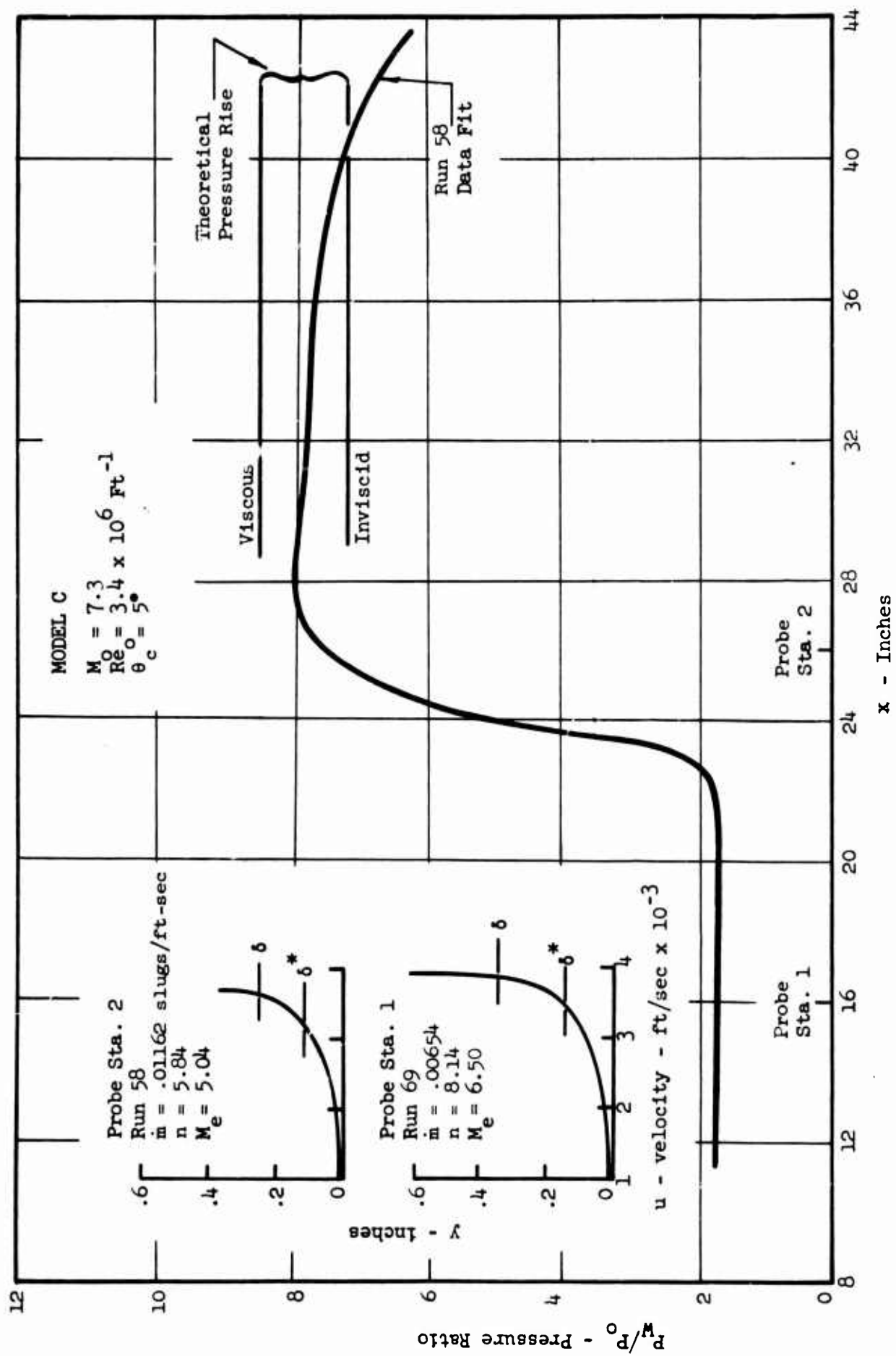


Figure 107 TURBULENT-TURBULENT INTERACTION DATA  
COMPOSITE

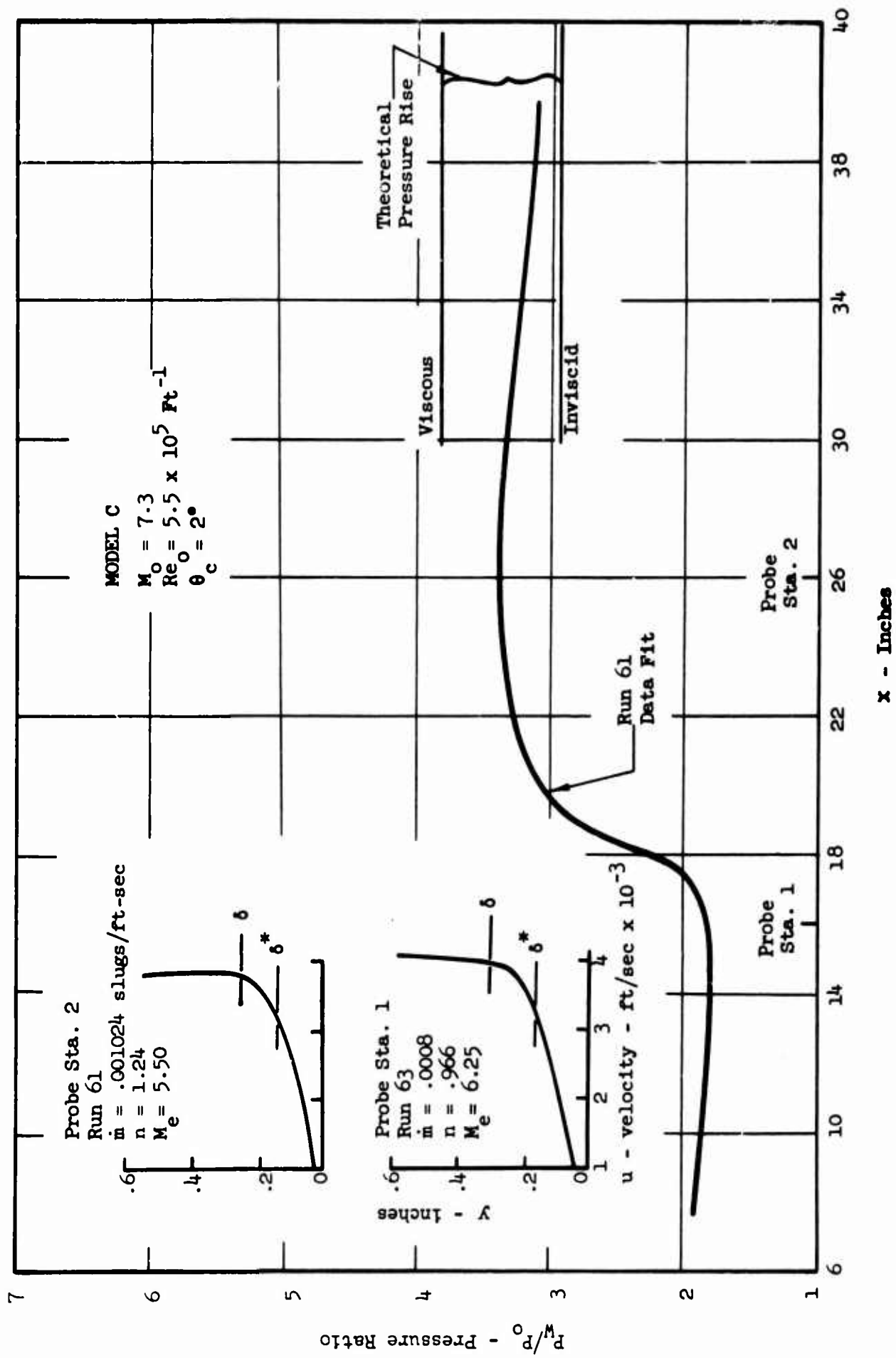


Figure 108 LAMINAR-LAMINAR INTERACTION DATA COMPOSITE

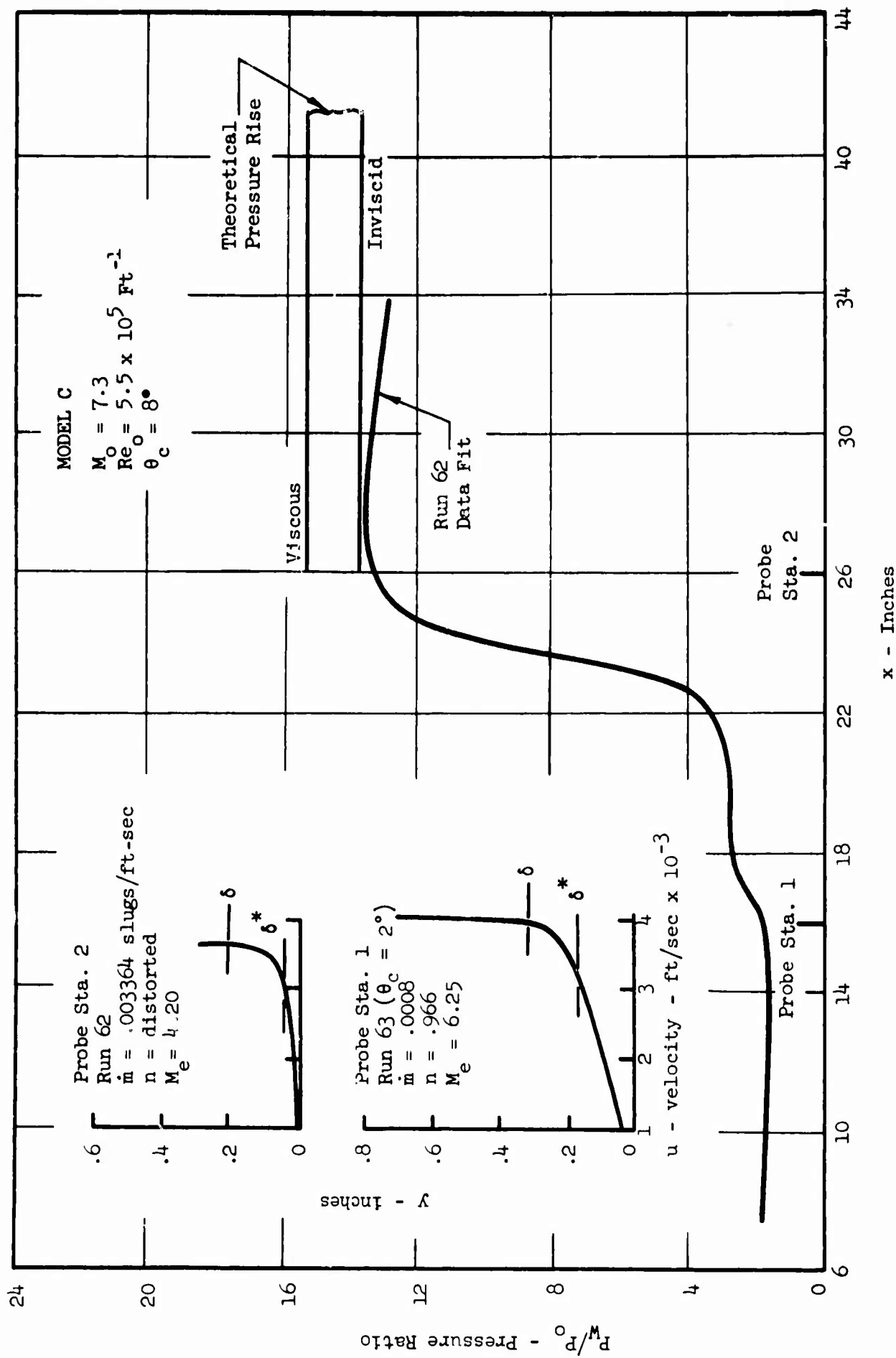


Figure 109 LAMINAR-TURBULENT INTERACTION DATA COMPOSITE

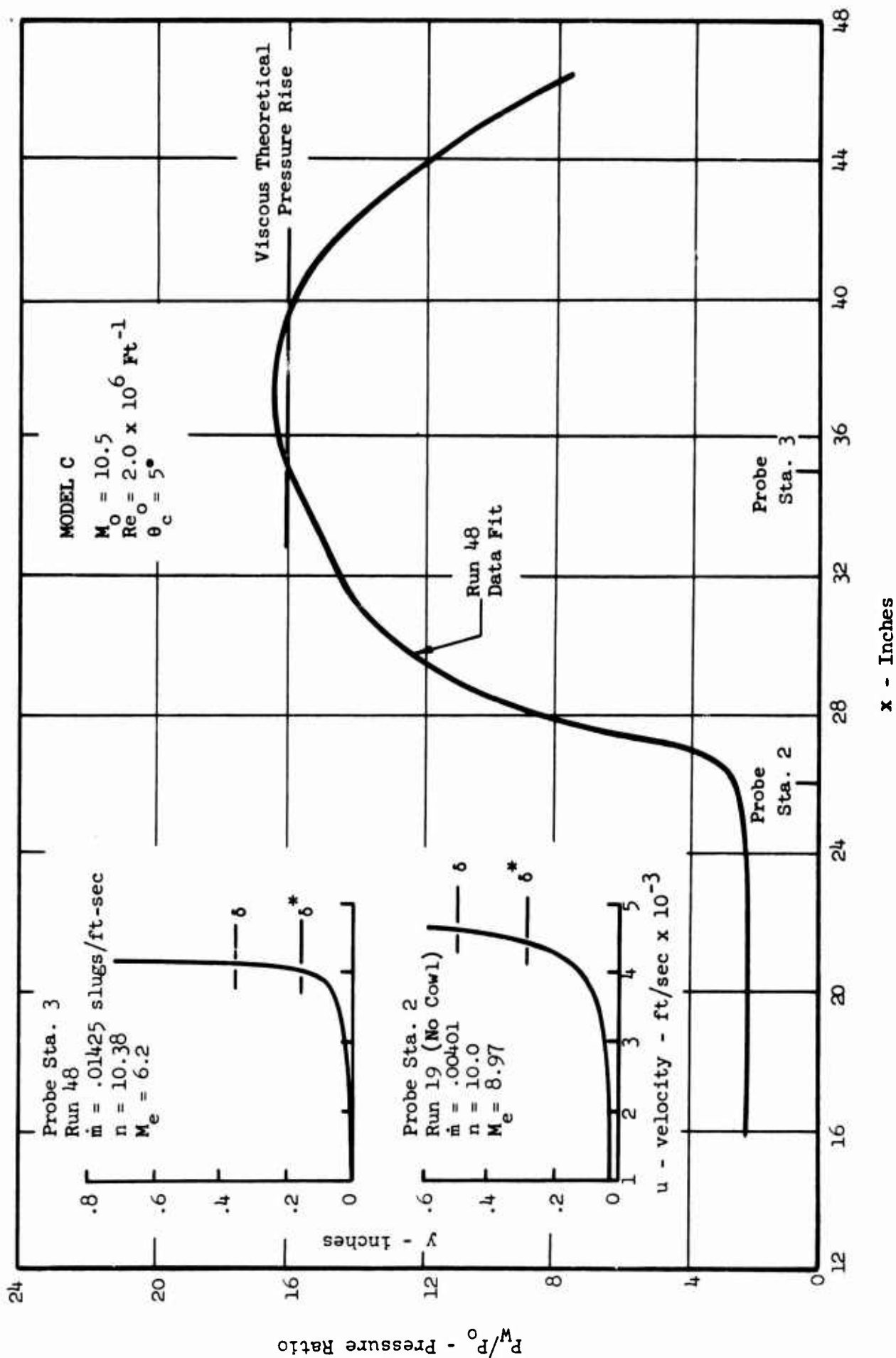


Figure 110 TURBULENT-TURBULENT INTERACTION DATA COMPOSITE



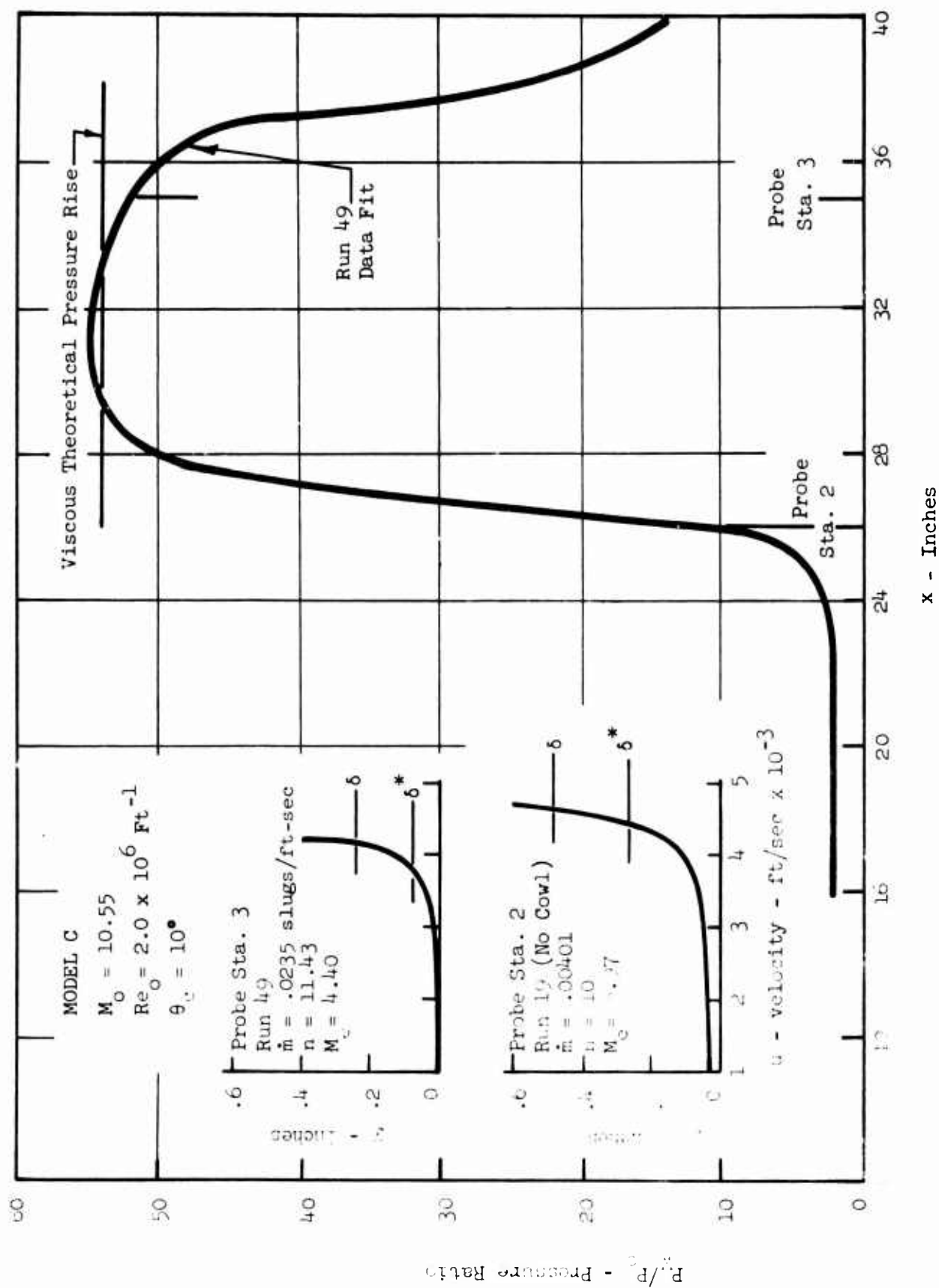


FIGURE 11. TURBULENT-TURBULENT INTERACTION DATA COMPOSITE

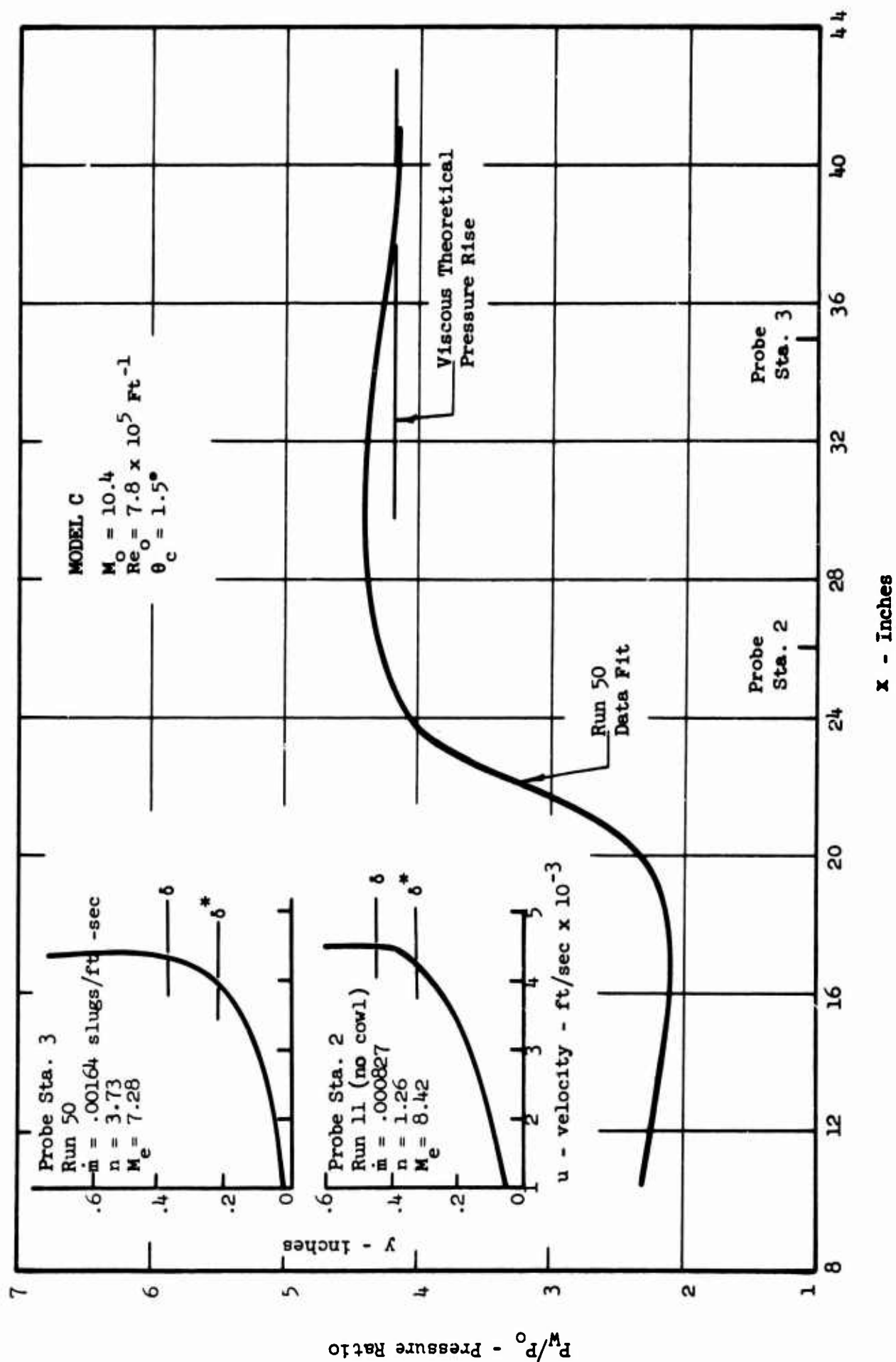


Figure 112 LAMINAR-TRANSITIONAL INTERACTION DATA COMPOSITE

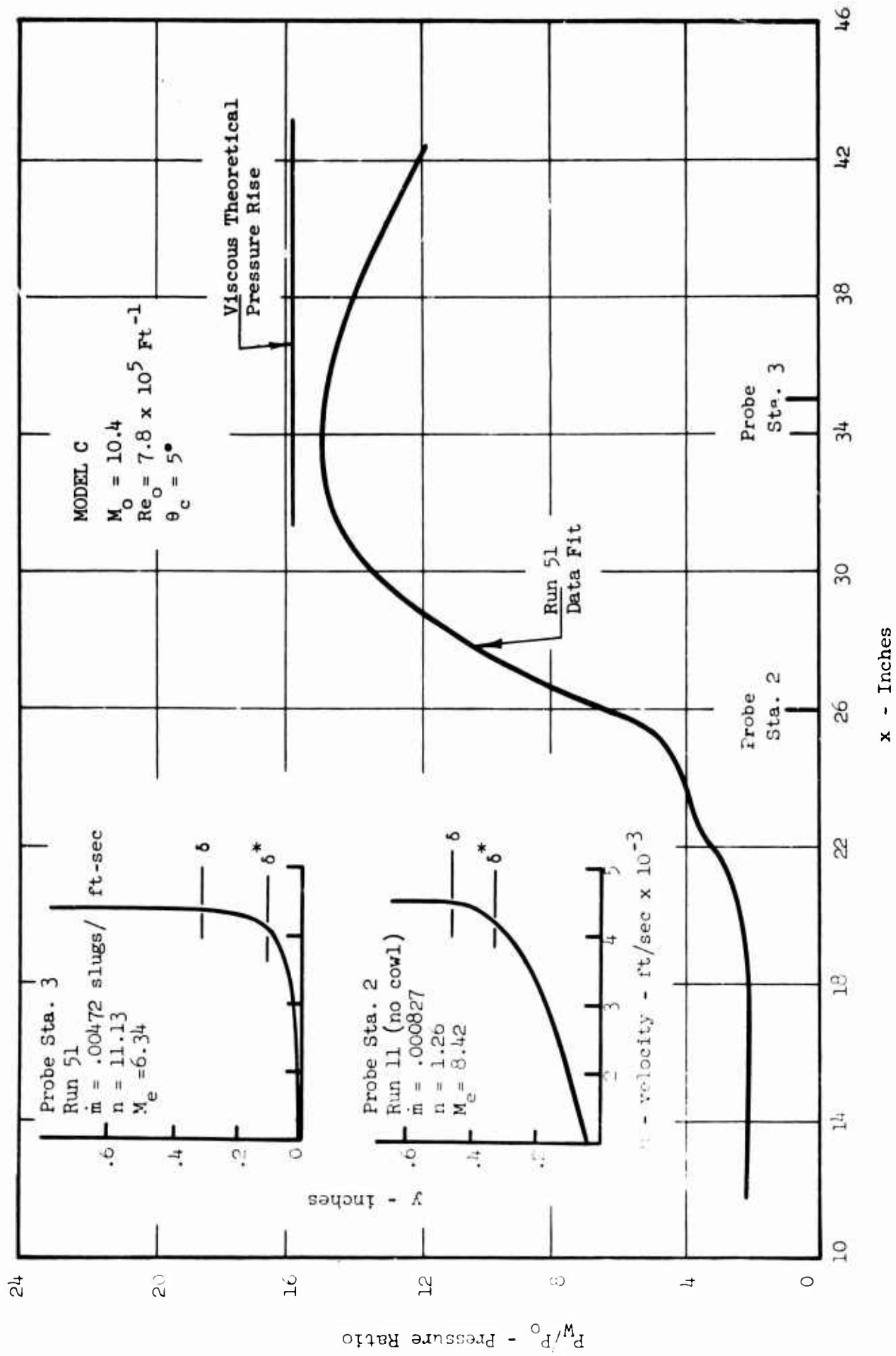
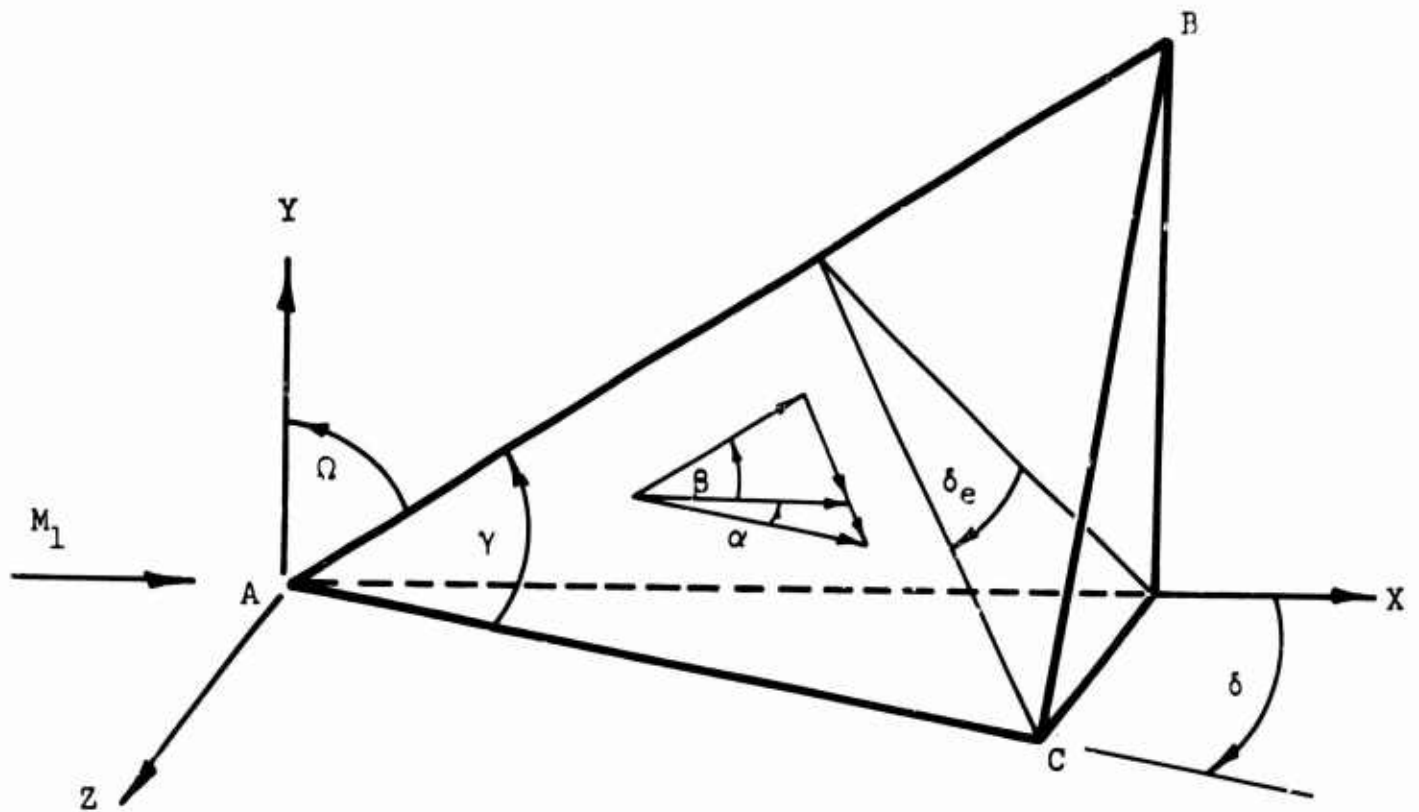


Figure 11 LAMINAR-TURBULENT INTERACTION DATA COMPOSITE



$$1. \delta_e = \arctan (\tan \delta / \cos \Omega)$$

In Plane ABC:

$$2. \gamma = \arcsin (\sin \delta / \sin \delta_e)$$

$$3. \beta = \arctan M_{2N} / \sqrt{T_1/T_2} M_1 \sin \Omega$$

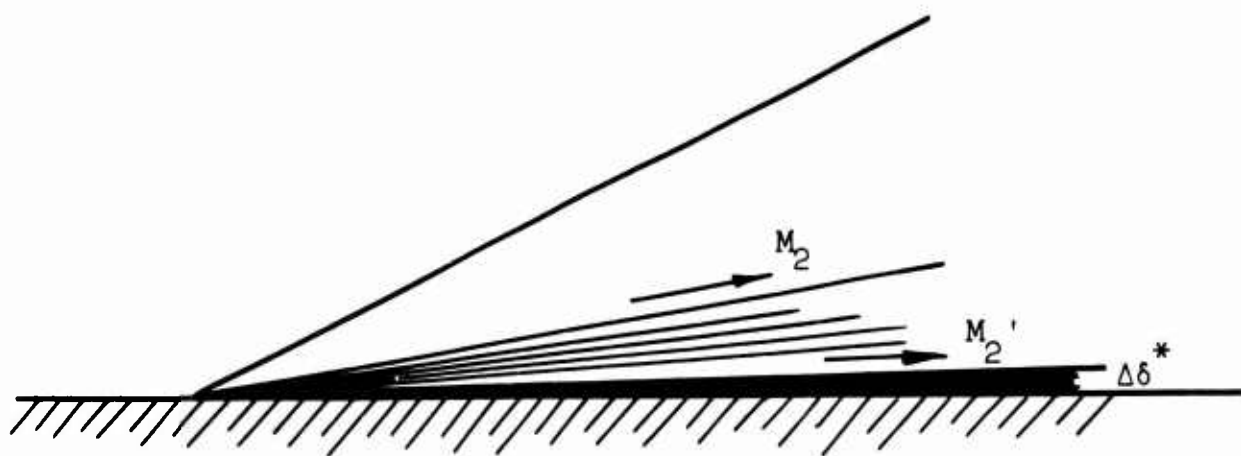
Where  $M_{2N}$  = normal component of the downstream Mach number

$$4. \alpha = \Delta v = (\gamma - \beta)$$

Figure 114 SHOCK-EXPANSION TECHNIQUE CALCULATION PROCEDURE

Diagram illustrating a Vane Generated Shock Sheet. The flow is characterized by upstream Mach number  $M_1$  and downstream Mach number  $Q_L$ . The vane surface is shown, and the shock sheet is generated by the vane. Points A are marked on the vane surface and the shock sheet.

Note: Shock-Expansion Technique:  $\Delta\delta^* = 0$   
Modified Shock-Expansion Technique:  $\Delta\delta^* \neq 0$



Section A-A

Figure 115 SHOCK-EXPANSION TECHNIQUE-FLOW MODEL

# MODEL D

- ① Inviscid strip Theory
- ② Viscous Strip Technique
- ③ Modified Shock-Expansion Technique

Symbol Key

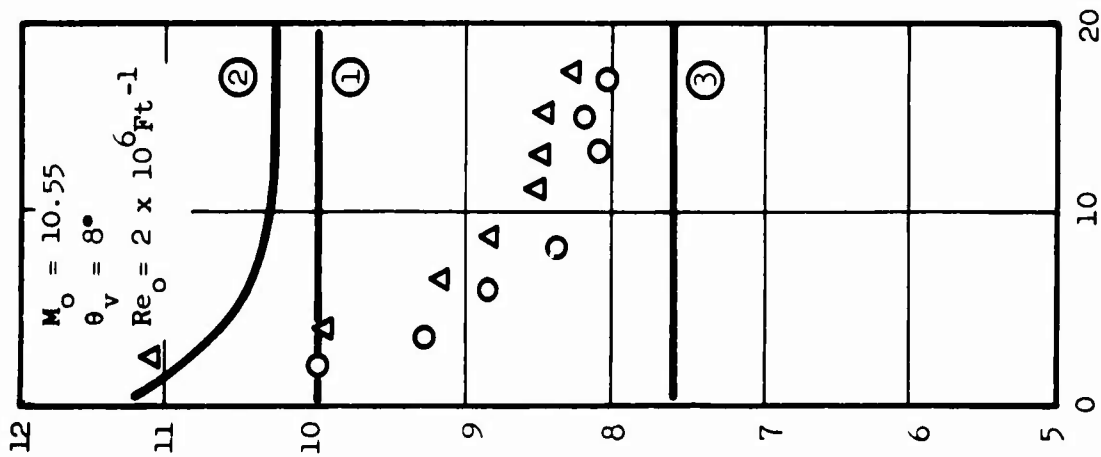
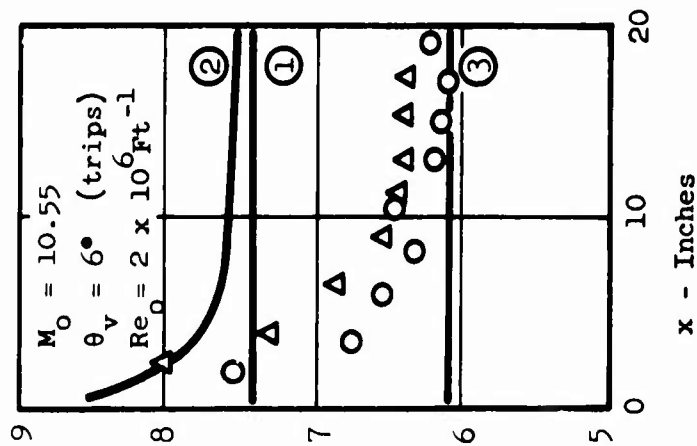
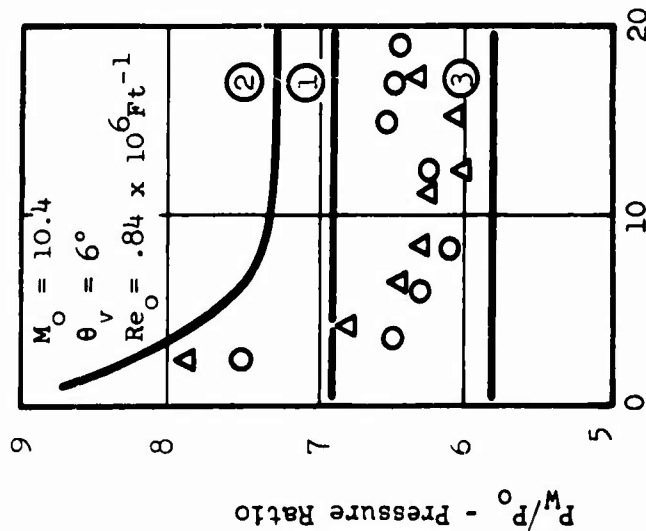
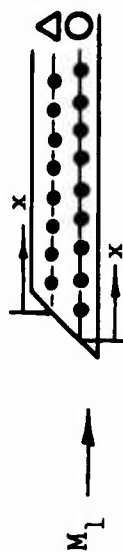


Figure 116 VANE PRESSURE DISTRIBUTIONS

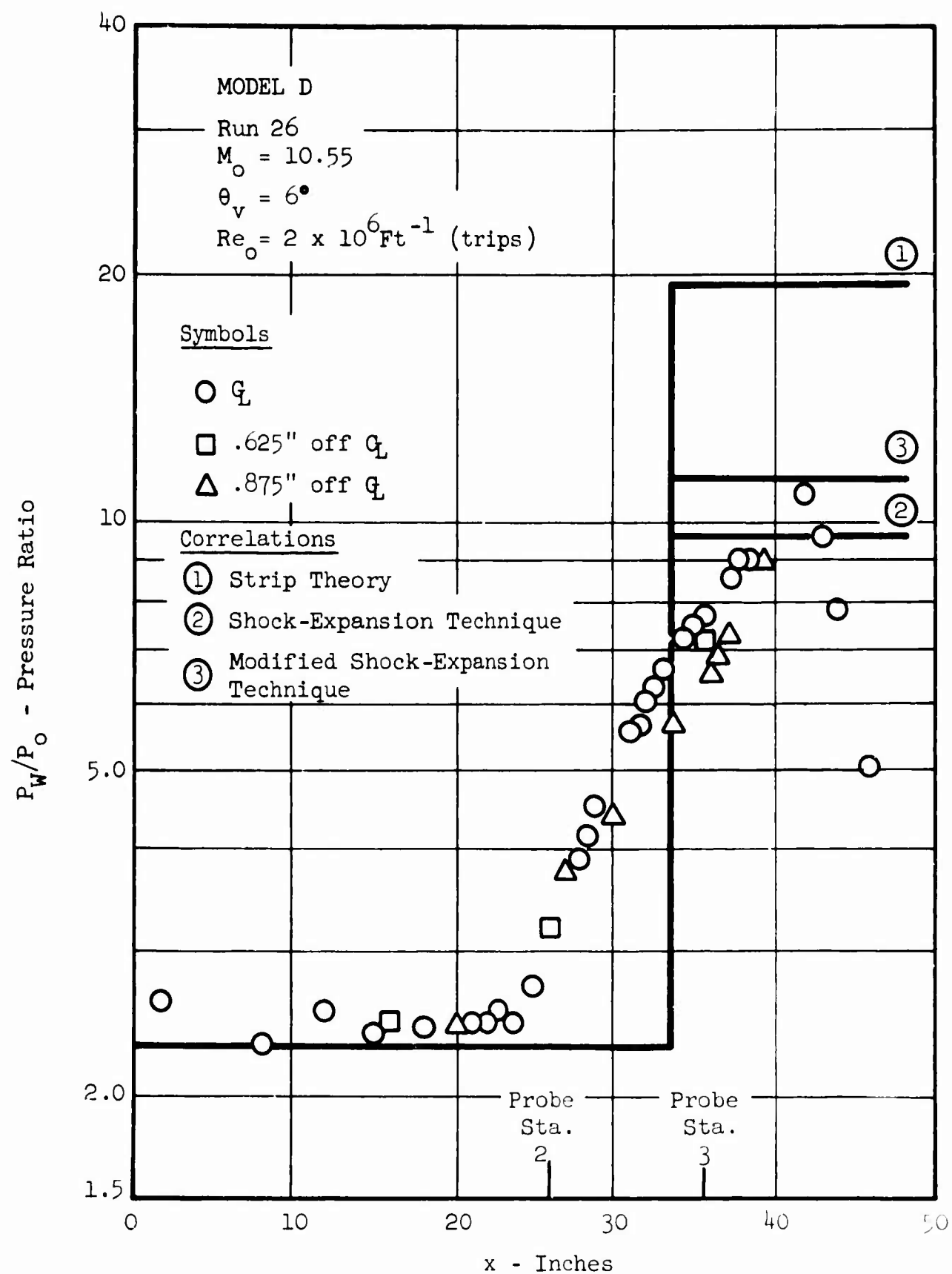


Figure 117 RAMP PRESSURE RISE THEORY/DATA COMPARISON

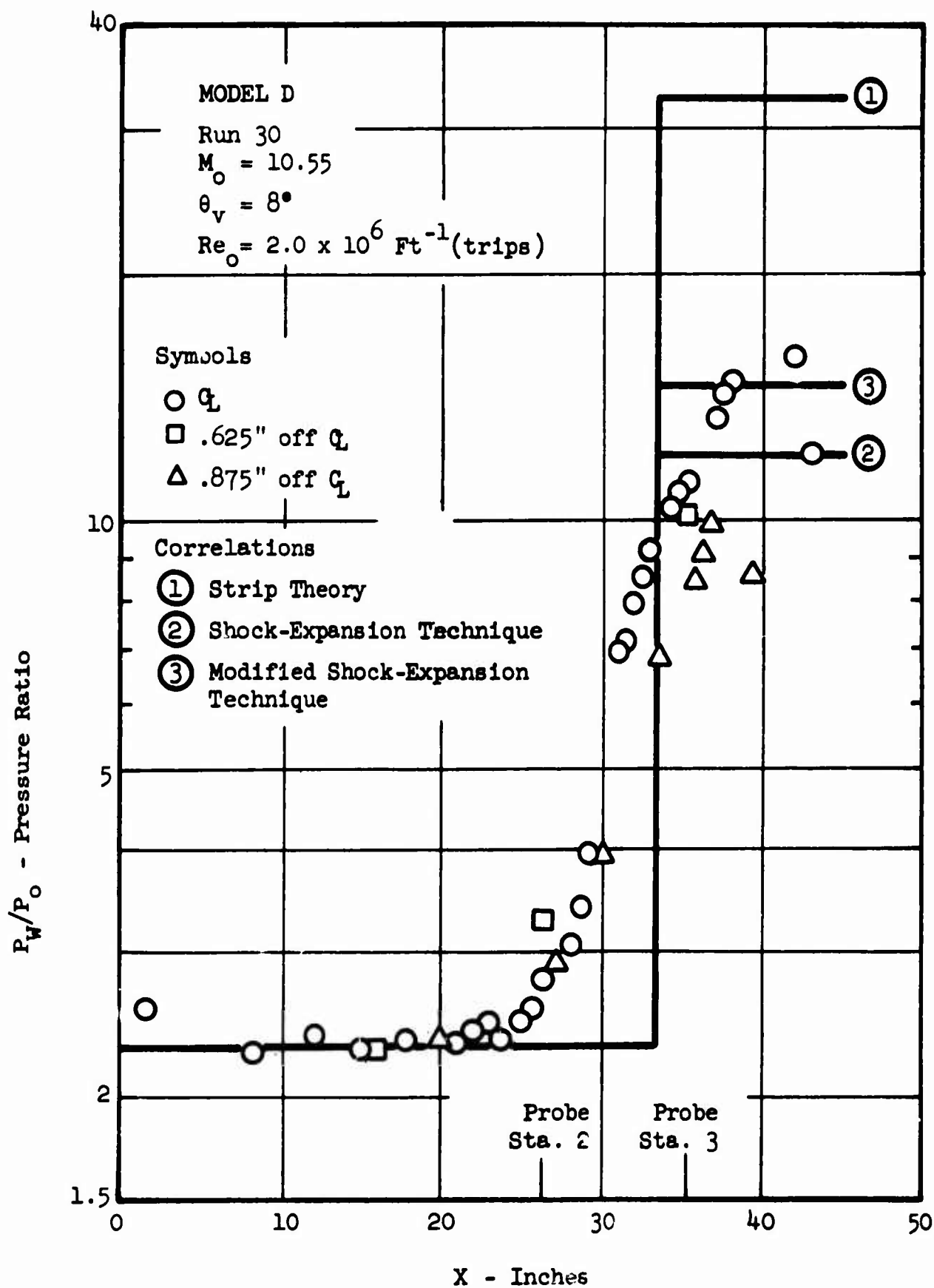


Figure 118 RAMP PRESSURE RISE THEORY/DATA COMPARISON



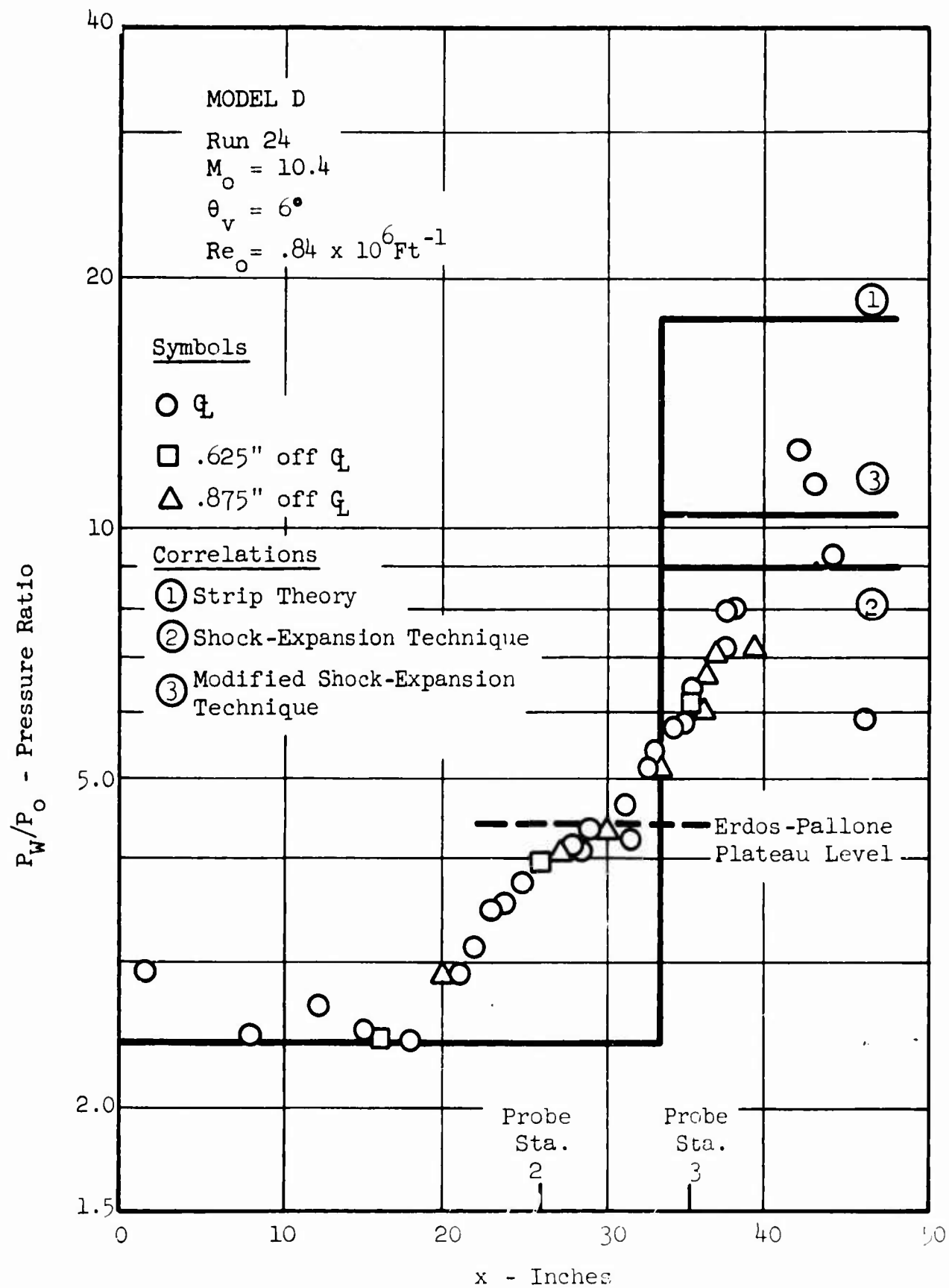


Figure 119 RAMP PRESSURE RISE THEORY/DATA COMPARISON

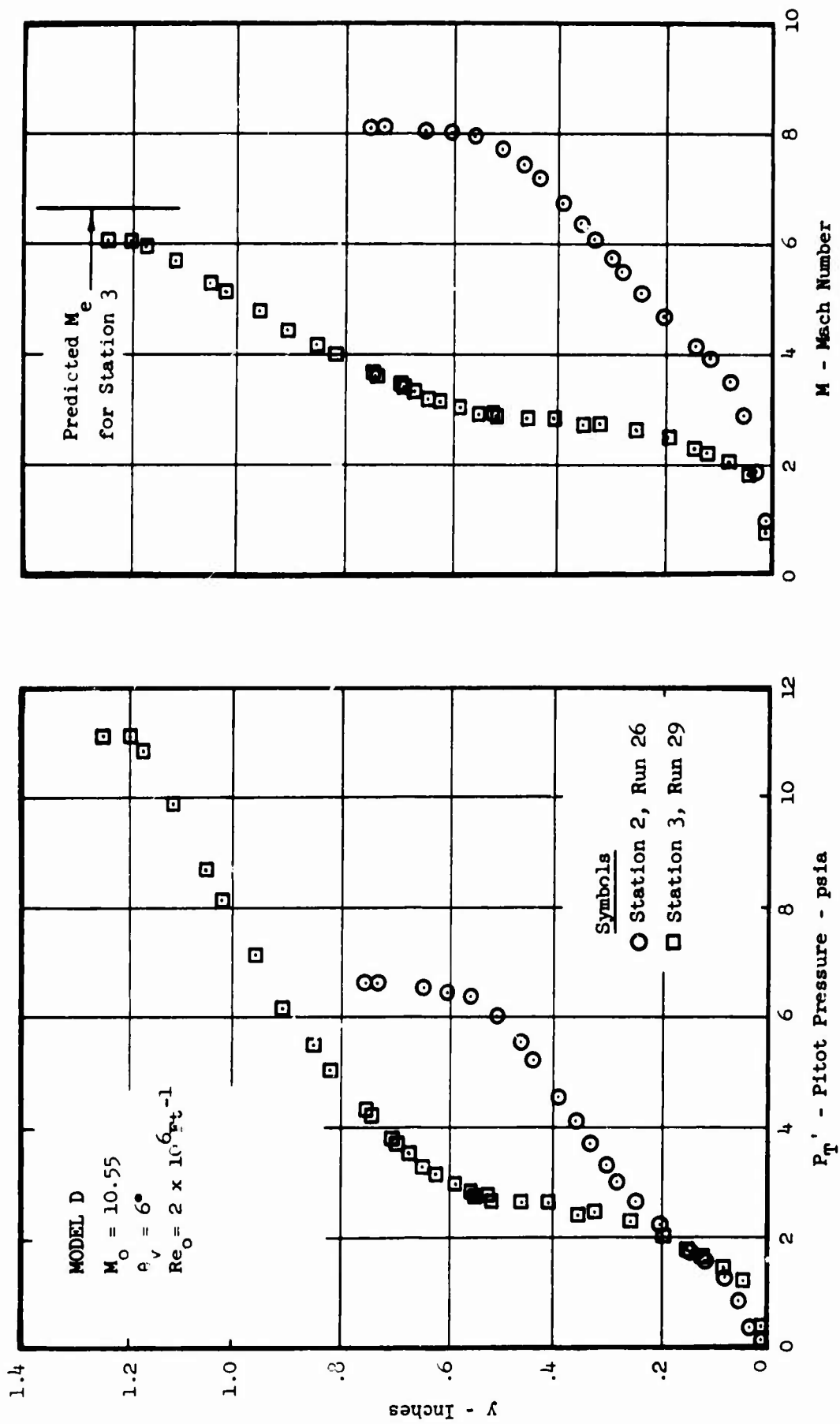


Figure 120 RAMP BOUNDARY LAYER PROFILE DATA

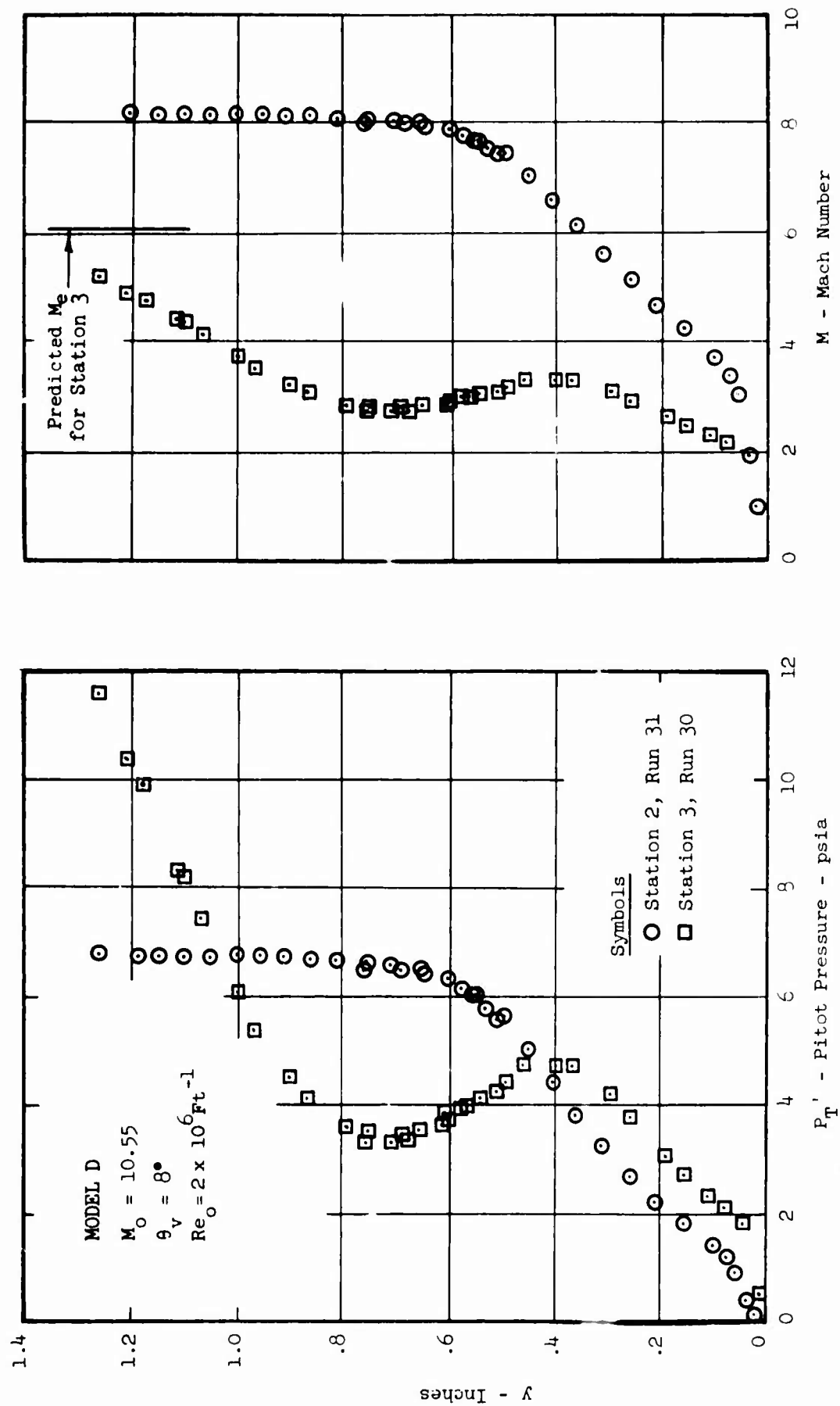


Figure 121 RAMP BOUNDARY LAYER PROFILE DATA

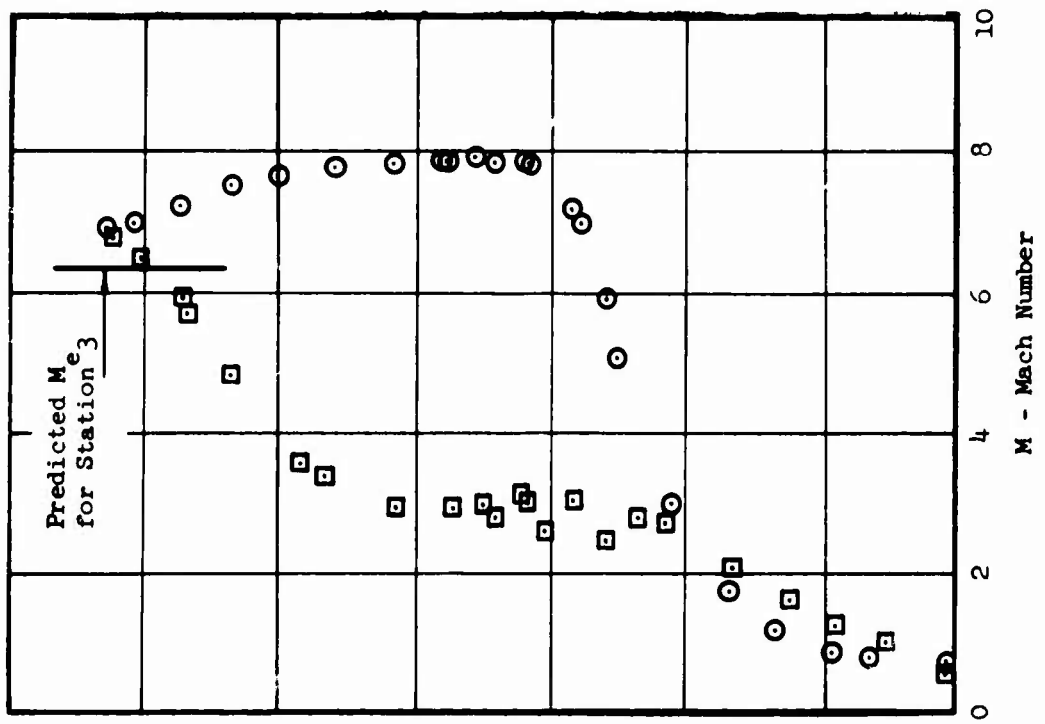
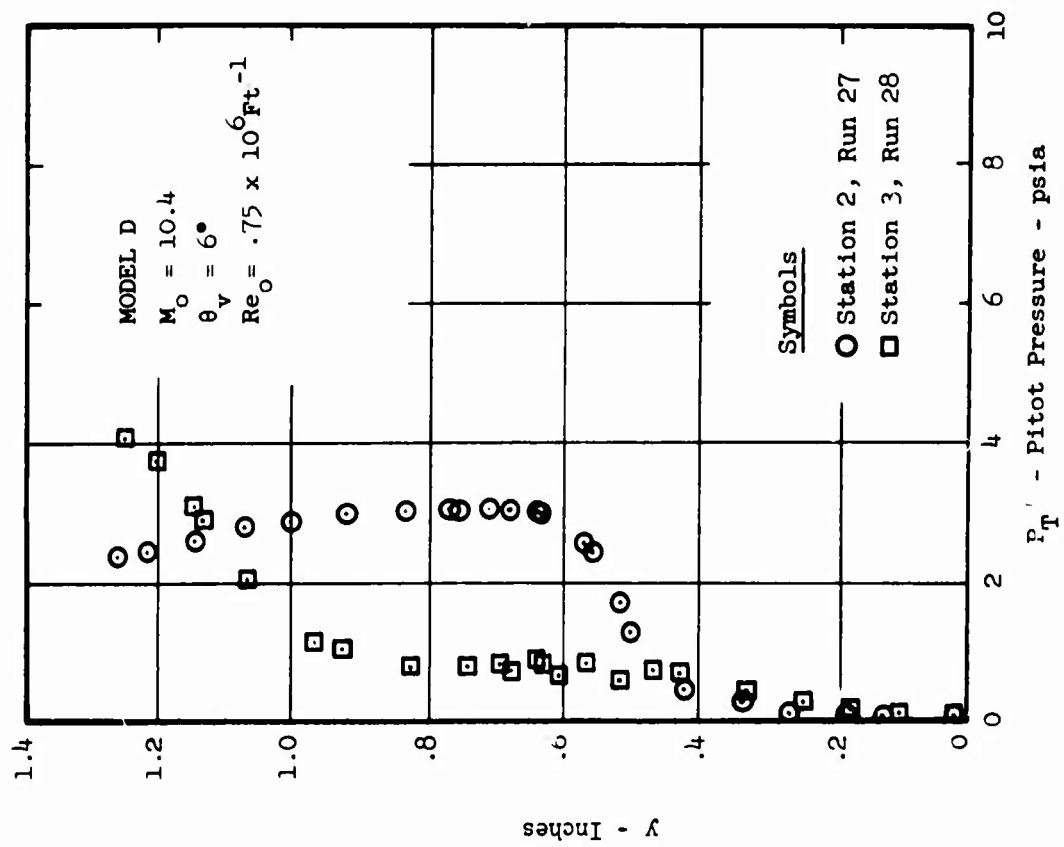


Figure 122 RAMP BOUNDARY LAYER PROFILE DATA

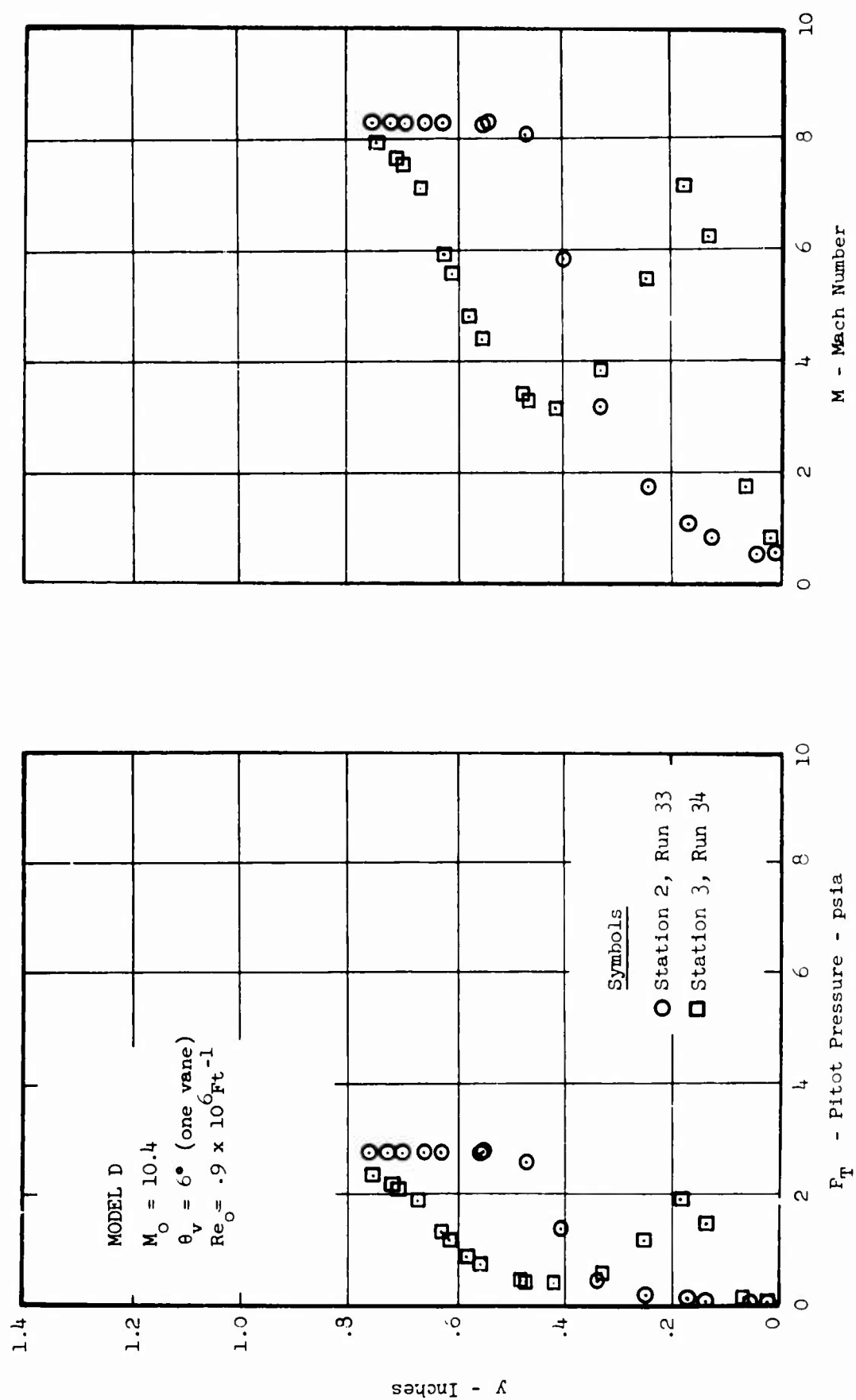


Figure 123 RAMP BOUNDARY LAYER PROFILE DATA

MODEL D (Probe Station 3 Profile Data)

Symbols

- Turbulent Flow,  $Re_o = 2.0 \times 10^6 \text{ Ft}^{-1}$  (trips)
- △ Laminar Flow,  $Re_o = .8 \times 10^6 \text{ Ft}^{-1}$
- One Vane - Laminar Flow,  $Re_o = .8 \times 10^6 \text{ Ft}^{-1}$

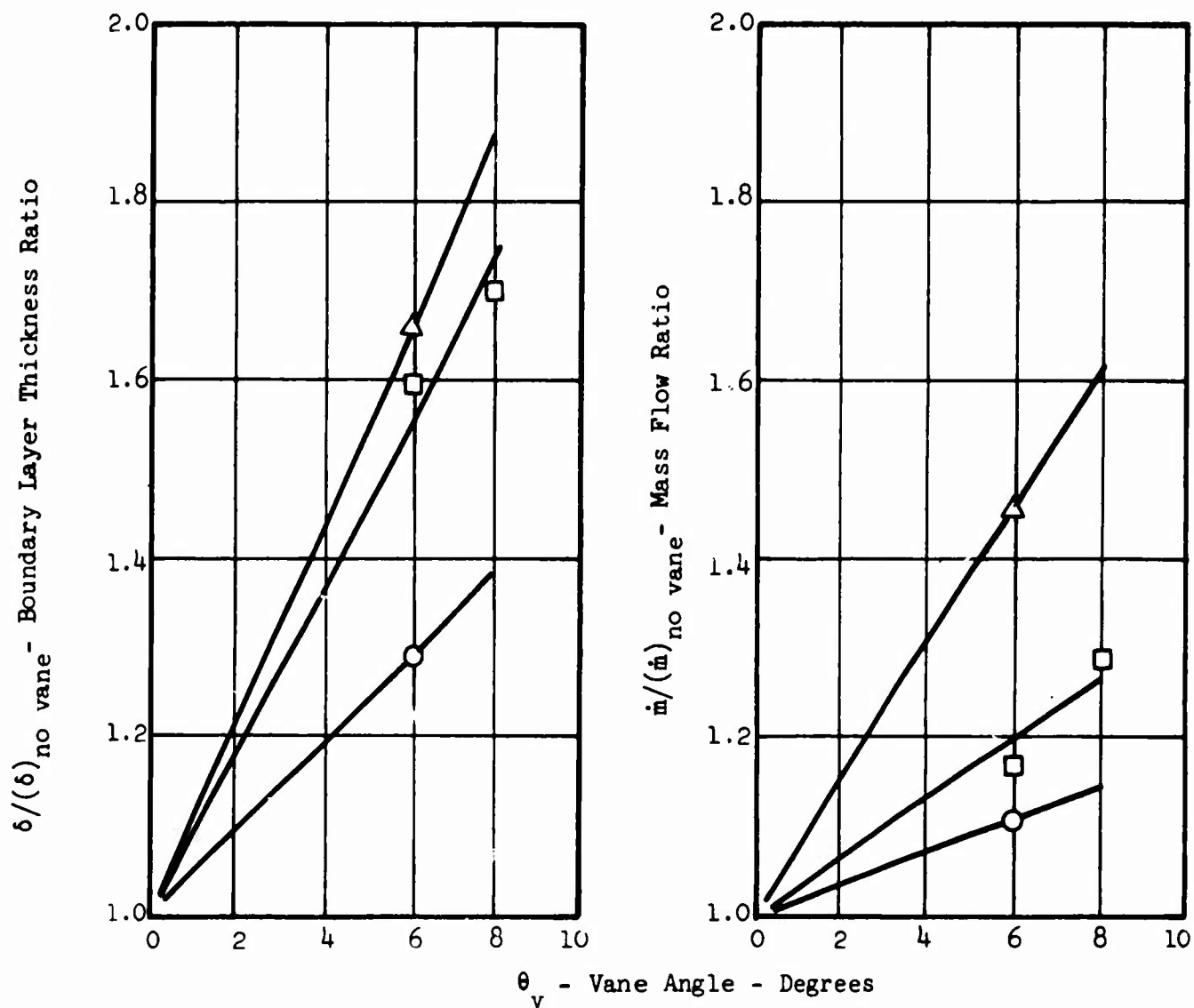


Figure 124 RAMP BOUNDARY LAYER THICKNESS AND MASS FLOW VARIATION

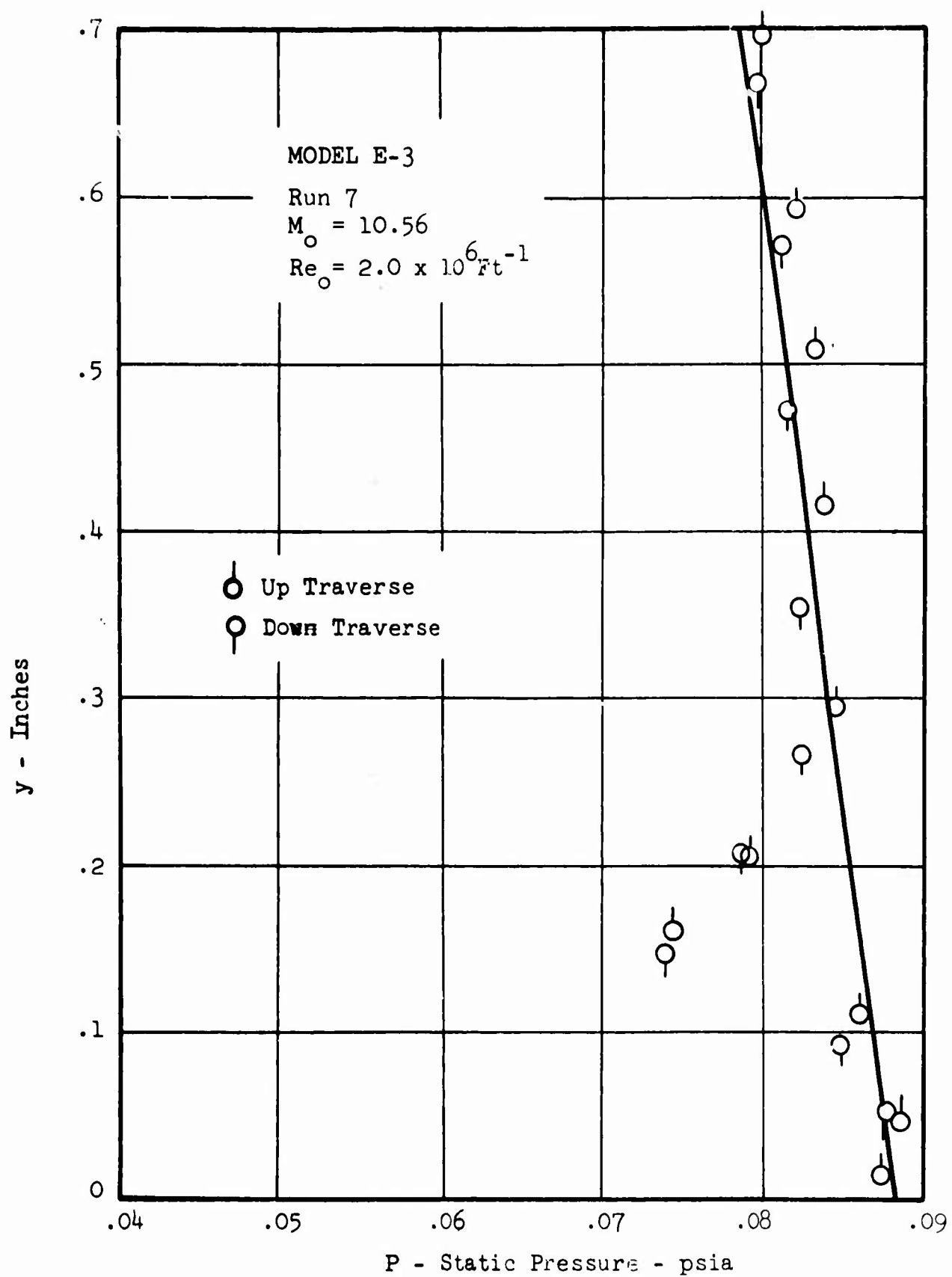


Figure 125 STATIC PRESSURE PROFILE THEORY/DATA COMPARISON

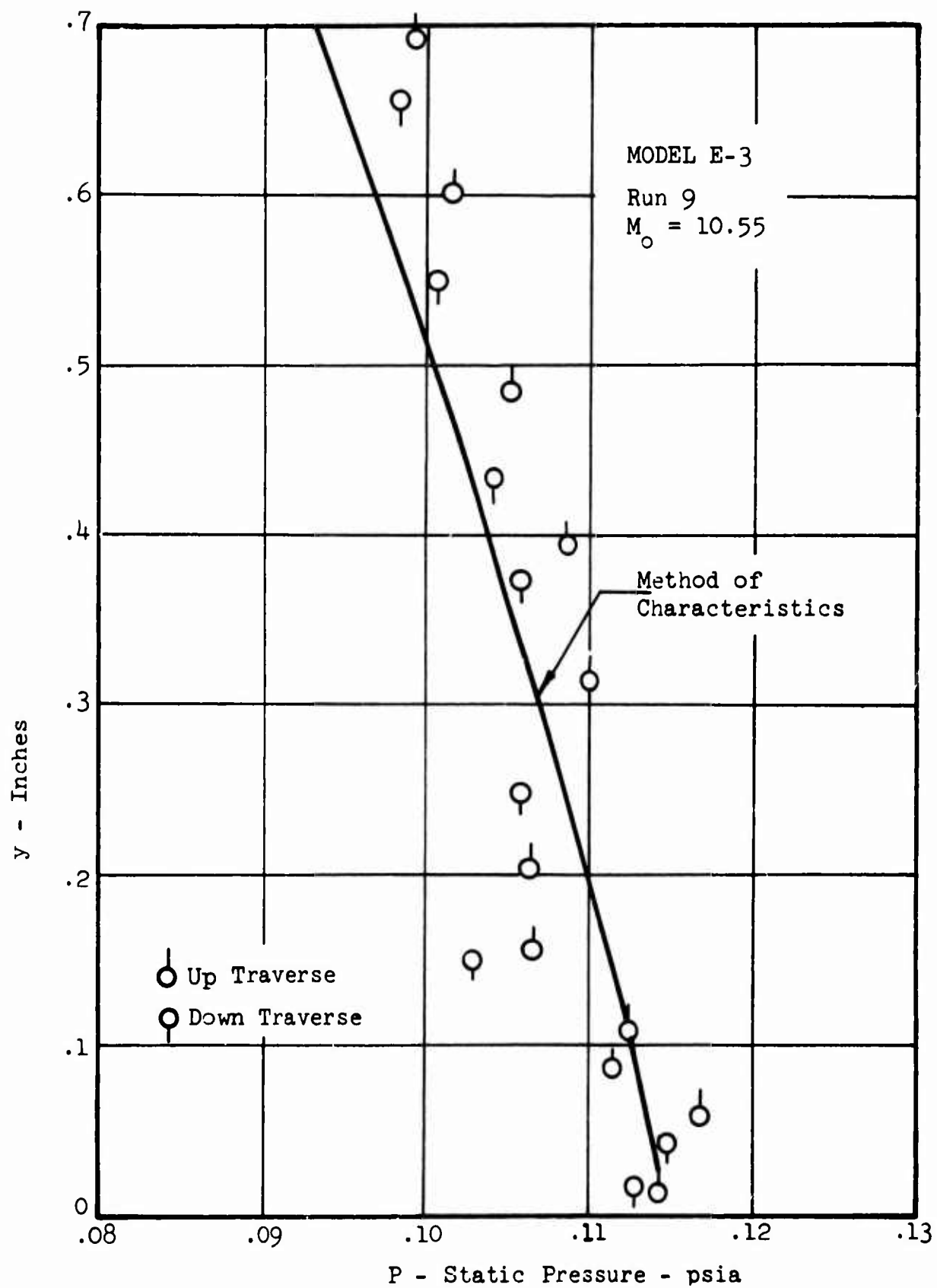


Figure 126 STATIC PRESSURE PROFILE THEORY/DATA COMPARISON



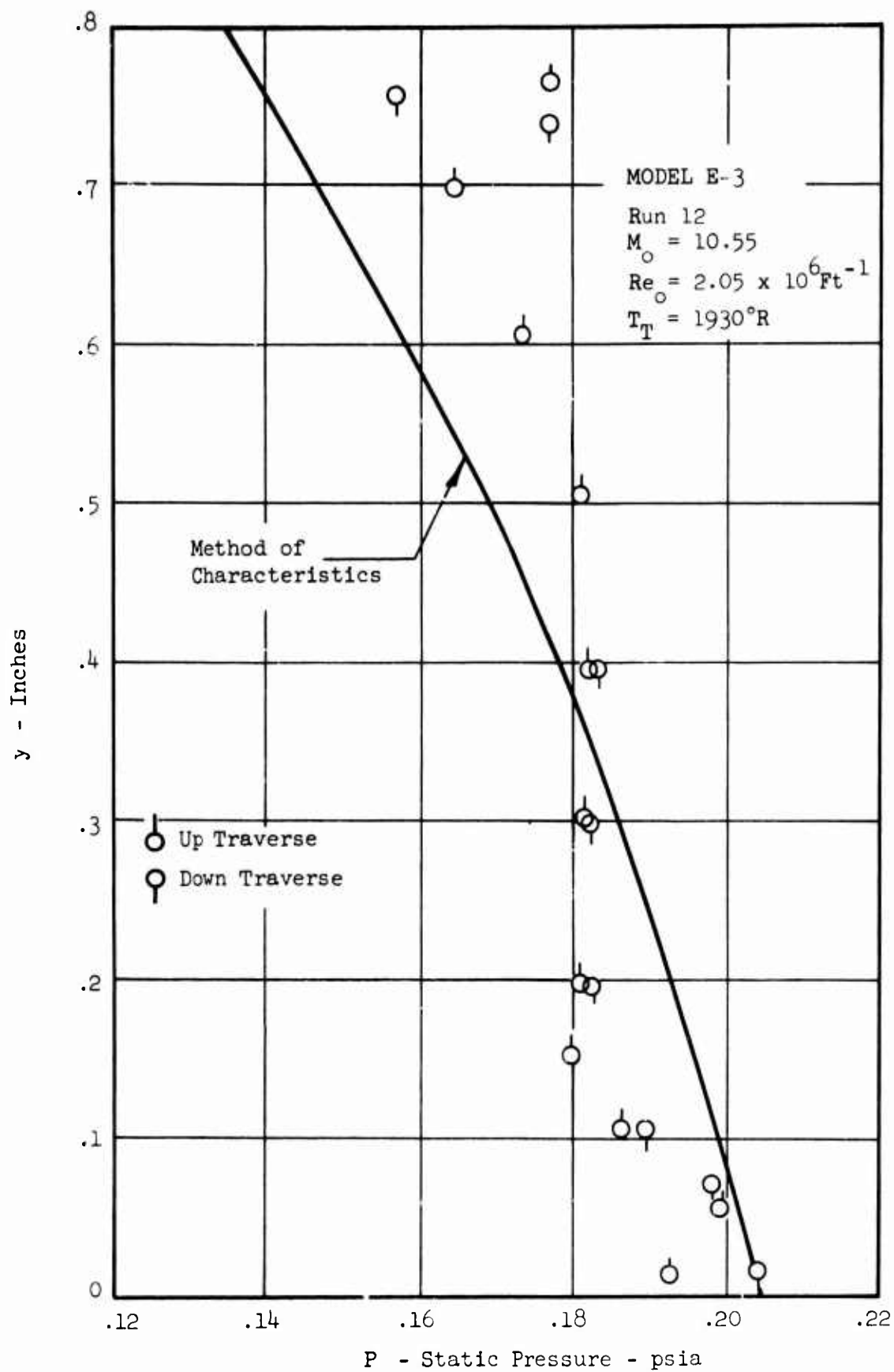


Figure 127 STATIC PRESSURE PROFILE THEORY/DATA COMPARISON

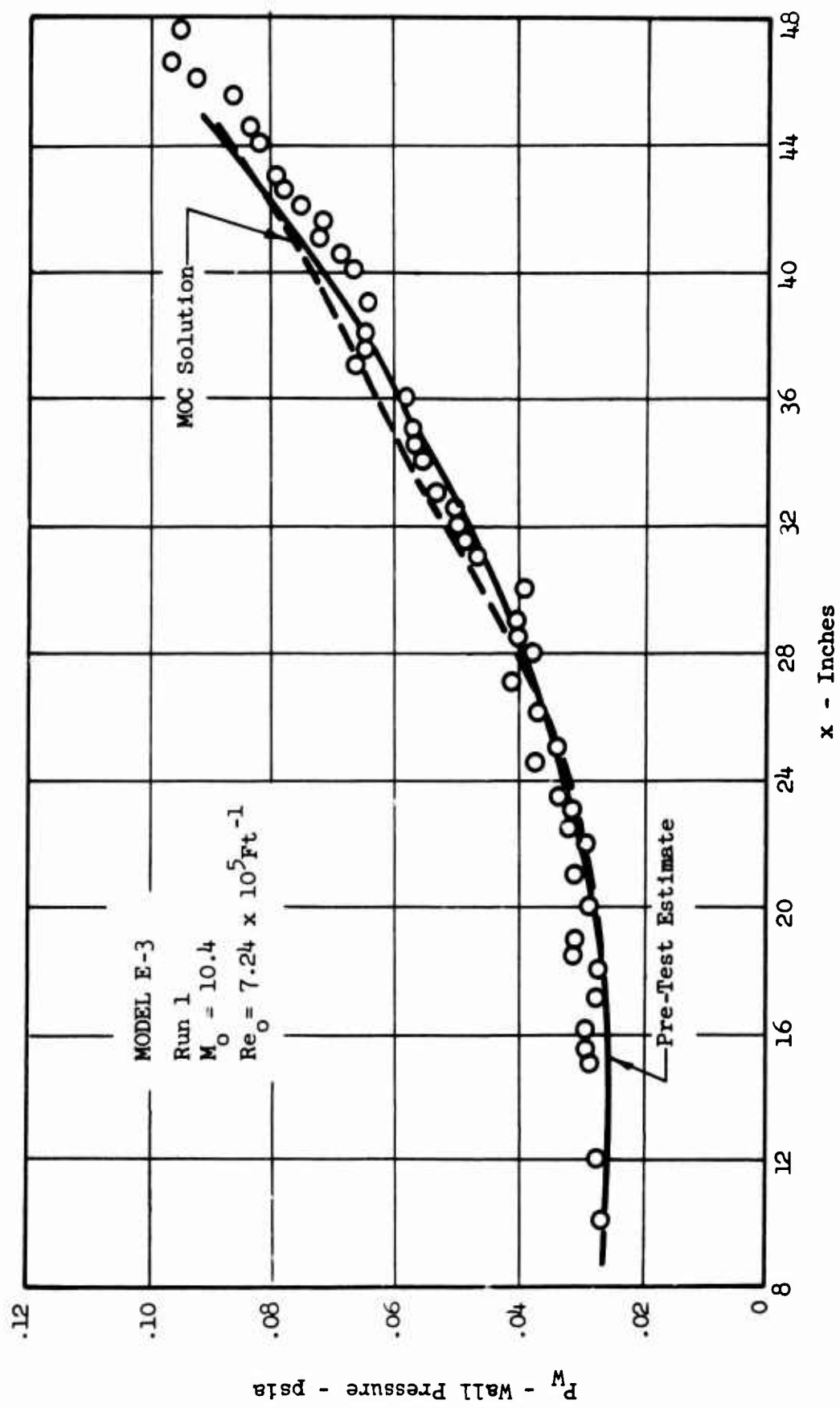


Figure 128 THEORY/DATA PRESSURE COMPARISON

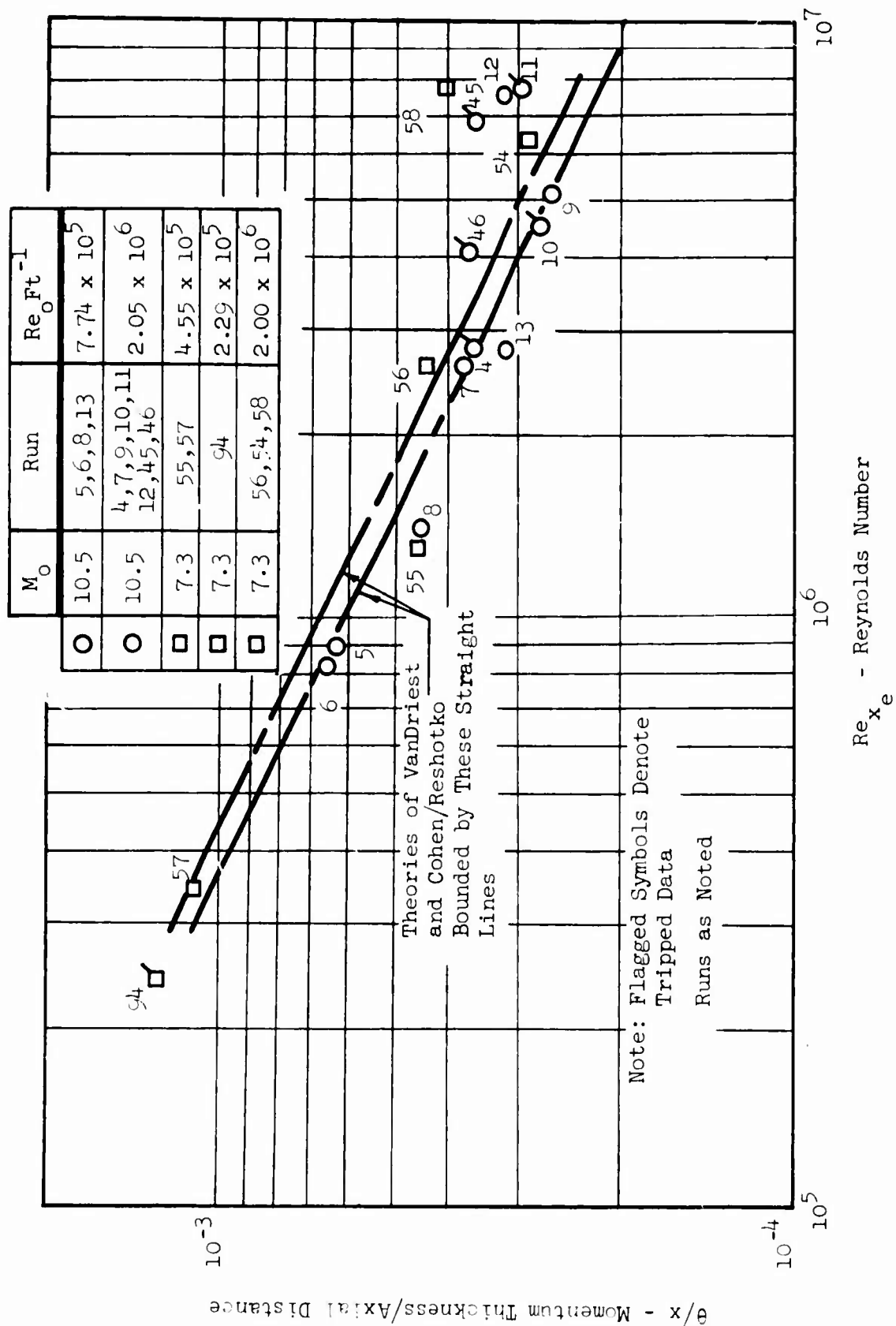


Figure 129 THEORY/DATA COMPARISON OF MOMENTUM THICKNESS

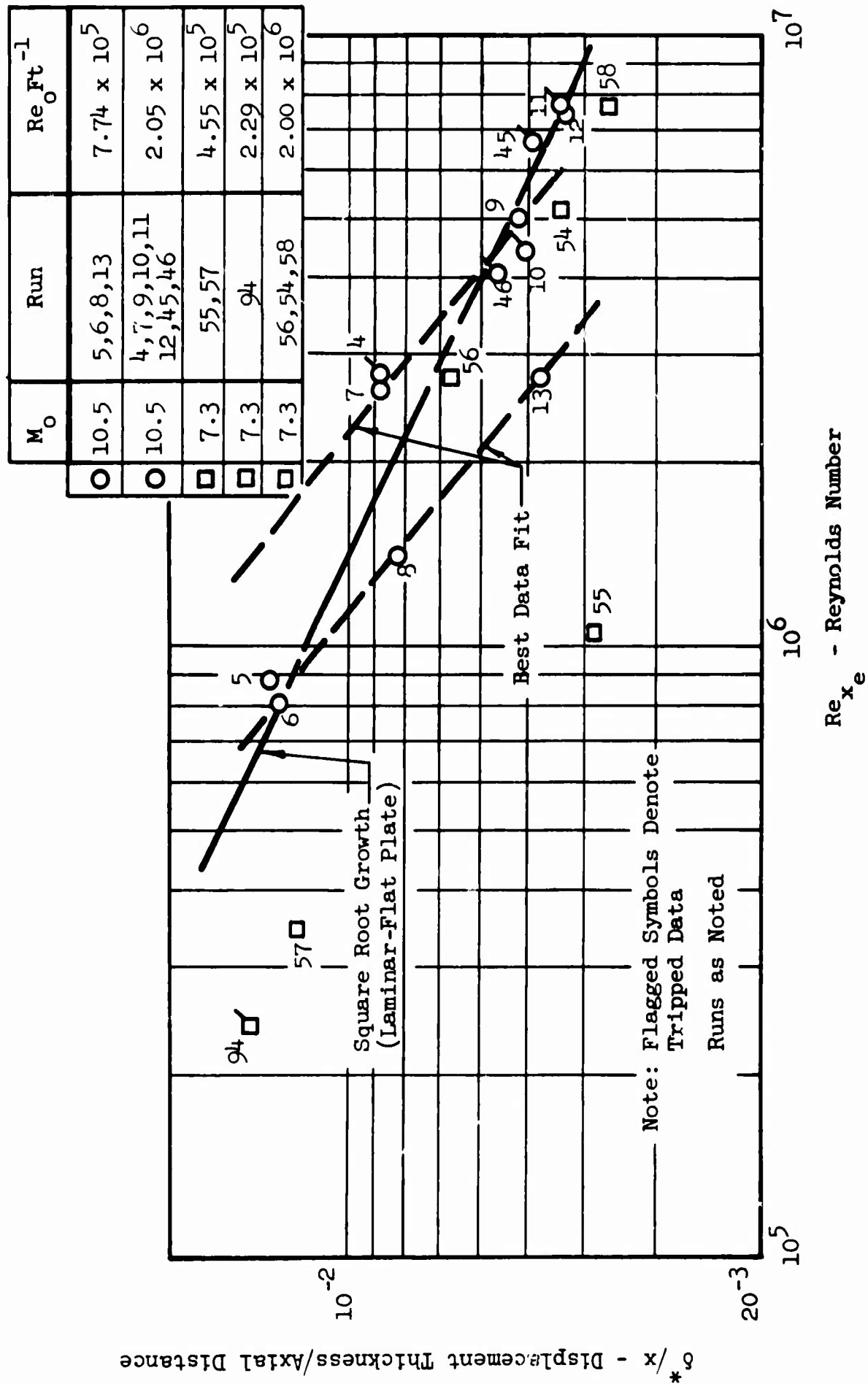


Figure 130 DISPLACEMENT THICKNESS DATA SUMMARY

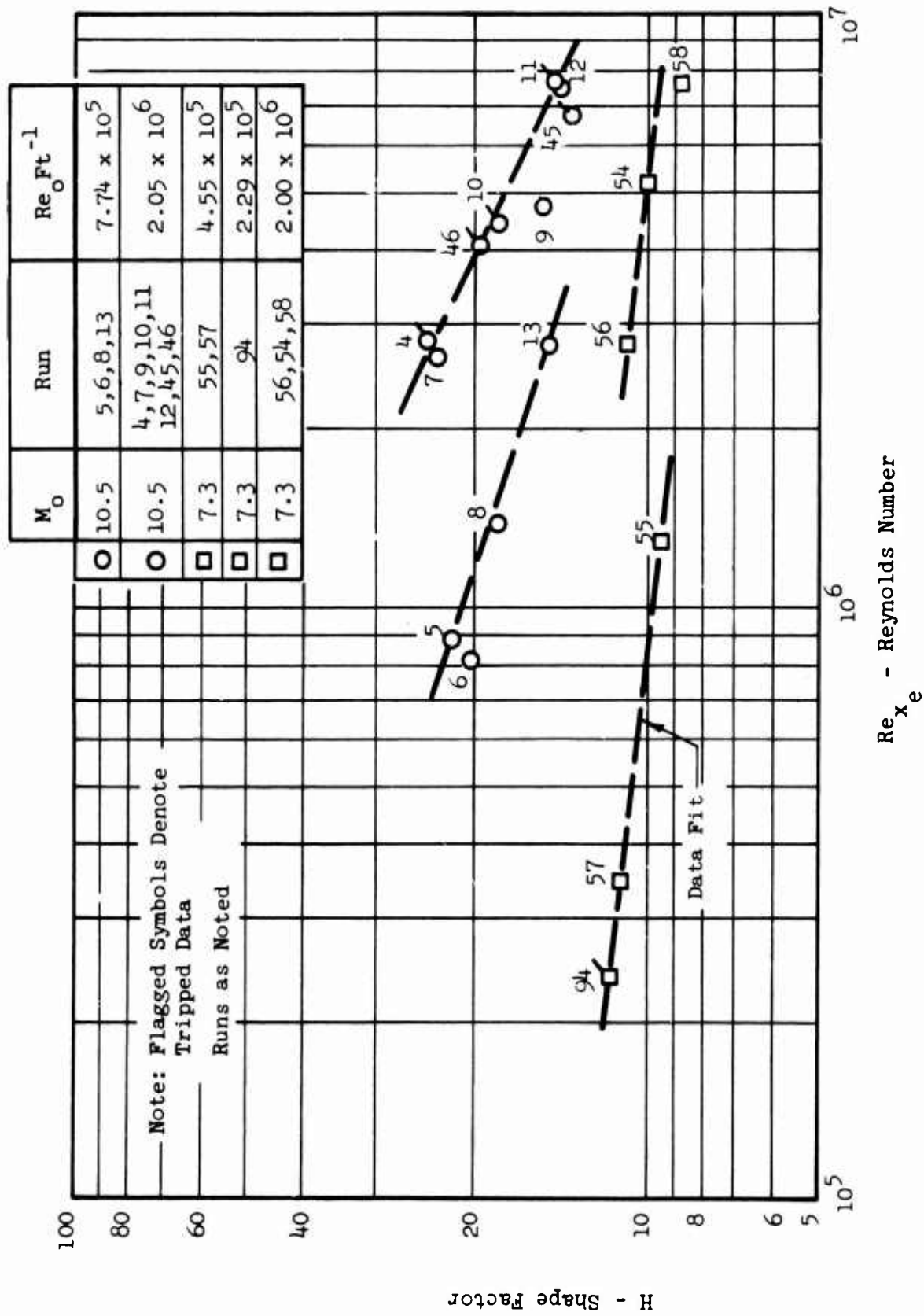


Figure 131 SHAPE FACTOR DATA SUMMARY

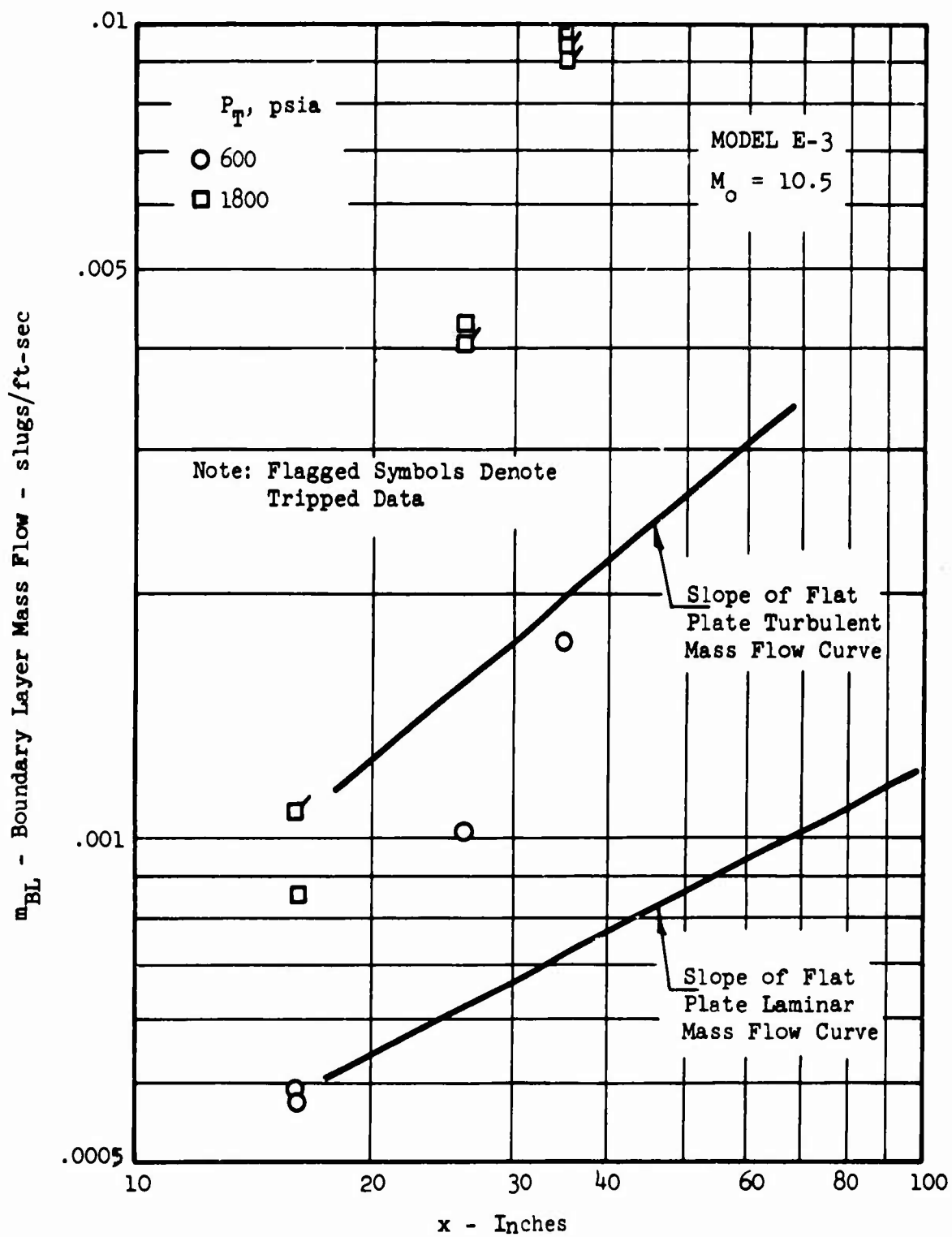


Figure 132 BOUNDARY LAYER MASS FLOW VERSUS AXIAL DISTANCE AT MACH 10.5

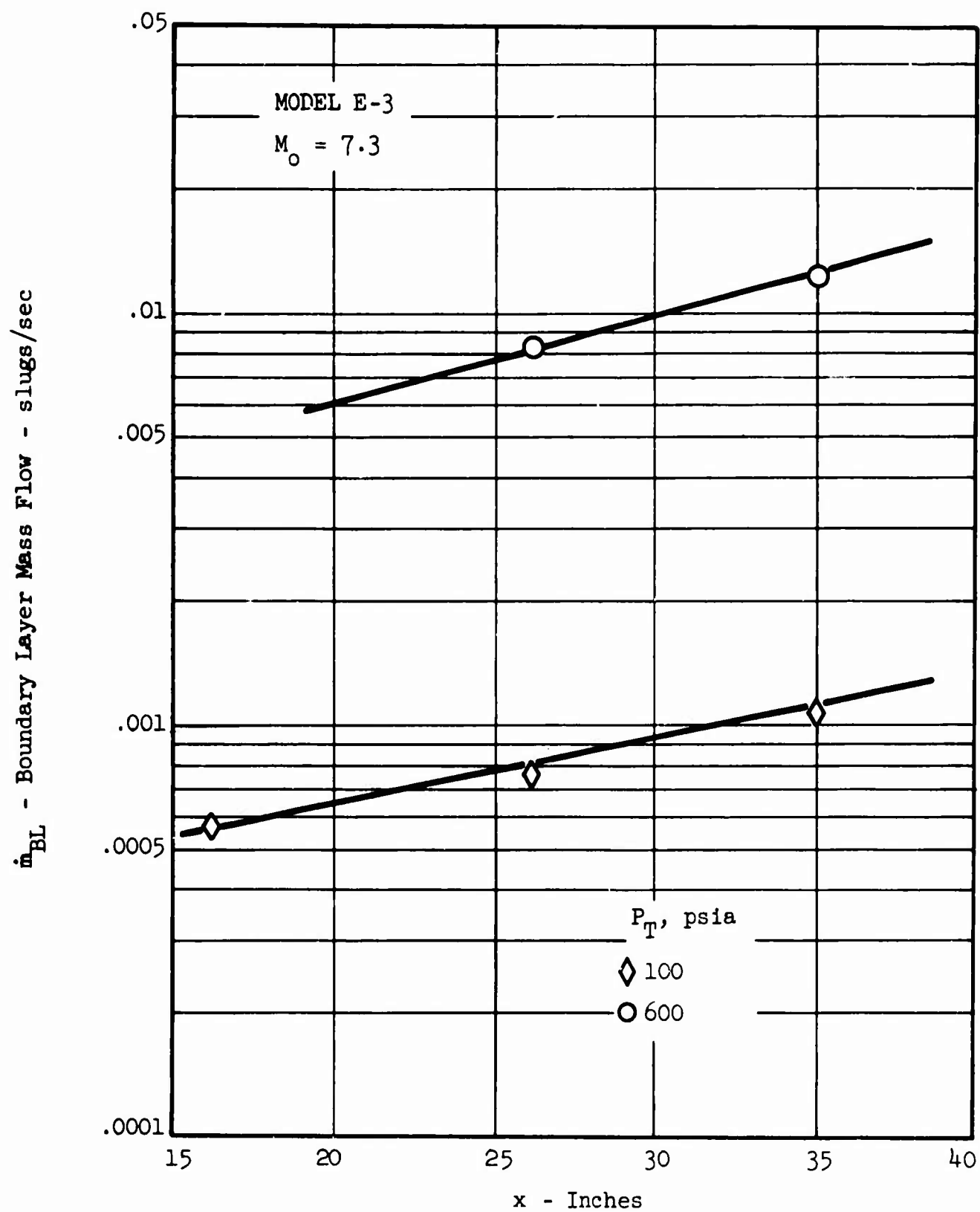


Figure 133 BOUNDARY LAYER MASS FLOW VERSUS AXIAL DISTANCE AT MACH 7.3

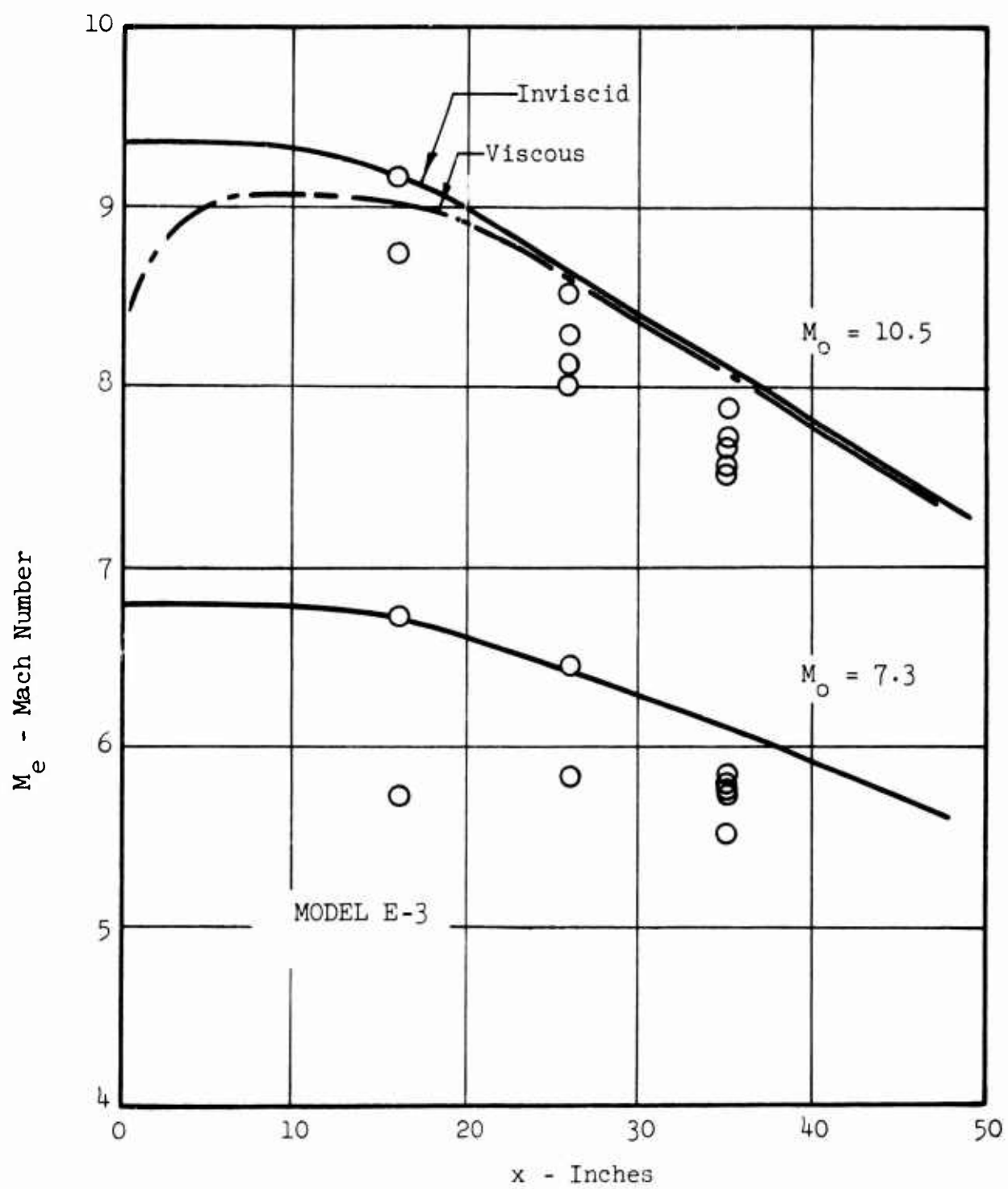


Figure 134 AXIAL MACH NUMBER DISTRIBUTION



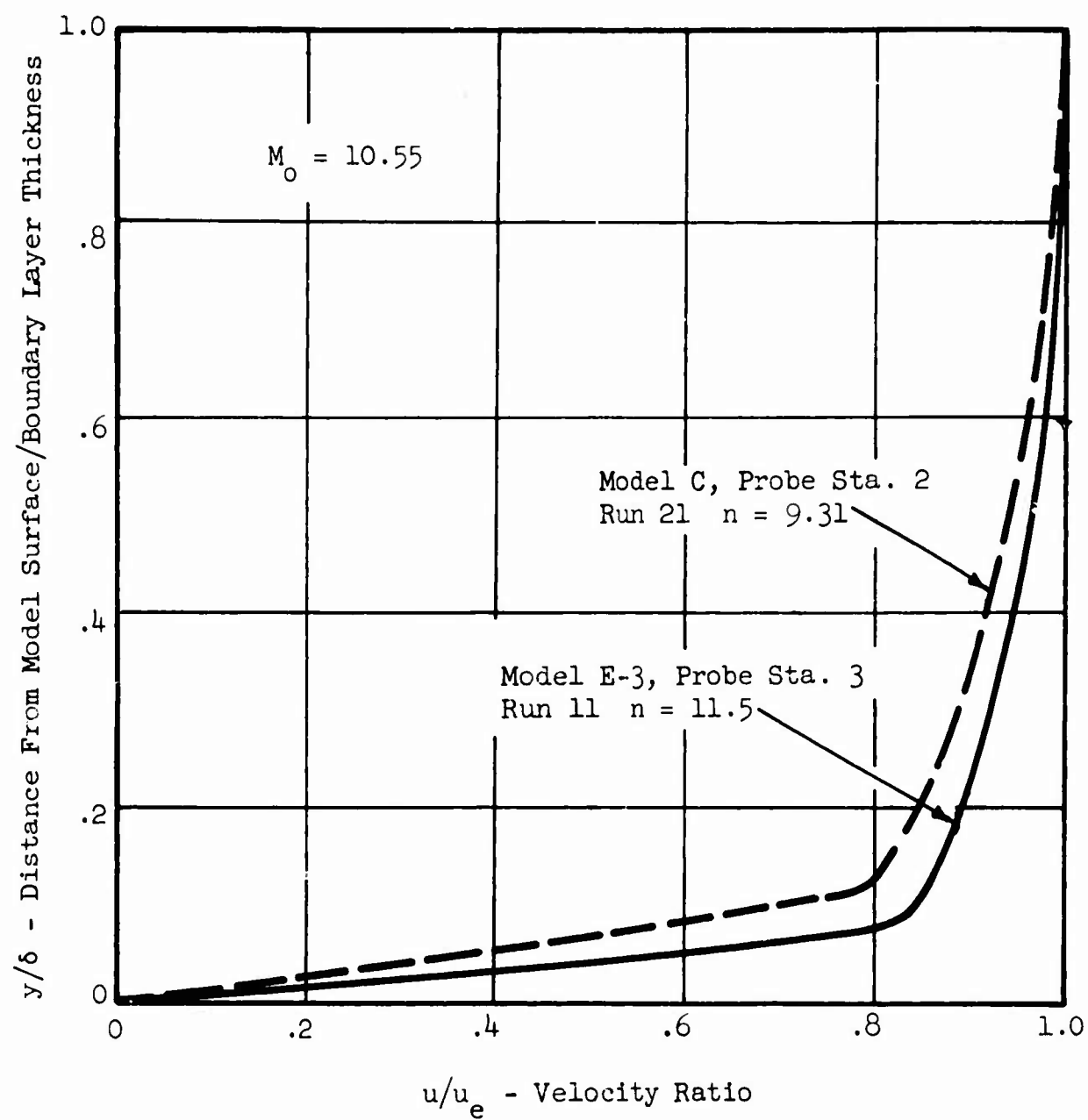


Figure 135 MODELS C AND E-3 TURBULENT PROFILE COMPARISON

Model E-3

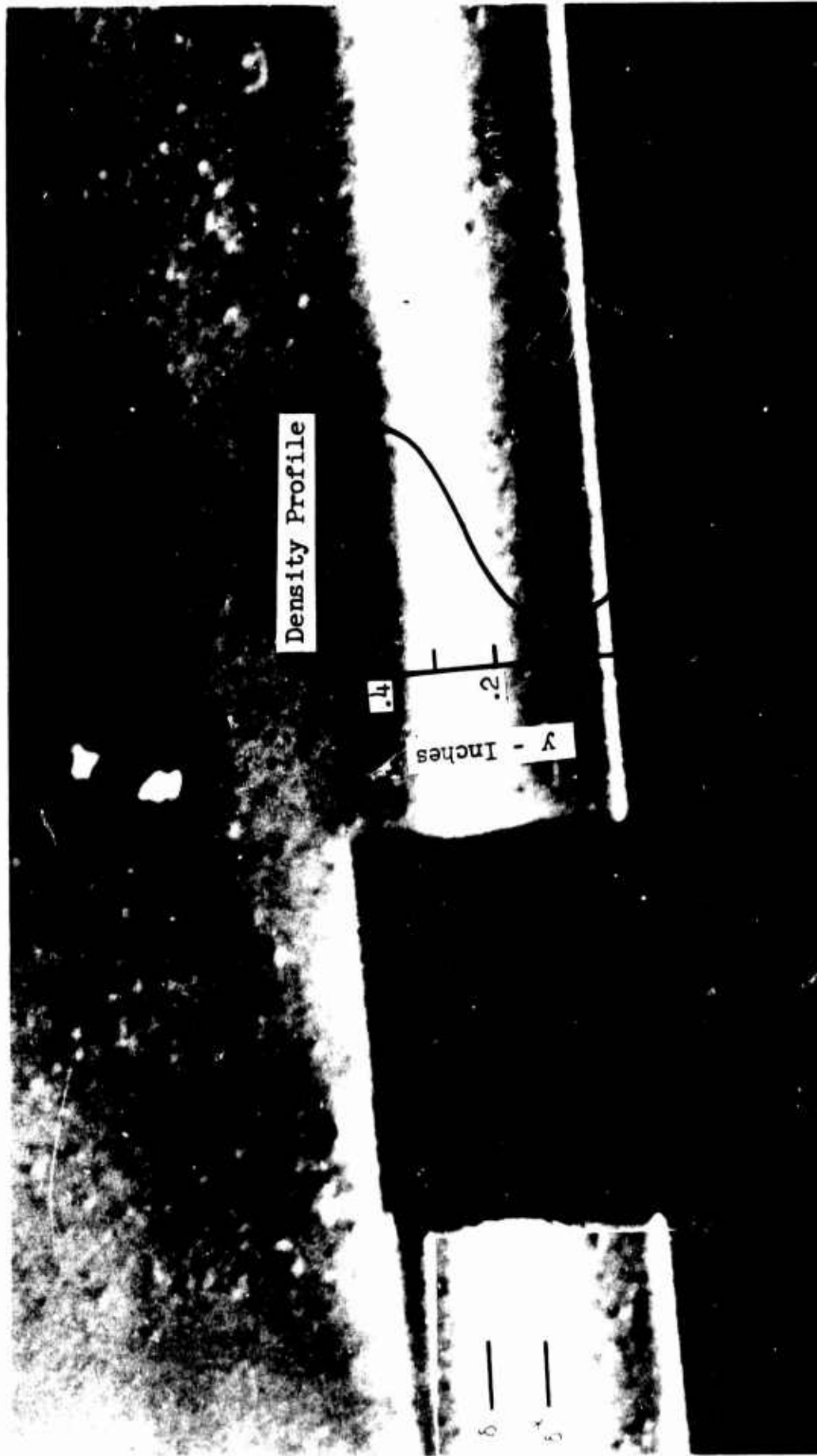


Figure 136 LAMINAR BOUNDARY LAYER SCHLIEREN-PROFILE  
DATA

Model E-3



Figure 137 TURBULENT BOUNDARY LAYER SCHLIEREN-PROFILE DATA

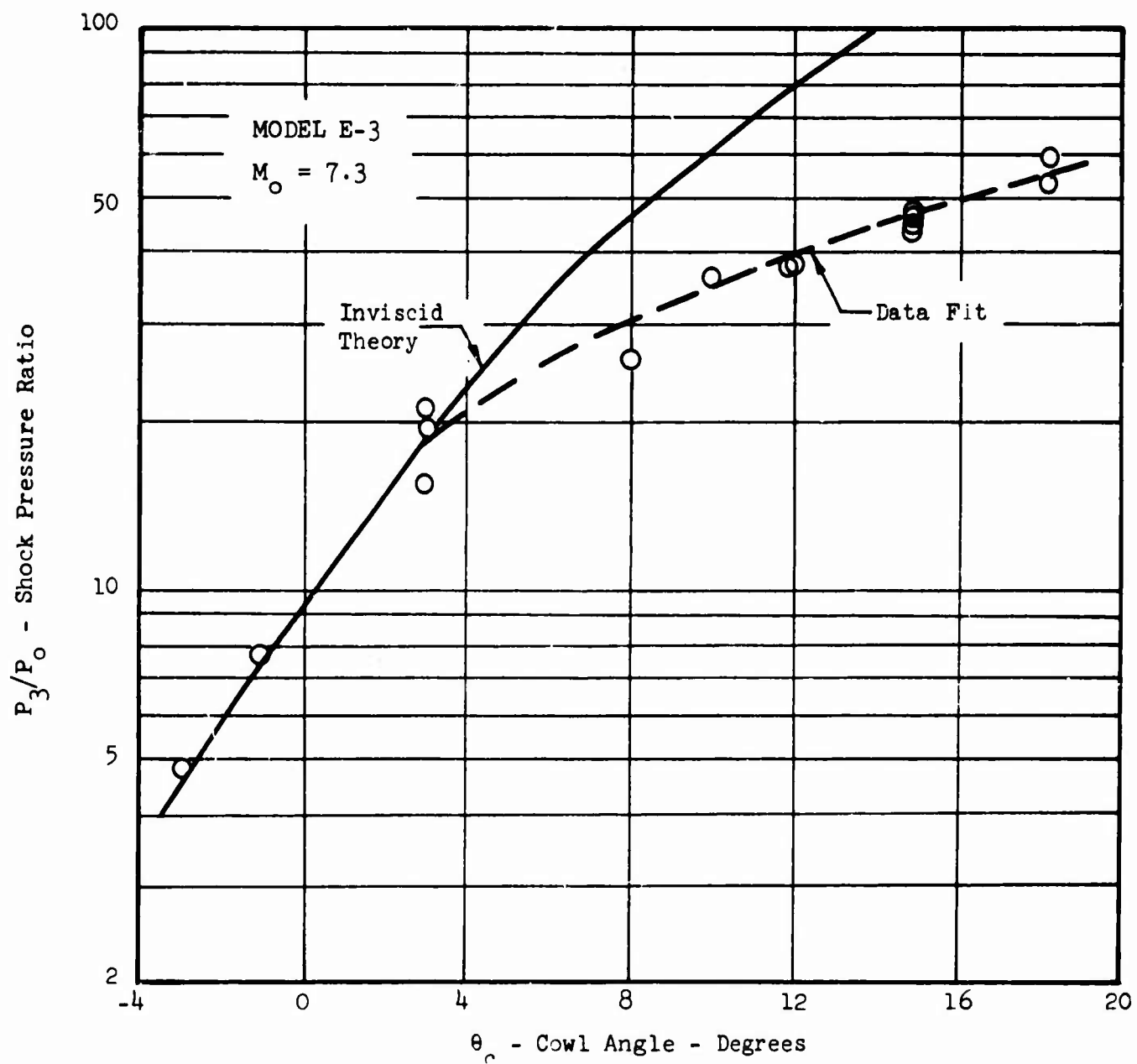


Figure 138 THEORY/DATA SHOCK PRESSURE RATIO COMPARISON

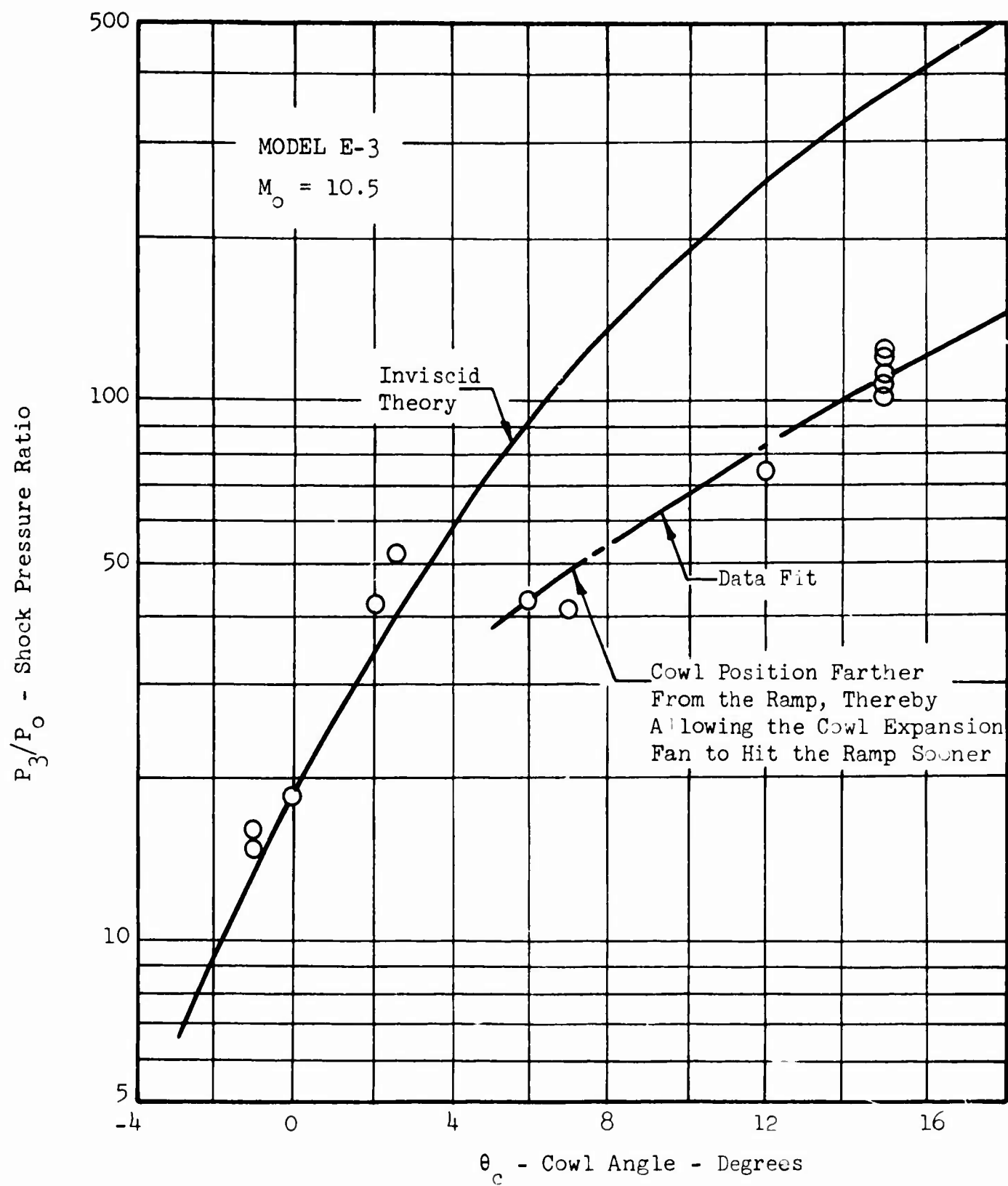


Figure 139 THEORY/DATA SHOCK PRESSURE RATIO COMPARISON

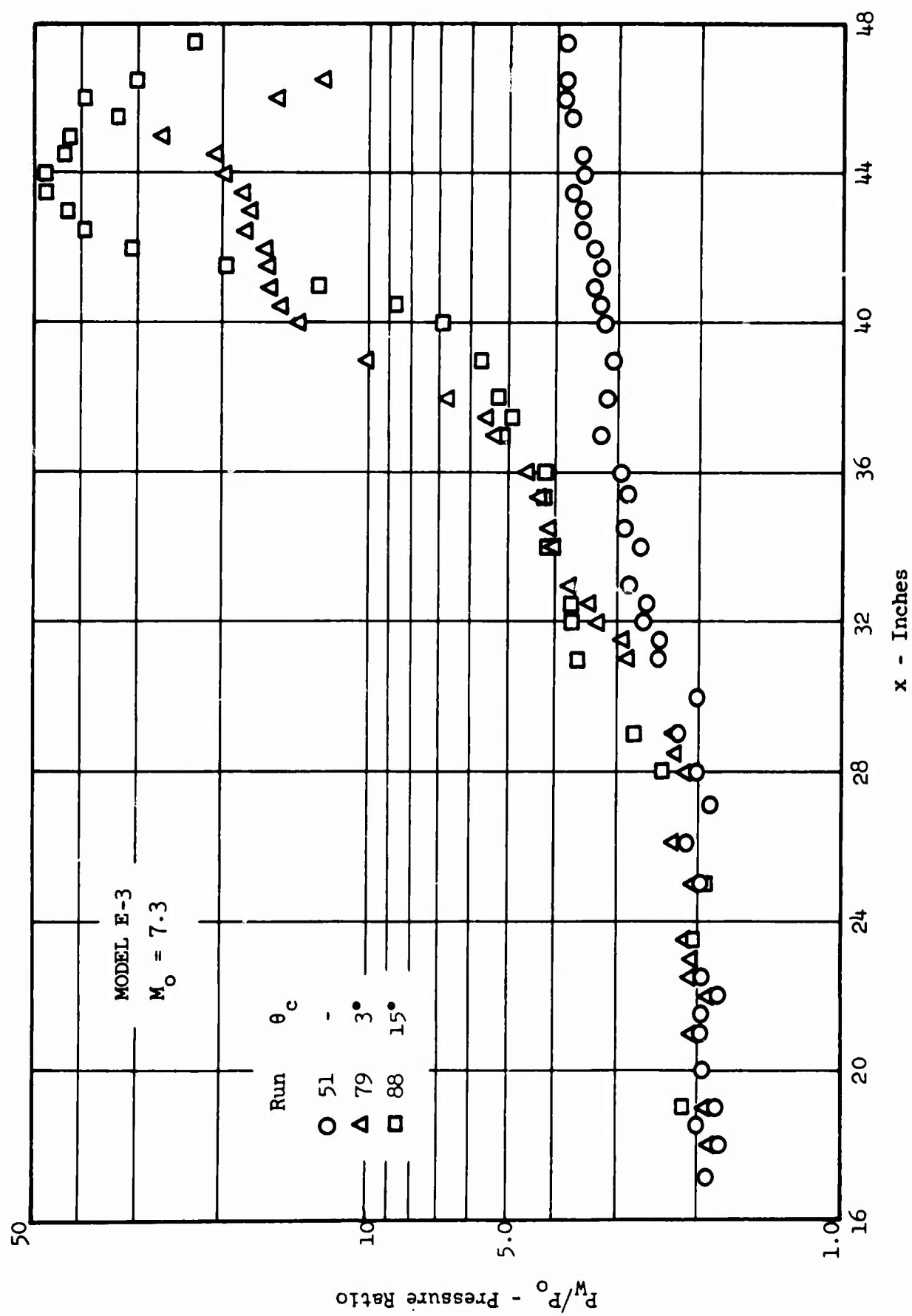


Figure 140 TYPICAL LAMINAR FLOW AXIAL PRESSURE DISTRIBUTION

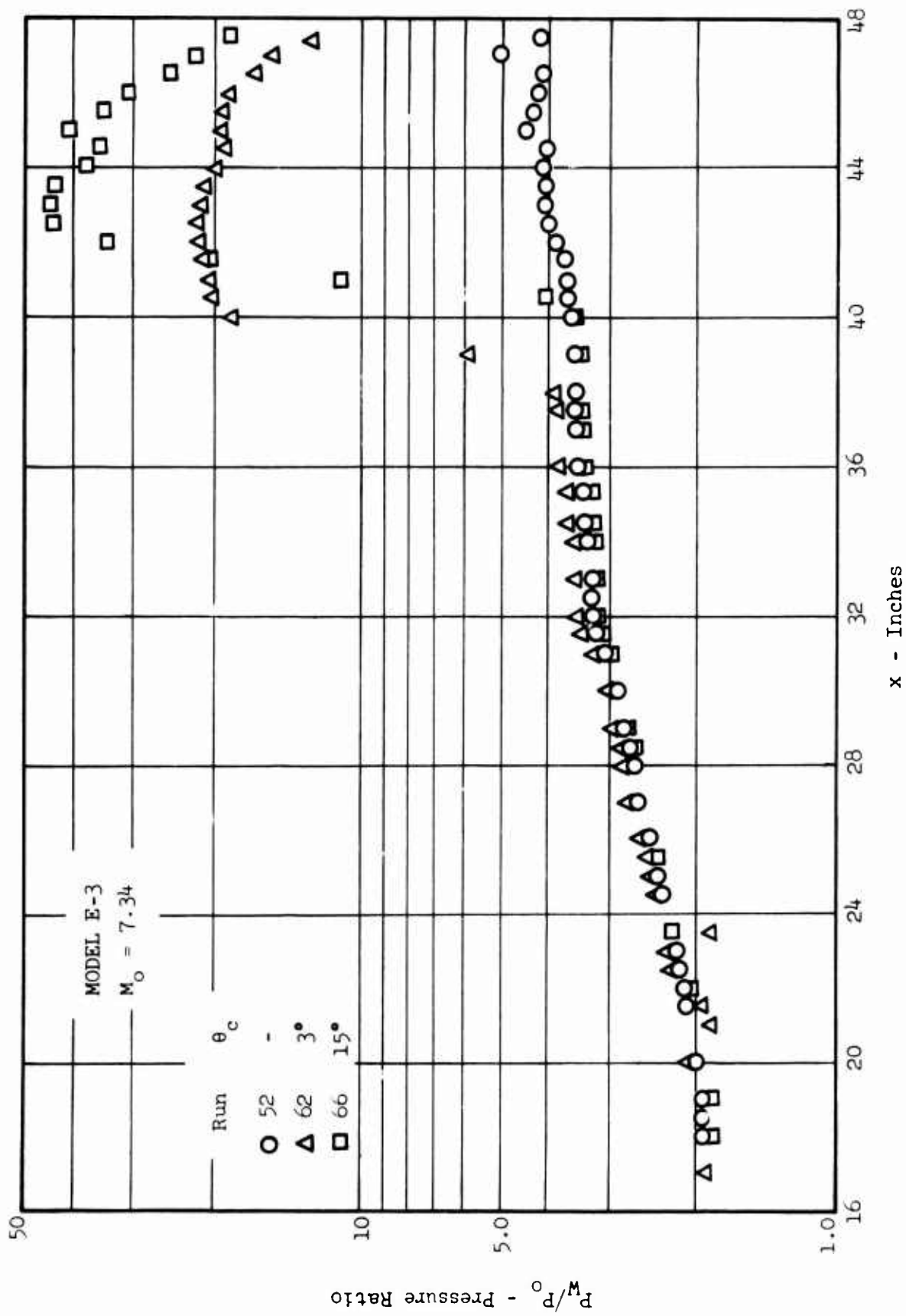


Figure 141 TYPICAL TURBULENT FLOW AXIAL PRESSURE DISTRIBUTION

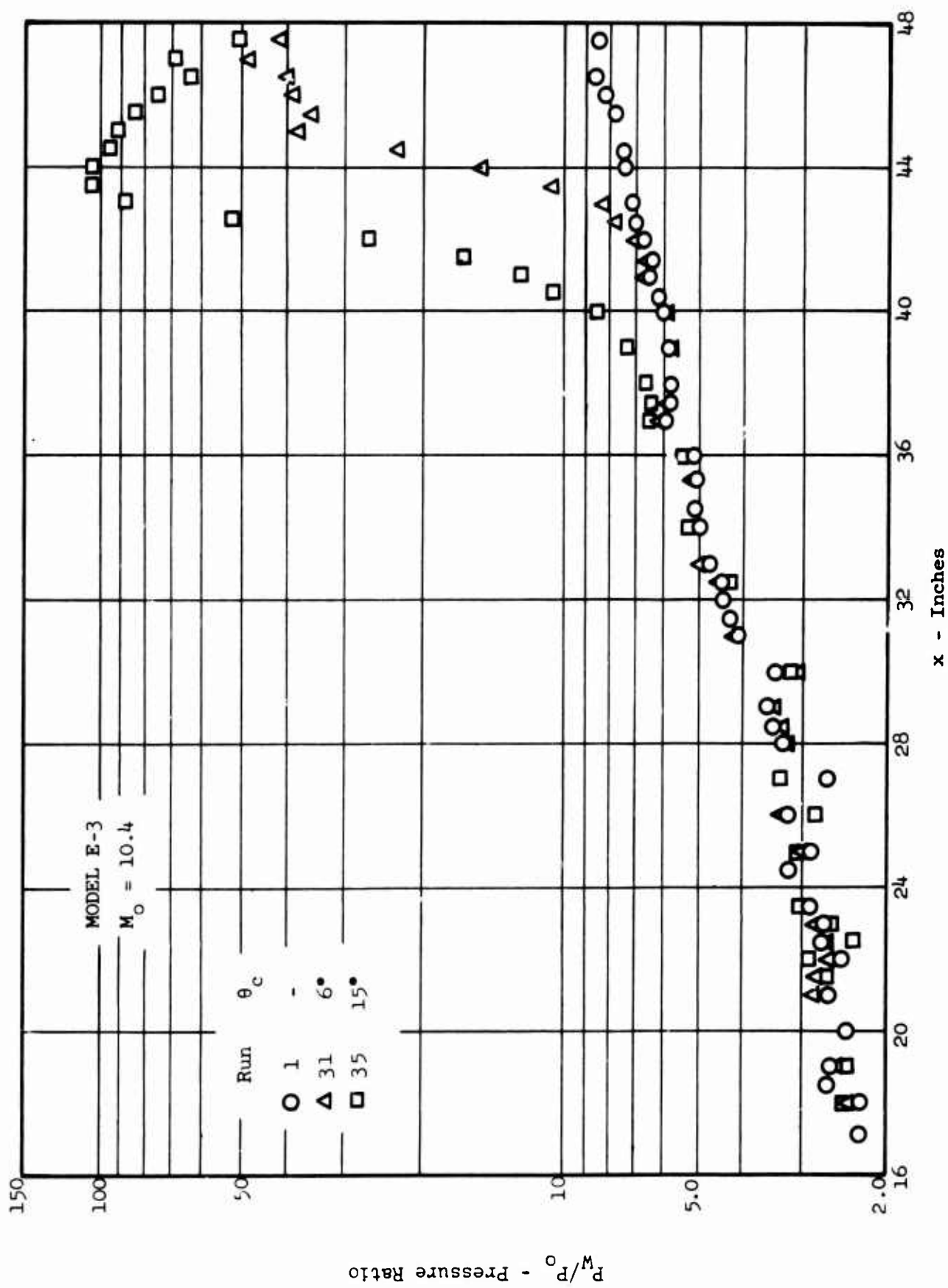


Figure 142 TYPICAL LAMINAR FLOW AXIAL PRESSURE DISTRIBUTION



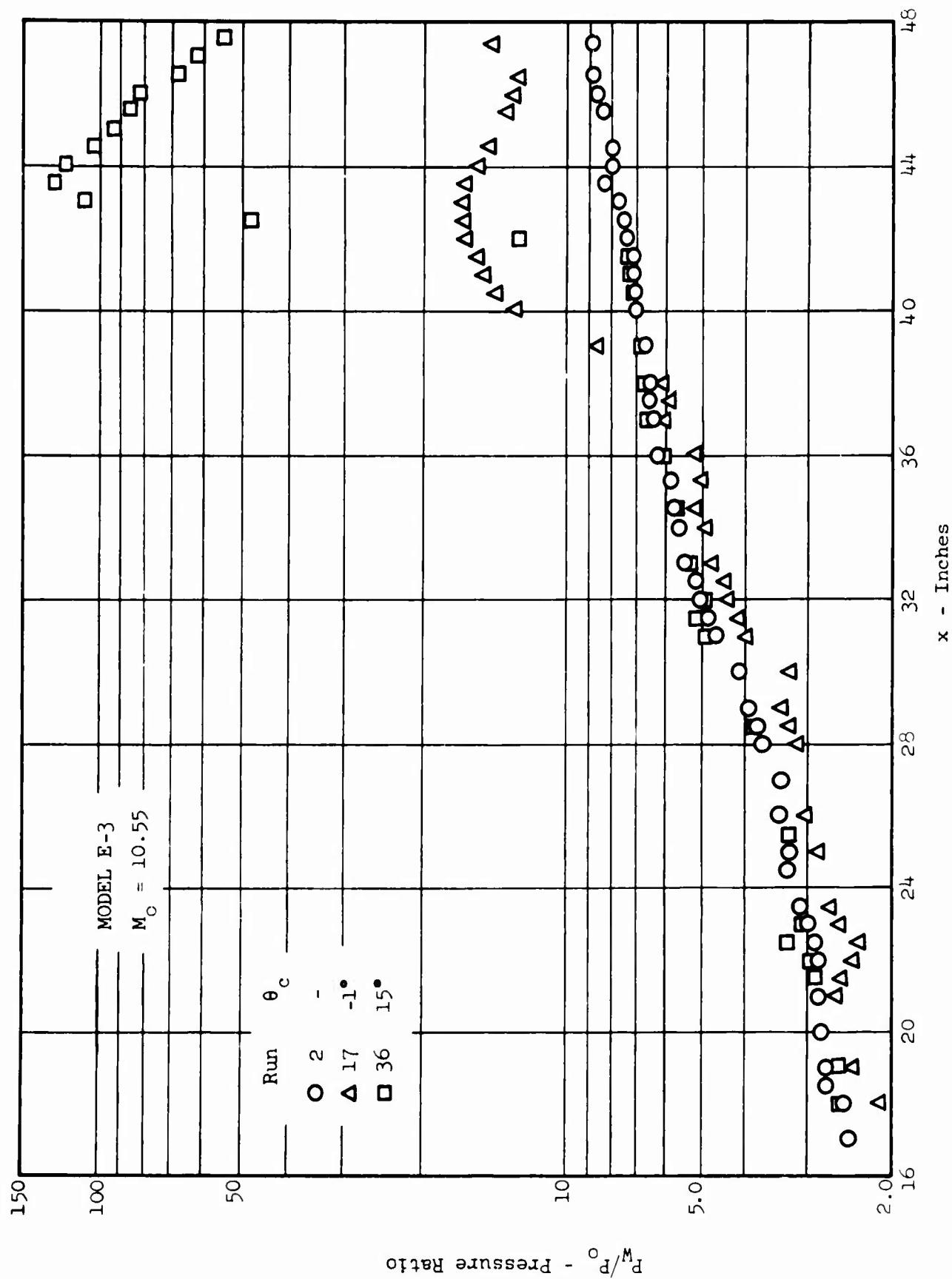


Figure 143 TYPICAL TURBULENT FLOW AXIAL PRESSURE DISTRIBUTION

MODEL E-3

Run 40

$M_o = 10.40$

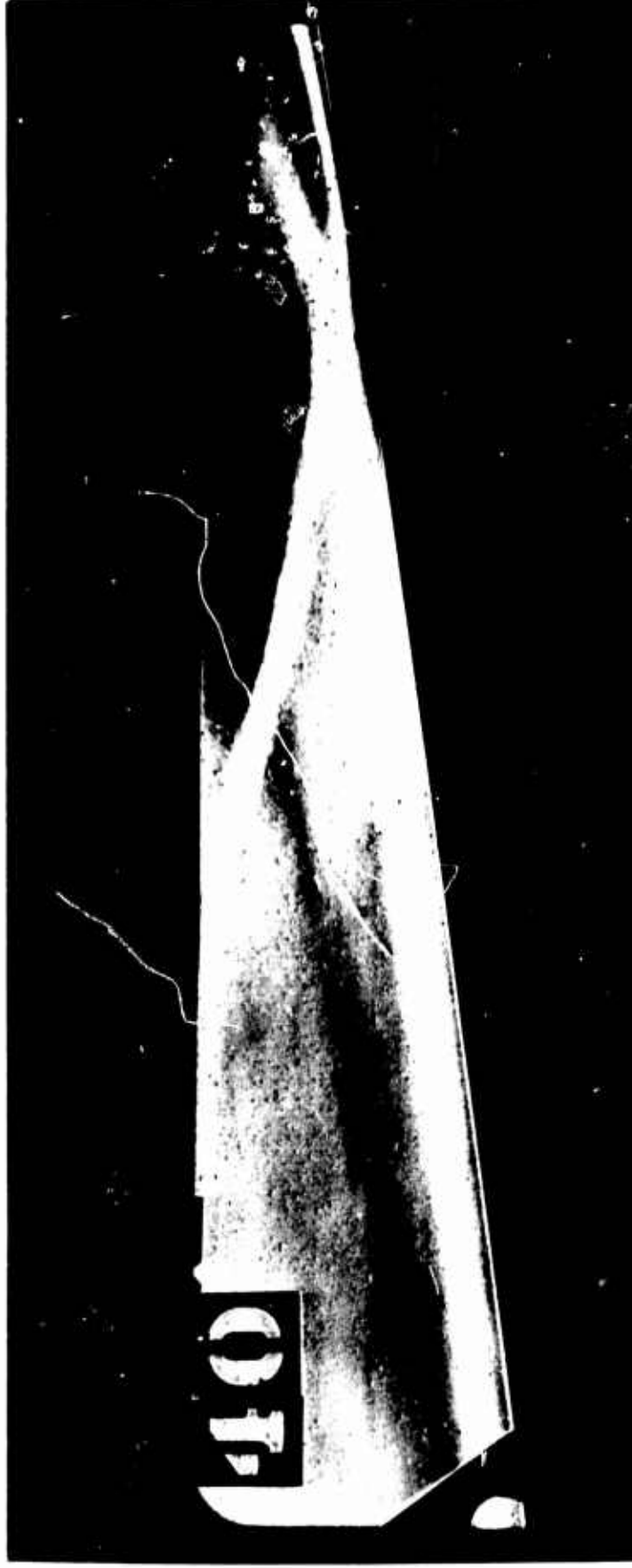


Figure 144 TYPICAL SCHLIEREN-LAMINAR INTERACTION

MODEL E-3

Run 38  
 $M_o = 10.55$



Figure 145 TYPICAL SCHLIEREN-TURBULENT INTERACTION

MODEL E-3

Run 64  
 $M_o = 7.30$



Figure 146 TYPICAL SCHLIEREN-LAMINAR INTERACTION

MODEL E-3

Run 62  
 $M_o = 7.34$



Figure 147 TYPICAL SCHLIEREN - TURBULENT INTERACTION

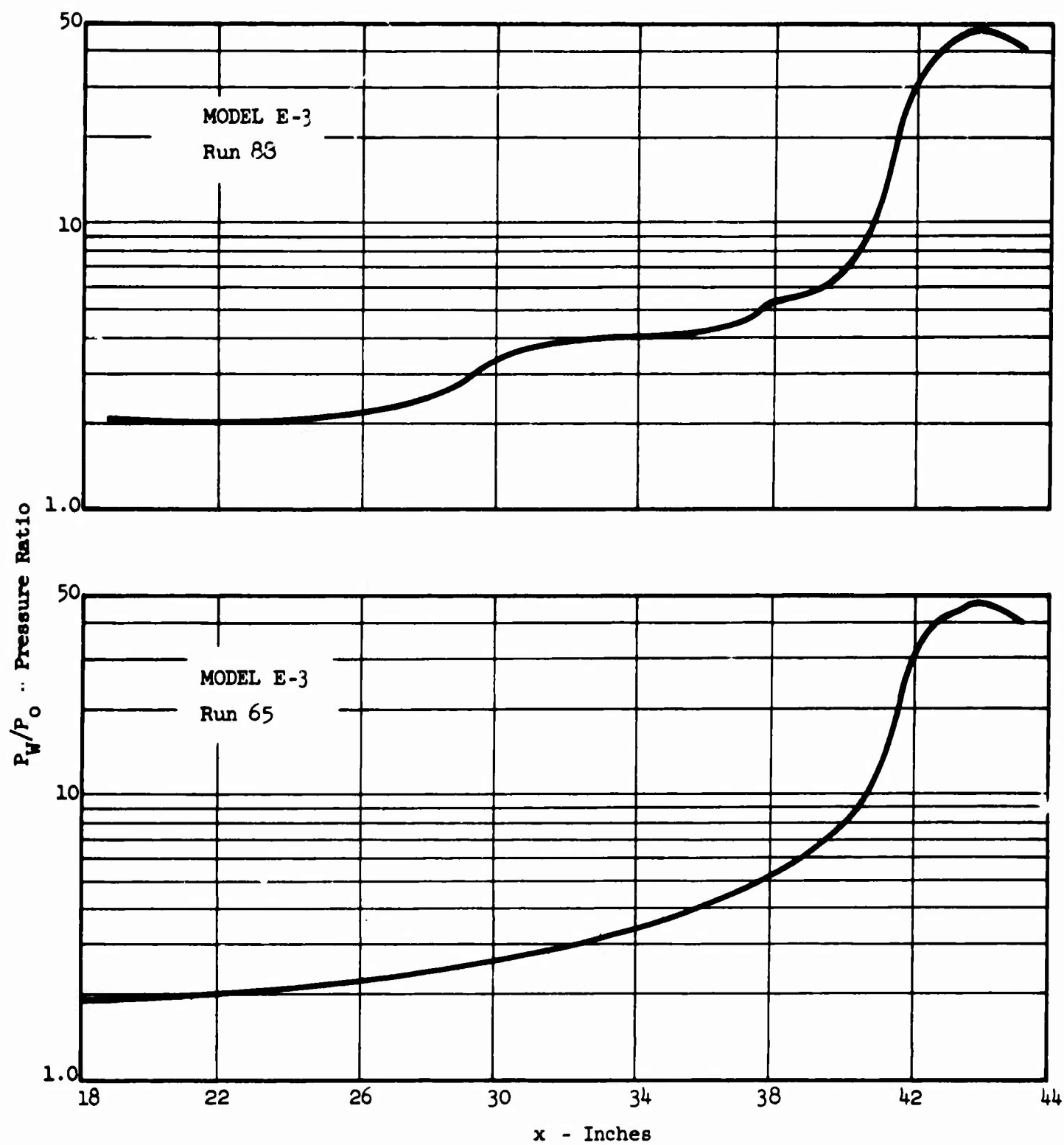


Figure 148      COMPARISON OF PRESSURE DISTRIBUTIONS FOR  
SIMILAR TEST CONDITIONS

A high-contrast, black and white photograph of a person's legs, heavily shadowed and textured, possibly wearing a dark garment or being in a dark environment. The image is oriented vertically.

Run 65  
 $M_O = 7.30$

55

**Figure 149      COMPARISON OF SCHLIEREN FOR SIMILAR TEST  
                                CONDITIONS**

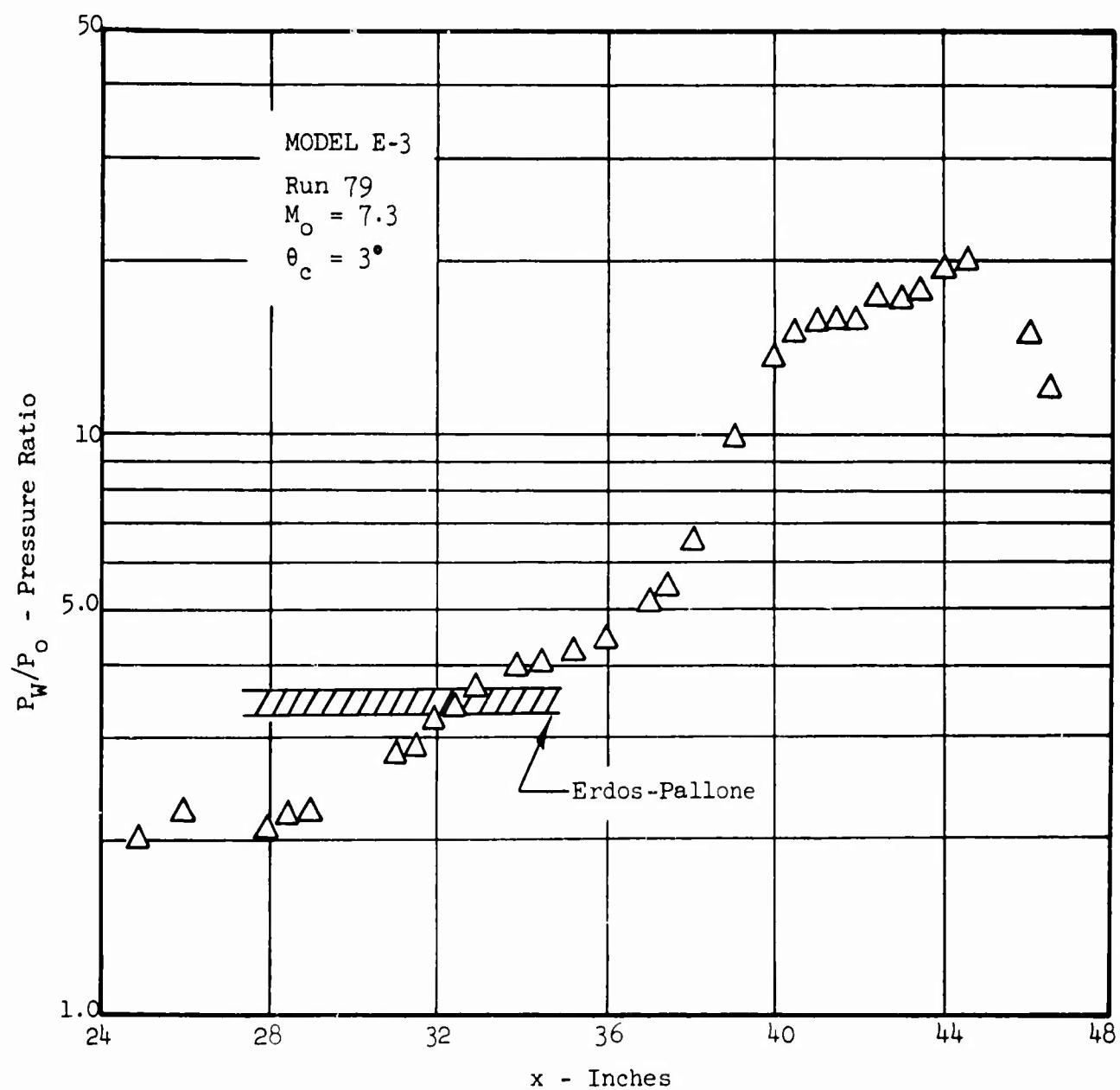


Figure 150 LAMINAR BOUNDARY LAYER INCIDENT SHOCK  
PRESSURE DISTRIBUTION



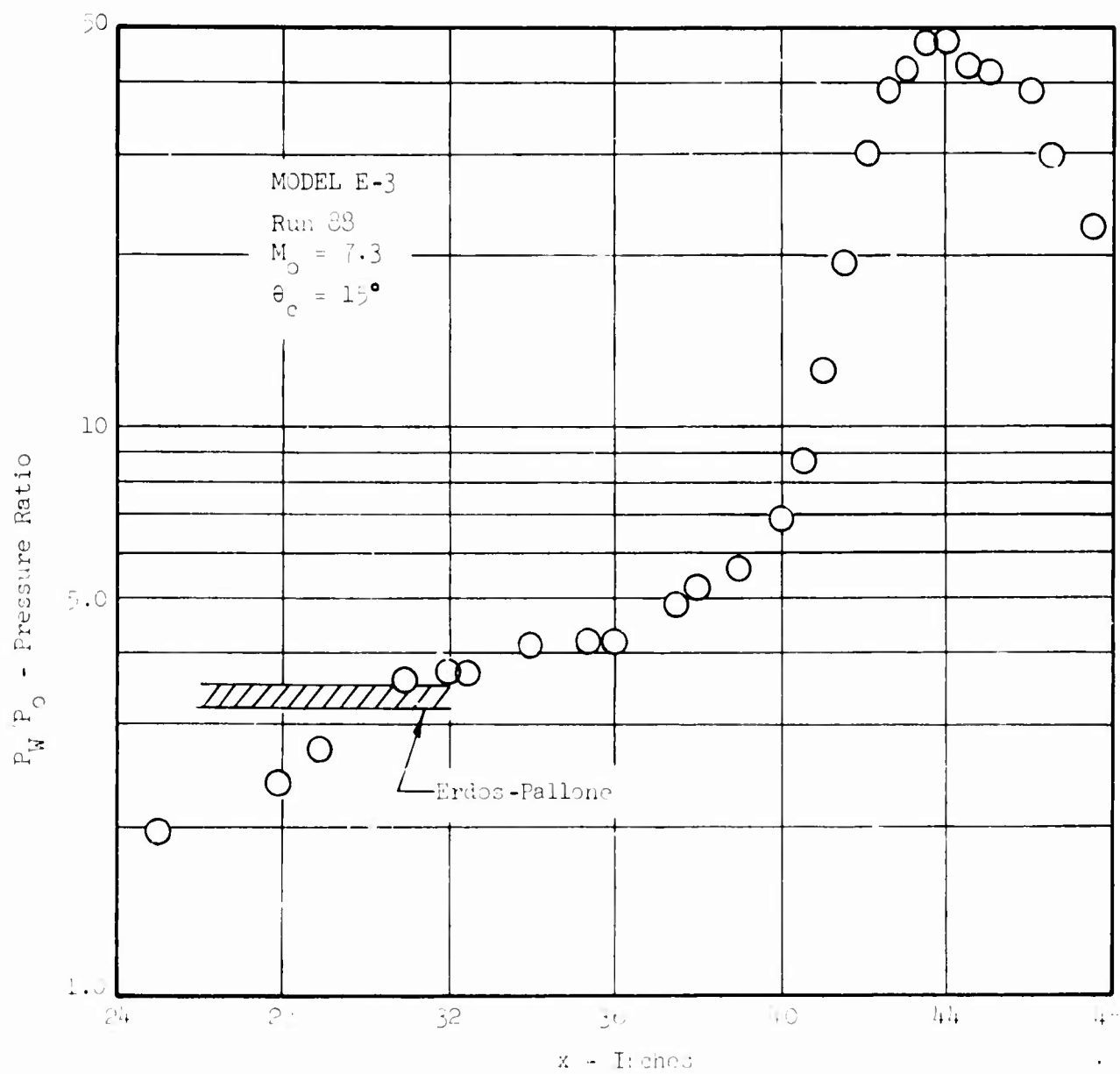


Figure 151 LAMINAR BOUNDARY LAYER INCIDENT SHOCK  
PRESSURE DISTRIBUTION

MODEL E-3

Run 69  
 $M_o = 7.34$   
 $Re_o = 2.0 \times 10^6 \text{ Ft}^{-1}$



Figure 152 TYPICAL TURBULENT INTERACTION SCHLIEREN

**BLANK PAGE**

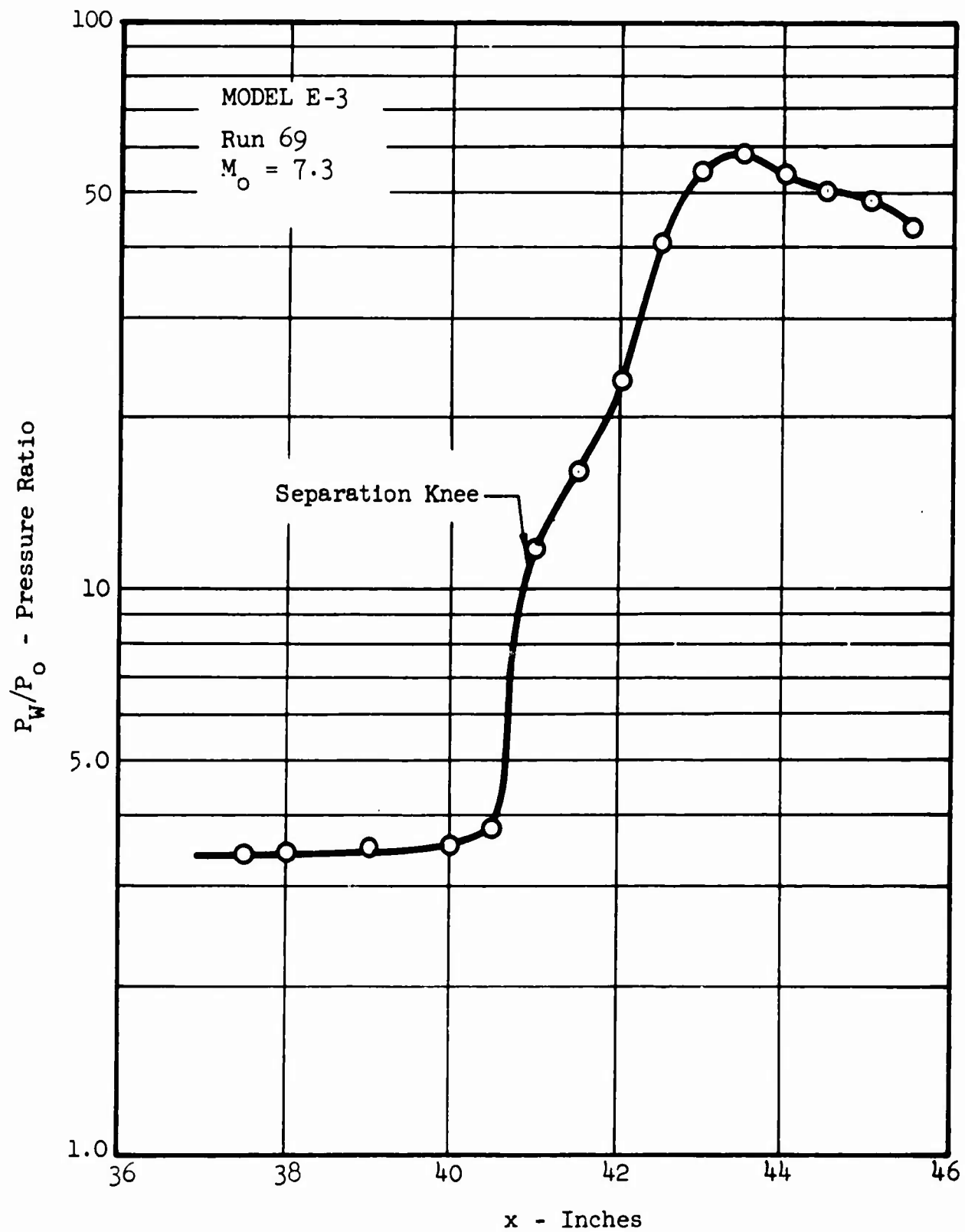


Figure 153      TURBULENT BOUNDARY LAYER INCIDENT SHOCK  
PRESSURE DISTRIBUTION

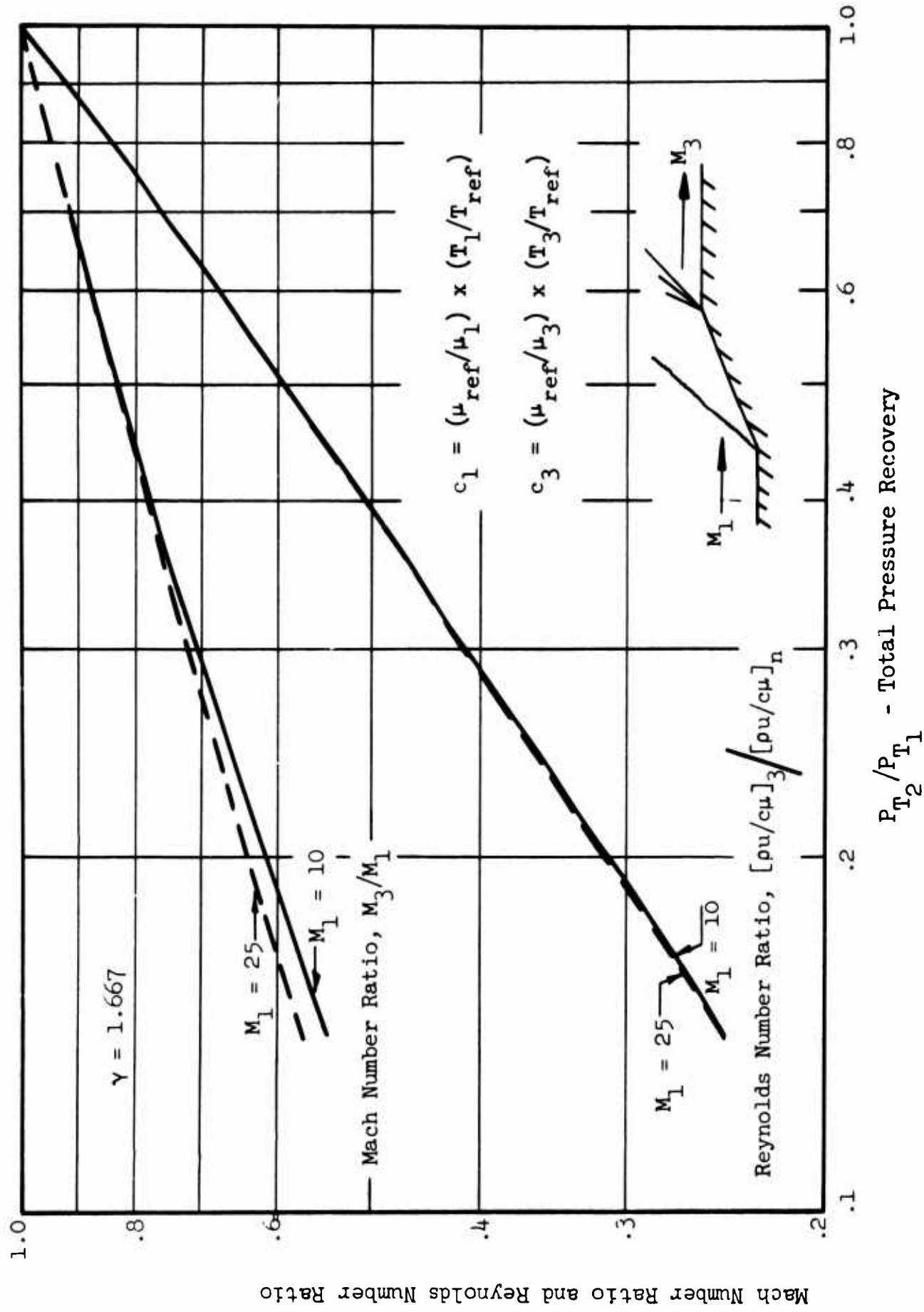


Figure 154 COMPUTATIONAL CURVES FOR REYNOLDS NUMBER AND MACH NUMBER PROGRAM INPUTS

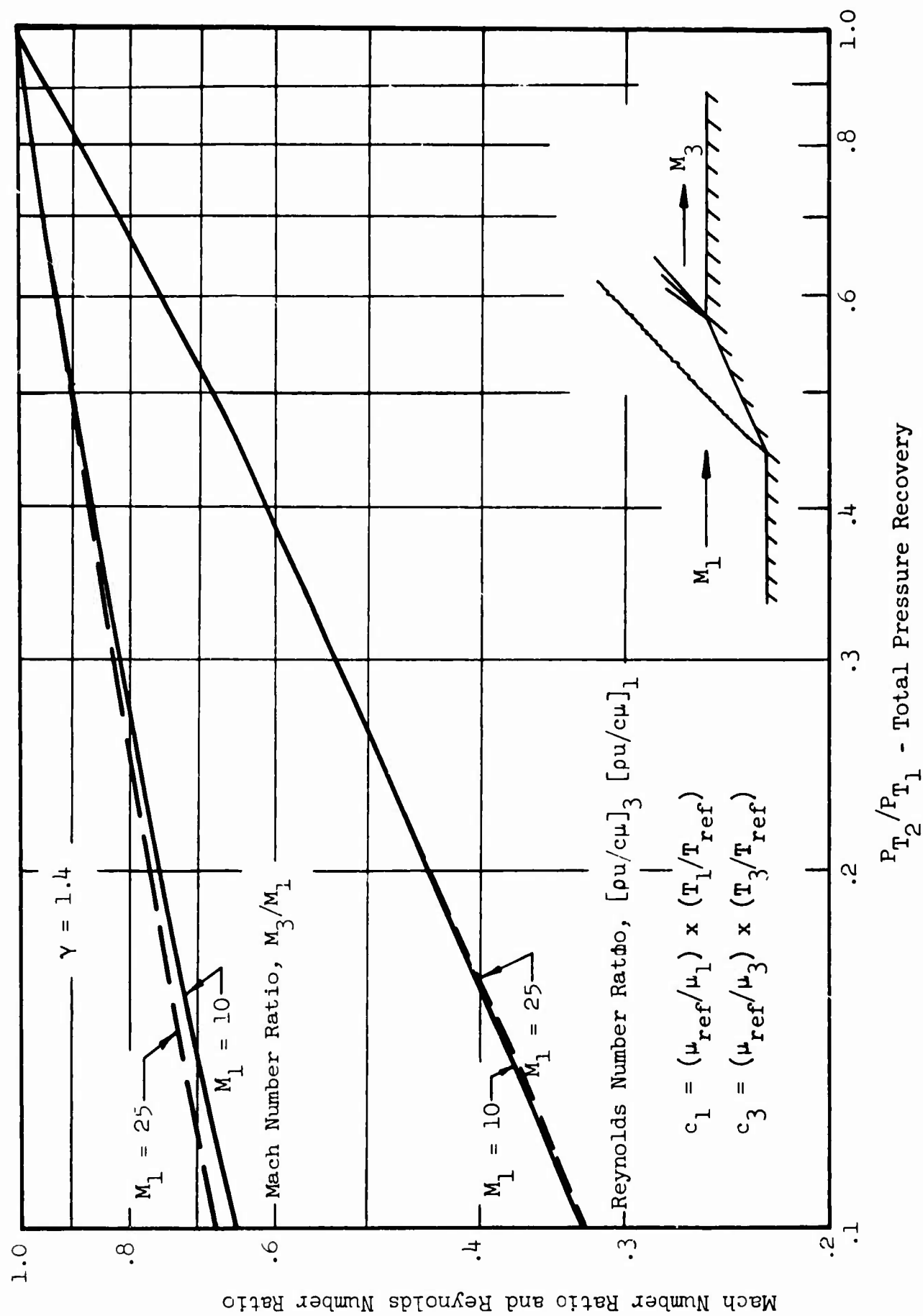


Figure 155 COMPUTATIONAL CURVES FOR REYNOLDS NUMBER  
AND MACH NUMBER PROGRAM INPUTS

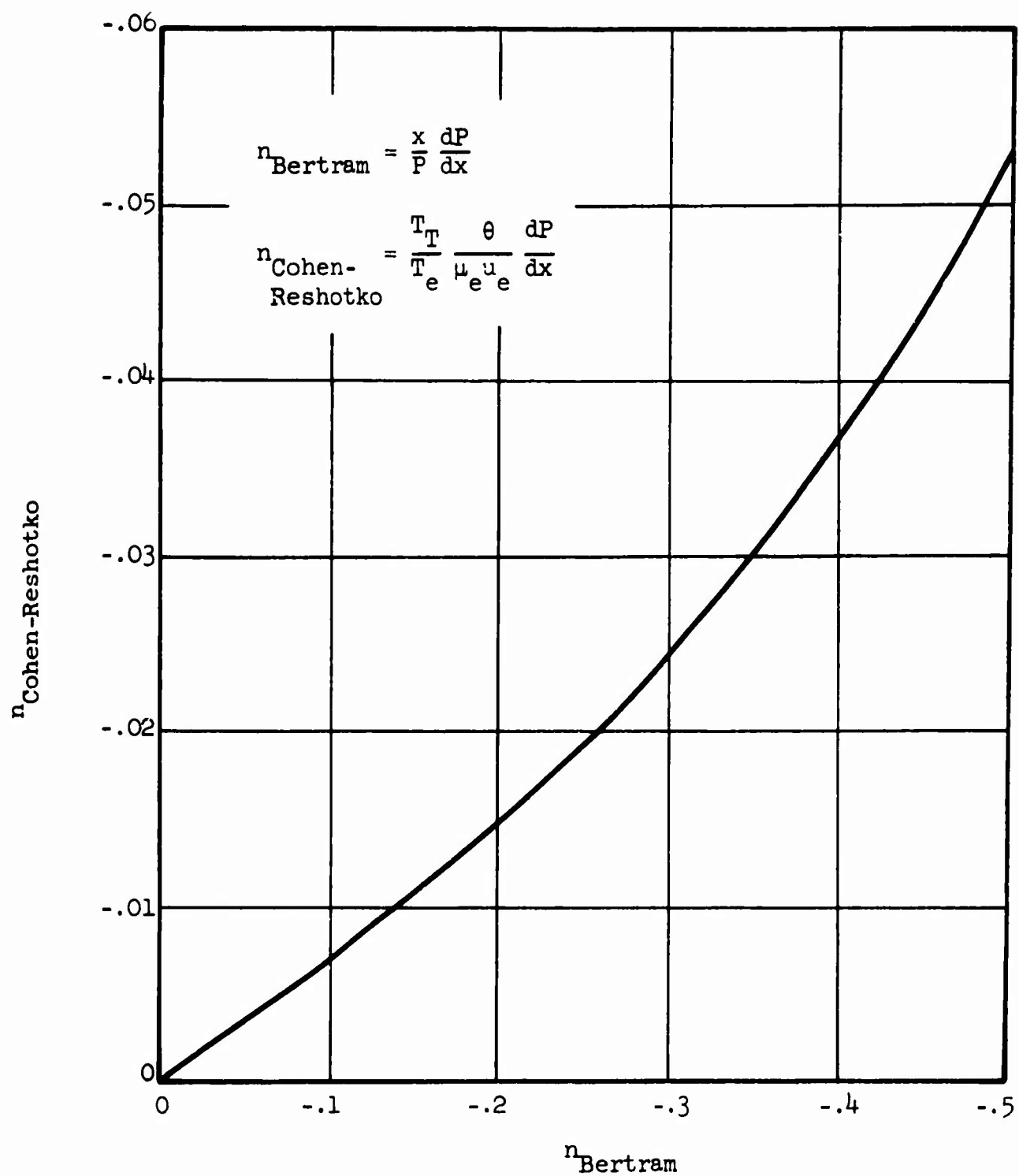


Figure 156 COMPARISON OF BOUNDARY LAYER PRESSURE GRADIENT PARAMETERS

## SOLUTION OF BOUNDARY LAYER GROWTH-

## STRONG SHOCK CONVERGENCE

AA = 0.  
BB = 5.2410E-02  
CC = 0.

BN = -0.2000  
B1 = 0.  
B4 = 0.0100  
FSN = 0.

X(HSHOCK) = 24.000C DEL THETA = 5.000  
H(H)/H(TOT) = 0.20C D(THETA\*NU)/DX = 0.

RAY=6.32E 04  
MACH = 10.40  
GAMMA= 1.400  
EOSDX= 0.060261

X	N(HAT)	MACH	P/P1	N	HTR	L	PHI PRIM	THETA	DELTA *	INV. Y	WBL
2	11.5369	9.1834	2.2874	-0.	0.5183	0.2205	0.1734	9.1957E-03	2.1413E-01	8.1878E-01	9.5031E-02
3	11.7869	9.1833	2.2876	C.0004	0.5184	0.2205	0.1734	8.2703E-03	2.1610E-01	8.3385E-01	9.5895E-02
4	12.0369	9.1830	2.1284	C.0013	0.5189	0.2204	0.1734	8.3435E-03	2.1806E-01	8.4892E-01	9.6747E-02
5	12.2869	9.1823	2.2892	C.0025	0.5198	0.2203	0.1733	8.4149E-03	2.2004E-01	8.6398E-01	9.7583E-02
6	12.5369	9.1811	2.2913	C.0045	0.5213	0.2201	0.1733	8.4840E-03	2.2202E-01	8.7908E-01	9.8403E-02
7	12.7869	9.1799	2.2947	C.0073	0.5239	0.2197	0.1732	8.5500E-03	2.2403E-01	8.9420E-01	9.9203E-02
8	13.0369	9.1758	2.3060	C.0112	0.5277	0.2191	0.1731	8.6118E-03	2.2608E-01	9.0934E-01	9.9977E-02
9	13.2869	9.1710	2.3079	C.0167	0.5332	0.2183	0.1729	8.6682E-03	2.2818E-01	9.2455E-01	1.0072E-01
10	13.5369	9.1641	2.3194	C.0243	0.5411	0.2171	0.1727	8.7174E-03	2.3037E-01	9.3984E-01	1.0142E-01
11	13.7869	9.1543	2.3359	C.0348	0.5523	0.2154	0.1723	8.7569E-03	2.3267E-01	9.5524E-01	1.0206E-01
12	14.0369	9.1405	2.3592	C.0491	0.5681	0.2130	0.1719	8.7835E-03	2.3514E-01	9.7081E-01	1.0263E-01
13	14.2869	9.1213	2.3923	C.0694	0.5901	0.2097	0.1712	8.7927E-03	2.3783E-01	9.8661E-01	1.0311E-01
14	14.5369	9.0945	2.4393	C.0977	0.6212	0.2049	0.1703	8.7782E-03	2.4086E-01	1.0027E-01	1.0346E-01
15	14.7869	9.0573	2.5050	C.1344	0.6648	0.1981	0.1690	8.7329E-03	2.4434E-01	1.0193E-01	1.0364E-01
16	15.0369	9.0142	2.6004	C.1833	0.7259	0.1885	0.1673	8.6489E-03	2.4845E-01	1.0365E-01	1.0364E-01
17	15.2869	8.9379	2.7353	C.2482	0.8118	0.1748	0.1650	8.5161E-03	2.5343E-01	1.0546E-01	1.0333E-01
18	15.5369	8.8483	2.9228	C.3112	0.9300	0.1554	0.1623	8.3329E-03	2.5958E-01	1.0739E-01	1.0289E-01
19	15.7869	8.7420	3.1646	C.3486	1.0830	0.1304	0.1596	8.1164E-03	2.6720E-01	1.0946E-01	1.0250E-01
20	16.0369	8.6314	3.4406	C.3338	1.2638	0.1019	0.1575	7.9009E-03	2.7649E-01	1.1170E-01	1.0251E-01
21	16.2869	8.5318	3.7124	C.2776	1.4570	0.0742	0.1566	7.7208E-03	2.8743E-01	1.1410E-01	1.0314E-01
22	16.5369	8.4507	3.9519	C.2198	1.6512	0.0500	0.1564	7.5870E-03	2.9982E-01	1.1665E-01	1.0432E-01
23	16.7869	8.3870	4.1524	C.1718	1.8427	0.0301	0.1567	7.4913E-03	3.1340E-01	1.1932E-01	1.0589E-01
24	17.0369	8.3378	4.3152	C.1317	2.0301	0.0143	0.1568	7.4236E-03	3.2792E-01	1.2208E-01	1.0774E-01
25	17.2869	8.2992	4.4479	C.1071	2.2171	0.0015	0.1568	7.3748E-03	3.4318E-01	1.2492E-01	1.0971E-01
26	17.5369	8.2689	4.5554	C.0814	2.4019	-0.0086	0.1565	7.3386E-03	3.5902E-01	1.2781E-01	1.1182E-01
27	17.7869	8.2458	4.6392	C.0627	2.5845	-0.0163	0.1558	7.3122E-03	3.7533E-01	1.3075E-01	1.1401E-01
28	18.0369	8.2279	4.7052	C.0488	2.7659	-0.0223	0.1548	7.2921E-03	3.9198E-01	1.3373E-01	1.1622E-01
29	18.2869	8.2133	4.7599	C.0427	2.9474	-0.0275	0.1535	7.2755E-03	4.0892E-01	1.3673E-01	1.1842E-01
30	18.5369	8.2033	4.7991	C.0205	3.1270	-0.0306	0.1518	7.2620E-03	4.2607E-01	1.3976E-01	1.2070E-01
31	18.7869	8.1958	4.8269	C.0264	3.3057	-0.0335	0.1501	7.2507E-03	4.4337E-01	1.4280E-01	1.2288E-01
32	19.0369	8.1888	4.8535	C.0166	3.4860	-0.0360	0.1482	7.2396E-03	4.6080E-01	1.4585E-01	1.2511E-01
33	19.2869	8.1849	4.8686	C.0079	3.6648	-0.0373	0.1461	7.2291E-03	4.7832E-01	1.4892E-01	1.2732E-01
34	19.5369	8.1822	4.8791	C.0091	3.8434	-0.0386	0.1439	7.2189E-03	4.9590E-01	1.5198E-01	1.2947E-01
35	19.7869	8.1810	4.8840	-0.0012	4.0218	-0.0391	0.1416	7.2082E-03	5.1352E-01	1.5506E-01	1.3165E-01
36	20.0369	8.1807	4.8850	C.0029	4.1999	-0.0396	0.1393	7.1972E-03	5.3115E-01	1.5813E-01	1.3374E-01
37	20.2869	8.1812	4.8832	-0.0060	4.3781	-0.0397	0.1369	7.1856E-03	5.4878E-01	1.6120E-01	1.3586E-01
38	20.5369	8.1827	4.8772	-0.0036	4.5560	-0.0396	0.1346	7.1732E-03	5.6639E-01	1.6427E-01	1.3790E-01
39	20.7869	8.1842	4.8713	-0.0058	4.7343	-0.0395	0.1322	7.1606E-03	5.8397E-01	1.6734E-01	1.3994E-01
40	21.0369	8.1869	4.8613	-0.0101	4.9125	-0.0391	0.1298	7.1485E-03	6.0152E-01	1.7041E-01	1.4196E-01
41	21.2869	8.1898	4.8498	-0.0081	5.0908	-0.0396	0.1274	7.1368E-03	6.1902E-01	1.7347E-01	1.4392E-01
42	21.5369	8.1927	4.8398	-0.0092	5.2695	-0.0383	0.1251	7.1158E-03	6.3646E-01	1.7652E-01	1.4588E-01
43	21.7869	8.1963	4.8248	-0.0129	5.4484	-0.0377	0.1228	7.1002E-03	6.5385E-01	1.7957E-01	1.4781E-01
44	22.0369	8.2002	4.8037	-0.0109	5.6276	-0.0371	0.1205	7.0828E-03	6.7118E-01	1.8261E-01	1.4969E-01
45	22.2869	8.2040	4.7953	-0.0116	5.8072	-0.0365	0.1183	7.0652E-03	6.8844E-01	1.8565E-01	1.5156E-01
46	22.5369	8.2081	4.7793	-0.0123	5.9872	-0.0358	0.1161	7.0467E-03	7.0562E-01	1.8868E-01	1.5341E-01
47	22.7869	8.2125	4.7632	-0.0137	6.1677	-0.0351	0.1140	7.0269E-03	7.2274E-01	1.9170E-01	1.5523E-01
48	23.0369	8.2170	4.7462	-0.0127	6.3488	-0.0344	0.1118	7.0064E-03	7.3978E-01	1.9471E-01	1.5701E-01
49	23.2869	8.2214	4.7297	-0.0128	6.5302	-0.0337	0.1097	6.9858E-03	7.5674E-01	1.9772E-01	1.5878E-01
50	23.5369	8.2258	4.7131	-0.0126	6.7122	-0.0330	0.1076	6.9645E-03	7.7362E-01	2.0072E-01	1.6052E-01
51	23.7869	8.2306	4.6954	-0.0144	6.8952	-0.0323	0.1057	6.9419E-03	7.9043E-01	2.0371E-01	1.6226E-01
52	24.0000	8.2347	4.6800	-0.0132	7.0518	-0.0317	0.1041	6.9219E-03	8.0699E-01	2.0625E-01	1.6369E-01
53	51.9900	6.7966	14.8140	C.0100	0.5628	0.2538	0.2035	9.3999E-03	1.4100E-01	2.8658E-01	3.9050E-01
54	51.4900	6.7979	14.7957	C.0028	0.5648	0.2535	0.2035	9.3324E-03	1.4023E-01	2.8388E-01	3.8714E-01
55	50.9900	6.7984	14.7866	C.0021	0.5682	0.2530	0.2033	9.2612E-03	1.3951E-01	2.8119E-01	3.8368E-01
56	50.4900	6.7989	14.7822	C.0023	0.5720	0.2524	0.2032	9.1894E-03	1.3881E-01	2.7850E-01	3.8017E-01
57	49.9900	6.7994	14.7750	C.0025	0.5762	0.2518	0.2031	9.1173E-03	1.3813E-01	2.7581E-01	3.7662E-01
58	49.4900	6.8000	14.7659	C.0028	0.5807	0.2511	0.2030	9.0451E-03	1.3748E-01	2.7312E-01	3.7301E-01



25	17.2859	0.1223	8.2992	4.4479	0.1971	2.2171	0.0315	0.1568	1.3743E-03	3.4318E-01	1.2492E	00	1.6971E-01
26	17.5369	0.1165	8.2689	4.5554	0.0914	2.4019	-0.0086	0.1565	7.3386E-03	3.5902E-01	1.2781E	00	1.1182E-01
27	17.7869	0.1137	8.2458	4.6392	0.0527	2.5845	-0.0163	0.1558	7.3122E-03	3.7533E-01	1.3075E	00	1.1401E-01
28	18.0369	0.1038	8.2279	4.7052	0.0488	2.7659	-0.0223	0.1548	7.2921E-03	3.9198E-01	1.3373E	00	1.1622E-01
29	18.2869	0.0973	8.2133	4.7599	0.0427	2.9474	-0.0375	0.1535	7.2755E-03	4.0892E-01	1.3673E	00	1.1842E-01
30	18.5369	0.0913	8.2033	4.7981	0.0205	3.1270	-0.0306	0.1518	7.2620E-03	4.2607E-01	1.3976E	00	1.2070E-01
31	18.7869	0.0854	8.1958	4.8269	0.0268	3.3057	-0.0335	0.1501	7.2507E-03	4.4337E-01	1.4280E	00	1.2288E-01
32	19.0369	0.0796	8.1888	4.8535	0.0166	3.4860	-0.0366	0.1482	7.2396E-03	4.6080E-01	1.4585E	00	1.2511E-01
33	19.2869	0.0744	8.1849	4.8646	0.0379	3.6648	-0.0373	0.1461	7.2291E-03	4.7832E-01	1.4892E	00	1.2732E-01
34	19.5369	0.0694	8.1822	4.8791	0.0591	3.8434	-0.0386	0.1439	7.2189E-03	4.9590E-01	1.5198E	00	1.2947E-01
35	19.7869	0.0659	8.1810	4.8840	-0.0012	4.0218	-0.0391	0.1416	7.2082E-03	5.1352E-01	1.5506E	00	1.3165E-01
36	20.0369	0.0604	8.1807	4.8850	0.0529	4.1959	-0.0396	0.1393	7.1972E-03	5.3115E-01	1.5813E	00	1.3374E-01
37	20.2869	0.0568	8.1812	4.8832	-0.0060	4.3781	-0.0397	0.1369	7.1855E-03	5.4878E-01	1.6120E	00	1.3586E-01
38	20.5369	0.0527	8.1827	4.8772	0.0336	4.5560	-0.0396	0.1346	7.1732E-03	5.6639E-01	1.6427E	00	1.3790E-01
39	20.7869	0.0496	8.1842	4.8713	-0.0058	4.7343	-0.0395	0.1322	7.1606E-03	5.8397E-01	1.6734E	00	1.3994E-01
40	21.0369	0.0467	8.1868	4.8613	-0.0101	4.9125	-0.0391	0.1298	7.1465E-03	6.0152E-01	1.7041E	00	1.4196E-01
41	21.2869	0.0438	8.1898	4.8498	-0.0081	5.0908	-0.0387	0.1274	7.1318E-03	6.1902E-01	1.7347E	00	1.4392E-01
42	21.5369	0.0400	8.1927	4.8388	-0.0092	5.2695	-0.0383	0.1251	7.1168E-03	6.3646E-01	1.7652E	00	1.4588E-01
43	21.7869	0.0337	8.1963	4.8248	-0.0129	5.4484	-0.0377	0.1228	7.1002E-03	6.5385E-01	1.7957E	00	1.4781E-01
44	22.0369	0.0364	8.2002	4.8097	-0.0109	5.6276	-0.0371	0.1205	7.0828E-03	6.7118E-01	1.8261E	00	1.4969E-01
45	22.2869	0.0342	8.2040	4.7953	-0.0116	5.8072	-0.0365	0.1183	7.0652E-03	6.8844E-01	1.8565E	00	1.5156E-01
46	22.5369	0.0321	8.2081	4.7799	-0.0123	5.9872	-0.0358	0.1161	7.0467E-03	7.0562E-01	1.8868E	00	1.5341E-01
47	22.7869	0.0304	8.2125	4.7632	-0.0137	6.1677	-0.0354	0.1140	7.0269E-03	7.2274E-01	1.9170E	00	1.5523E-01
48	23.0369	0.0287	8.2170	4.7462	-0.0127	6.3488	-0.0344	0.1118	7.0064E-03	7.3978E-01	1.9471E	00	1.5701E-01
49	23.2869	0.0271	8.2214	4.7297	-0.0128	6.5302	-0.0337	0.1097	6.9858E-03	7.5674E-01	1.9772E	00	1.5878E-01
50	23.5369	0.0254	8.2258	4.7131	-0.0126	6.7122	-0.0330	0.1076	6.9645E-03	7.7362E-01	2.0072E	00	1.6052E-01
51	23.7869	0.0247	8.2306	4.6954	-0.0144	6.8952	-0.0323	0.1057	6.9419E-03	7.9043E-01	2.0371E	00	1.6226E-01
52	24.0300	0.0231	8.2347	4.6800	-0.0132	7.0518	-0.0317	0.1041	6.9219E-03	8.0469E-01	2.0678E	00	1.6369E-01
53	51.3700	0.0096	6.7966	14.8140	0.0100	0.5628	0.2538	0.2035	9.3324E-03	1.4023E-01	2.8388E	00	3.9050E-01
54	51.4900	0.0101	6.7979	14.7957	0.0328	0.5648	0.2535	0.2035	9.3324E-03	1.4023E-01	2.8388E	00	3.9050E-01
55	53.9900	0.0109	6.7984	14.7886	0.0021	0.5682	0.2533	0.2033	9.2612E-03	1.3951E-01	2.8119E	00	3.8368E-01
56	50.4900	0.0116	6.7989	14.7822	0.0323	0.5720	0.2524	0.2032	9.1894E-03	1.3881E-01	2.7850E	00	3.8017E-01
57	49.9900	0.0125	6.7994	14.7750	0.0025	0.5762	0.2518	0.2031	9.1173E-03	1.3813E-01	2.7581E	00	3.7662E-01
58	49.4900	0.0135	6.8000	14.7669	0.0028	0.5807	0.2511	0.2030	9.0451E-03	1.3748E-01	2.7312E	00	3.7301E-01
59	48.9900	0.0145	6.8006	14.7584	0.0027	0.5857	0.2503	0.2028	8.9726E-03	1.3686E-01	2.7044E	00	3.6935E-01
60	48.4900	0.0156	6.8013	14.7491	0.0032	0.5911	0.2495	0.2027	8.8999E-03	1.3627E-01	2.6776E	00	3.6565E-01
61	47.9900	0.0168	6.8021	14.7390	0.0037	0.5969	0.2486	0.2025	8.8272E-03	1.3571E-01	2.6509E	00	3.6188E-01
62	47.4900	0.0181	6.8030	14.7253	0.0041	0.6032	0.2476	0.2023	8.7547E-03	1.3520E-01	2.6241E	00	3.5806E-01
63	46.9900	0.0195	6.8041	14.7110	0.0045	0.6101	0.2466	0.2021	8.6821E-03	1.3473E-01	2.5975E	00	3.5416E-01
64	46.4900	0.0211	6.8052	14.6950	0.0050	0.6177	0.2454	0.2019	8.6096E-03	1.3432E-01	2.5709E	00	3.5019E-01
65	45.9900	0.0228	6.8066	14.6771	0.0055	0.6260	0.2441	0.2016	8.5373E-03	1.3397E-01	2.5443E	00	3.4614E-01
66	45.4900	0.0247	6.8080	14.6571	0.0061	0.6352	0.2427	0.2013	8.4652E-03	1.3369E-01	2.5178E	00	3.4201E-01
67	44.9900	0.0267	6.8097	14.6347	0.0067	0.6452	0.2412	0.2010	8.3934E-03	1.3348E-01	2.4914E	00	3.3779E-01
68	44.4900	0.0288	6.8114	14.6108	0.0076	0.6562	0.2395	0.2007	8.3217E-03	1.3335E-01	2.4651E	00	3.3352E-01
69	43.9900	0.0312	6.8134	14.5842	0.0080	0.6684	0.2376	0.2004	8.2505E-03	1.3332E-01	2.4389E	00	3.2915E-01
70	43.4900	0.0337	6.8157	14.5529	0.0090	0.6816	0.2355	0.2000	8.1803E-03	1.3338E-01	2.4127E	00	3.2468E-01
71	42.9900	0.0366	6.8183	14.5176	0.0099	0.6962	0.2332	0.1996	8.1100E-03	1.3357E-01	2.3867E	00	3.2010E-01
72	42.4900	0.0397	6.8213	14.4760	0.0109	0.7124	0.2307	0.1991	8.0427E-03	1.3389E-01	2.3608E	00	3.1539E-01
73	41.9900	0.0430	6.8244	14.4358	0.0109	0.7303	0.2278	0.1986	7.9750E-03	1.3436E-01	2.3351E	00	3.1059E-01
74	41.4900	0.0466	6.8279	14.3890	0.0129	0.7501	0.2247	0.1981	7.9085E-03	1.3498E-01	2.3095E	00	3.0566E-01
75	40.9900	0.0504	6.8320	14.3350	0.0142	0.7718	0.2212	0.1975	7.8440E-03	1.3579E-01	2.2841E	00	3.0065E-01
76	40.4900	0.0545	6.8366	14.2745	0.0158	0.7957	0.2174	0.1969	7.7813E-03	1.3681E-01	2.2589E	00	2.9549E-01
77	39.9900	0.0591	6.8418	14.2061	0.0176	0.8221	0.2131	0.1963	7.7209E-03	1.3806E-01	2.2339E	00	2.9020E-01
78	39.4900	0.0639	6.8478	14.1277	0.0202	0.8513	0.2083	0.1956	7.6633E-03	1.3957E-01	2.2092E	00	2.8483E-01
79	38.9900	0.0690	6.8546	14.0341	0.0221	0.8835	0.2031	0.1948	7.6089E-03	1.4140E-01	2.1849E	00	2.7930E-01
80	38.4900	0.0744	6.8622	13.9404	0.0245	0.9194	0.1972	0.1940	7.5576E-03	1.4356E-01	2.1608E	00	2.7367E-01
81	37.9900	0.0801	6.8710	13.8285	0.0278	0.9590	0.1907	0.1932	7.5105E-03	1.4612E-01	2.1372E	00	2.6793E-01
82	37.4900	0.0860	6.8811	13.7004	0.0317	1.0027	0.1835	0.1924	7.4683E-03	1.4913E-01	2.1140E	00	2.6208E-01
83	36.9900	0.0921	6.8927	13.5541	0.0360	1.0511	0.1755	0.1916	7.4316E-03	1.5265E-01	2.0913E	00	2.5617E-01
84	36.4900	0.0983	6.9062	13.3876	0.0408	1.1046	0.1669	0.1907	7.4012E-03	1.5676E-01	2.0692E	00	2.5022E-01
85	35.9900	0.1044	6.9218	13.1982	0.0466	1.1638	0.1574	0.1900	7.3777E-03	1.6156E-01	2.0478E	00	2.4424E-01
86	35.4900	0.1103	6.9398	12.9825	0.0532	1.2293	0.1472	0.1893	7.3622E-03	1.6714E-01	2.0272E	00	2.3828E-01
87	34.9900	0.1158	6.9606	12.7385	0.0605	1.3018	0.1362	0.1887	7.3552E-03	1.7362E-01	2.0074E	00	2.3235E-01
88	34.4900	0.1207	6.9855	12.4640	0.0689	1.3819	0.1245	0.1883	7.3573E-03	1.8115E-01	1.9888E	00	2.2649E-01

53	51.9900	0.0596	6.7966	14.6140	0.0100	0.5629	0.2534	0.2035	9.3999E-03	1.4100E-01	2.8658E	00	3.9050E-01
54	51.4900	0.0101	6.7979	14.7957	0.0228	0.5648	0.2535	0.2035	9.3324E-03	1.44023E-01	2.8388E	00	3.8714E-01
55	50.9900	0.0108	6.7984	14.7846	0.0231	0.5682	0.2530	0.2033	9.2612E-03	1.3951E-01	2.8119E	00	3.8368E-01
56	50.4900	0.0116	6.7989	14.7782	0.0233	0.5720	0.2524	0.2032	9.1894E-03	1.3681E-01	2.7850E	00	3.8017E-01
57	49.9900	0.0125	6.7994	14.7750	0.0235	0.5762	0.2518	0.2031	9.1173E-03	1.3481E-01	2.7581E	00	3.7662E-01
58	49.4900	0.0135	6.8000	14.7659	0.0228	0.5807	0.2511	0.2030	9.0451E-03	1.3374E-01	2.7312E	00	3.7301E-01
59	48.9900	0.0145	6.8006	14.7584	0.0227	0.5857	0.2503	0.2028	8.9726E-03	1.3268E-01	2.7044E	00	3.6935E-01
60	48.4900	0.0156	6.8013	14.7491	0.0232	0.5911	0.2495	0.2027	8.8999E-03	1.3162E-01	2.6776E	00	3.6565E-01
61	47.9900	0.0168	6.8021	14.7390	0.0237	0.5969	0.2486	0.2025	8.8272E-03	1.3057E-01	2.6509E	00	3.6188E-01
62	47.4900	0.0181	6.8030	14.7210	0.0241	0.6032	0.2476	0.2023	8.7547E-03	1.2952E-01	2.6241E	00	3.5806E-01
63	46.9900	0.0195	6.8041	14.7110	0.0245	0.6101	0.2466	0.2021	8.6821E-03	1.2847E-01	2.5975E	00	3.5419E-01
64	46.4900	0.0211	6.8052	14.6950	0.0250	0.6177	0.2454	0.2019	8.6096E-03	1.2742E-01	2.5709E	00	3.5036E-01
65	45.9900	0.0228	6.8066	14.6771	0.0255	0.6260	0.2441	0.2016	8.5373E-03	1.2637E-01	2.5441E	00	3.4641E-01
66	45.4900	0.0247	6.8080	14.6571	0.0261	0.6352	0.2427	0.2013	8.4652E-03	1.2532E-01	2.5178E	00	3.4247E-01
67	44.9900	0.0267	6.8097	14.6347	0.0267	0.6452	0.2412	0.2010	8.3934E-03	1.2427E-01	2.4914E	00	3.3852E-01
68	44.4900	0.0288	6.8114	14.6108	0.0267	0.6562	0.2395	0.2007	8.3217E-03	1.2322E-01	2.4651E	00	3.3457E-01
69	43.9900	0.0317	6.8134	14.5842	0.0280	0.6684	0.2376	0.2004	8.2505E-03	1.2217E-01	2.4388E	00	3.2915E-01
70	43.4900	0.0337	6.8157	14.5529	0.0290	0.6816	0.2355	0.2000	8.1803E-03	1.2112E-01	2.4127E	00	3.2468E-01
71	42.9900	0.0366	6.8183	14.5176	0.0299	0.6962	0.2332	0.1996	8.1100E-03	1.2007E-01	2.3867E	00	3.2010E-01
72	42.4900	0.0397	6.8213	14.4780	0.0309	0.7124	0.2307	0.1991	8.0427E-03	1.1902E-01	2.3608E	00	3.1539E-01
73	41.9900	0.0430	6.8244	14.4358	0.0319	0.7303	0.2278	0.1986	7.9750E-03	1.1797E-01	2.3351E	00	3.1059E-01
74	41.4900	0.0466	6.8279	14.3890	0.0329	0.7501	0.2247	0.1981	7.9085E-03	1.1692E-01	2.3095E	00	3.0566E-01
75	40.9900	0.0504	6.8320	14.3350	0.0342	0.7718	0.2212	0.1975	7.8420E-03	1.1587E-01	2.2841E	00	3.0065E-01
76	40.4900	0.0546	6.8366	14.2745	0.0358	0.7957	0.2174	0.1969	7.7813E-03	1.1482E-01	2.2589E	00	2.9549E-01
77	39.9900	0.0591	6.8418	14.2061	0.0376	0.8221	0.2131	0.1963	7.7209E-03	1.1377E-01	2.2339E	00	2.9020E-01
78	39.4900	0.0639	6.8478	14.1277	0.0402	0.8513	0.2083	0.1956	7.6633E-03	1.1272E-01	2.2092E	00	2.8483E-01
79	38.9900	0.0690	6.8546	14.0391	0.0421	0.8835	0.2031	0.1948	7.6089E-03	1.1167E-01	2.1849E	00	2.7930E-01
80	38.4900	0.0744	6.8622	13.9404	0.0445	0.9194	0.1972	0.1940	7.5576E-03	1.1062E-01	2.1608E	00	2.7367E-01
81	37.9900	0.0801	6.8710	13.8285	0.0478	0.9590	0.1907	0.1932	7.5105E-03	1.0957E-01	2.1372E	00	2.6793E-01
82	37.4900	0.0860	6.8811	13.7004	0.0517	1.0027	0.1835	0.1924	7.4683E-03	1.0852E-01	2.1140E	00	2.6208E-01
83	36.9900	0.0921	6.8927	13.5541	0.0560	1.0511	0.1756	0.1916	7.4316E-03	1.0747E-01	2.0913E	00	2.5617E-01
84	36.4900	0.0984	6.9062	13.3876	0.0608	1.1046	0.1669	0.1907	7.4012E-03	1.0642E-01	2.0692E	00	2.5022E-01
85	35.9900	0.1044	6.9218	13.1982	0.0666	1.1638	0.1574	0.1900	7.3777E-03	1.0537E-01	2.0478E	00	2.4424E-01
86	35.4900	0.1103	6.9398	12.9825	0.0732	1.2293	0.1472	0.1893	7.3622E-03	1.0432E-01	2.0272E	00	2.3828E-01
87	34.9900	0.1158	6.9606	12.7385	0.0805	1.3018	0.1362	0.1887	7.3522E-03	1.0327E-01	2.0074E	00	2.3235E-01
88	34.4900	0.1207	6.9845	12.4640	0.0889	1.3819	0.1245	0.1883	7.3573E-03	1.0222E-01	1.9888E	00	2.2649E-01
89	33.9900	0.1248	7.0121	12.1552	0.0988	1.4702	0.1124	0.1880	7.3694E-03	1.0117E-01	1.9713E	00	2.2079E-01
90	33.4900	0.1279	7.0436	11.8145	0.1073	1.5680	0.0999	0.1879	7.3910E-03	1.0012E-01	1.9551E	00	2.1525E-01
91	32.9900	0.1296	7.0791	11.4423	0.0986	1.6759	0.0873	0.1879	7.4218E-03	0.9907E-01	1.9395E	00	2.0994E-01
92	32.4900	0.1299	7.1191	11.0393	0.1085	1.7949	0.0748	0.1881	7.4612E-03	0.9802E-01	1.9276E	00	2.0488E-01
93	31.9900	0.1288	7.1632	10.6131	0.1177	1.9262	0.0627	0.1883	7.5073E-03	0.9697E-01	1.9165E	00	2.0008E-01
94	31.4900	0.1261	7.2113	10.1689	0.1266	2.0711	0.0512	0.1884	7.5581E-03	0.9592E-01	1.9075E	00	1.9559E-01
95	30.9900	0.1220	7.2633	9.7123	0.1345	2.2305	0.0406	0.1883	7.6114E-03	0.9487E-01	1.9006E	00	1.9139E-01
96	30.4900	0.1164	7.3190	9.2491	0.1412	2.4054	0.0312	0.1880	7.6644E-03	0.9382E-01	1.8960E	00	1.8754E-01
97	29.9900	0.1098	7.3780	8.7860	0.1461	2.5974	0.0232	0.1872	7.7139E-03	0.9277E-01	1.8939E	00	1.8403E-01
98	29.4900	0.1023	7.4395	8.3302	0.1486	2.8080	0.0165	0.1860	7.7555E-03	0.9172E-01	1.8938E	00	1.8083E-01
99	28.9900	0.0942	7.5025	7.8905	0.1471	3.0395	0.0108	0.1842	7.7888E-03	0.9067E-01	1.8972E	00	1.7792E-01
100	28.4900	0.0858	7.5670	7.4678	0.1406	3.2929	0.0067	0.1817	7.8033E-03	0.8959E-01	1.9027E	00	1.7537E-01
101	27.9900	0.0771	7.6319	7.0683	0.1366	3.5711	0.0034	0.1787	7.8120E-03	0.8854E-01	1.9108E	00	1.7304E-01
102	27.4900	0.0686	7.6968	6.6925	0.1389	3.8757	0.0013	0.1750	7.7983E-03	0.8749E-01	1.9215E	00	1.7107E-01
103	26.9900	0.0604	7.7620	6.3374	0.1318	4.2091	0.0003	0.1707	7.7647E-03	0.8644E-01	1.9346E	00	1.6931E-01
104	26.4900	0.0528	7.8269	6.0052	0.1263	4.5747	0.0004	0.1658	7.7101E-03	0.8539E-01	1.9502E	00	1.6782E-01
105	25.9900	0.0457	7.8911	5.6959	0.1173	4.9766	0.0010	0.1605	7.6331E-03	0.8434E-01	1.9683E	00	1.6654E-01
106	25.4900	0.0390	7.9540	5.4102	0.1090	5.4191	0.0022	0.1547	7.5336E-03	0.8329E-01	1.9886E	00	1.6550E-01
107	24.9900	0.0329	8.0155	5.1461	0.1000	5.9073	0.0039	0.1485	7.4111E-03	0.8224E-01	2.0113E	00	1.6467E-01
108	24.4900	0.0278	8.0760	4.9006	0.0925	6.4478	0.0060	0.1422	7.2646E-03	0.8119E-01	2.0361E	00	1.6406E-01
109	24.0000	0.0232	8.1341	4.6777	0.0831	7.0360	0.0082	0.1358	7.0978E-03	0.8014E-01	2.0625E	00	1.6360E-01

Figure 157

TYPICAL LAMINAR BOUNDARY SOLUTION PRINTOUT

**BLANK PAGE**



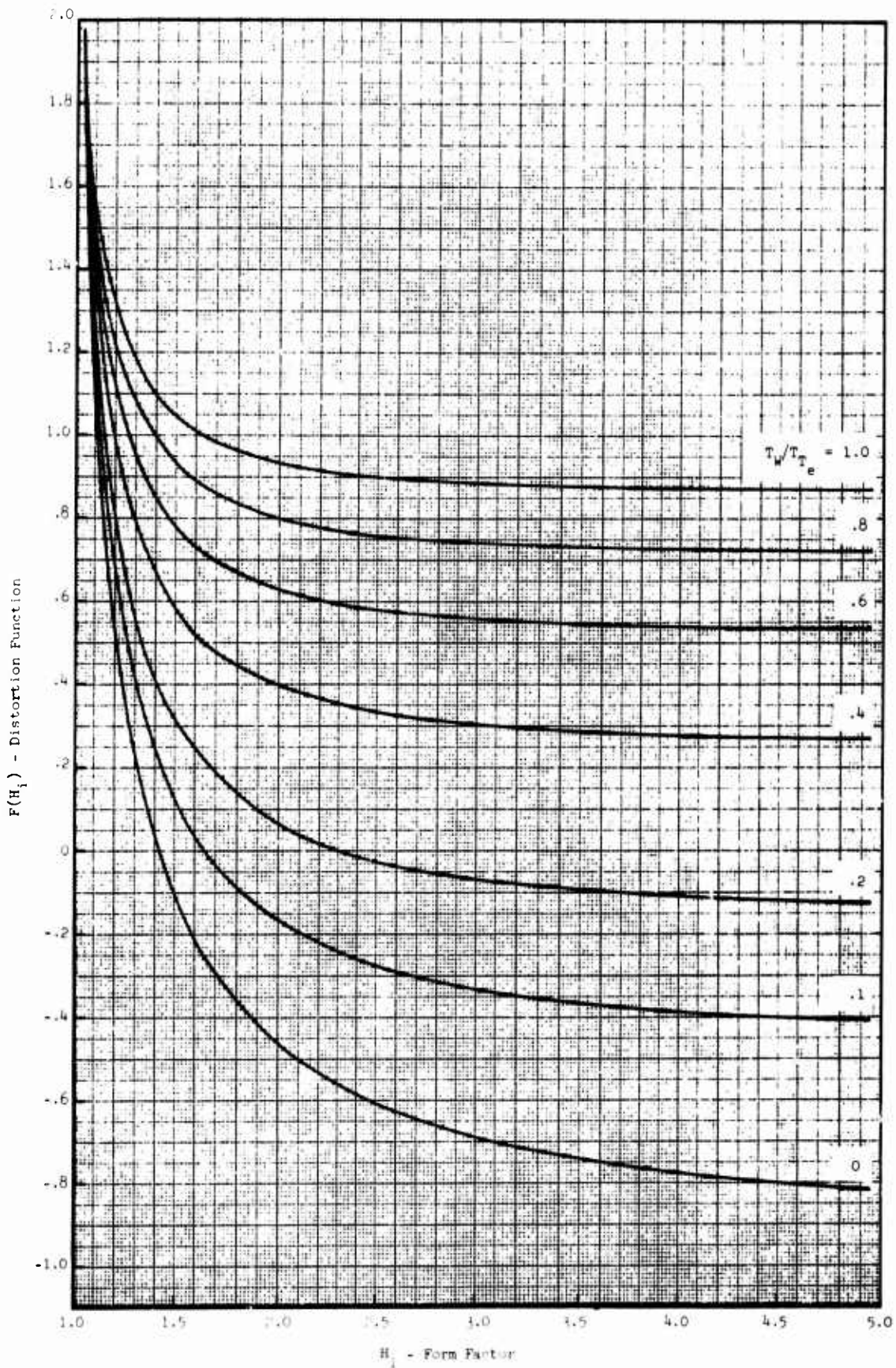


Figure 158 POWER LAW PROFILE DISTORTION FUNCTION

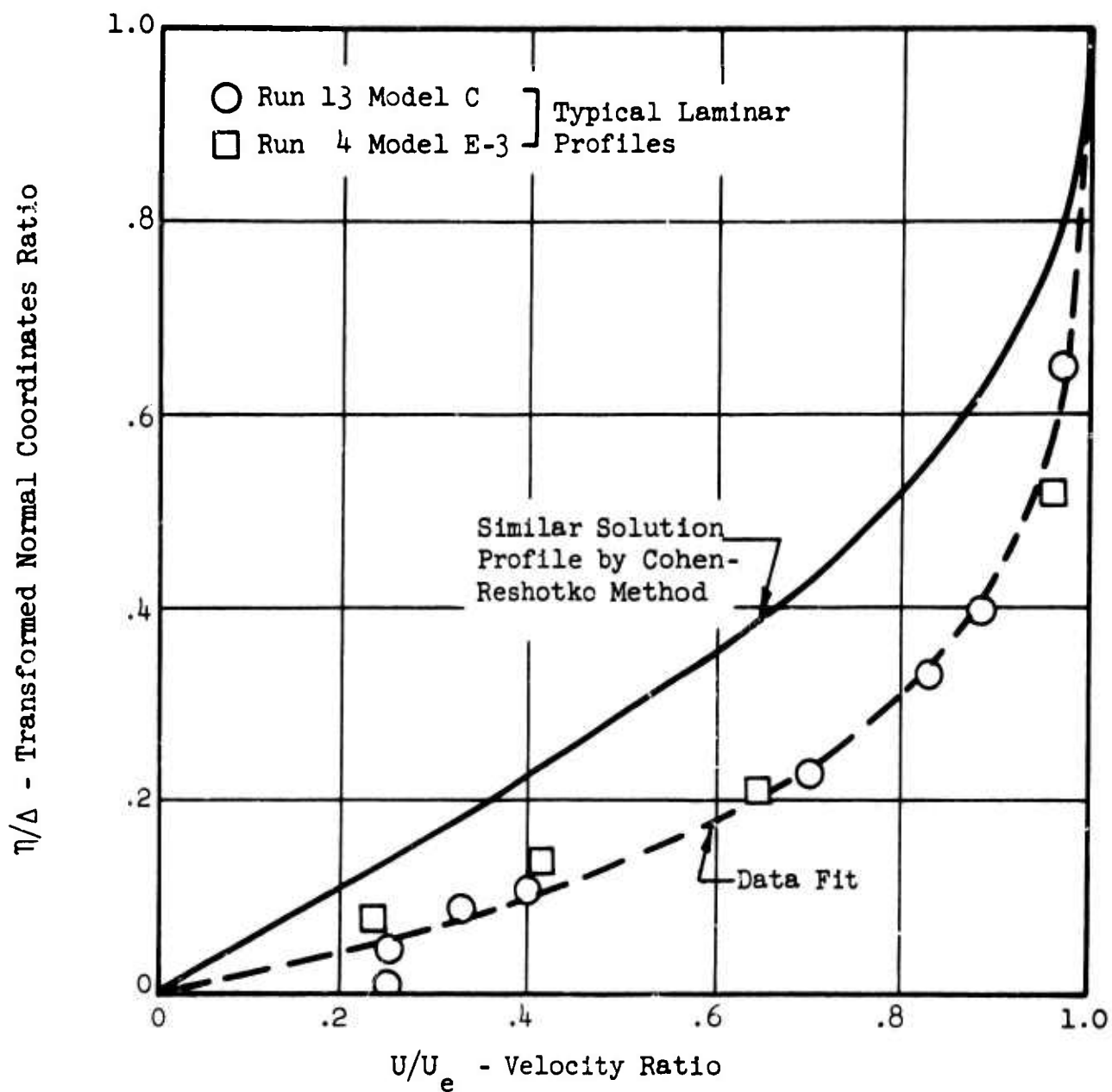


Figure 159 THEORY/DATA VELOCITY PROFILE COMPARISON

## FREE STREAM FLOW CONDITIONS

MACH NO. = 7.29  
 STATIC TEMPERATURE = 134.27  
 DENSITY = 4.65314-06

TOTAL PRESSURE = 58.70  
 VELOCITY = 4139.23  
 UNIT MASS FLOW = 2.7439-02  
 WALL PRESSURE = 0.034900

TOTAL TEMPERATURE = 1515.00  
 STATIC PRESSURE = 0.010647  
 WALL TEMPERATURE = 547.00  
 RECOVERY FACTOR = 1.0000

Y (INCHES)	PISTON PRESS (LBS/IN <sup>2</sup> )	TOTAL TEMP (DEGS R)	STATIC PRESS (LBS/IN <sup>2</sup> )	MACH NO.	STATIC TEMP (DEGS R)	VELOCITY (FT/SEC)	DENSITY (SLUGS/FT <sup>3</sup> )	UNIT MASS FLOW (SLUGS/FT-SEC)
8.00000-03	5.34900-02	4.43420+02	3.53300-02	8.95914-01	7.28937+02	1.14369+03	4.06671-06	4.81374-03
8.10000-02	5.89200-02	4.43129+02	3.43600-02	9.12652-01	7.30150+02	1.20679+03	3.94849-06	4.76499-03
1.33000-01	7.33400-02	7.71272+02	3.47400-02	1.28559+00	7.33813+02	1.70408+03	4.00081-06	6.81769-03
1.46000-01	1.77110-01	1.14164+03	3.45500-02	1.83648+00	6.72513+02	2.40867+03	4.31181-06	1.03857-02
2.36000-01	2.59300-01	1.27520+03	3.40200-02	3.44644+00	5.66907+02	2.97050+03	5.03514-06	1.49569-02
2.91000-01	5.20810-01	1.39385+03	3.30200-02	3.44372+00	4.23851+02	3.47727+03	6.55049-06	2.27778-02
3.44000-01	7.83600-01	1.45807+03	3.30200-02	4.24616+00	3.25473+02	3.75473+03	4.53044-06	3.20295-02
4.95000-01	1.05328+00	1.49575+03	3.29200-02	4.94327+00	2.61643+02	3.91800+03	1.05794-05	4.14502-02
4.47000-01	1.22362+00	1.51319+03	3.25200-02	5.36531+00	2.30738+02	3.79391+03	1.18546-05	4.73463-02
4.97000-01	1.27361+00	1.51799+03	3.23300-02	5.49871+00	2.22033+02	4.01485+03	1.22171-05	4.90499-02
5.52000-01	1.27648+00	1.51891+03	3.21200-02	5.52630+00	2.20374+02	4.01844+03	1.22218-05	4.91172-02
6.01000-01	1.27533+00	1.51975+03	3.17400-02	5.54956+00	2.18824+02	4.02254+03	1.21895-05	4.90328-02
6.53000-01	1.26902+00	1.52007+03	3.15300-02	5.55870+00	2.18253+02	4.02391+03	1.21214-05	4.87756-02
7.84000-01	1.25059+00	1.52050+03	3.11400-02	5.57135+00	2.17465+02	4.02579+03	1.20341-05	4.84468-02

## CONDITIONS AT BOUNDARY-LAYER EDGE

MACH NO. = 5.41  
 VELOCITY = 4001.80  
 DENSITY = 1.2064-05

TOTAL TEMPERATURE = 1515.00  
 STATIC PRESSURE = 0.03272  
 UNIT MASS FLOW = 4.9297-02

STATIC TEMPERATURE = 227.47

Y	DISPLACEMENT	MOMENTUM	ENERGY	INT DISPLAC (INCHES)	INT MOMENT (INCHES)	INT ENERGY (INCHES)	INT MASSFLOW (SLUGS/SEC)	ETA
8.00000-03	9.00334-01	7.01859-02	9.09461-02	3.60134-03	2.480743-04	3.63784-04	1.60458-06	2.61600-03
8.10000-02	9.01343-01	6.87056-02	9.96243-02	6.93626-02	5.35758-03	6.95681-03	3.07399-05	2.68557-02
1.33000-01	8.58842-01	8.10483-02	1.15561-01	1.15127-01	9.25638-03	1.22932-02	5.8357-05	4.39803-02
1.86000-01	7.80463-01	8.56045-02	1.37130-01	1.58698-01	1.36727-02	1.85895-02	4.39266-05	6.22321-02
2.36000-01	6.20325-01	7.94060-02	1.39145-01	1.95571-01	1.78077-02	2.58939-02	1.46624-04	8.15931-02
2.91000-01	5.28397-01	6.19145-02	1.15272-01	2.27036-01	2.17025-02	3.25946-02	2.33099-04	1.07991-01
3.44000-01	3.36344-01	4.09429-02	7.93580-02	2.52015-01	2.44256-02	3.80590-02	3.54132-04	1.41104-01
3.95000-01	1.41795-01	1.79717-02	3.55658-02	2.64220-01	2.59273-02	4.09896-02	5.10276-04	1.81479-01
4.47000-01	1.97189-02	1.93273-03	3.86164-03	2.68419-01	2.64454-02	4.20147-02	7.02669-04	2.29808-01
4.97000-01	-1.55531-02	-3.31260-03	-5.63450-03	2.68523-01	2.64109-02	4.19454-02	3.03494-04	2.79669-01
5.52000-01	-1.67467-02	-4.32944-03	-8.67730-03	2.67630-01	2.62007-02	4.15242-02	1.12846-03	3.35354-01
6.01000-01	-1.51794-02	-5.26276-03	-1.05228-02	2.66842-01	2.59657-02	4.10531-02	1.32885-03	3.84907-01
6.53000-01	-2.87239-03	-5.57932-03	-1.11494-02	2.66130-01	2.56838-02	4.04878-02	1.54077-03	4.37279-01
7.84000-01	-3.06717-03	-6.01269-03	-1.20514-02	2.65343-01	2.49245-02	3.89649-02	2.07144-03	5.68371-01

Figure 160 TYPICAL DATA REDUCTION PRINTOUT

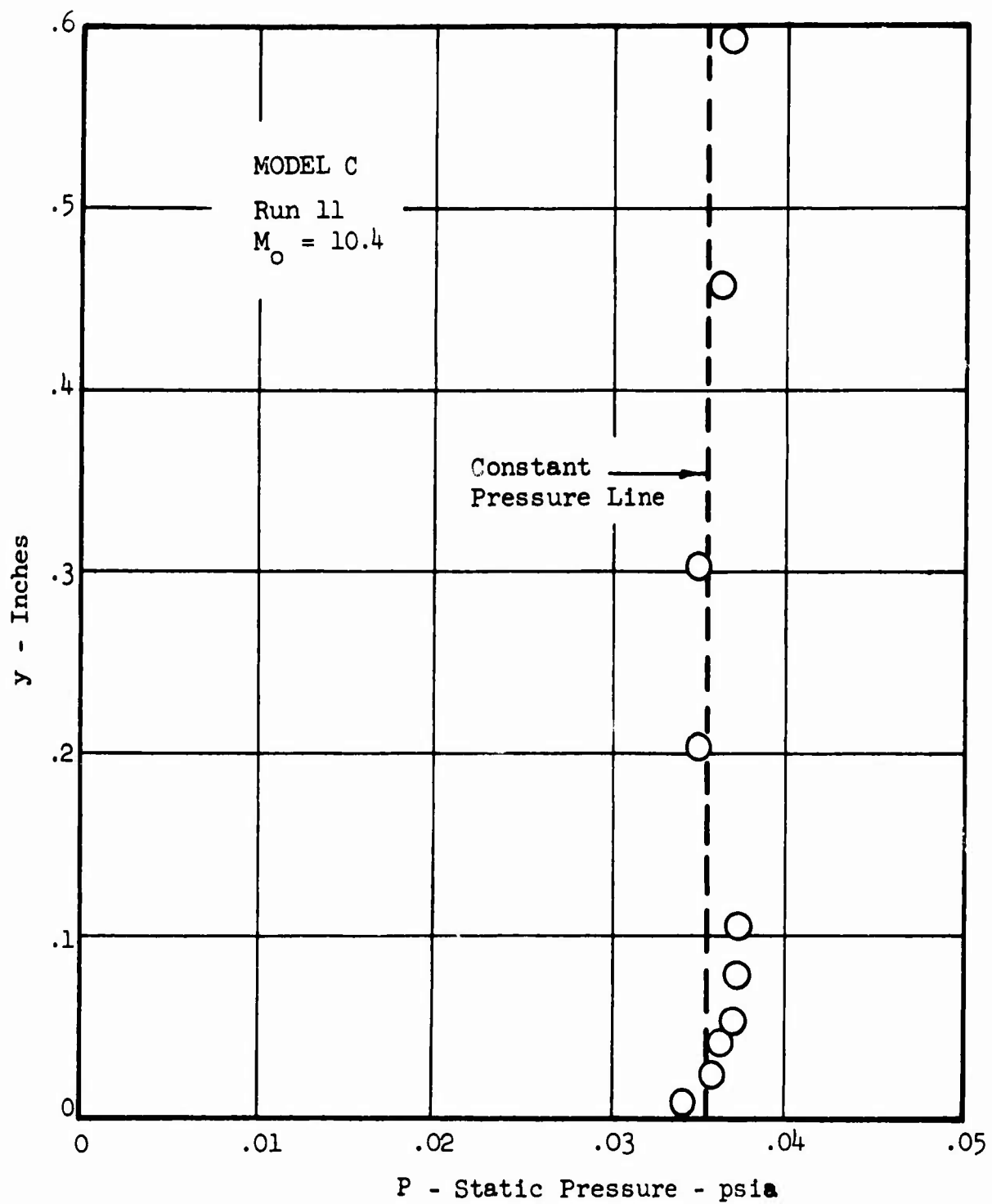


Figure 161 TYPICAL STATIC PRESSURE PROFILE

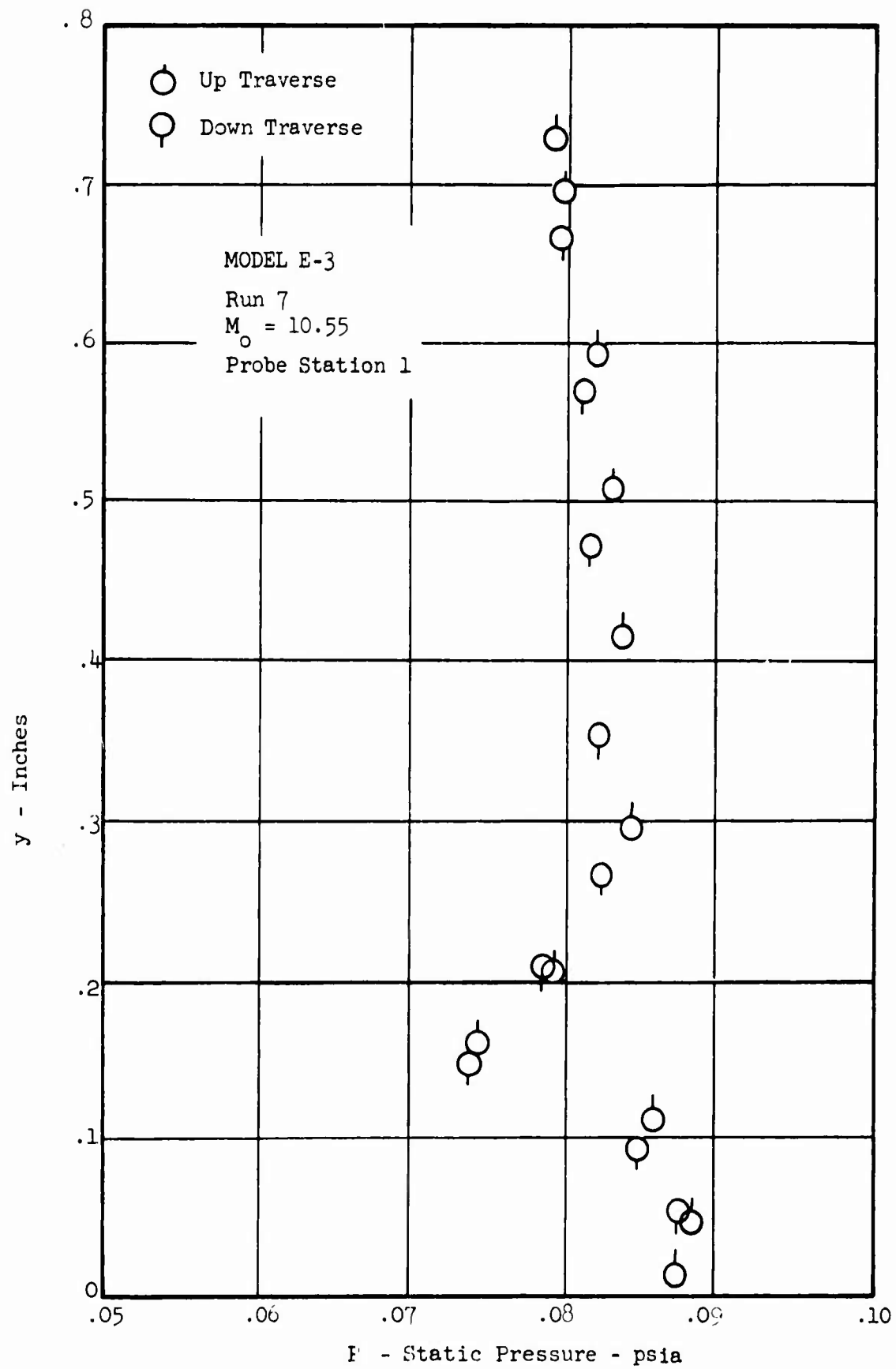


Figure 162 TYPICAL STATIC PRESSURE PROFILE



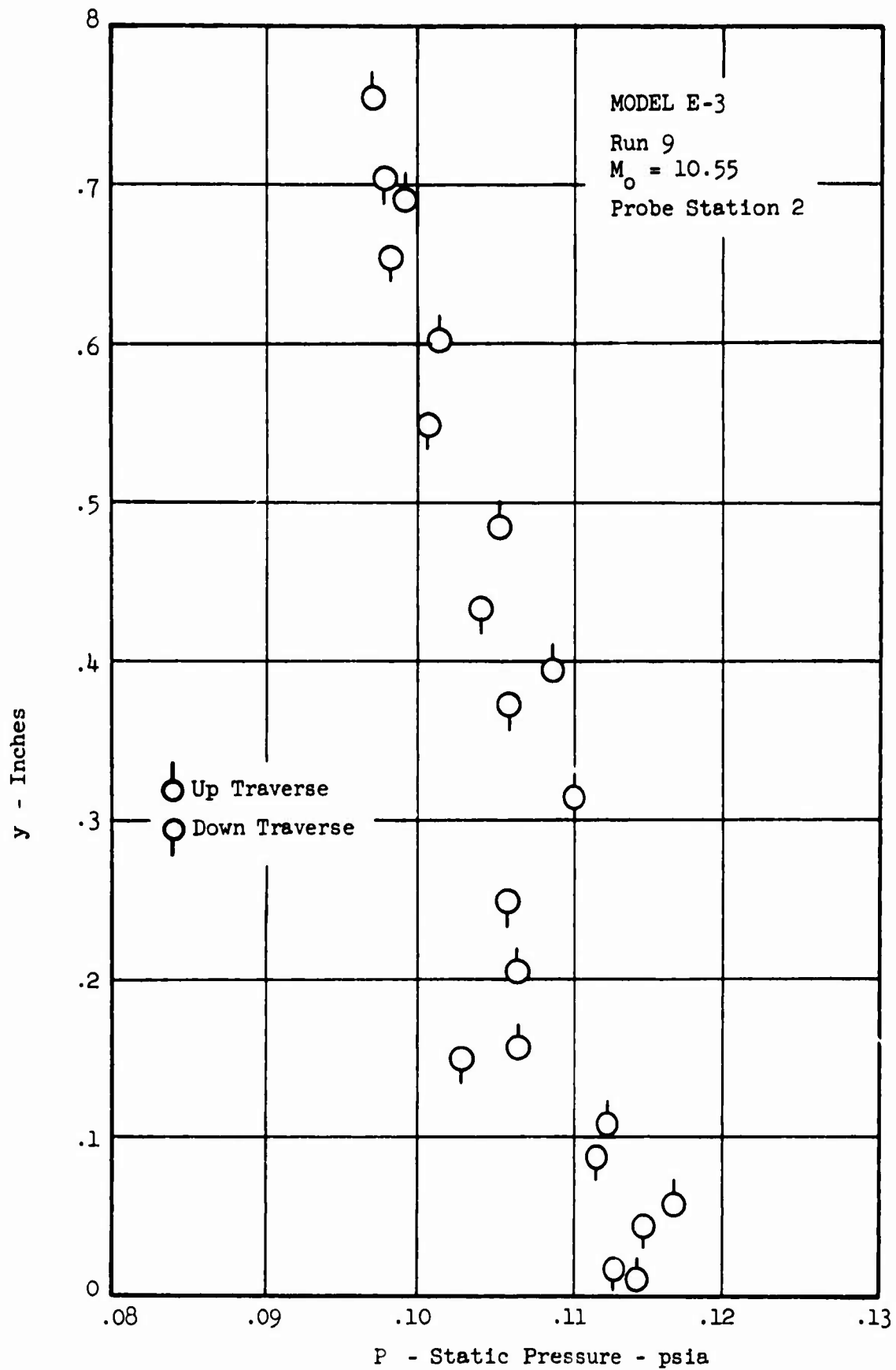


Figure 163 TYPICAL STATIC PRESSURE PROFILE

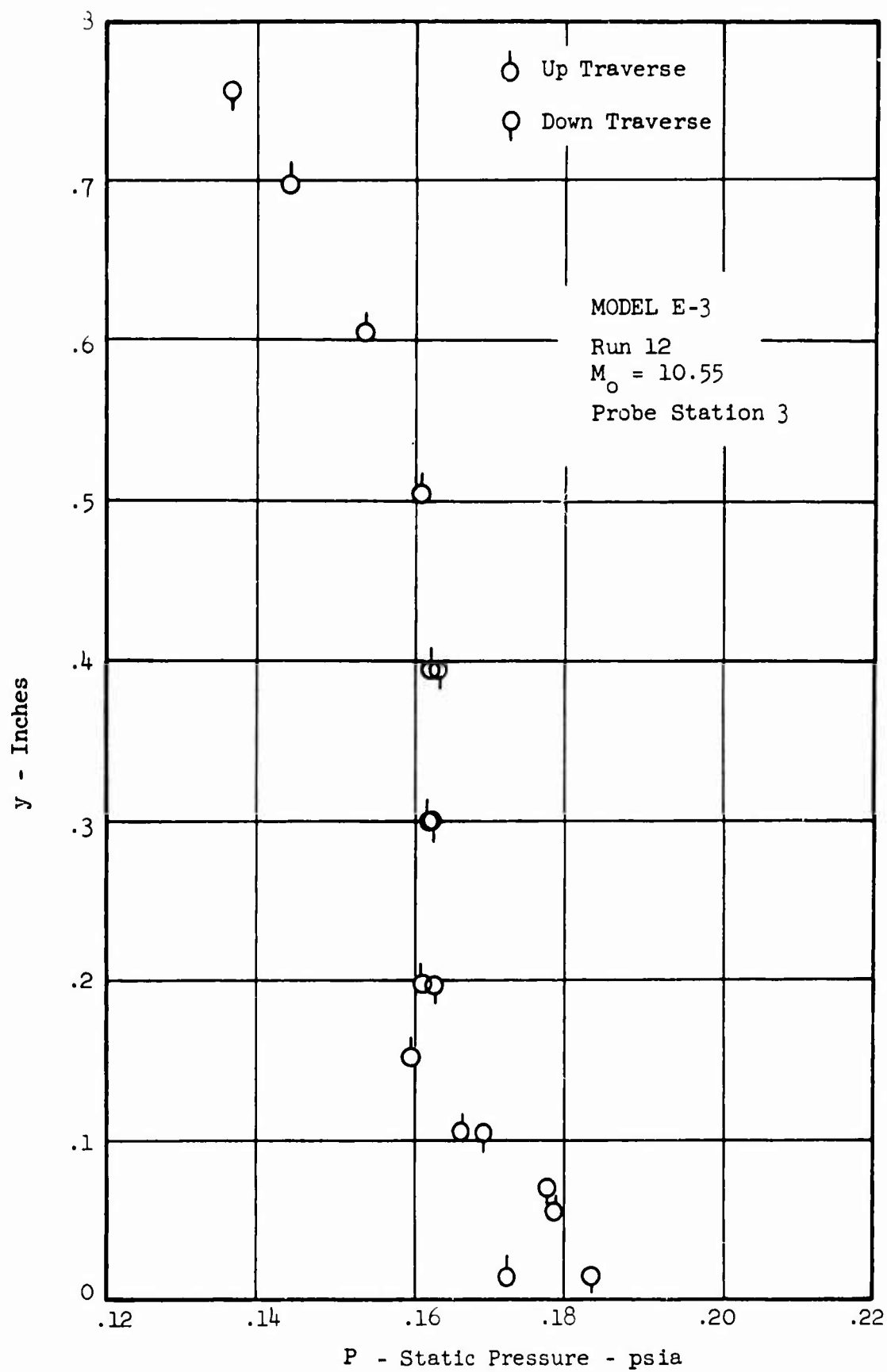


Figure 164 TYPICAL STATIC PRESSURE PROFILE

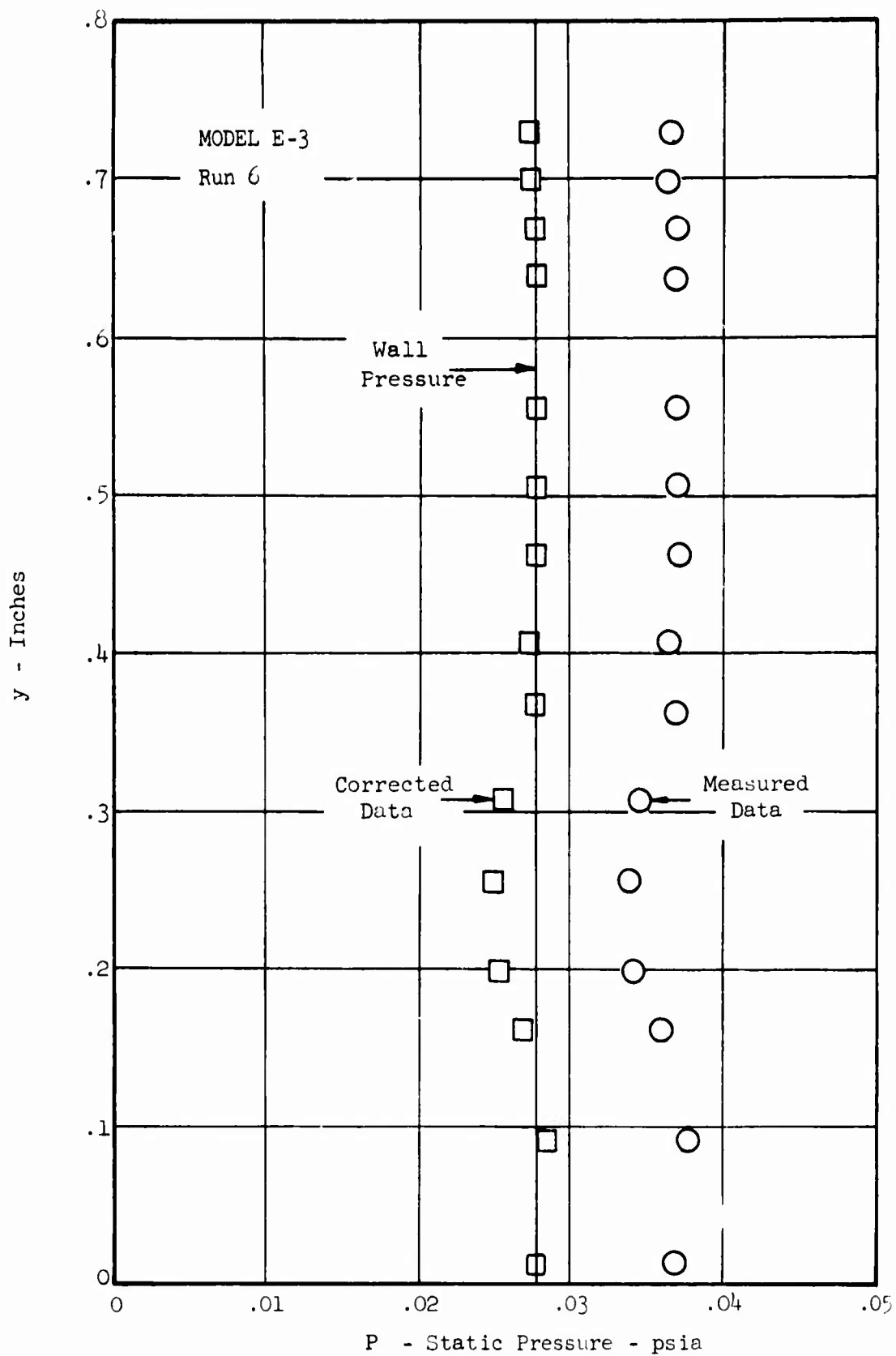


Figure 165 TYPICAL STATIC PRESSURE PROFILE CORRECTION

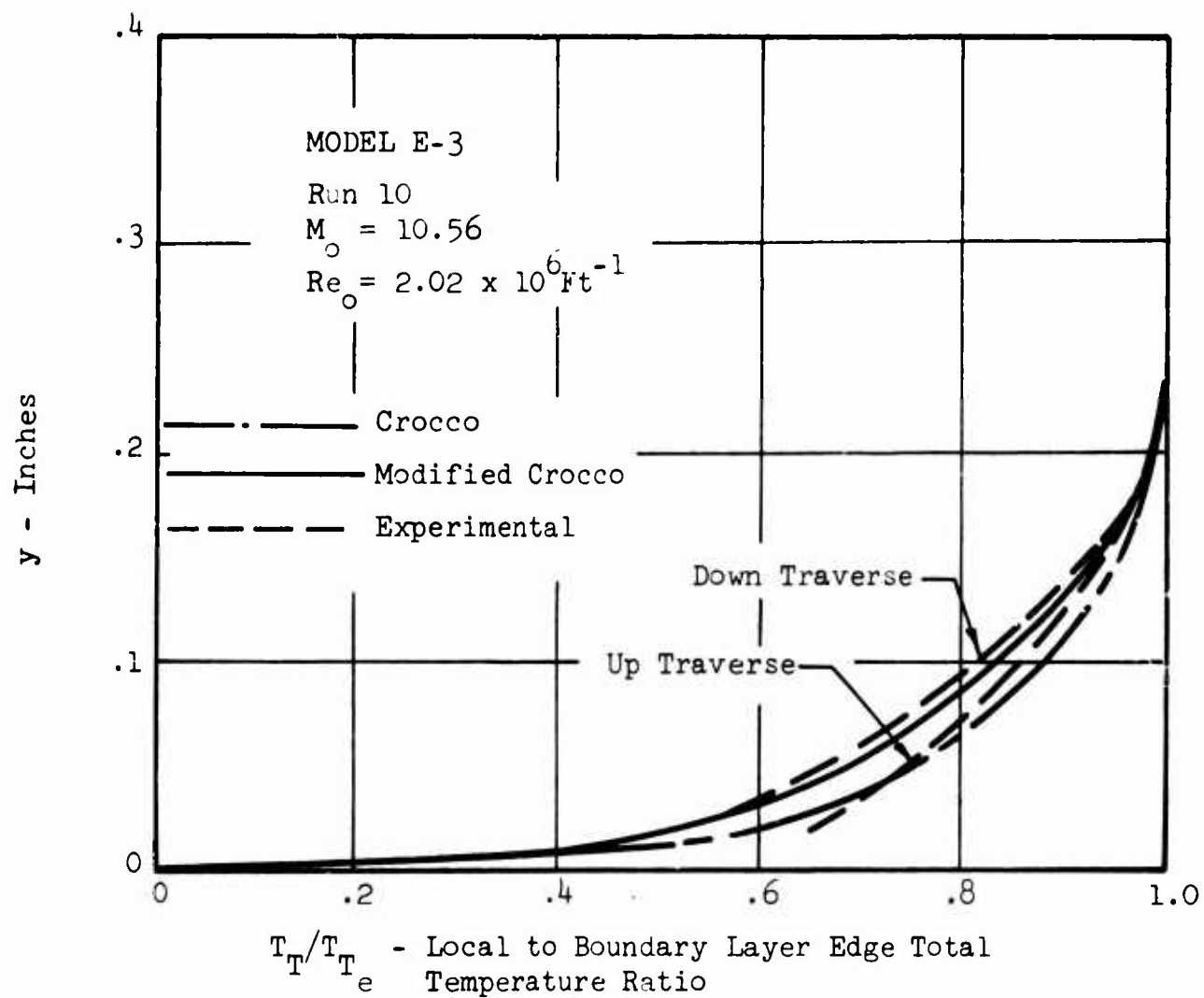


Figure 166 THEORY/DATA TOTAL TEMPERATURE PROFILE COMPARISON

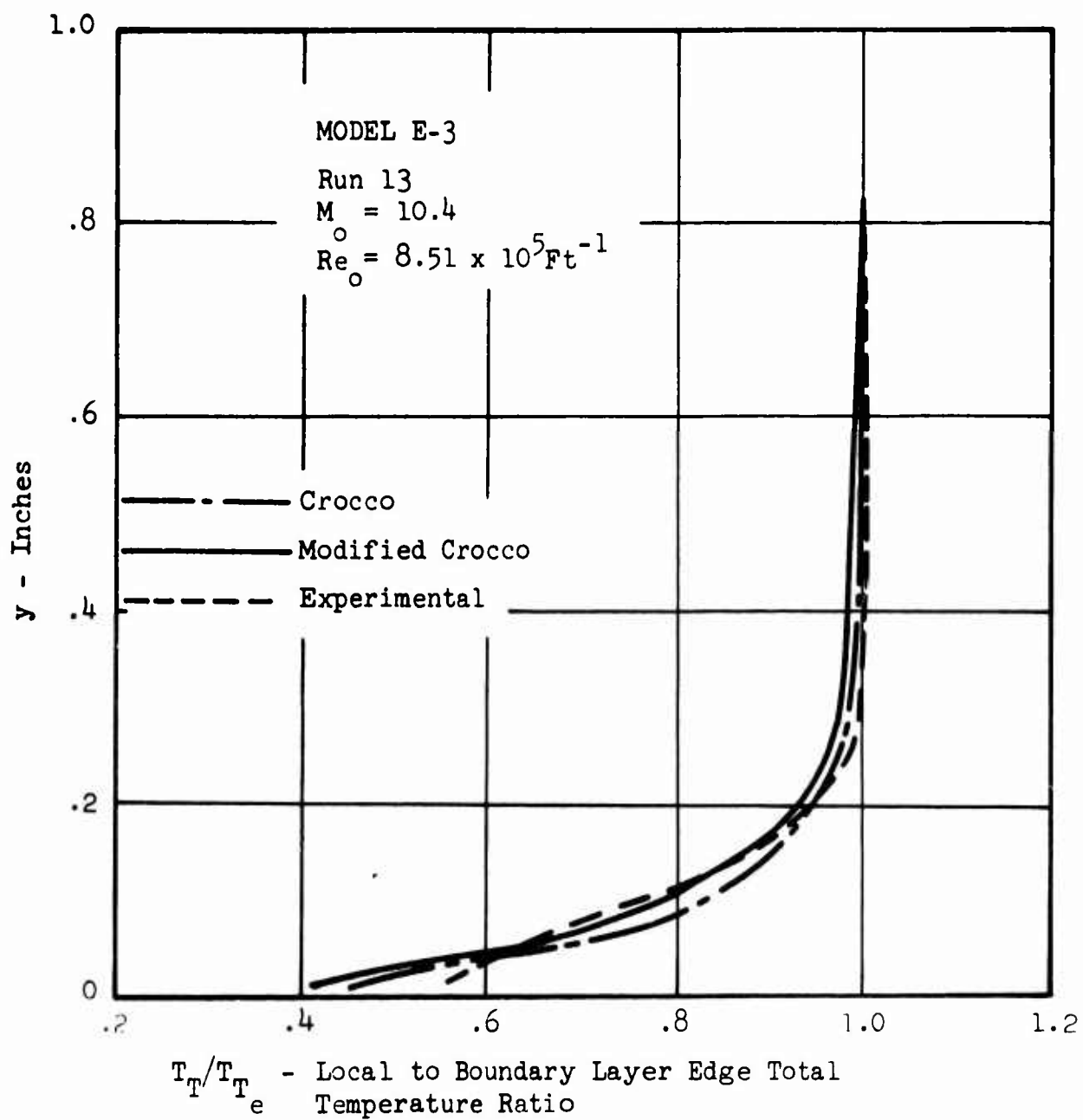


Figure 167 THEORY/DATA TOTAL TEMPERATURE PROFILE COMPARISON

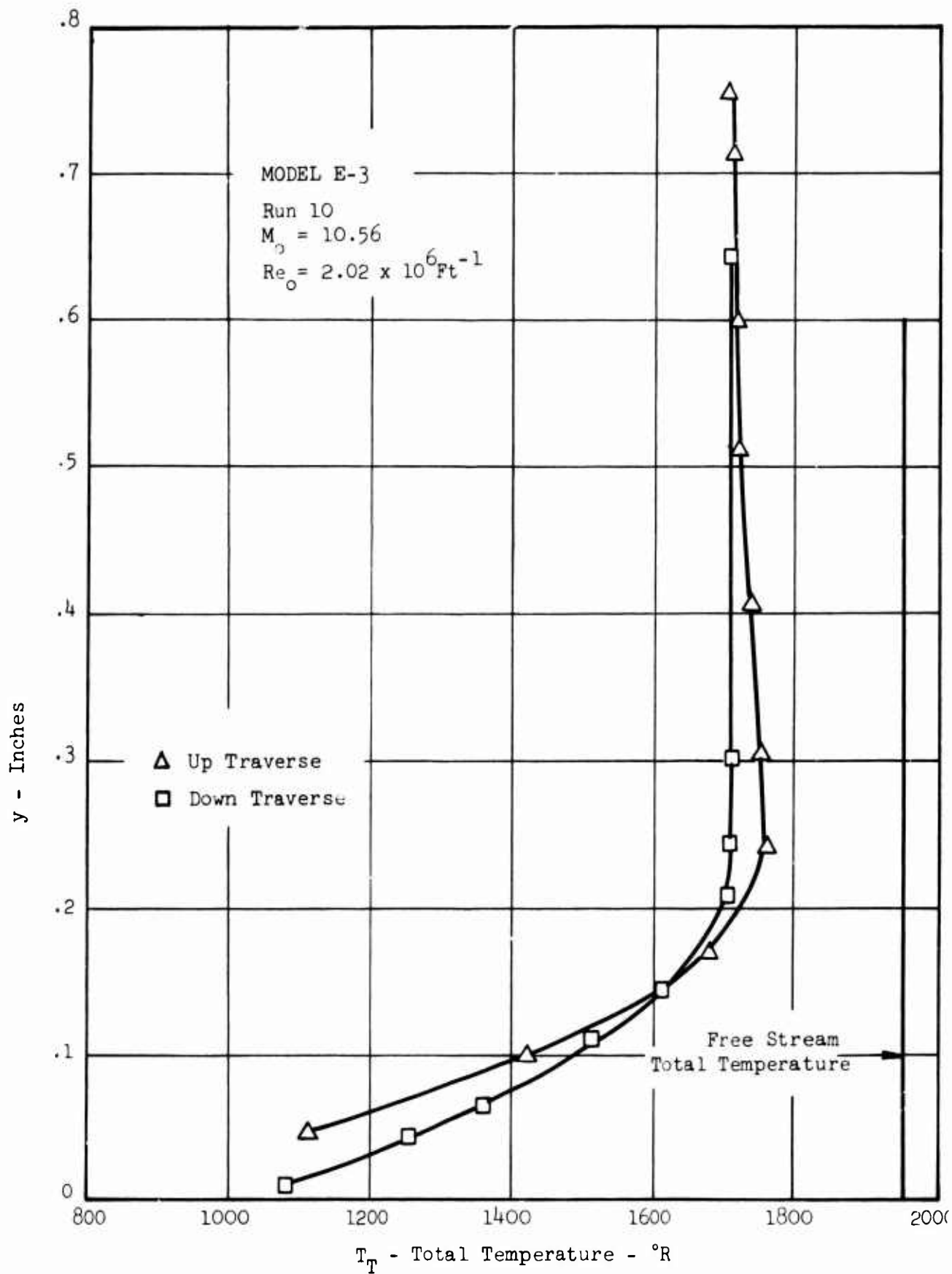


Figure 168 TYPICAL TOTAL TEMPERATURE PROFILE DATA

**BLANK PAGE**

TABLE I

MODEL C (RAMP ONLY)

PROFILE ANALYSIS SUMMARY

RUN	M <sub>O</sub>	STA	Re <sub>e</sub> (FT) <sup>-1</sup>	δ* (IN)	θ (IN)	n	M <sub>e</sub>
22	10.55	1	2.31X10 <sup>6</sup>	.146	.00560	.960	9.06
10	10.55	2	2.34X10 <sup>6</sup>	.173	.00698	3.08	9.02
14	10.55	3	2.29X10 <sup>6</sup>	.214	.00941	6.56	9.00
15	10.55	3	2.62X10 <sup>6</sup>	.214	.00911	6.22	9.01
20	10.55	1	2.31X10 <sup>6</sup>	.183	.00770	3.79	9.07
19	10.55	2	2.33X10 <sup>6</sup>	.262	.01177	10.0	8.97
21	10.55	2	2.24X10 <sup>6</sup>	.242		9.30	9.00
18**	10.55	3	1.51X10 <sup>6</sup>	.322	.01470	11.2	8.06
23	10.40	1	1.00X10 <sup>6</sup>	.231	.00870	.942	8.80
11	10.40	2	7.56X10 <sup>5</sup>	.323	.01270	1.26	8.42
13	10.40	3	8.37X10 <sup>5</sup>	.324	.01355	1.24	8.58
71	7.34	1	2.94X10 <sup>6</sup>	.0943	.00691	3.96	6.50
76	7.34	2	3.31X10 <sup>6</sup>	.162	.0126	8.34	6.60
74	7.34	3	2.66X10 <sup>6</sup>	.220	.0176	7.95	6.50
69	7.34	1	3.76X10 <sup>6</sup>	.149	.0106	8.14	6.54
68	7.34	2	3.22X10 <sup>6</sup>	.221	.0166	7.42	6.58
73	7.34	3	3.60X10 <sup>6</sup>	.283	.0212	6.96	6.55
75	7.34	3	3.29X10 <sup>6</sup>	.272	.0210	6.82	6.55
70***	7.30	1	4.94X10 <sup>5</sup>	.207	.0108	.640	6.20
67	7.30	2	4.97X10 <sup>5</sup>	.201	.0152	1.14	6.12
72	7.30	3	5.86X10 <sup>5</sup>	.261	.0194	1.08 <sup>L</sup> 2.08 <sup>U</sup>	6.12

L Lower portion of boundary layer

U Upper portion of boundary layer

\*\* Survey did not extend to boundary layer edge

\*\*\* Survey indicated boundary layer separation



TABLE II

MODEL C

PROFILE ANALYSIS SUMMARY

RUN	$M_o$	ST <sub>A</sub>	$\theta_c$ (DEGREES)	$Re_e$ (FT) <sup>-1</sup>	$\delta^*$ (IN)	$\theta$ (IN)	n	$M_e$
48	10.55	3	5	$4.71 \times 10^6$	.143	.01219	10.4	6.20
49	10.55	3	10	$4.96 \times 10^6$	.077	.01196	11.3	4.40
50	10.40	3	1.5	$1.03 \times 10^6$	.218	.01262	3.7	7.28
51	10.40	3	5	$1.70 \times 10^6$	.109	.00848	11.1	6.34
58	7.34	2	5	$6.28 \times 10^6$	.109	.01246	5.84	5.04
61	7.30	2	2	$9.14 \times 10^5$	.140	.01249	1.24	5.50
62	7.30	2	8	$1.12 \times 10^6$	.044	.00729	20.0**	--

\*\* Outer edge of boundary layer

TABLE III

## MODEL E-3

## PROFILE ANALYSIS SUMMARY

RUN	M <sub>0</sub>	STA	TRIP	θ <sub>c</sub> (DEGREES)	Re <sub>e</sub> (FT) <sup>-1</sup>	δ* (IN)	θ (IN)	n	M <sub>e</sub>
5	10.40	1		--	6.58X10 <sup>5</sup>	.219	.00999	1.13	8.30
6	10.40	1		--	6.08X10 <sup>5</sup>	.210	.0104	1.18	7.97
8	10.40	2		--	6.38X10 <sup>5</sup>	.213	.0116	1.05	7.30
13	10.40	3		--	9.48X10 <sup>5</sup>	.165	.01105	2.65	7.22
4	10.55	1	#1	--	2.09X10 <sup>6</sup>	.141	.00581	1.27	8.79
10	10.56	2	#1	--	2.03X10 <sup>6</sup>	.130	.00707	3.58	7.90
46	10.56	2	#2	--	1.87X10 <sup>6</sup>	.146	.00961	3.45	7.72
11	10.56	3	#1	--	2.65X10 <sup>6</sup>	.151	.0103	11.5	7.36
45	10.56	3	#2	--	2.33X10 <sup>6</sup>	.170	.0125	13.6	7.27
7	10.56	1		--	1.96X10 <sup>6</sup>	.141	.00607	1.14	8.50
9	10.55	2		--	2.31X10 <sup>6</sup>	.133	.00679	3.50	8.14
12	10.56	3		--	2.56X10 <sup>6</sup>	.156	.0110	11.8	7.35
29	10.40	3		-1	7.12X10 <sup>5</sup>	.166	.0121	4.04	6.68
30	10.55	3	#2	-1	2.18X10 <sup>6</sup>	.161	.0118	12.5	6.96
50	10.56	2	#2	14.9	1.91X10 <sup>6</sup>	.141	.0074	9.17	7.80
38	10.56	3	#2	15.1	2.77X10 <sup>6</sup>	.175	.0115	13.5	7.57
94	7.30	1		--	1.79X10 <sup>5</sup>	.238	.0205	1.23	5.56
102	7.29	3		--	2.65X10 <sup>5</sup>	.268	.0264	1.25	5.41
57	7.30	1		--	2.56X10 <sup>5</sup>	.197	.0176	1.23	5.22
60	7.30	3		--	4.21X10 <sup>5</sup>	.150	.0157	4.08	5.36
56	7.34	1		--	2.05X10 <sup>6</sup>	.108	.0100	1.09	6.51
54	7.34	2		--	2.35X10 <sup>6</sup>	.113	.0111	8.87	6.27
58	7.34	3		--	2.61X10 <sup>6</sup>	.123	.0140	11.3	5.63
100	7.30	2		8.0	2.21X10 <sup>5</sup>	.239	.0279	1.42	5.37
79	7.30	3		3.0	2.64X10 <sup>5</sup>	.345	.0308	.907**	4.53
101	7.30	3		8.2	--	.498	.0543	Separated	3.66
78	7.30	3		15.0	3.17X10 <sup>5</sup>	.180	.0183	1.29 <sup>L</sup> 2.94 <sup>U</sup>	4.71
82	7.34	2		15.0	2.17X10 <sup>6</sup>	.112	.0109	9.40	6.04
92	7.34	3		3.0	2.36X10 <sup>6</sup>	.141	.0163	9.83	5.63
76	7.34	3		15.0	2.46X10 <sup>6</sup>	.131	.0143	9.63	5.65

L Lower portion of boundary layer

U Upper portion of boundary layer

\*\* Survey indicated boundary layer separation